Micro patterning of complex Waveguide Resonant Gratings (WRG)

Erieta-Katerina Koussi

N° ordre NNT: 2020LYSES027

THESE de DOCTORAT DE L'UNIVERSITE DE LYON

Opérée au sein du
Laboratoire Hubert-Curien

Ecole Doctorale N° 488
Sciences Ingénierie Santé SIS

Spécialité: Optique, Photonique, Hyperfréquences

Soutenue publiquement le **22/10/2020** par :

Erieta Katerina KOUSSI

Micro patterning of complex Waveguide Resonant Gratings (WRG)

Devant le jury composé de :

Stéphane CALVEZ	CR CNRS, HDR, LAAS, Toulouse	Rapporteur
Frédéric DUMAS-BOUCHIAT	Professeur, IRCER, Université de Limoges	Rapporteur
Marwan ABDOU AHMED	Docteur HDR, IFSW, University of Stuttgart	Examinateur
Laurent DUBOST	Ingénieur Chercheur, HEF/IREIS, Saint-Etienne	Invité
Christophe DONNET	Professeur, LabHC, Université Jean Monnet, Saint-Etienne	Examinateur
Florent BOURQUARD	Maître de Conférences, LabHC, Université Jean Monnet, Saint-Etienne	Co-directeur de thèse
Isabelle VERRIER	CR CNRS, HDR, LabHC, Saint- Etienne	Invitée
Yves JOURLIN	Professeur, LabHC, Université Jean Monnet, Saint-Etienne	Directeur de thèse

Δῶς μοι πᾶ στῶ καὶ τὰν γᾶν κινάσω

"Give me somewhere to stand and I will move the earth"

Archimedes, 287-212 BC,
Mathematician, physicist, engineer, inventor and astronomer

Acknowledgements

This dissertation, the fruit of three years of hard work and perseverance, is fully dedicated to my family, partner, friends, colleagues and mentors as a token of gratitude for their continued contribution and support. First, I would like to thank my Mom Alexandra and my Dad Sotiris not only for their constant encouragement but also for their unwavering love and ideals that they passed on to me during my life. In addition, I owe special thanks to my boyfriend Georgios Aznaouridis who believed in me and strongly motivated me not to quit my effort, helping me to overcome my daily obstacles. His love and patience strengthened the faith on me and inspired me to be better every day. I would also like to acknowledge my friend Elena who is always there when I need her and who pushed me to write down my thesis during the last summer despite the ups and downs we have spent together. Throughout the years of my thesis, I had the privilege of meeting some amazing people, who all had a part in shaping both me and my work. I would like to thank my friend and colleague Andrei Ushkov, who is an inexhaustible source of knowledge and who was always willing to explain anything I could not understand. My friend and colleague Rim Faraj with whom we pushed each other to achieve more. The other office colleagues, Maria Usuga, Marion Hochedel, Hugo Bruhier, Arnaud Valour, Julie Dutems, Emilie Laffond, Ratish Rao, members of the grating group, who made everyday life enjoyable.

My sincerest thanks to my thesis tutor, Yves Jourlin, who supervised me and always encouraged me to push my boundaries and strive for more. I am especially grateful to my co-supervisor and friend Florent Bourquard, who offered me the opportunity to work in the Hubert Curien Laboratory and was constantly present and scientifically curious like I was in the project we started together. Within this project, I would like to thank Laurent Dubost, collaborator of the HEF Company who offered me a good expertise on the magnetron-sputtering machine. Moreover, I would like to recognize Isabelle Verrier who took me under her wing and provided valuable guidance in the most critical points of this thesis. Finally, I would like to acknowledge Olivier Parriaux for the fruitful discussions we had.

Contents

Résumé

Cette thèse de doctorat intitulée “**Micro structuration de Réseaux Résonants complexes**” étudie les dispositifs de détection optique, qui impliquent diverses techniques de photolithographie et outils de micro/nanotechnologie pour leur fabrication. Ces dispositifs, dans leur forme classique, consistent en un réseau de diffraction formé de lignes microscopiques gravées périodiquement sur une surface photosensible, qui est déposée sur une couche diélectrique, le guide d'onde. Les deux couches sont supportées par un substrat. Pour activer les fonctions de détection, le réseau de diffraction doit être extrêmement sélectif, c'est-à-dire qu'il doit avoir la capacité de rejeter toutes les composantes spectrales reçues, en ne sélectionnant qu’une seule longueur d'onde pour la coupler au guide d'onde. Après le découplage, une réflexion dite résonante liée à sa très grande amplitude et sélectivité spectrale et angulaire se produit. Différents types de composants en fonction de l'application envisagée peuvent être réalisés sur différents types de substrats, matériaux ou géométries (plan, cylindrique).

L'un des projets de cette thèse consiste à concevoir des WRG (Waveguide Resonant Gratings) sur les parois intérieures d'un tube pour coupler les modes TE et TM à l’intérieur du guide d’onde. La fabrication est réalisée par un masque de phase radial spécialement conçu, tandis que la fonction optique est mise en évidence en utilisant un miroir conique, capable de réfléchir la lumière de manière isotrope pour l'excitation des modes.

De plus, des matériaux innovants peuvent être utilisés pour leur intégration dans des structures résonantes planaires. L'un des matériaux à l'étude pour le deuxième type de composant est le dioxyde de vanadium (VO_2), qui subit respectivement des transitions de phase de premier ordre (isolant vers métal) à basses et hautes températures. La fabrication d'un composé aussi délicat est complétée par deux méthodes de synthèse différentes, le dépôt par laser pulsé et la pulvérisation cathodique magnétron. La capacité d'induire une résonance en déclenchant thermiquement le dispositif est destinée aux applications de sécurité laser afin d'éviter l’endommagement lors d'une surchauffe.

Abstract

This PhD thesis entitled "**Micro patterning of complex Waveguide Resonant Gratings (WRG)"** studies the optical sensing devices, which involve various photolithography techniques and nanotechnology tools with clean room processes for their fabrication. These devices, in their classic form, consist of a diffraction grating formed by microscopic lines engraved periodically on a photosensitive surface, which is deposited on a dielectric layer, the waveguide. Both layers are supported by a substrate. To enable sensing functions, the diffraction grating must be extremely selective, i.e. it must have the ability to reject all the received spectral components, while selecting only one wavelength to couple it into the waveguide. After the out coupling, a reflection with a very large amplitude and great finesse occurs. Different types of components depending on the intended application can be produced on different types of substrates, materials or geometries (plane, cylindrical).

One of the projects of this thesis engineers WRG on the interior walls of a tube to couple TE and TM modes into the waveguide. The fabrication is achieved by a specially designed radial phase mask, whereas the optical function is highlighted by the use of a conical mirror, able to reflect light isotropically for mode excitation.

In addition, innovative materials can be used for their integration into flat WRG. One of the materials under study for the second type of device is the Vanadium Dioxide (VO_2), which undergoes first-order phase transitions (Insulator to Metal) at low and high temperatures respectively. The fabrication of such a delicate compound is completed by two different synthesis methods, the Pulsed Laser Deposition and Magnetron Sputtering. The ability to induce resonance by thermally triggering the device is intended for laser safety applications to avoid damage during overheating.

General Introduction

The "**Micro patterning of complex Waveguide Resonant Gratings (WRG)**" PhD thesis has been financed by the LabEX MANUTECH SISE (ANR-10-LABX-0075) of Université de Lyon, within the program "Investissements d'Avenir" (ANR-11-IDEX-0007) operated by the French National Research Agency (ANR) ANR project.

This PhD Thesis has been proposed in the project R2EX (Design and realization of resonant gratings with extreme efficiency) within the Axis 3 (Perception Engineering & White Light Processing) of the Labex MANUTECH SISE. The aim of the Axis 3 of the Labex MANUTECH SISE is to develop quantitative characterization methods (adjusted for example to human perception), but beyond that, to develop real materials and surface engineering for perceptual specifications or specific interactions with light. This project was in close collaboration between the Laboratory Hubert Curien and HEF /IREIS Company.

The objective of this thesis is to develop sensors for optical filtering applications using WRG (Waveguide Resonant Grating) configurations. These latter are proposed with complex geometries in cylindrical form or with integrated layers of attractive materials (VO_2) in waveguides for optical resonances.

Waveguide resonant gratings or resonant waveguide gratings, guided mode resonant gratings or also waveguide-mode resonant gratings have been known for a long time, since the beginning of the eighties. They are used in the fields of lasers (wavelength filtering, polarization control, transverse mode control…), sensors (bio, chemical sensors), photo-detectors, color rendering and color effects, energy (solar cells) … Most of the time, Waveguide Resonant Gratings combine surface microstructures and dielectric thin films to exploit the so-called 100% efficiency resonant (abnormal) reflection for one wavelength (and one polarization), in opposition to the so-called abnormal and extraordinary transmission when one describes plasmonics based waveguide in a metallic thin film, embedded in a dielectric film. WRGs use periodic microstructures, such as gratings and high refractive index for the dielectric thin film. In order to couple wave-guided modes in the thin film, gratings are high spatial frequency gratings to only use the 0^{th} order that is a subwavelength grating. Even though WRG are well known theoretically, they are not extensively exploited in industry and in everyday life. One of the reasons, which could explain such fact, is the difficulty to fabricate high efficiency and reproducible WRG. To achieve 100% resonant reflection, according to the design and modeling

of the WRG, many parameters must be well controlled: grating parameters (duty cycle, depth, roughness, homogeneity….), and waveguide parameters (thickness, refractive index, roughness…).

Within this PhD thesis, we propose to exploit two separate approaches using WRG. The first one deals with a perfect circular grating, printed inside the inner surface of a tube, in order to measure resonant reflection considering an infinite WRG, in a complex measurement set-up. The grating has been fabricated using the cylindrical lithography-based phase mask technique developed a few years ago at the Laboratoire Hubert Curien. The second approach is well known and exploit thermally activated waveguides, using VO_2 phase change material. In the latter case, the idea is to control the resonant reflection thermally and to propose an ingenious design. In both approaches, modeling, design, fabrication and measurement are well described and discussed.

The manuscript consists of 5 chapters:

Chapter 1 introduces the basic principles of WRG configurations with a comprehensive analysis of their structure and operation. In the first part, a historical review describes Wood‘s first observations of the resonance phenomenon, which was initially identified as an anomaly, and continues with the long-term study of its understanding and exploitation in sensing. Such resonances, which correspond to sharp peaks in reflection, occur once the incident light is coupled to the waveguide modes propagating in the waveguide layer. To direct incident light in the waveguide region a corrugation on its top is necessary. The space between the corrugation grids is called period and must be of the order of micrometers and below to generate fine optical responses in the range of the visible and near infrared. These structures dependent largely on the angle and polarization of the incident light, but also on the effective index of the layers and structural characteristics. The aforementioned parameters, except polarization, are involved in the grating equation, which calculates mathematically the diffraction orders that are expected to be supported by the structure, while a graphical geometrical representation using the Ewald Sphere illustrates the direction of the modes. For additional optimization, dedicated programs as “MC Gratings” and Modal Collinear method predict the final features of the resonance (spectral and angular width).

Following the theoretical analysis, the studied structure must be completed through high technological methods, precise control and customized tools. Chapter 2 describes all the technical steps followed for the construction of the configuration studied in this dissertation,

which consists of a waveguide and a diffraction grating. To fabricate thin layers with well-controlled properties, we used a negative-based sol gel resist for waveguide deposition and a positive S1805 photoresist for grating patterning. The protocol of the sol gel is developed at Hubert Curien Laboratory to be adaptable to waveguide films. Spin and dip coating techniques were used for layer deposition, compatible with flat and cylindrical substrates respectively. The micro patterning of the positive photoresist is performed with a photolithography process; laser interferential lithography obtained from the contribution of two optical fibers for planar structures and phase mask lithography for cylindrical devices as it will be discussed below. In both cases, the interferogram becomes immediately visible after the development in the TMAOH (trimethylamine N-oxide). As presumed, each treatment step is highly dependent on ambient temperature and conditions and requires clean room elaboration for contaminant free and well-structured patterns. At the end of the process and in case of a slightly altered grating, a plasma technique can be implemented to adjust the thickness to the original simulated one.

Once the techno-optical expertise has been gained, Chapter 3 proceeds with the presentation of the one of the main works of this dissertation: the WRG fabrication on the inner walls of a miniaturized cylindrical substrate. This project presents an 8-mm diameter tube of fused silica that is structured on its inside cavity with a thin sol gel waveguide and a positive photoresist grating. The patterning of the grating is performed by a radial phase mask, which is conceived, designed and fabricated exclusively for cylindrical grating fabrication. This technological compound is specially designed to diffract only the ±1 orders transversally to the tube axis while extinguishing the 0^{th} order parallel to it. After a proper alignment of the tube with the radial phase mask, the interference of the orders leads to a stitchingless cylindrical grating that appears upon TMAOH development **(Figure 1)**.

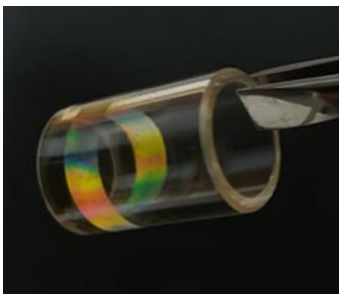

Figure 1: Micro patterned grating on a TiO_2 sol gel-made waveguide layer in the hollow of a fused silica tube.

The resonance efficiency of the prepared device is characterized with the aid of a 90° apex conical mirror that enables the transformation of plane waves into cylindrical waves. The mirror

is inserted to the hollow of the tube and the incident light after being circularly polarized, impinges on the mirror and is reflected holistically to the annular WRG. At the end of the mode coupling, the expected resonances in TE and TM polarizations in the near infrared range are measured by an optical spectrometer. The device is planned for gas or liquid sensing applications.

Chapter 4 displays an extensive study on the fabrication of VO_x (with x as close to 2 as possible) layers. The VO_2 chemical element is a high interest element that undergoes an insulator to metal (IMT) transition at a critical temperature of T~68°C, with simultaneous electrical and optical switching in the near infrared. Usually in the form of thin films, VO_2 is attempted to be manufactured by two methods: The Pulsed Laser Deposition (PLD) developed at the Hubert Curien Laboratory and the pulsed DC magnetron sputtering technique performed at the HEF Group Company (IREIS). The first method in combination with the Rapid Thermal Annealing (RTA) aimed to lower as much as possible the annealing temperature to be compatible with several substrates. Thus, various substrates are tested as well as oxygen pressures during deposition and annealing, temperature and annealing time whose effects on VO_2 synthesis is investigated **(Figure 2)**.

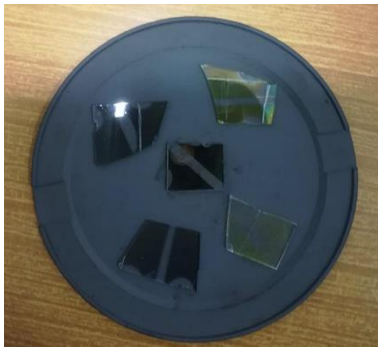

Figure 2: Various substrates that have undergone the effect of oxygen pressure during deposition and of annealing process.

The second method also succeeded in forming a VO_2 layer with a homemade vacuum furnace on SiO_2 substrates. Upon completion of the VO_2 thin films Raman, AFM, and SEM measurements are performed. Systematically, the optical transmission and hysteresis width between cold and hot states, phase transition temperature and transmittance amplitude are measured and compared by spectroscopic means.

Chapter 5 utilizes the PLD or pulsed DC Magnetron Sputtered switching layers to incorporate them into WRG demonstrators for Q-switching laser prospects. The devices can be then thermally triggered and emit or absorb optical dielectric resonant excitations in the NIR band.

According to the synthesis method, two designs are proposed. The PLD VO_2 film is deposited in the proximity of a TiO_2 anatase film to form a bilayer waveguide with almost equal refractive indices that enhance the total reflection criteria. An upper positive photosensitive layer is patterned on the waveguide and the overall is supported by a SiO_2 substrate. This configuration permits the propagation of the fundamental mode. The magnetron sputtered design consists of a triple layer waveguide, which is calculated to only propagate the second mode. The thin VO_2 film is covered up and down with a Si_3N_4 layer that protects it from oxidation while above it is structured by a positive resist corrugation. The whole slab is deposited on a SiO_2 substrate **(Figure 3)**.

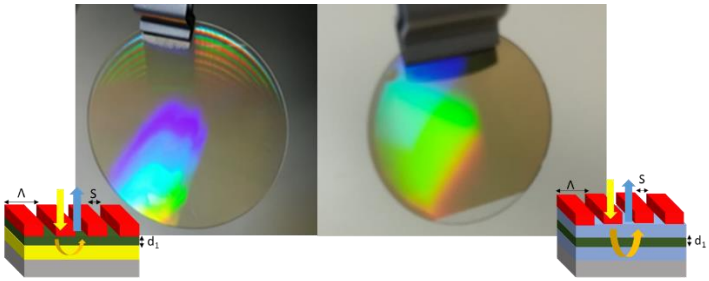

Figure 3: Fabricated structures on 1-inch substrates with the corresponding illustration; lower right for PLD-made (left) and pulsed DC magnetron sputtered (right), VO_2 layer.

The operational wavelength for both was set to λ=1500 nm. The resonance performance of these two structures are compared in reflection and transmission in TE polarization under ambient and heating temperatures with optical spectrometry. In addition to optical measurements, AFM and SEM analysis provided additional information on the fabricated structural features.

CHAPTER 1

Introduction to Waveguide Resonant Gratings

1.1 Introduction

This chapter starts with a brief overview of the history and development of grating science and technologies. In the research of gratings, the diffraction gratings are demonstrated and the basic principles are explained. Examples of different profiles and features are given, which show the particular behavior in illumination under different diffraction regimes. The grating equation quantifies this behavior by including the resulting diffracted orders, angles of the incident and diffracted light and refractive indices. A geometrical configuration using the Ewald sphere summarizes graphically all the simultaneous actions and sheds light on diffraction and mode coupling mechanism. Following, the effect of polarization on grating responses is discussed. Extending the study of Waveguide Resonant Grating (WRG), a simple configuration of a 1D planar waveguide below the diffraction grating is described. The resonance and the mode coupling inside the waveguide and under different conditions of illumination (incidence and polarization) are evaluated mathematically and graphically, resorting to the necessary Ewald Sphere reference. Then, a study on structural features and polarization states shows the impact on resonance performance and spectral responses respectively. In the final section, some numerical simulations decompose the grating problem and examine the electromagnetic field and the dielectric permittivity at each interface. All the modeling codes used in this doctoral dissertation are based on the Rigorous Coupled Wave Analysis and the Modal Collinear code of the MC Gratings method [1].

1.2 Historical Review

In 1786, Rittenhouse was the first to conceive a primitive form of diffraction grating by fabricating a frame of 50 hairs with a half-inch of distance between them, spaced by two fine threaded screws [2]. 35 years later, Joseph von Fraunhofer fabricated a metal wire diffraction grating for spectroscopic measurements. The grating dispersion enabled him to quantify the absorption lines of the solar spectrum, known since then as Fraunhofer lines [3]. In 1902, Wood

noticed unexpected fluctuation in the intensity of the reflected light when illuminating a metal grating with incandescent vertical polarized light with respect to the grating grooves. Instead of having a continuous spectrum he had found a drop from maximum to minimum illumination by a factor of 10 occurred "within a range of wavelengths not greater than the distance between the sodium lines" [4]. Since then, the already known principles of diffraction grating were unable to explain the phenomenon named "singular anomalies" or Wood's Anomalies. Lord Rayleigh in 1907 demonstrated that the profile of such spectra is due to higher propagating diffraction orders, which emerge in a tangential angle to the grating surface. Such anomaly occurs at specific wavelengths where diffracted orders change from evanescent-to propagating, now known as the Rayleigh wavelengths [5]. Rayleigh related all the parameters to one equation **(Equation 1.1)** that proved to be useful for calculating the Wood's anomalies.

$$n_i \sin(\theta_i) = n_d \sin(\theta_m) \pm \frac{m\lambda}{\Lambda} \qquad \textbf{Equation 1.1}$$

Where θ_i is the incident angle in which the anomaly occurs and θ_m the diffracted angle of the m^{th} order with m an integer number, λ the wavelength, n_i , n_d the refractive indices of the incident and diffractive medium respectively and Λ denotes the period of the grating corrugation. In 1941, U. Fano, made a step forward by defining two types of anomalies: the Rayleigh-type and the diffuse anomaly. The first one is characterized by the presence of a sharp drop in the intensity of the high-diffracted orders. Under a specific wavelength and angle of incidence, these orders are diffracted with a grazing angle along the surface. The second type, termed for the sake of Fano diffuse anomaly is revealed by a nonlinear diffusion with abrupt minimum to maximum intensity changes associated with lossy metal gratings [6]. Several years later, Palmer showed that even under P-polarization illumination parallel to the grooves could bear anomalies if the grating depth is deep enough [7]. The influence of the shape of the grating has concerned also Lippmann that used the approximations of Rayleigh to reexamine the wave scattering for deep gratings [8]. In the decade of 60's some mathematical analyses followed and addressed multiple scattering problems based on the well-defined electromagnetic scattering from different obstacles in order to clarify further the anomalies [9]. In 1965, Hessel & Oliner introduced the concept of guided waves as opposed to the approach of scattered waves, offering likewise a new understanding of Wood's anomalies. An explanation of the second type of the Fano "diffuse anomaly" is related to the guided complex wave supportable by the grating, i.e. the leakage of the field out of the structure that remains in phase and interferes constructively

producing anomaly [10]. In 1973, a theoretical work of Neviere *et al.* proposed a new structure consisting of a dielectric coated metal grating where resonance phenomena could be sustained by both polarizations, perpendicular [11] and parallel [12] to the grooves. The authors attributed this behavior to optical modes that existed in the waveguide underneath the grating. In 1985, Mashev & Popov noted a breakthrough when they have experimentally demonstrated the efficiency of up to 100% of zero-order reflection **(Figure 1.1)** derived by the guided mode excitation in a corrugated waveguide [13].

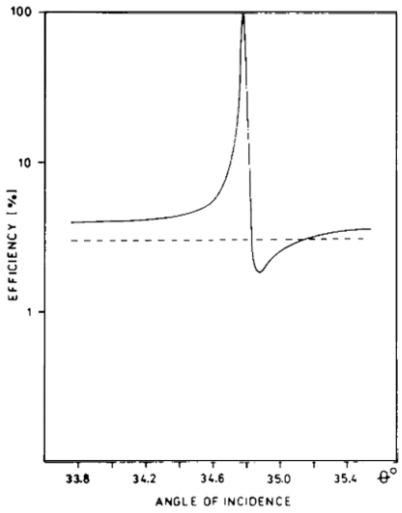

Figure 1.1: Zero-order reflected efficiency of a sinusoidal grating coated with a 0.7 μm thin dielectric layer (solid line) and non-coated grating (dashed line) as a function of angle of incidence [13].

Later, Avrutsky and Sychugov associated the radiative losses in the structure to the angular linewidths and resonance response for normal and oblique incidence [14].

Further research was conducted by Magnusson and Wang who calculated by RCWA the exact positions of the resonances in high-modulated gratings. For weak grating modulations, the guided mode wavenumber condition is used to predict the wavelength or range of the incident angle capable of exciting the resonances **(Figure 1.2)** [15].

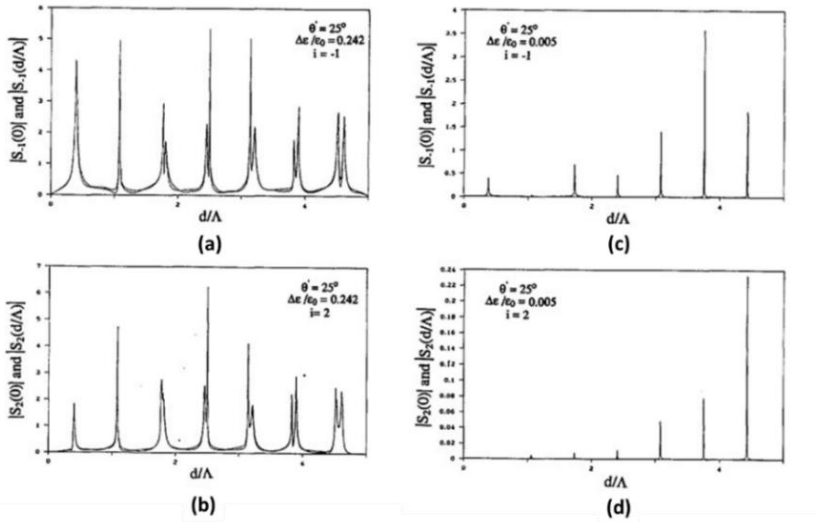

Figure 1.2: S_i (*0*) and Si (*d/Λ*) amplitudes of evanescent waves in a high and low-modulated grating with a step size of Δ (*d/Λ*) = 1×10^{-2} (a), (b) and Δ (*d/Λ*) = 6.25×10^{-3} (c), (d) respectively, (*d* the width of the waveguide and *Λ* the grating period) [15].

Based on the obtained experimental and computed narrowband spectra, they proposed a series of applications like electro-optic switches and optical filters [16]. Afterwards, an increasingly number of researchers followed, to analyze the resonance characteristics [17–24] and to construct their own devices [25–27] **(**Figure 1.3**)** with improved performances [28–33].

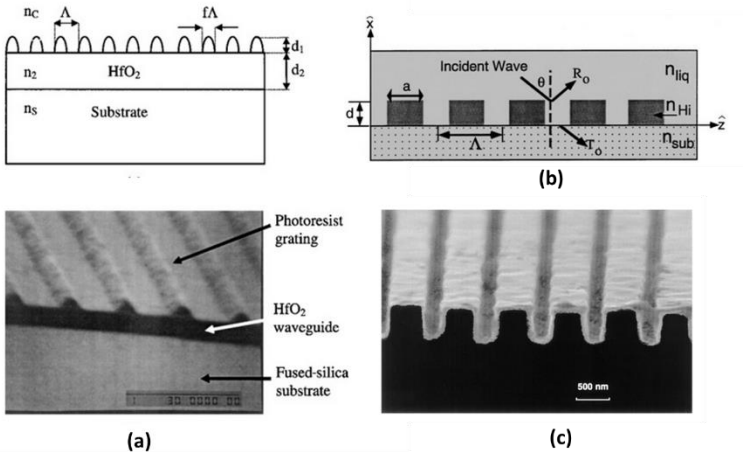

Figure 1.3: Design of Resonant Grating Devices consisting of a fused-silica substrate, HfO_2 waveguide and Photoresist Grating (a), fused-silica substrate and a high-index Si_3N_4 grating surrounded by liquid (b), Si_3N_4 substrate and Si grating (c) [25–27].

These devices have been referred to as Resonant Waveguide Gratings (RWGs), also known as Guided Mode Resonant (GMR) gratings, Waveguide-Mode Resonances (WMRs), leaky mode Resonant Gratings, Resonant Subwavelength Gratings (SWGs) or Resonance Grating Couplers.

The development of these configurations has been of great interest ever since and their performance is one of the main objectives of subsequent research. Searching to understand and reduce the losses, Norton *et al.* [34] used the coupled mode theory to describe the radiative coupling loss of the planar waveguide dielectric grating with an approximate analytical closed-form expression. This model was combined with the approximated Lorentzian function resonance response, formulated by Neviere [12], who linked radiative loss to spectral and angular linewidth. Additionally, Sharon and Rosenblatt introduced the interference approach to correlate the absorption/scattering losses in the resonance bandwidth and shift in lossy dielectric structures [18,20]. Immediately after, they have demonstrated a very narrow spectral width with a finesse of 6000**,** easily obtained at a normal incidence for a wavelength of ~1.5 µm **(Figure 1.4)** [18].

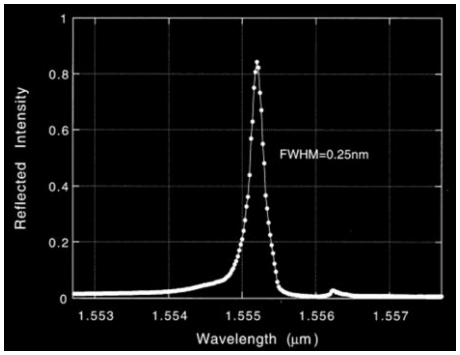

Figure 1.4: Experimental reflected intensity of the Grating Waveguide Structure (GWS) semiconductor as a function of wavelength [18].

In search of a better understanding of the resonance effect, a deeper study of the electromagnetic properties is carried out by Tamir and Zhang [23], who studied the power flux and the field inside the dielectric grating by the rigorous theory **(Figure 1.5)**.

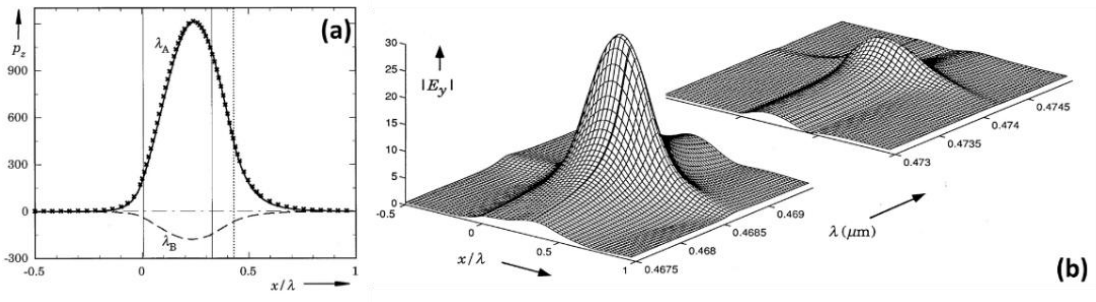

Figure 1.5: Power flux p_z (a) and transverse field amplitude (b) variation for a dielectric grating [23].

Moreover, a clearer insight of light propagation is achieved after the computation of leaky stop bands for photonic crystals and dielectric waveguides [24].

However, even if narrow spectral linewidths were well attained, the angular tolerance criteria for finite widths remained inadequate. A proposed structure by Lemarchand *et al.* [35] with double corrugated grating seemed suitable for solving the problem by using the coupling mechanism. Under normal incidence and using a double (2D) period grating, there is a possibility of enhancing the counter-propagating mode coupling, which promotes the widening of the angular linewidth **(Figure 1.6)**.

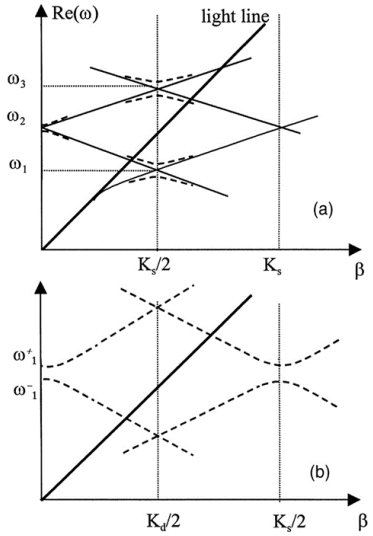

Figure 1.6: Dispersion curves of a gratingless structure (solid lines) and Single Resonant Grating (SRG) (dashed lines) (a) Double Resonant Grating (DRG) (dashed lines) (b) for increased angular tolerance [35].

Later, this was also feasible under oblique incidence [36]. Given the limitation of the angular problem, a study by Jacob *et al.* [22] suggested minimizing the dependence of the angular and spectral width by coupling the incident beam to a high-order mode. Fehrembach and Sentenac predicted high efficiency filtering of 2D gratings for unpolarized light using a phenomenological approach of diffraction gratings by perturbing a planar waveguide [37].

Since GMR structures presented a number of geometries and their properties were thoroughly analyzed, many scientific fields are based on the resonant characteristics for the application of technologies in: biosensors [38–42], anti-reflection coatings and solar cells [43–47], polarizers and quarter-wave plates [48–56], active tunable filters [57–62], spectrometers [63–67], photodetectors [68–72], laser resonators or mirrors [73–76], and optical and color security [77–80].

1.3 Principle of Diffraction Grating

1.3.1 Profile of diffraction gratings

A grating consists of a pattern of lines or apertures etched periodically on a surface and the space between two corrugations is called grating period Λ.

The most common grating is a 1D grating which is the subject of numerous studies because of its simplicity of understanding and ease of construction. However, a 1D grating can be encountered with various profiles such as rectangular or binary, blazed and sinusoidal structuration **(Figure 1.7)**. These distinctions are not exclusive since various configurations have been proposed and tailored according to the targeted applications. Apart from 1D grating corrugations of period Λ, 2D crossed gratings are also on the rise and are extensively suggested mostly for filter development due to their polarization insensibility [81–83] **(Figure 1.8)**. As follows, the grating architecture varies and can be extended to all sorts of materials and surfaces (supple, rigid, conical, cylindrical etc.). In any case, the diffractive patterns are unique according to the grating morphology **(Figure 1.9)**.

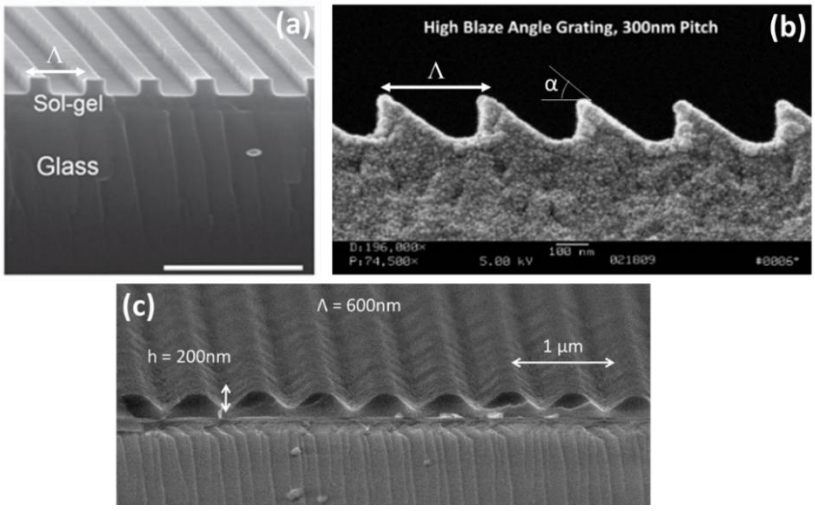

Figure 1.7: 1D surface relief gratings cross section SEM (Scanning Electron Microscopy) photograph (a) [84], (b) [85], (c) [86].

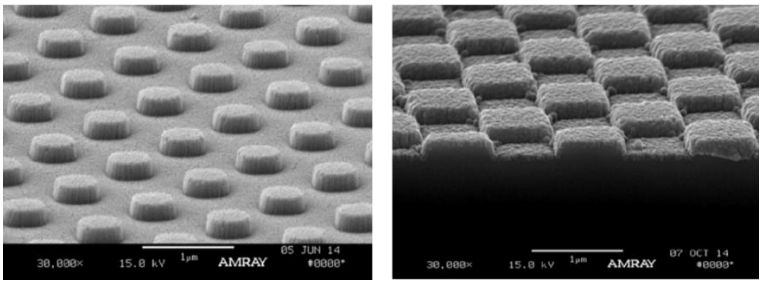

Figure 1.8: SEM photographs of two types of double-crossed corrugated gratings [87].

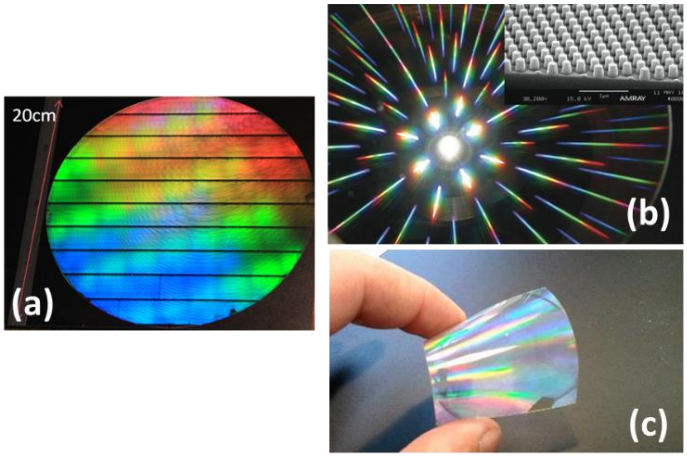

Figure 1.9: Diffraction of light by 1D rectangular grating [88] (a) and 2D patterned gratings [87] (b), [89] (c).

1.3.2 Grating Illumination

The diffraction effect of these elements may arise by two different types of illumination: conical or collinear.

For the collinear illumination, the normal or oblique incidence (θ_i) of the light beam is lying on the plane of incidence, which is perpendicular to the grating array (**Figure 1.10-a)**.

The light incidence though, may also form an angle Φ with the x tangent axis to the grating lines and an angle θ_i with the z-axis vertical to the plane of grating. As all the combination of angles are possible, the incident beam may form an invisible cone with respect to the origin axis O. This type is known as conical **(Figure 1.10-b)**.

The influence of type of incidence is commonly exploited for security reasons and is obvious in watermarks. A see-through element can change its color depending on the direction of light incidence [90] **(Figure 1.11)**.

Within this thesis, only collinear incidence will be used.

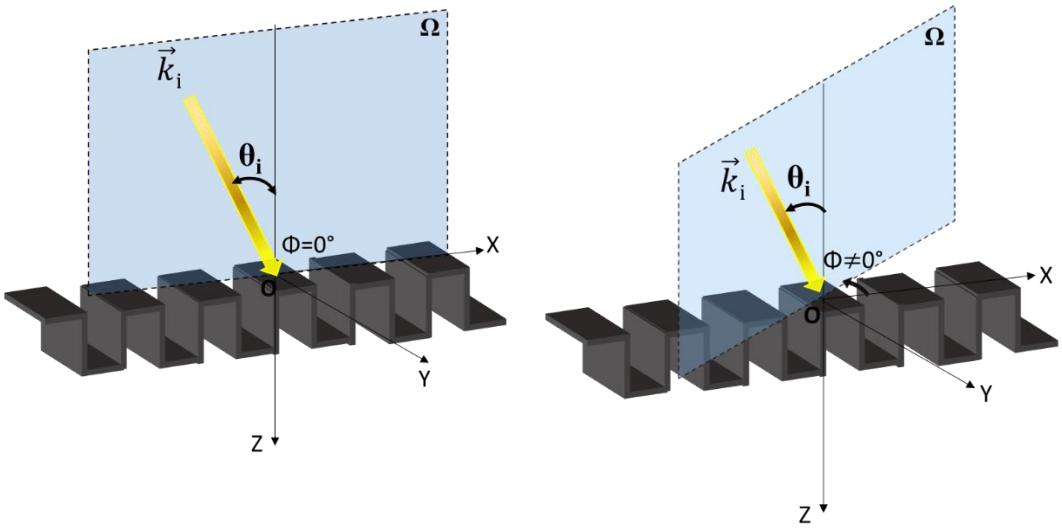

(a) **(b)**

Figure 1.10: Representation of the total collinear (a) and conical (b) incidence on a grating.

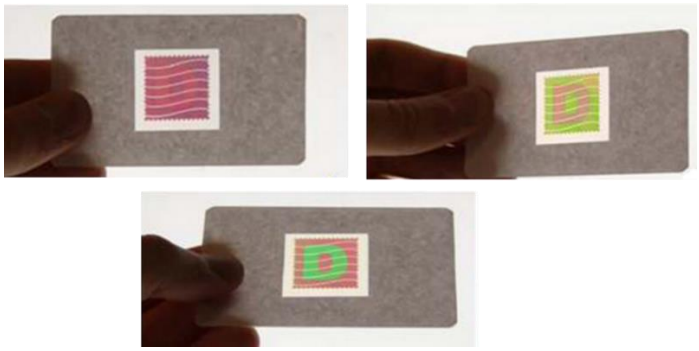

Figure 1.11: Watermark color change under a non-polarized white light seen in transmission under different angular directions [90] .

1.3.3 Diffraction regimes

A comparison between the order of magnitude of the grating period and the wavelength λ of light, can distinguish three regimes.

The diffraction regime where $\Lambda > \lambda_{surrounding}$, the near wavelength regime that is an intermediated regime with $\lambda_{grating} < \Lambda < \lambda_{surrounding}$ and the deep subwavelength regime with $\Lambda < \lambda_{grating}$ where $\lambda_{grating}$ and $\lambda_{surrounding}$ are the wavelengths in the corresponding medium (grating or surrounding media) **(Figure 1.12)**.

It is interesting to mention that in the intermediate region of near wavelength regime we meet the High Contrast Gratings (HCG) that are different from the Waveguide Resonant Gratings discussed in the **Section 1.5**. HCG support multiple vertical Bloch modes between the upper and lower grating boundaries that interfere strongly with the leaky waveguide modes (propagating waves along the grating) modifying likewise their dispersion equation [91].

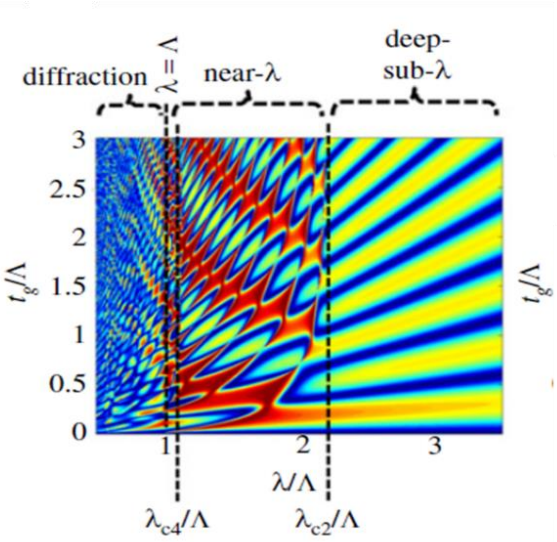

Figure 1.12: Reflectivity as a function of wavelength and grating thickness of three different gratings when radiated with a TE-polarized normal incidence. The mode cutoffs (λc_2, λc_4) and the first-order diffraction threshold $\lambda=\Lambda$ trace the limits of the three different wavelength regimes: deep-subwavelength, near-wavelength, and diffraction [91].

1.3.4 Diffracted orders and Grating Equation

A diffraction grating is an element that produces a set of reflected and transmitted beams named orders. Upon diffraction, an incident electromagnetic wave on a grating splits in multiple directions and the electric field amplitude or/and phase, is modified due to the periodic variation Λ of the grating. The diffraction grating can be physically compared to the Young slits where each ray of light diffracted by a slit interferes constructively with another ray of slit leading to the appearance of diffraction orders m **(Figure 1.13)**.

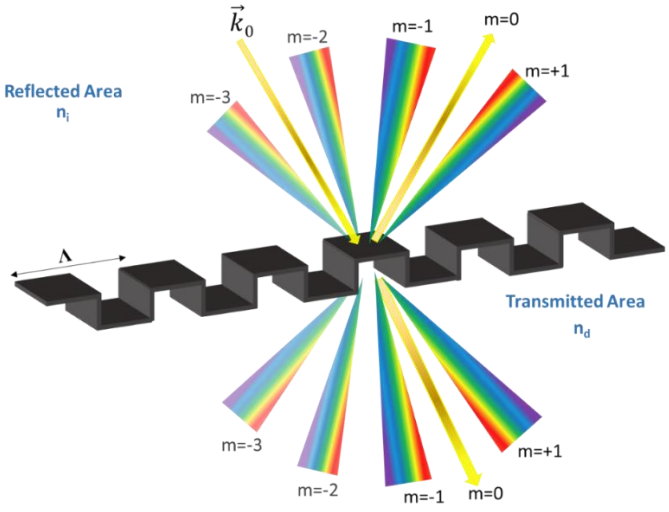

Figure 1.13: Diffraction Grating with diffracted orders in reflected and transmitted region.

The different arising directions of the orders m in reflection and transmitted regions are called spatial harmonics and are easily predictable by the grating equation. Respecting the afore-illustrated convention of angle direction we obtain:

For transmission:

$$k_0 n_i \sin\theta_i + mK_g = k_0\, n_d\, \sin\theta_m \qquad \textbf{Equation 1.2}$$

For reflection:

$$k_0 n_i \sin\theta_i - mK_g = k_0 n_d\, \sin\theta_m \qquad \textbf{Equation 1.3}$$

With $\|\overrightarrow{k_0}\| = 2\pi/\lambda_0$ the free space wave vector, $\|\overrightarrow{K_g}\| = \frac{2\pi}{\Lambda}$ the grating wave vector, n_i the refractive index of the medium of the incident beam, n_d the refractive index of the medium below the grating, θ_i the algebraic values of the incident beam and and θ_m the diffracted angle of the m diffracted order.

It is worth noting that the period of diffraction gratings is much larger than the impinging wavelength ($\Lambda \gg \lambda_0/n_i$) and for this reason, these gratings are also known as high order gratings **(Figure 1.13)**.

1.3.5 Representation in the reciprocal space with Ewald Sphere

The grating equation can be linked graphically to a vector construction on a diagram (called the k diagram) or Ewald sphere also called the reciprocal/indirect space. The Ewald sphere is a geometric representation of all the diffracted orders that propagate to and from the grating structure at a given wavelength. The diffracted orders (reflected and transmitted) as well as the incident beam are considered as wave vectors, and designed as horizontal projections in the indirect space or reciprocal space (k-space). They are transferred by the real grating geometry (direct space) to the Ewald sphere (indirect space). The different media are represented as semicircles with radius equal to the product of the free wave space vector multiplied to the refractive index of each medium i.e. $k = n_i k_0$. The origin is O, the x-axis separates the two semicircles and the y-axis is normal to the grating.

1.3.5.1 Normal Incidence

In normal incidence $\theta_i = 0°$, the orders ±1 are diffracted under the same angle. With a symmetric grating, the diffracted orders have the same efficiency either in reflection or in transmission when they pass from low to higher refractive index medium ($n_d > n_i$). In **(Figure 1.14)** the reflected orders in the incident medium are illustrated with black color and the transmitted with green. The grating vector K_g is configured by the projection of the diffracted orders on the k_x axis corresponding in the reciprocal space.

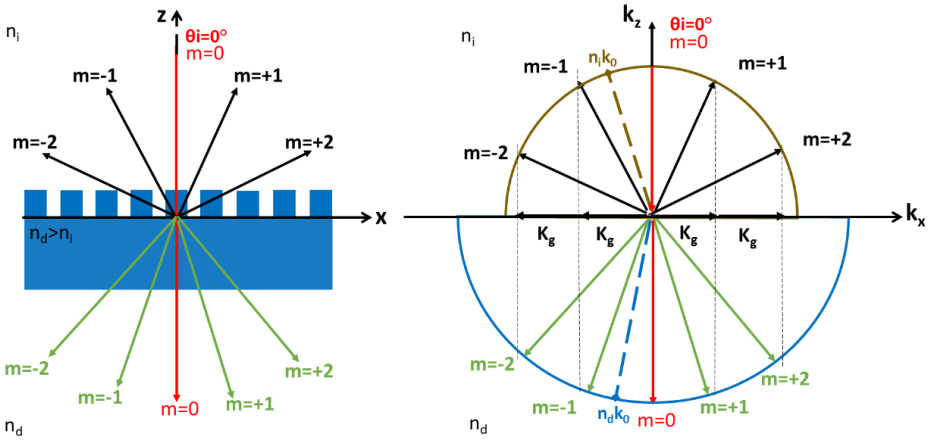

(a) **(b)**

Figure 1.14: Transfer from direct space (a) to the Ewald diagram (indirect space) (b) with normal incidence.

1.3.5.2 Oblique Incidence

In oblique incidence $\theta_i \neq 0°$, the diffracted orders are oriented symmetrically with respect to the angle of incidence. If the angle of incidence is highly inclined, it is possible that two opposite diffracted orders are not in the same optical medium and do not share the same efficiency as before. Now the projection on the z-axis of the incident wave vector is smaller than the $n_i k_0$ radius and the origin of the vector is not designed on the circumference of the upper semicircle **(Figure 1.15)**.

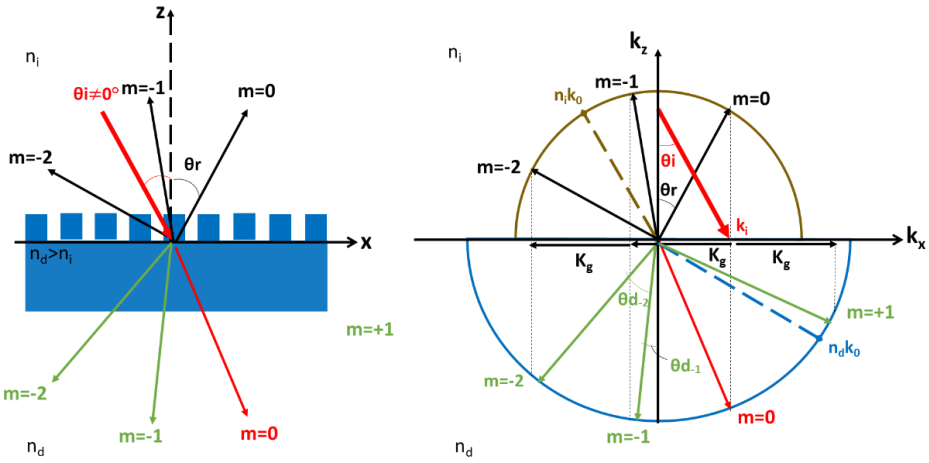

(a) **(b)**

Figure 1.15: Representation of the oblique incidence beam in direct space (a) and transfer to the Ewald diagram (indirect space) (b).

All the directions of the diffracted orders can be calculated using the diffraction equation **(Equation 1.2)** or **(Equation 1.3)** either for normal or oblique incidence.

1.3.6 Subwavelength Gratings

In a diffractive optical element we decrease the grating period until it is smaller than the order of the wavelength ($\Lambda \ll \frac{\lambda_0}{n_i}$), the diffracted orders can be eliminated and the grating works as an optical filter while allowing in one only order to exit. The light beam propagates undisturbed and energy is evenly distributed. This is defined as subwavelength grating. Under this geometry, only the zeroth diffraction order is propagating, while the higher orders are evanescent. Since subwavelength gratings maintain only the zeroth order, all power that is not transmitted through the zeroth diffraction order is reflected back and high reflectivity is achieved **(Figure 1.16)**.

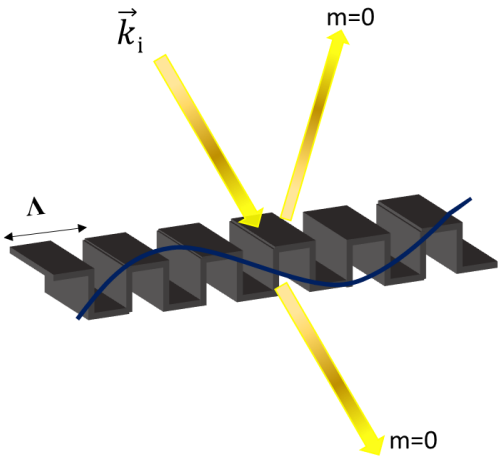

Figure 1.16: Schematic of the mechanism of a subwavelength grating with equal distribution of energy (in blue color).

1.4 Diffraction Gratings under polarized light

1.4.1 Polarization States

The plane wave is an optic transverse wave composed of electric and magnetic field that could oscillate randomly, but always perpendicular to each other and to the propagation path. This non-coherence characterizes the sun light, which is called non-polarized. Using special optical components, we can intervene on the natural light and fix the direction of its electric field rendering it polarized. The polarization of light often refers to the property of its electric field, which oscillates in only one direction: vertically, horizontally or even diagonally **(Figure 1.17)**. All these three orientations can be attributed as linear polarization, which is the most commonly used.

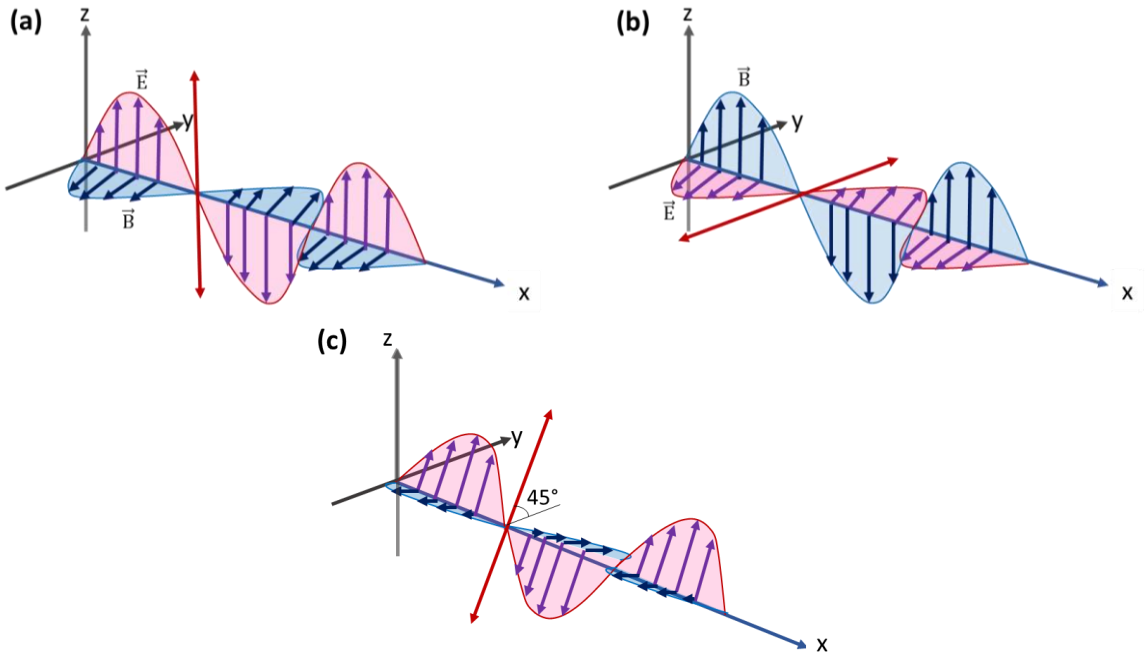

Figure 1.17: Linear vertical (a), horizontal (b) and diagonal (c) polarization. The red arrow illustrates the direction of polarization and the x-axis the direction of propagation.

However, in addition to linear polarization there are also other types such as circular and elliptical.

For the circular polarization, the electric field rotates when the wave propagates and its extremity describes a circle. This rotation can be clockwise (right hand) or counter-clockwise (left hand) when observed from the source. Along the propagation, the circular polarization maintains equal 90° phase difference between the two perpendicular components of the wave, which are of equal amplitudes **(Figure 1.18)**.

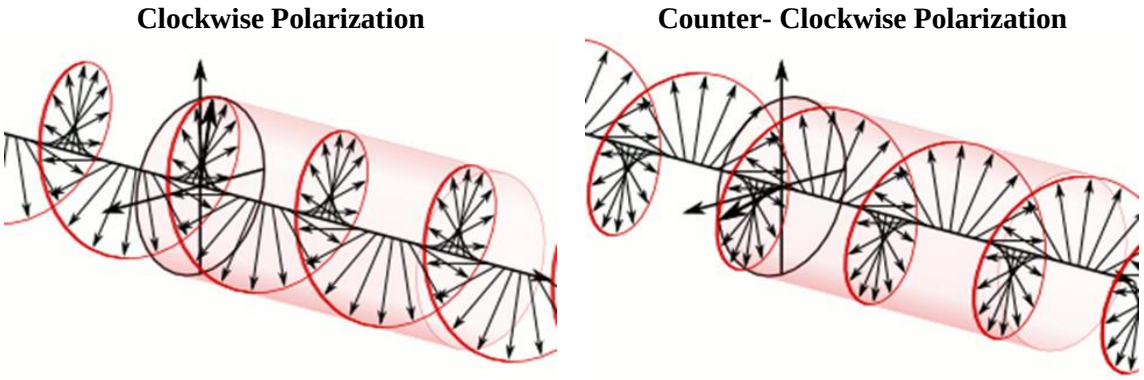

Figure 1.18: Clockwise or right hand (a) and counter-clockwise or left hand (b) circular polarization observed from the source [92].

The elliptical polarization differs from the circular polarization in amplitude or in phase. The elliptical polarization consists of two perpendicular components with 90° phase difference but with unequal amplitudes or even with equal amplitudes but phase $\varphi \neq \pm\pi/2 + m\pi$. This inequality makes the eccentricity less than 1 (e=1 for the circle) that attributes the form of ellipse to the extreme points of the electric field. There are also two orientations of the right and left hand for the propagation of the waves **(Figure 1.19)**.

Despite the fact that the elliptical polarization can be considered as a special case, it is in reality the dominant category that includes the two previous polarizations, linear and circular.

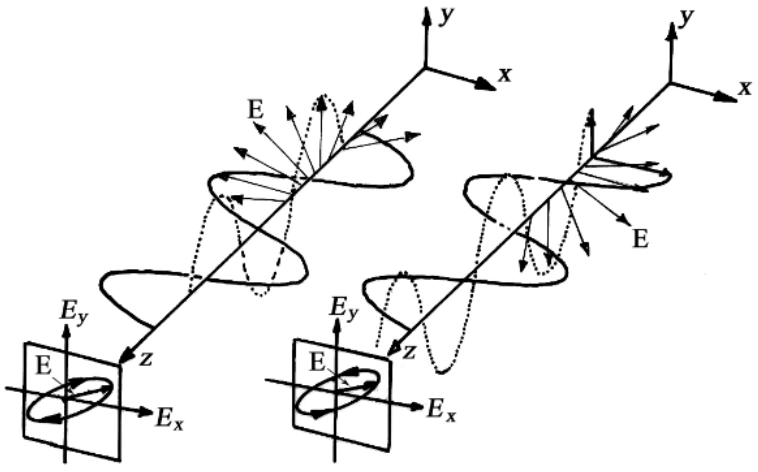

Figure 1.19: Clockwise (a) and counter-clockwise (b) elliptical propagation [93].

In our brief analysis, the polarization is described by the superposition of all the extreme points of electric field along time and space. However, if we examine the polarization at a given moment making a spatial cross-section of the beam we can distinguish additional categories [94]. Three types are typically mentioned, radial, azimuthal and spiral polarization **(Figure 1.20)** that are obtained with special optical vortex converters [95,96].

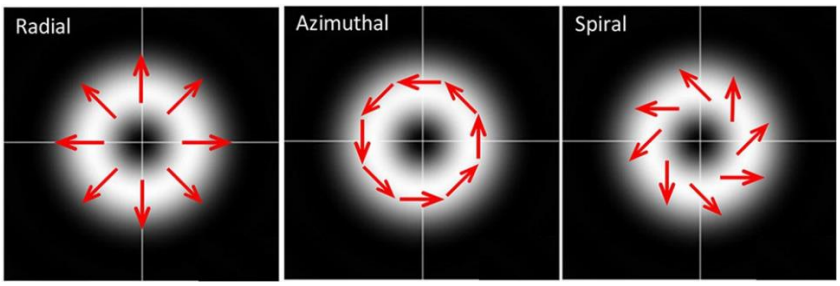

Figure 1.20: Local change of direction of polarization with red arrows on cylindrical vector beams [96].

As it will be discussed below, the polarization of light is a state that interacts with matter such as other properties like orientation and intensity. Fresnel Equations and Snell-Descartes law give a total overview of these interactions when light passes from one optical medium to another. Next, we will examine the light behavior when it impinges on corrugated surfaces such as diffraction gratings.

1.4.2 Diffraction grating dependence on light polarization

To form complex polarization states [97–99] or even use them to excite light in non-standard grating geometries **(see Chapter 3)** special diffraction elements are extremely useful. In other words, the relation between polarization and diffractive optical element is inextricably linked and will be discussed below.

Initially, we consider the interaction of electromagnetic light with a simple rectangular diffraction grating on a substrate. When light impinges on a grating with collinear incidence, the field vectors form a trihedral with the wave vector that lies in the plane of incidence Ω (Ω defined by $\overrightarrow{k_i}$ and z direction). Transverse electric or transverse magnetic polarization is defined as a function of their relative orientation with the grating lines. Electrical transverse (TE) or s-polarization is the configuration in which the projection of the electric field vector on the plane of the grating is normal to the plane of incidence or parallel to the grating lines and the magnetic field vector is in the plane of the incident wave. In magnetic transverse (TM) or

p-polarization, the vector of the magnetic field is normal to the plane of incidence or parallel to the lines of the grating and the electric field vector is in the plane of the incident wave. These configurations are illustrated in **Figure 1.21**.

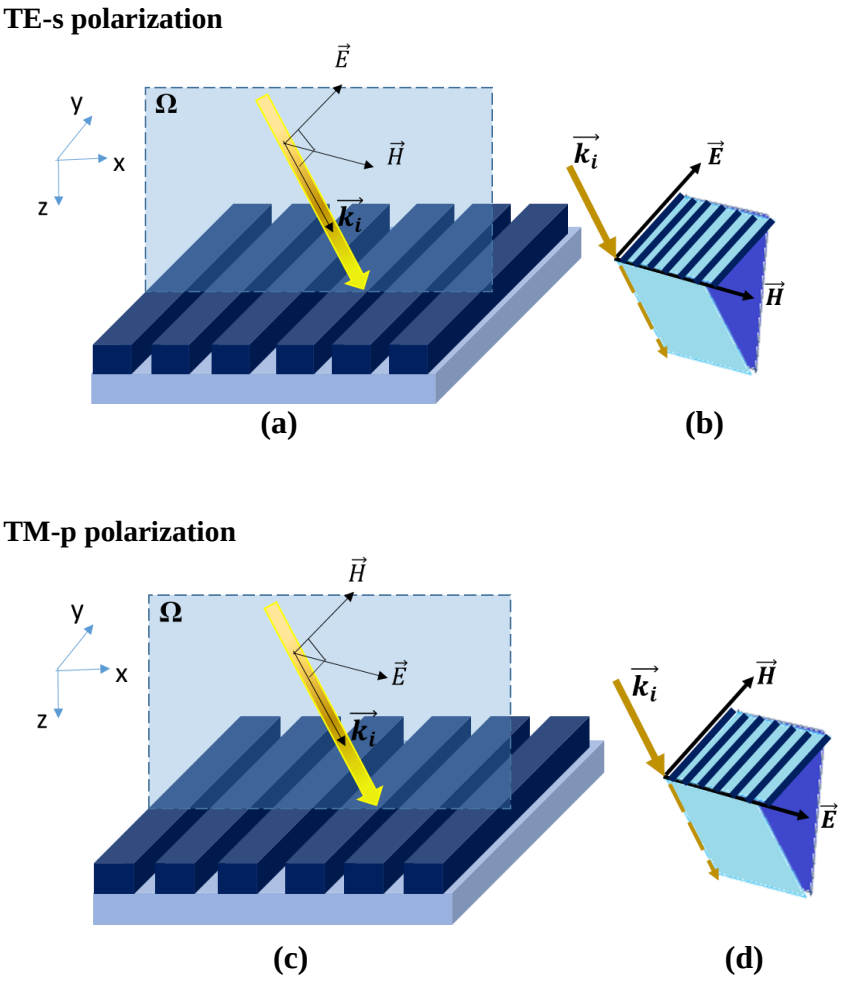

Figure 1.21: Polarization of incident light in relation to grating lines. TE (a) and TM polarization (c) of the incident $\overrightarrow{k_1}$ light and representation of the vectors forming a trihedral (b), (d) respectively.

1.5 Waveguide Resonant Grating

1.5.1 Structure of a Waveguide Resonant Grating (WRG)

The Waveguide Resonant Grating (WRG), also referred as Subwavelength Resonant Grating (SWG) or Guided Mode Resonant Grating (GMR) is a configuration usually consisting of a substrate, a high-index thin waveguide film in optical contact with an additional transparent layer in which a grating is etched.

The main structural characteristics of a 1D (periodic according to a single direction) WRG are illustrated in **(Figure 1.22)**.

Prior to the presentation of the resonance mechanism **(Section 1.6)**, the planar waveguide under the diffraction grating and the propagation of the modes within the guide are studied in the following **Section 1.5.2**.

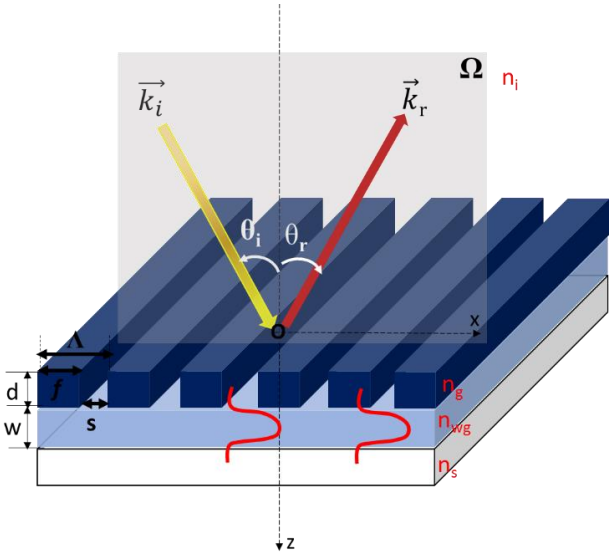

Figure 1.22: Geometrical structure of 1D Waveguide Resonant Grating.

Where:

n_i, n_g, n_{wg}, n_s are the refractive indices of superstrate, grating, waveguide and substrate respectively.

$\overrightarrow{k_i}$ and θ_i are the wave vector and angle of the incident beam respectively.

$\overrightarrow{k_r}$ and θ_r are the wave vector and angle of the reflected wave in the m=0 diffraction order.

d, w are grating height and waveguide thickness.

f, s are grating ridge and grating groove width respectively.

$FF = \frac{f}{\Lambda}$, the Filing Factor or Duty Cycle: (For binary gratings, the *FF* corresponds to Duty cycle).

$AR = \frac{d}{f}$, the Aspect Ratio.

1.5.2 Planar Waveguide

1.5.2.1 Dispersion Equation

In this Section, we decompose the waveguide resonant problem by initially focusing on the study of the planar waveguide-slab. As described above the insertion of light in a planar waveguide is realized by a grating or alternatively by a prism. After light insertion and mode propagation in the waveguide, a sharp resonance appears if only two specific conditions are fulfilled:

- the total reflection $n_s < n_{eff} < n_{wg}$, with n_{eff} the effective index, which states a number that relates the velocity of a light beam in the waveguide, seen as a propagative mode in the waveguide (for a given polarization and considering $n_s > n_i$).

- the constructive interference in the planar waveguide, which follows the dispersion equation.

The figure below illustrates the optical path of light and the needed geometry for the second condition **(Figure 1.23)**.

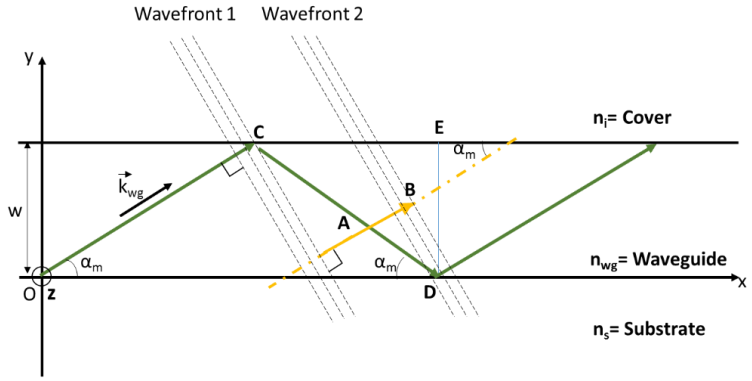

Figure 1.23: Representation of light propagation in a planar waveguide.

The plane wave in the medium of the waveguide is described by $e^{j(\omega t-\vec{k}_{wg}\vec{r})}$, where $|\vec{k}_{wg}|=k_0\, n_{wg} = \frac{2\pi}{\lambda_0} n_{wg}$ expresses the wave vector k_0 that is the free space wave vector and n_{wg} the refractive index of the waveguide. The propagation of the wave in the layer of the waveguide will take place if the wave interferes with itself constructively, i.e. if the phase difference between the two wave fronts is the same along their optical paths AB and CD and equal to 0 or $2m\pi$.

$$\Delta\Phi_{(CD\text{-}AB)} = \Phi_{CD} + \varphi_{(wg\text{-}i)} + \varphi_{(wg\text{-}s)} - \Phi_{AB} = 2m\pi \qquad \textbf{Equation 1.4}$$

The phase shifts $\varphi_{(wg\text{-}i)}$ and $\varphi_{(wg\text{-}s)}$ are due to the total reflection at each interface *i* (cover (i) or substrate (s)).

Following the geometry of the figure, we take:

$$\mathrm{CD} = \frac{\mathrm{w}}{\sin\alpha_m} \quad \text{and} \quad \mathrm{AB} = \mathrm{CB}\cos\alpha_m$$

Therefore, the related phases become:

$$\Phi_{\mathrm{AB}} = \mathrm{k_{wg}}\frac{\mathrm{w}(\cos^2\alpha_m - \sin^2\alpha_m)}{\sin\alpha_m} \text{ and } \Phi_{\mathrm{CD}} = \mathrm{k_{wg}}\frac{\mathrm{w}}{\sin\alpha_m}$$

The phase differences at the interfaces are equal to:

$$\varphi_{wg-j} = -2\arctan\frac{\sqrt{\cos^2\alpha_m - (n_j/n_{wg})^2}}{\sin\alpha_m} \qquad \text{(for TE polarization)}$$

$$\varphi_{wg-j} = -2\arctan\left(\frac{n_{wg}}{n_j}\right)^2\frac{\sqrt{\cos^2\alpha_m - \left(n_j/n_{wg}\right)^2}}{\sin\alpha_m} \qquad \text{(for TM polarization)}$$

With $n_j = n_i, n_s$ the refractive indices for cover and substrate respectively.

We define the effective index as $n_{eff} = n_{wg}\cos\alpha_m$ and the constant propagation β of the guided wave in the waveguide medium that is inseperably connected to the effective index by $\beta = k_{wg}\cos\alpha_m = k_0 n_{eff}$.

The replacements of the above relations to the initial **Equation 1.4** give:

$$\Delta\Phi_{\text{(CD-AB)}} = 2\mathrm{m}\pi = 2k_0 w\sqrt{{n_{wg}}^2 - n_{eff}^2} - 2\arctan\xi_{wg,s}\sqrt{\frac{n_{eff}^2 - n_s^2}{n_{wg}^2 - n_{eff}^2}} - 2\arctan\xi_{wg,i}\sqrt{\frac{n_{eff}^2 - n_i^2}{n_{wg}^2 - n_{eff}^2}}$$

Equation 1.5

With m = 0, +1, +2… and $\xi_{wg,j} = n_{wg}^2/n_j^2$ for TM polarization and $\xi_{wg,j} = 1$ for TE.

The above **Equation 1.5** is known as dispersion equation and calculates the effective index of the waveguide according to the polarization TE or TM. The relation implies that every m order corresponds to one effective index and to one and only angle of propagation α_m in the waveguide layer.

1.5.2.2 Mode Cut-off

The thickness of the waveguide will determine the number of modes that will be propagated within it. Multimode or single mode behavior can be forecasted a priori through the frequency for which the propagation angle α_m reaches its critical value α_{cr} or in other words when $n_{eff} = n_s$.

For TE polarization the cut off frequency ω_c and thus the cut-off wavelength λ_c is given by:

$$\frac{\omega}{c}\Big|_{\text{cut off}} = k_0 = 2\pi/\lambda_c = \frac{1}{w\sqrt{n_{wg}^2 - n_s^2}}\left[m\pi + \arctan\sqrt{\frac{n_s^2 - n_i^2}{n_{wg}^2 - n_s^2}}\right] \qquad \textbf{Equation 1.6}$$

And for TM polarization:

$$\frac{\omega}{c}\Big|_{\text{cut off}} = k_0 = \frac{2\pi}{\lambda_c} = \frac{1}{w\sqrt{n_{wg}^2 - n_s^2}}\left[m\pi + \arctan\left(\frac{n_{wg}^2}{n_s^2}\sqrt{\frac{n_s^2 - n_i^2}{n_{wg}^2 - n_s^2}}\right)\right] \qquad \textbf{Equation 1.7}$$

With m = 0, +1, +2...

In the case of a multimode waveguide, the dispersion equation **(Equation 1.5)** can be simplified considering that the "arctan" terms are small compared to $k_0 w\sqrt{n_{wg}^2 - n_{eff}^2}$. Then, n_{eff} varies with the square of its order: $n_{eff} \cong n_{wg} - \frac{1}{2n_{wg}}\left(\frac{m\pi}{k_0 w}\right)^2$

As mentioned before, the propagation constant β is dependent on the frequency $\beta = \frac{\omega}{c} n_{eff} = k_0 n_{eff} = \left(\frac{2\pi}{\lambda_0}\right) n_{eff}$. If we solve the dispersion equation numerically for different guided modes, we can plot the dispersion diagram that gives explicitly the region of the guided modes **(Figure 1.24)**. This region is placed between two straight lines $\beta = \frac{\omega}{c} n_s$ and $\beta = \frac{\omega}{c} n_{wg}$ and describes the propagation of the plane waves in the homogeneous infinite media of index n_s and n_{wg}.

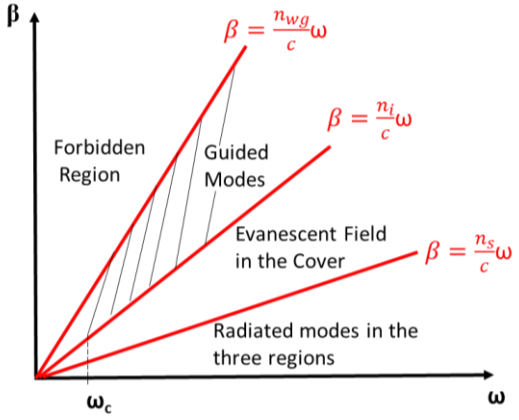

Figure 1.24: Dispersion diagram for the three regions: Substrate, Waveguide and Cover. The ω_c denotes the cut-off frequency.

1.5.2.3 Propagated power of the modes

Every mode carries an energy, therefore a power along its optical path. This power can be expressed through the Poynting theorem according to:

$$P = \int \vec{S}\,\overrightarrow{dr} \qquad \textbf{Equation 1.8}$$

with $\overrightarrow{S} = \frac{1}{2}Re(\vec{E} \times \vec{H}^*)$ and $\overrightarrow{dr} = \overrightarrow{a_z}\overrightarrow{a_x}dy$.

For a TE mode inside the waveguide parallel to the x-axis (perpendicular to the grating lines), the vertical transverse component y of magnetic field is $H_y = \frac{\beta}{\omega\mu_0}Ex$, and after the replacement in **(Equation 1.8)**, the carrying power of a mode is:

$$P = \frac{\beta}{2\omega\mu_0}\int_{-\infty}^{\infty}|Ex|^2\,dy \qquad \textbf{Equation 1.9}$$

For TM polarization, the relation becomes:

$$P = \frac{\beta}{2\omega n_{wg}^2\varepsilon_0}\int_{-\infty}^{\infty}|Hx|^2\,dy \qquad \textbf{Equation 1.10}$$

with $E_y = \frac{\beta}{\omega n_{wg}^2\varepsilon_0}Hx$

In the waveguide region, the power is related to the wave vectors in each medium (cover, substrate, waveguide) and results as follows:

$$P = \frac{\beta}{4\omega\mu_0}B_1^2\frac{k_i^2 + k_{wg}^2}{k_{wg}^2}\left[\frac{1}{k_0k_s} + \frac{1}{k_0k_i} + w\right] \qquad \textbf{Equation 1.11}$$

With B_1 a constant expressing the field amplitude in the interface cover-guide and

$k_s = \sqrt{{n_{eff}}^2 - {n_s}^2}$, $k_{wg} = \sqrt{{n_{wg}}^2 - {n_{eff}}^2}$ and $k_i = \sqrt{{n_{eff}}^2 - {n_i}^2}$

The parenthesis can be seen as the effective width or the electromagnetic width of the waveguide and is expressed like:

$$w_{eff} = \frac{1}{k_0\sqrt{n_{eff}^2 - n_s^2}} + \frac{1}{k_0\sqrt{n_{eff}^2 - n_i^2}} + w \qquad \textbf{Equation 1.12}$$

Specific parameters in the effective width should be taken into account if we deal with dielectric waveguides with symmetrical ($n_s = n_i$) and non-symmetrical guide for achieving optimum power confinement [100].

1.6 Resonance Study

1.6.1 Resonance Principle

When an incident beam impinges in a WRG structure **(Figure 1.22)**, part of the beam is directly transmitted and part is diffracted and trapped in the waveguide layer as waveguide modes. During propagation, the guided light leaks out of the waveguide and interferes destructively with the transmitted beam while constructively with the reflected in the superstrate. This leads to complete interference of light yielding to zero transmission [18], [101] **(Figure 1.25)**. Depending on the specific wavelength and angular orientation of the incident light, a very high reflection occurs, the so-called resonance. In normal incidence and for a monomode waveguide, the structure resonates with only one wavelength whereas in oblique incidence two resonating wavelengths appear **(Figure 1.26)**. The oblique incidence causes the splitting of the resonance **(Figure 1.27)** followed by coupling of the +1 and −1 diffracted orders to the leaky modes of the waveguide appearing at two different wavelengths [102]. For a large range of angles the symmetrical gap starting from 0°, increases with the angle increment.

These resonances display a Fano or Lorentzian profile with linewidth as narrow as 0.1 nm [103]. The reflection coefficient or resonance is the contribution of the eigenmodes of the grating presented as perturbed area with strong scattering by ridges and grooves. The resonance can only be achieved by taking into account an infinite waveguide grating excited by means of a plane wave.

Thanks to the sharp resonance of WRG, filtering applications are highly recommended. In addition, the use of transparent dielectric-based configurations avoid thermal effects in contrast to metallic structures [104].

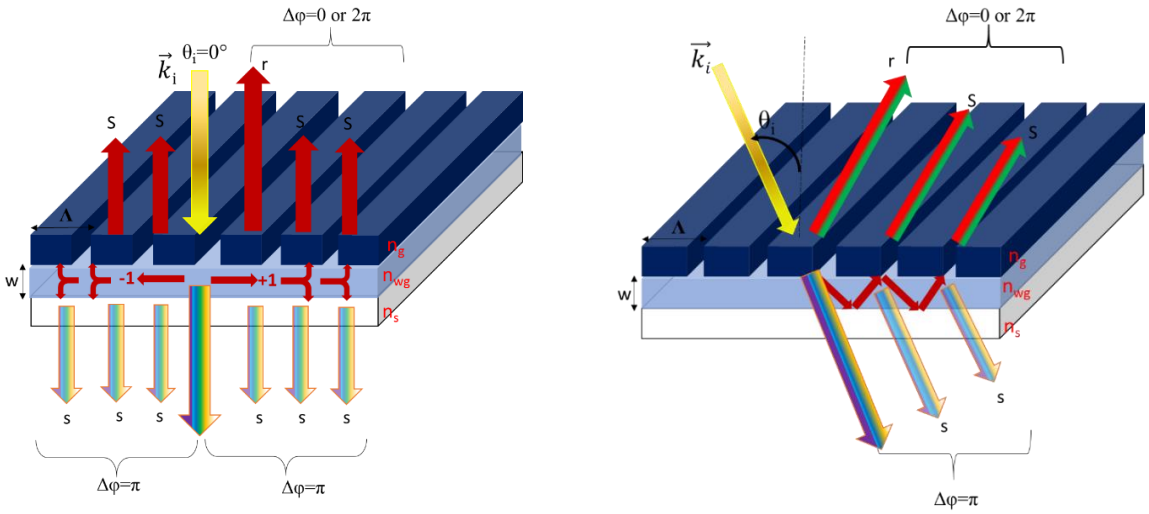

(a) **(b)**

Figure 1.25: Schematic representation of the resonance process through the mode coupling by a corrugated grating with normal incidence (a) and oblique incidence (b). The letter s marks the radiated beam outward the cladding.

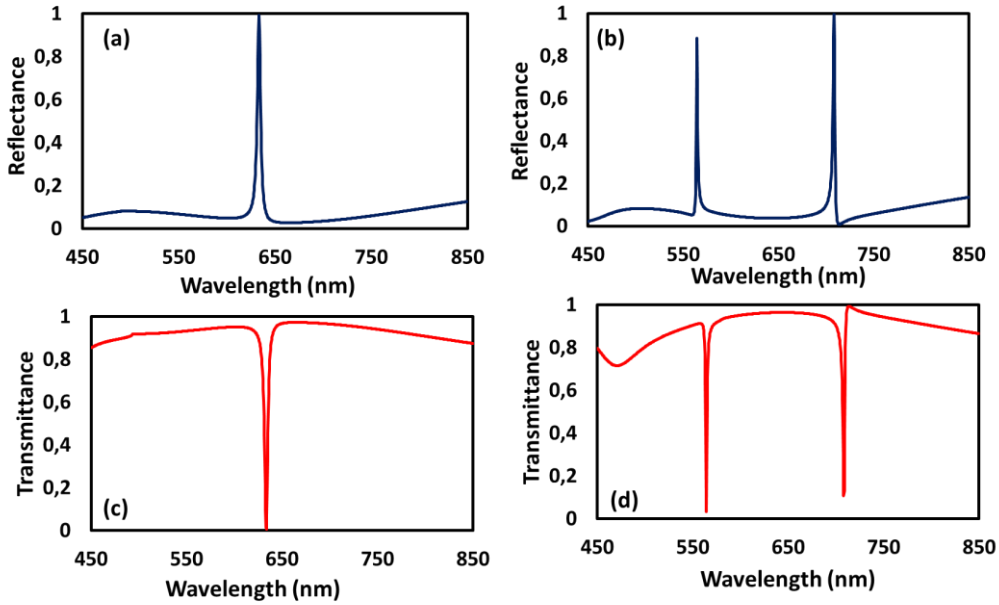

Figure 1.26: Efficient resonances in Reflectance and Transmittance as a function of wavelength λ for a monomode waveguide under normal (a), (c) and oblique incidence θ_i = 15° (b), (d).

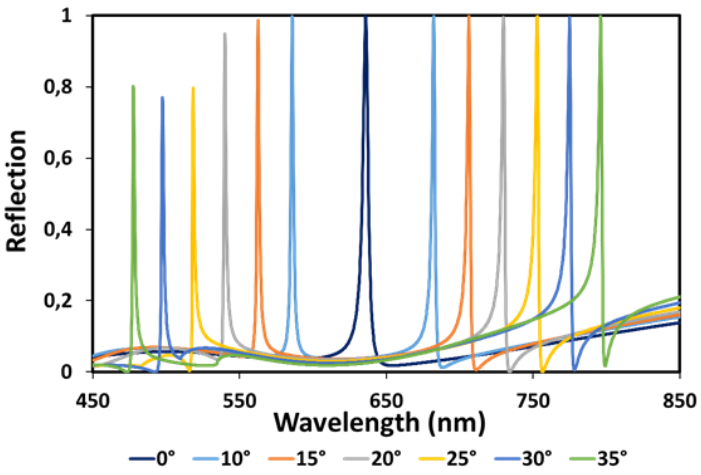

Figure 1.27: Spectral distribution of a wide range of oblique angles.

1.6.2 Mode Coupling

The mode coupling description imperatively demands a geometrical representation to include all the simultaneous actions taking place in the structure; i.e. the impinging incident light (normal or oblique) to the grating, the mode excitation by the resonant wavelength and the propagating direction of the orders. All the three parameters can be designed in the Ewald sphere and simply calculated by the grating equation that fulfills the coupling synchronism and incorporates the effective index n_{eff} of the waveguide:

$$k_0 n_i \sin\theta_i + mK_g = k_0 n_{eff} \qquad \textbf{Equation 1.13}$$

From which results:

$$n_{eff} = \mathrm{m}\frac{\lambda_0}{\Lambda} + n_i \sin\theta_i \qquad \textbf{Equation 1.14}$$

The replacement of the orders m in the formula sets the value of n_{eff}, which in turn has to fulfill the total reflexion criterion $n_s < n_{eff} < n_{wg}$.

The mechanism of the Ewald Sphere will be below explained notably based on the most commonly encountered structure in this thesis (binary diffraction grating of positive photoresist (PR) on a TiO_2 solgel waveguide and a glass substrate) **(Figure 1.28)**. The technique can be generalized to other grating geometries as well.

Figure 1.28: Binary structure of photoresist, TiO_2 solgel and glass substrate with n_g = 1.67 and k = 0, n_{wg} = 2.34 and n_s = 1.511 respectively.

The study of the Ewald Sphere is analyzed extensively for two types of incidence; normal and oblique under TE polarization.

1.6.2.1 Normal Incidence

Considering a normal incidence and a monomode waveguide resonant grating, a coupling between the incident light beam and the fundamental mode occurs. The vertical line in the Ewald circle represents the incident beam and guarantees the existence of symmetry; two propagative (forward) and contra- propagative (backward) orders $m = \pm 1$ excite the mode that lies at equal distance from the origin of axis O, represented by the distance corresponding to the vector norm of the propagative mode equal to $k_0 n_{eff}$ and equal to the vector K_g in the case of normal incidence, when synchronism phase and mode excitation occur. It should be noted that the mode is placed outside the substrate and in the proximity of the substrate semicircle **(Figure 1.29)**. This is completely legitimate since the effective index of the mode is usually slight larger than the refractive index of the substrate. In the opposite case, no coupling would appear between incident beam and waveguide propagative mode. Finally, the coupling leads to a high resonance and the type of mode is depicted with the form of lobes in a 2D electric field **(Figure 1.30)** scan by Modal Collinear Programming **(Section 1.7)**. Using the convention of axis orientation depicted in **(Figure 1.12)** for TE polarization. The lobes represent the propagation of standing waves in a single or more periods of the structure.

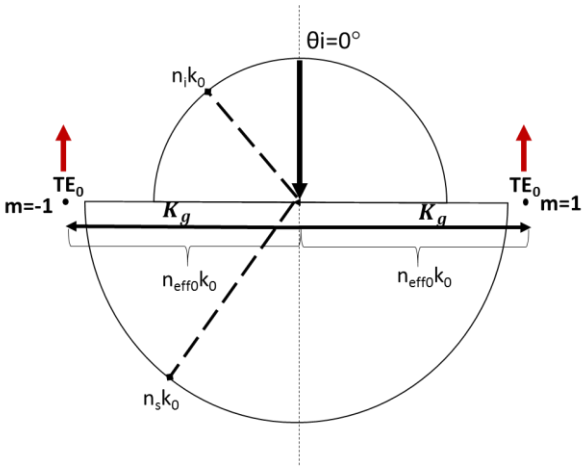

Figure 1.29: Ewald sphere representation for a monomode waveguide of effective index under normal incidence illumination for TE polarization.

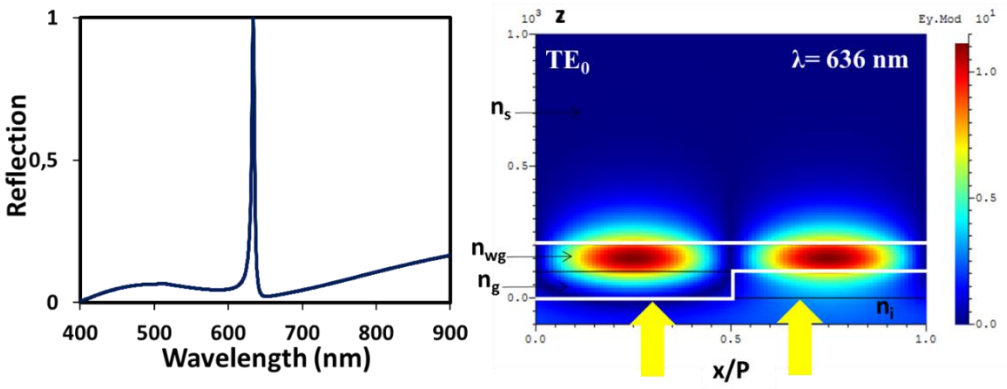

(a) **(b)**

Figure 1.30: Resonance for TE polarization at λ = 636 nm (a) and TE_0 mode electric field amplitude distribution Ey scanned for a single period at the same resonant wavelength (b). The tested structure consists of d = 100 nm of photoresist grating, w = 102 nm of waveguide width, 340 nm of period and DC = 0.5.

For bimodal guide and normal incidence, two modes are excited. Having already calculated the appropriate width of the waveguide for two mode-propagation in the TE polarization, we demonstrate that two distinct wavelengths yield to the excitation of the fundamental TE_0 and TE_1 mode (**Figure 1.31**) by means of symmetry.

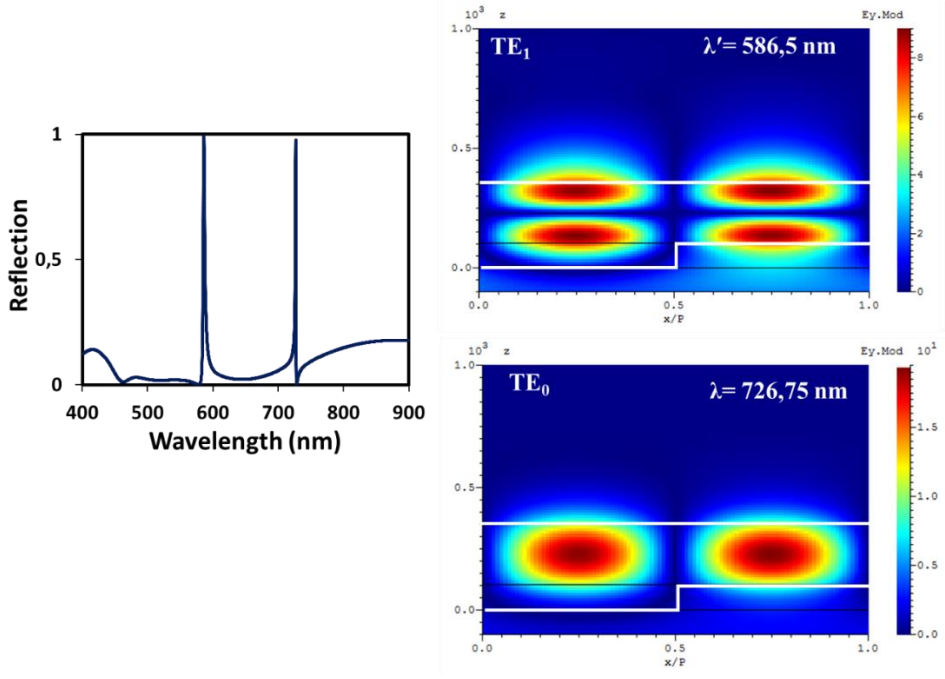

(a) **(b)**

Figure 1.31: The left resonant wavelength peak corresponds to λ′ = 586.5 nm and the right to λ = 726.75 nm exciting the TE_1 and TE_0 mode respectively (a), 2D electric field amplitude distributions on λ′ and λ respectively scanned for a single period (b). The tested structure consists of a TiO_2 waveguide of w = 250 nm and a subwavelength binary resist grating of d = 100 nm, Λ = 340 nm and DC = 0.5.

Following the geometry of the configuration, each wavelength corresponds to separate Ewald circle with different circle radius for superstrate and substrate medium. The highest wavelength (λ = 726.75 nm) corresponds to the smaller Ewald circle and excites the fundamental mode TE_0. The n_{eff0} of the TE_0 is calculated by the **(Equation 1.14)** and is equal to 2.13, therefore placed outside the semicircle of its substrate. The smaller wavelength (λ′ = 586.5 nm) with bigger Ewald circle excites the TE_1 of $n_{eff1} = 1.725$ and thus is placed in proximity to the substrate. In this Ewald circle the fundamental mode is placed at the left of TE_1 ($n_{eff1} < n_{eff0}$) and cannot be reached with the same K_g vector. As a fixed value imposed by the structural proceeding, the $K_g = 2\pi/\Lambda$ unit is the same for both wavelengths λ and λ′ and equal to $k_0 n_{eff0}$ or $k_0{}' n_{eff1}$ respectively as it is illustrated in the **Figure 1.32**.

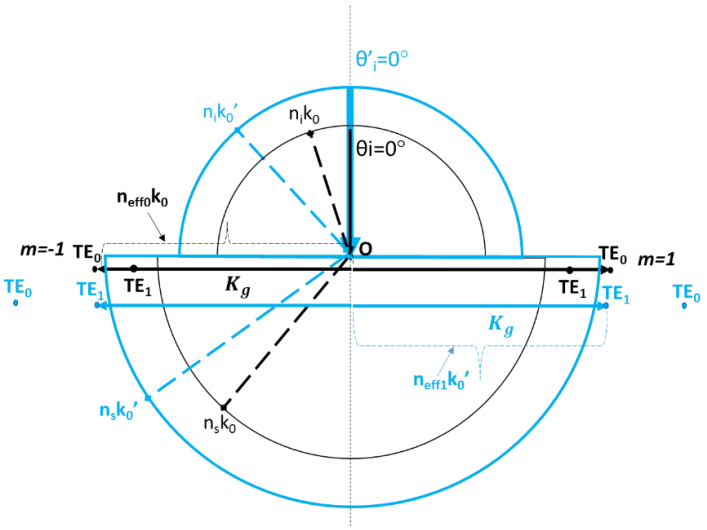

Figure 1.32: Ewald sphere configuration for bimodal waveguide under normal incidence illumination for TE polarization for two wavelengths λ (black) and λ′ (blue).

For high multi-modal waveguide and normal incidence, the mechanism remains the same but becomes more and more cumbersome to represent. For TM polarization, the approach is identical but prior calculations need to be included for the waveguide width.

1.6.2.2 Oblique Incidence

In oblique incidence, the incident wave vector is tilted according to the incidence plane normal to the grating grooves, with an angle corresponding to the incident angle θ_i.

For a monomode waveguide and a tilted angle, the resonant reflection peak splits into two peaks with different amplitudes. Now, the 2D electrical field distribution for the mode identification appears as a homogeneous zone in the guide (**Figure 1.33)**.

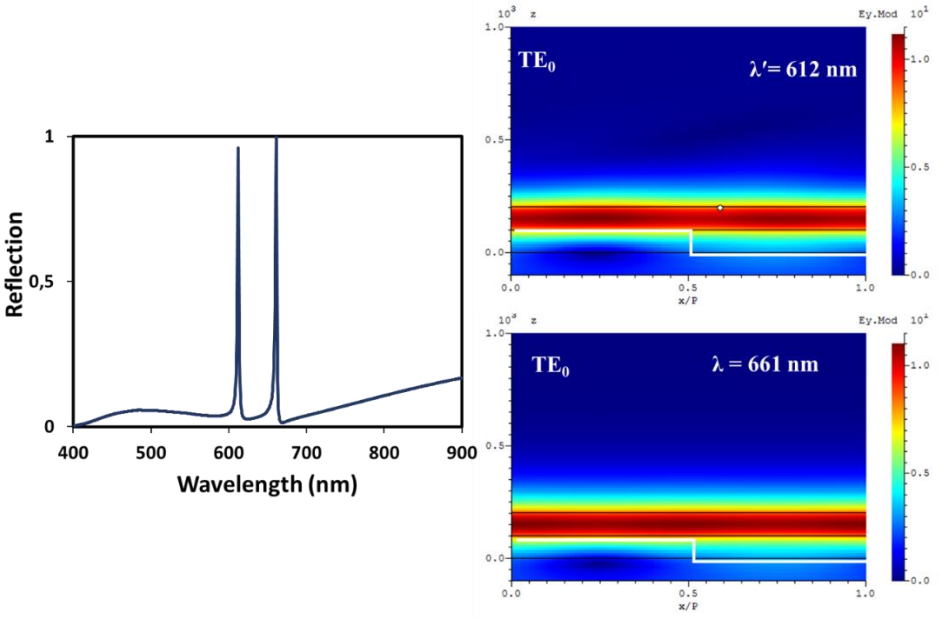

(a) **(b)**

Figure 1.33: The 612 nm resonance peak excites the TE_0 mode (forward) and the 661 nm the TE_0 mode (backward) (a). 2D electric amplitude field distribution for both excitation wavelengths (b). The current structure consists of a TiO_2 waveguide of w = 102 nm and the incidence angle of study is 5°. The other parameters are as previously (d = 100 nm, FF = 0.5, Λ = 340 nm).

Now, the 2D electric field distribution cannot clearly distinguish the TE mode propagation direction. Further 2D scanning of power flow is helpful for the order identification.

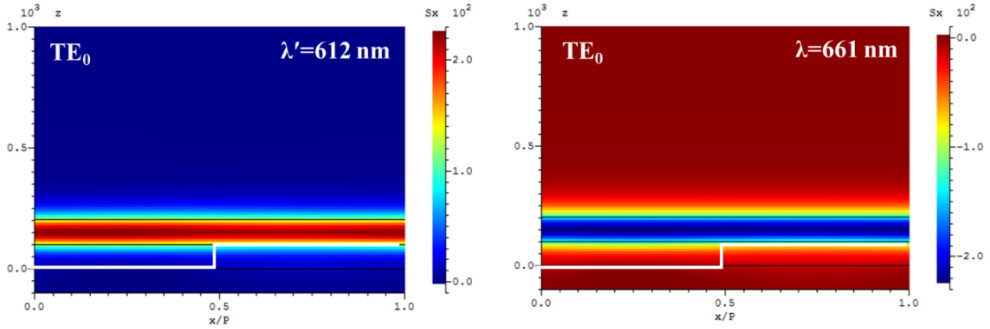

(a) **(b)**

Figure 1.34: 2D power flow scanning along x direction. The 612 nm resonance peak excites the TE_0 mode with m = +1 order (a), and the 661 nm the TE_0 with m = -1 order (b).

Schematically, the tilted incident beam is transferred without any modifications from the direct space to the right hemisphere of the reciprocal space of Ewald circle. The projection of the incident beam at x-axis results $n_i k_0 \sin\theta_i$. As analyzed before, for two different wavelengths, we study two embedded Ewald circles with separate geometric characteristics. The K_g vector

is designed from the end of the incident's beam projection and with a fixed period, K_g can excite a mode through the positive or negative m = ±1 order. As seen schematically in the forward propagation direction, the distance of the mode is equal to $k_0{}'n_{eff0} = n_i k_0 \sin\theta_i + K_g$ while $k_0 n_{eff0}$ in the backward propagation. The TE_0 mode is not placed symmetrically since the $k_0 n_{eff0}$ differentiates from each semicircle **(Figure 1.35)**.

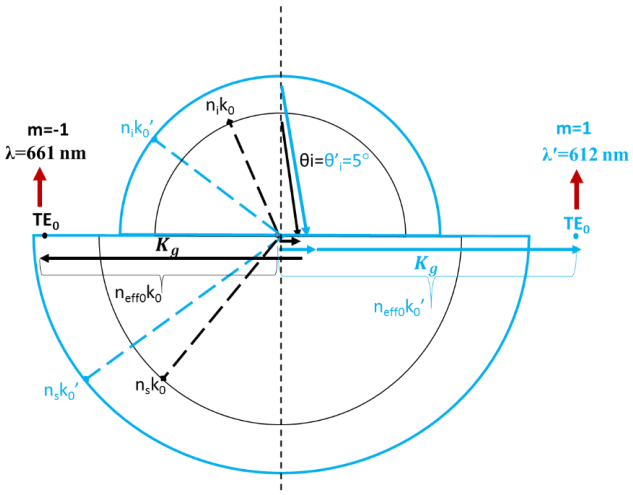

Figure 1.35: Ewald sphere for oblique incidence at 5° for a monomode waveguide for TE polarization for two wavelengths.

With a different configuration, it might be also possible to excite a mode other than the fundamental one, with a more elevated order, m = ±2 for instance **(Figure 1.36)**. In such a case, two resonant wavelengths appear having different amplitudes but neither of them is at 100% since part of the energy is also carried by the modes excited by the ±1 orders.

For a waveguide supporting n modes and an oblique incidence, it is clear that the resonance peaks become 2n as well as the number of the Ewald configurations. Equivalently, the direction of propagation is calculated for each wavelength through the coupling synchronism and the mode identification is realized through the 2D electric field distribution and power flow **(Figure 1.37)**.

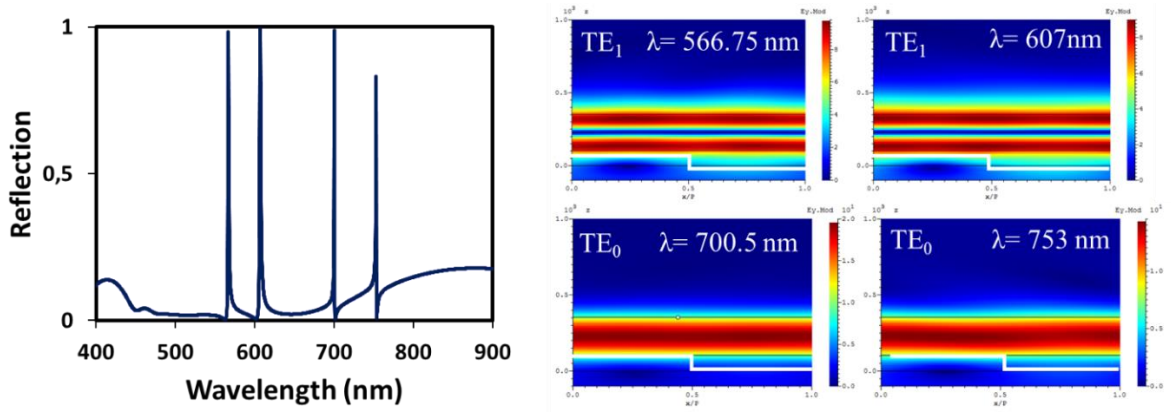

(a) **(b)**

Figure 1.36: Bimodal waveguide with excitation mode resonances that correspond to λ_{TE1}=566.75 nm, λ_{TE1}=607 nm, λ_{TE0}=700.5 nm and λ_{TE0}=753 nm (a) with the corresponding fields amplitude starting from top left (b). The structure consists of d = 102 nm PR, w = 250 nm waveguide, Λ= 340 nm period, DC = 0.5 and θ_i = 5°.

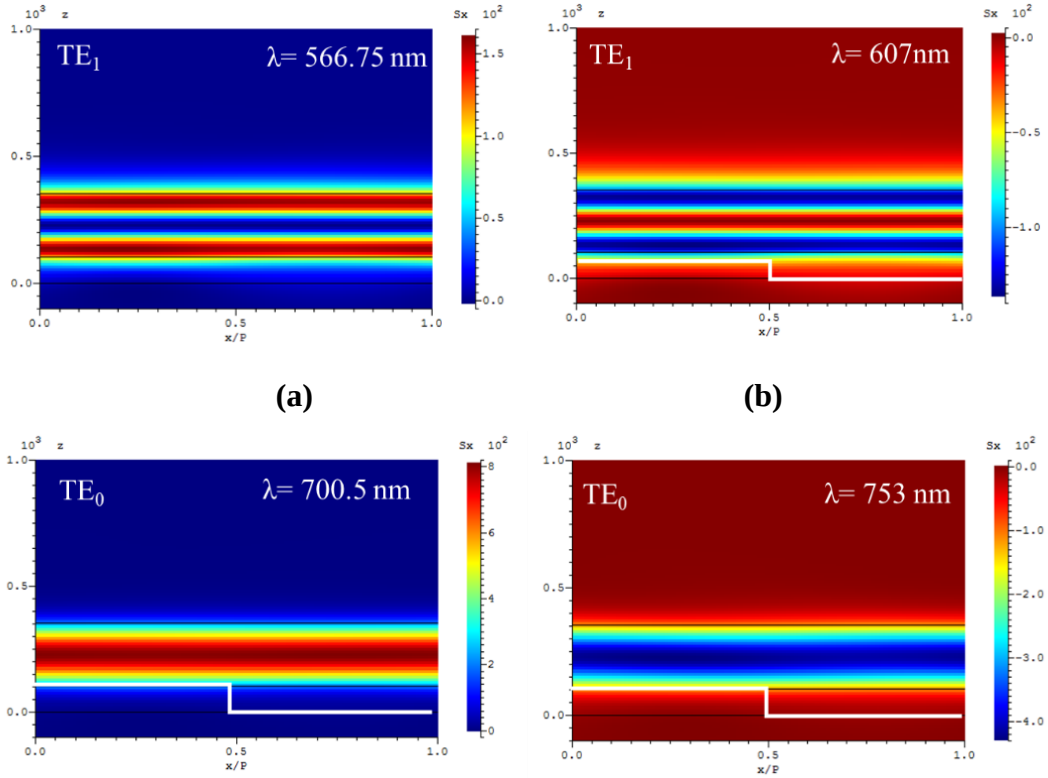

(a) **(b)**

(c) **(d)**

Figure 1.37: Power flow distribution along x-axis exhibiting the TE_1 and TE_0 forward (a), (c) and backward mode (b), (d) respectively.

1.6.3 Polarization dependence of the resonance response

In both cases TE or TM, the polarization can influence the resonance by shifting the position of the wavelength or even by broadening the linewidths of the peaks **(Figure 1.38)**.

The primary reason for this is due to the effective index difference for TE and TM propagative modes in the waveguide.

Moreover, the resonance peak linewidth difference can be attributed to the radiation coefficient that is large for TE polarization, while very small for TM. The TE polarization has a short propagation length in the waveguide, therefore a high radiation coefficient ($L_p=1/\alpha$) **(See also Section 1.6.4)** that results in a wide spectral width. With another perspective, we could consider the material particles of the grating corrugation as small dipoles that can be excited differently by each polarization when illuminated under normal incidence. For TM polarization, the vibration of the electric field in the grating corrugation is normal to the waveguide plane. This vibration movement provokes a parallel to the grating lines radiation inducing simultaneously a damping radiation at the z-axis of our interest. In contrast, for TE polarization the vibration of the electric field is essentially parallel to the grating lines yielding a reinforced radiation at z-axis [105].

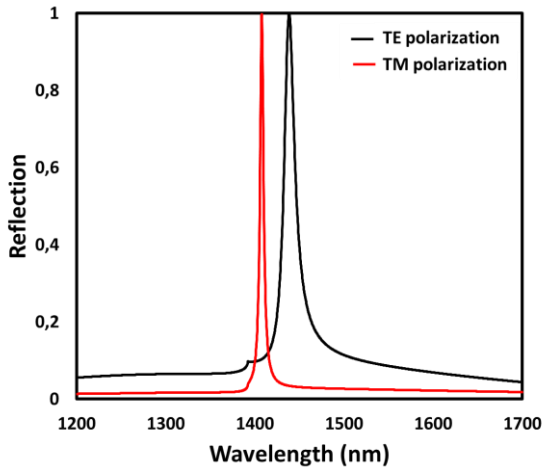

Figure 1.38: Position shift and spectral width difference between TE and TM polarization under normal incidence for a structure with d = 376 nm, w = 340 nm, Λ = 960 nm, s = 480 nm, n_s = 1.45, n_{wg} = 1.7, n_g = 1.67.

1.6.4 Dimensioning resonance with optogeometrical grating waveguide parameters

To meet the filtering purposes of WRG structures, narrow spectral and angular bandwidths are required. Structural features strongly influence the resonance characteristics, so it is necessary to handle them properly for resonance shaping and tuning. The characteristics of waveguide grating coupling depend on a large number of optogeometrical parameters (wavelength, period, incidence angle, waveguide index and thickness, grating depth, duty cycle…).

Shin *et al.* demonstrated dependence of the linewidth ($\Delta\lambda/\lambda$) on the modulation of a grating $\Delta\varepsilon = n_H^2 - n_L^2$ and the duty cycle in both TE and TM polarizations in a single layer configuration **(Figure 1.39)** [106]. It is shown, that maximum linewidth is achieved with DC = 0.5.

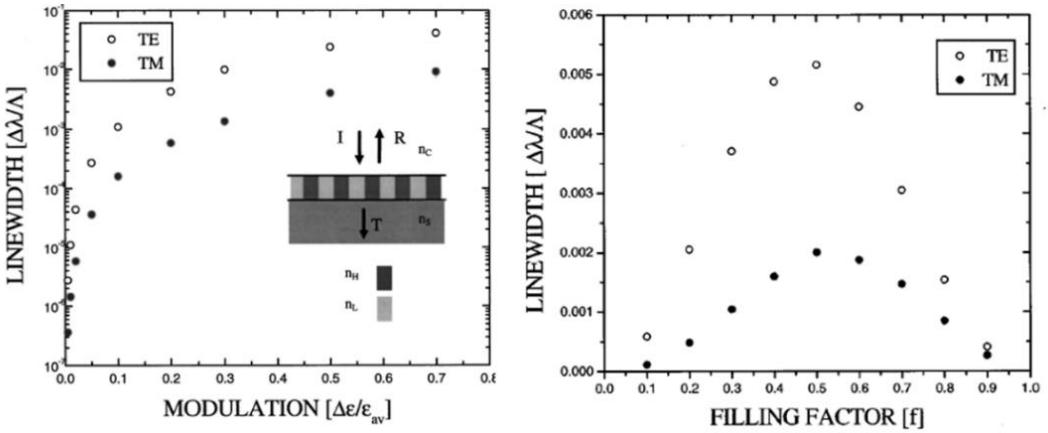

(a) (b)

Figure 1.39: Filter linewidth dependence on the modulation index (a) and filling factor (b) for a single layer reflection grating [106].

Moreover, he pointed out that the profile of the grating can have an impact on the resonance. The rectangular grating presents wider resonance, which is excited at a shorter wavelength compared to that of the narrow trapezoidal **(Figure 1.40)**.

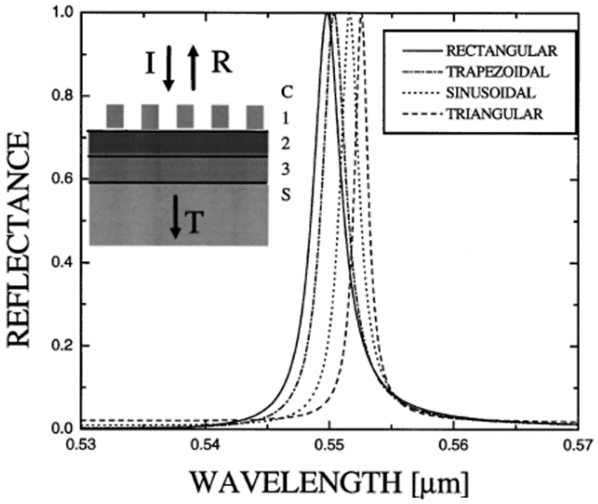

Figure 1.40: Grating form dependence on the resonance for a triple-layer WRG structure under TE polarization [106].

For rectangular gratings, the duty cycle DC can also determine the angular spectrum of the resonance that can be broadened through appropriate settings [107].

Other significant properties tied to structural characteristics and grating profile are the effective index n_{eff} of the concerned waveguide mode (or its propagation constant $\beta = k_0 n_{eff}$), the radiation coefficient $\boldsymbol{\alpha}$ of the waveguide grating, and the second order intraguide coupling coefficient $\boldsymbol{\kappa}$ encountered under normal incidence.

High-indexed Si_3N_4, Ta_2O_5 or TiO_2 films deposited on glass or silica substrates are highly recommended as they offer high confinement of the field at the guide-cover interface and thus high efficient coupling structures.

The parameter $\boldsymbol{\kappa}$ (kappa) results from the coupling between the counter-propagating mode to itself through the 2nd diffraction order under normal incidence. Hence, a strong kappa limits the propagation length $\boldsymbol{L_p}$ of the mode since it is reflected in itself in the opposite direction. The mode "sees" a smaller number of grating periods. The main effect of kappa is to increase the angular width of the resonant reflection whereas the wavelength spectrum is moderately affected.

The strength of the modal field amplitude in the waveguide is characterized by the radiation coefficient $\boldsymbol{\alpha}$, stating the coupling between incident beam and guided mode through +1 and -1 order. In other words, the radiation coefficient $\boldsymbol{\alpha}$ expressing the rate of radiation escaping from the grating is in the TE case proportional to $(k_0 d)^2(n_{wg}^2 - n_{eff}^2)/(n_{eff} w)$ according to a derivation

under the Rayleigh approximation of shallow corrugation [108,109] where $k_0 = 2\pi/\lambda$, d is the grating corrugation depth, n_{wg} is the waveguide index, n_{eff} the mode effective index, and w is the waveguide thickness. This implies that $\boldsymbol{\alpha}$ increases (i.e. the propagation length $\boldsymbol{L_p} = 1/\boldsymbol{\alpha}$ decreases) as the square of the corrugation depth and approximately as the ratio n_{wg}/w.

Studying the shallow corrugated waveguides as well, Avrutsky *et al.* [14] showed that for oblique incidence, the wavelength bandwidth $\Delta\lambda$ of the resonance can be predicted through the radiation coefficient $\boldsymbol{\alpha}$.

However, for normal incidence the same approximation is no longer valid. Lyndin *et al.*[110] after searching the possible ways of filtering the fundamental Transverse Mode in the C-band in a laser resonator, he stated that at normal incidence and for a finite-width illumination beam, the linewidth of the resonance is related to the radiation coefficient $\boldsymbol{\alpha}$ and to the coupling strength $\boldsymbol{\kappa}$. Their dependence on the intrinsic optogeometrical features of the structure precludes simple analytical approaches but allows only numerical modelling **(See 1.7.3)**.

In contrast, for deep gratings, the influence on the profile becomes more critical. According to the EMT (Effective Medium Theory) or Homogenization theory developed at the early 80's, the subwavelength gratings with depths larger than $\lambda/4$ can be seen as homogeneous thin layers. This accord becomes more accurate with increasing grating depth where evanescent waves can be ignored. This can be demonstrated mathematically by solving the Maxwell's equations with boundary conditions on the grating interfaces. In particular, for deeper gratings the effective indices present intrinsic properties to the grating structure whereas for shallow gratings the optical indices depend mostly on the optical indices of the surrounding media of the grating. The EMT approach stands valid in front of the widely used diffraction theory. A comparison between the EMT approximation and RCWA for 1D grating structures shows good conformity for TE polarization but small deviation is presented for the polarized TM structure [111], [112].

Apart from the impact of structural features, the resonance form can be also affected by the illumination beam size. The incident beam diameter D_i should be $D_i >> \boldsymbol{L_p} \sim \Lambda Q$, with $\boldsymbol{L_p}$ the propagation length of the guided mode, Λ the period of the grating and Q the expected quality factor of the resonance.

1.7 Numerical Modeling

The approaches presented in the previous sections for calculating the influence of a structure interface on an incident light beam try to keep the mathematical treatment analytical in order to give a comprehensive and intuitive understanding of coupling and resonance mechanisms allowing goal-oriented designs to be found. This comes at some point always at the price of using certain simplifications and approximations according to the type of arrangement of structures considered. However, not all real microstructures respect the limitations for the validity of those approaches, so there is a big interest for developing rigorous, numerical methods that allow in general manner to calculate the field distribution inside periodic optical elements as well as its diffraction efficiencies. This structural design of RWGs has largely concerned the authors over years that attempted to find the most suitable numerical model to optimize the fabrication tolerances and enhance the diffraction efficiencies. A plethora of algorithms has proposed to handle typical or complex structures with the minimum possible computational time.

In this section, the three most prevalent numerical methods are reviewed: the modal methods including the RCWA (Rigorous Coupled Wave Analysis) and the True Modal Method (TMM), as well as Chandenzon (C-method) method. All combine accuracy and high efficiency for optical grating simulation especially for WRG.

1.7.1 RCWA (Rigorous Coupled Wave Analysis)

The Fourier Modal Method (FMM) or Rigorous Coupled Wave Analysis is a prominent computational tool that determines the Electro-Magnetic (EM) field within the grating region and in the non-diffractive upward and downward area of the grating. This region decomposition is the simplest formalism for a binary grating, but not exclusive, as in some cases, the grating region must be divided into further sub-regions to adjust the morphology **(Figure 1.41)**.

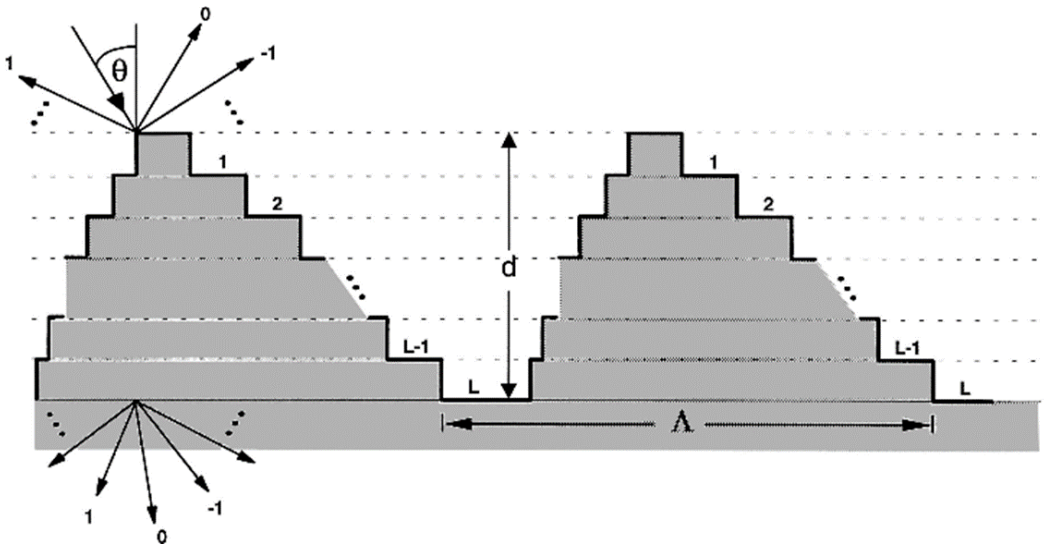

Figure 1.41: Decomposition of a blazed grating in different layers leading to the staircase effect [113].

Moharam *et al.* [114] has examined the modal problem using an elementary optogeometrical structure. The problem involves a monochromatic incident plane wave that impinges on a one-dimensional, rectangular surface-relief dielectric grating with refractive index of n_s surrounded by a media of refractive index of n_i. Its period, denoted Λ is composed successively by two refractive indices, this of n_i and this of n_s. The quantity *f* is the fraction of the grating period. The grating is considered as infinite in x and z dimensions **(Figure 1.42)**.

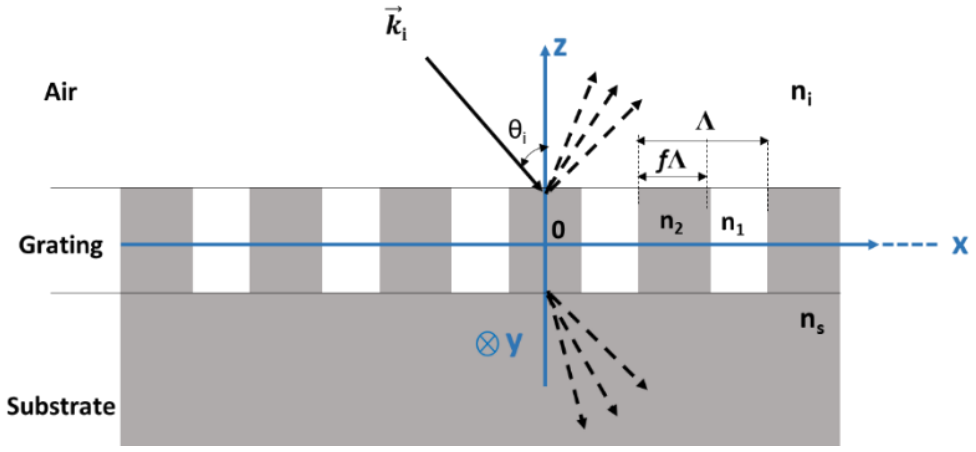

Figure 1.42: Schematic representation of the modal problem in a binary rectangular grating.

The fundamental steps of this method can be divided into four parts:

(1) Expand all the dielectric permittivity function and the electromagnetic field in the plane of the grating in a set of Fourier harmonics.
(2) Solve the Maxwell's equations in the non-diffracted regions (i.e. medium of the incident- reflected and the transmitted wave by the diffraction grating).
(3) Solve the Maxwell's equations in the internal diffractive region of the grating considering the EM field as an infinite number of forward and backward propagating and non-propagating state-variable eigenmodes.
(4) Matching boundary conditions to the solutions of steps (2) and (3) in the different interfaces.

The unknown coefficients in the expressions of the total electromagnetic fields are determined by resolving the linear system of equations in the individual regions. These coefficients give finally the field distribution, diffraction efficiency, diffraction phases and polarization state.

1.7.2 True-Modal Method (TMM)

In this section, we examine the lossless binary corrugated dielectric grating with the second modal theory, the True-Modal Method (TMM). This analysis has a different mathematical approach compared to the one of RCWA. TMM approach preserves the real form of the corrugation and represents the grating as an infinite periodical structure while remaining in the spatial domain, as opposed to RCWA that uses the Fourier domain. Hence, the electromagnetic field is composed of the superposition of modes that obey Maxwell's equations and each mode is characterized with a field distribution and a propagation constant β_q. The β_q propagation constant of the mode in an infinite grating upon z direction at the q order can be expressed by the dispersion equation that reveals the eigenvalues for every period of the grating. Detailed computational process is given in the papers [115],[116].

The use of the two modal methods RCWA or TMM is equally broad for simple cases of dielectric gratings. When the grating structure becomes more complex with the presence of shallow or lossy metallic gratings, the true modal method appears to be more reliable than the RCWA. Specifically, in the case of a metal-dielectric grating and a TM polarized incident beam, the Fourier Modal Method (FMM) suffers from numerical instabilities due to the truncation of the infinite matrix including the coefficients of the differential system. The truncated terms that contain physical characteristics such as coupling, interference and resonance effects of the plasmon-like Fourier modes are not taken into account, thereby leading to a poor convergence to the exact value [117].

1.7.3 C-Method

The C-method named after Chandenzon and co – workers in 1980 is a formalism proposed for surface relief grating treatment [118]. Structures with smooth profiles and no sharp edges like 3D periodic aggregates or stack of sinusoidal surfaces can be simulated with a simplified approach, suitable for both TE and TM polarizations. The rationale of this method is to make a curvilinear variable transformation of the Maxwell Equations in order to transpose a corrugated surface into a planar coordinate system in the Fourier space. Likewise, the solution of the boundary conditions is facilitated with good convergence rates especially if the stack of layers is identical. In other cases, each layer must be treated with the RCWA method leading to a more complex problem [119]. The C method though, provides a classical and an extended version, appropriate to model layers with different profiles.

In the reference of Vallius *et al.* [120] a comparison between RCWA and C-method for the case of multileveled conducting discontinuous gratings under the TM polarization is carried out. The simulation of the system highlighted a high accuracy and reliability for the C-method noting smaller computational times compared to these of RCWA. The minimization of time stems from the principle that convergence is alike for both TE and TM polarizations and renders the C-method a highly versatile tool for sinusoidal grating simulation.

1.8 Conclusion

In this chapter, as a general introduction to the doctoral dissertation, we have extensively examined the Waveguide Resonant Gratings named WRG or Guided Mode Resonances. These configurations employ subwavelength gratings with periodicity almost equal to the order of a wavelength to couple light into a thin film guide. The coupling-decoupling process results in narrow sharp reflectance-resonance responses appropriate for filtering functions. Depending strongly on the orientation and polarization of light the spectral response can change brutally. This effect is illustrated with the Ewald Sphere, a geometrical representation that transfers the wave vectors from direct space to indirect space. It illustrates the diffraction mechanism and the mode coupling in combination to the structural characteristics. An agreement between the structural features of the WRG and the resonance response is thoroughly investigated. Further modeling with appropriate codes is used for the optimization design, and understanding of the resonance phenomena. For efficient optimization, the MC Gratings and Modal Collinear method based on the RCWA and True Modes method have been succinctly presented and explained.

Bibliography

[1] Modal and C Methods Grating Software. https://mcgrating.com (Oct.2020)

[2] F. Hopkinson, D. Rittenhouse, "An Optical Problem, Proposed by Mr. Hopkinson, and Solved by Mr. Rittenhouse", *Trans. Am. Philos. Soc.* 2 (1786) 201–206.

[3] J.A. Plascyk, "The MK II Fraunhofer Line Discriminator (FLD-II) for Airborne and Orbital Remote Sensing of Solar-Stimulated Luminescence", *Opt. Eng.* 14 (1975) 144339.

[4] R.W. Wood, "XLII. On a remarkable case of uneven distribution of light in a diffraction grating spectrum", *Lond. Edinb. Dublin Philos. Mag. J. Sci.* 4 (1902) 396–402.

[5] J.W. Strutt, "On the dynamical theory of gratings", *Proc R Soc Lond A.* 79 (1907) 399–416.

[6] U. Fano, "The Theory of Anomalous Diffraction Gratings and of Quasi-Stationary Waves on Metallic Surfaces (Sommerfeld's Waves)", *JOSA.* 31 (1941) 213–222.

[7] C.H. Palmer, "Parallel Diffraction Grating Anomalies", *JOSA.* 42 (1952) 269–276.

[8] B.A. Lippmann, "Note on the Theory of Gratings", *JOSA.* 43 (1953) 408–408.

[9] V. Twersky," Multiple Scattering of Waves and Optical Phenomena", *JOSA.* 52 (1962) 145–171.

[10] A. Hessel, A.A. Oliner," A New Theory of Wood's Anomalies on Optical Gratings", *Appl. Opt.* 4 (1965) 1275–1297.

[11] M. Neviere, P. Vincent, R. Petit, M. Cadilhac, "Systematic study of resonances of holographic thin film couplers", *Opt. Commun.* 9 (1973) 48–53.

[12] M. Neviere, R. Petit, M. Cadilhac, "About the theory of optical grating coupler-waveguide systems", *Opt. Commun.* 8 (1973) 113–117.

[13] L. Mashev, E. Popov, "Zero order anomaly of dielectric coated gratings", *Opt. Commun.* 55 (1985) 377–380.

[14] I.A. Avrutsky, V.A. Sychugov, "Reflection of a Beam of Finite Size from a Corrugated Waveguide", *J. Mod. Opt.* 36 (1989) 1527–1539.

[15] S.S. Wang, R. Magnusson, J.S. Bagby, M.G. Moharam, "Guided-mode resonances in planar dielectric-layer diffraction gratings", *JOSA A.* 7 (1990) 1470–1474.

[16] R. Magnusson, S.S. Wang, "New principle for optical filters", *Appl. Phys. Lett.* 61 (1992) 1022–1024.

[17] S.M. Norton, T. Erdogan, G.M. Morris, "Coupled-mode theory of resonant-grating filters", *JOSA A.* 14 (1997) 629–639.

[18] A. Sharon, D. Rosenblatt, A.A. Friesem," Resonant grating–waveguide structures for visible and near-infrared radiation", *JOSA A.* 14 (1997) 2985–2993.

[19] D. Rosenblatt, A. Sharon, A.A. Friesem," Resonant grating waveguide structures", *IEEE J. Quantum Electron.* 33 (1997) 2038–2059.

[20] A. Sharon, S. Glasberg, D. Rosenblatt, A.A. Friesem, "Metal-based resonant grating waveguide structures", *JOSA A.* 14 (1997) 588–595.

[21] D.K. Jacob, S.C. Dunn, M.G. Moharam, "Design considerations for narrow-band dielectric resonant grating reflection filters of finite length", *JOSA A.* 17 (2000) 1241–1249.

[22] D.K. Jacob, S.C. Dunn, M.G. Moharam, "Normally incident resonant grating reflection filters for efficient narrow-band spectral filtering of finite beams", *JOSA A.* 18 (2001) 2109–2120.

[23] T. Tamir, S. Zhang, "Resonant scattering by multilayered dielectric gratings", *JOSA A.* 14 (1997) 1607–1616.

[24] Y. Ding, R. Magnusson, "Band gaps and leaky-wave effects in resonant photonic-crystal waveguides", *Opt. Express.* 15 (2007) 680–694.
[25] Z.S. Liu, S. Tibuleac, D. Shin, P.P. Young, R. Magnusson, "High-efficiency guided-mode resonance filter", *Opt. Lett.* 23 (1998) 1556–1558.
[26] S.M. Norton, G.M. Morris, T. Erdogan, "Experimental investigation of resonant-grating filter lineshapes in comparison with theoretical models", *JOSA A.* 15 (1998) 464–472.
[27] D.L. Brundrett, E.N. Glytsis, T.K. Gaylord, "Normal-incidence guided-mode resonant grating filters: design and experimental demonstration", *Opt. Lett*. 23 (1998) 700–702.
[28] S.S. Wang, R. Magnusson, "Design of waveguide-grating filters with symmetrical line shapes and low sidebands", *Opt. Lett.* 19 (1994) 919–921.
[29] S.S. Wang, R. Magnusson, "Multilayer waveguide-grating filters", *Appl. Opt.* 34 (1995) 2414–2420.
[30] S. Tibuleac, R. Magnusson, "Reflection and transmission guided-mode resonance filters", *JOSA A.* 14 (1997) 1617–1626.
[31] D.K. Jacob, S.C. Dunn, M.G. Moharam, "Flat-top narrow-band spectral response obtained from cascaded resonant grating reflection filters", *Appl. Opt.* 41 (2002) 1241–1245.
[32] S.T. Thurman, G.M. Morris, "Controlling the spectral response in guided-mode resonance filter design", *Appl. Opt.* 42 (2003) 3225–3233.
[33] Y. Ding, R. Magnusson, "Doubly resonant single-layer bandpass optical filters", *Opt. Lett.* 29 (2004) 1135–1137.
[34] S.M. Norton, T. Erdogan, G.M. Morris, "Coupled-mode theory of resonant-grating filters", *JOSA A.* 14 (1997) 629–639.
[35] F. Lemarchand, A. Sentenac, H. Giovannini, "Increasing the angular tolerance of resonant grating filters with doubly periodic structures", *Opt. Lett.* 23 (1998) 1149–1151.
[36] A. Sentenac, A.-L. Fehrembach, "Angular tolerant resonant grating filters under oblique incidence", *JOSA A.* 22 (2005) 475–480.
[37] A.-L. Fehrembach, D. Maystre, A. Sentenac, "Phenomenological theory of filtering by resonant dielectric gratings", *JOSA A.* 19 (2002) 1136–1144.
[38] M. Zourob, A. Lakhtakia, "Optical Guided-wave Chemical and Biosensors II", *Springer Science & Business Media*, 2010.
[39] H.N. Daghestani, B.W. Day, "Theory and Applications of Surface Plasmon Resonance, Resonant Mirror, Resonant Waveguide Grating, and Dual Polarization Interferometry Biosensors", *Sensors.* 10 (2010) 9630–9646.
[40] S. Geschwindner, J.F. Carlsson, W. Knecht, "Application of Optical Biosensors in Small-Molecule Screening Activities", *Sensors.* 12 (2012) 4311–4323.
[41] A. Fernández Gavela, D. Grajales García, J.C. Ramirez, L.M. Lechuga, "Last Advances in Silicon-Based Optical Biosensors", *Sensors.* 16 (2016) 285.
[42] M. Paulsen, S. Jahns, M. Gerken," Intensity-based readout of resonant-waveguide grating biosensors: Systems and nanostructures", *Photonics Nanostructures - Fundam. Appl.* 26 (2017) 69–79.
[43] B. Michel, N. Moll, R. Ghannam, "Light-reflecting grating structure for photovoltaic devices", *US9985147B2*, 2018.
[44] A.D. Khan, A.D. Khan, F.E. Subhan, M. Noman, "Efficient Light Management in Ultrathin Crystalline GaAs Solar Cell Based on Plasmonic Square Nanoring Arrays", *Plasmonics* 14 (2019) 1963–1970.
[45] O.A.M. Abdelraouf, A. Shaker, N.K. Allam, "Front dielectric and back plasmonic wire grating for efficient light trapping in perovskite solar cells", *Opt. Mater.* 86 (2018) 311–317.

[46] X. Li, Z. Wang, Y. Hou, "Ultra-broadband and wide-angle perfect absorber based on composite metal–semiconductor grating", *Opt. Commun.* 406 (2018) 95–102.
[47] Z. Khezripour, F.F. Mahani, A. Mokhtari, "Double-sided TiO_2 nano-gratings for broadband performance enhancement of organic solar cells", *JOSA B.* 35 (2018) 2478–2483.
[48] W. Liu, T. Yu, Y. Sun, Z. Lai, Q. Liao, T. Wang, L. Yu, H. Chen, "Highly Efficient Broadband Wave Plates Using Dispersion-Engineered High-Index-Contrast Subwavelength Gratings", *Phys. Rev. Appl.* 11 (2019) 064005.
[49] A. Hu, F. Chu, C. Guo, G. Li, J. Wu, "Wideband reflective quarter-wave plates based on subwavelength mixed metal dielectric gratings", *Optik.* 163 (2018) 120–125.
[50] C. Stock, T. Siefke, U. Zeitner, "Metasurface-based patterned wave plates for VIS applications", *JOSA B.* 36 (2019) D97–D102.
[51] Y.-Y. Ji, F. Fan, X.-H. Wang, S.-J. Chang, "Broadband controllable terahertz quarter-wave plate based on graphene gratings with liquid crystals", *Opt. Express.* 26 (2018) 12852–12862.
[52] K. Hisano, M. Ota, M. Aizawa, N. Akamatsu, C.J. Barrett, A. Shishido, "Single-step creation of polarization gratings by scanning wave photopolymerization with unpolarized light [Invited]", *JOSA B.* 36 (2019) D112–D118.
[53] M.T. Posner, N. Podoliak, D.H. Smith, P.L. Mennea, P. Horak, C.B.E. Gawith, P.G.R. Smith, J.C. Gates, "Integrated polarizer based on 45° tilted gratings", *Opt. Express.* 27 (2019) 11174–11181.
[54] H.M. Hoffmann, S.K. Jawla, M.A. Shapiro, G. Hanson, R.J. Temkin, "Grating Polarizers at 170 GHz for ECRH Systems: Low Power Tests and Simulations", *IEEE Trans. Antennas Propag.* 66 (2018) 4719–4728.
[55] S. Shen, Y. Yuan, Z. Ruan, H. Tan, "Optimizing the design of an embedded grating polarizer for infrared polarization light field imaging", *Results Phys.* 12 (2019) 21–31.
[56] J. Zhang, J. Yang, L. Liang, W. Wu, "Broadband TM-mode-pass polarizer and polarization beam splitter using asymmetrical directional couplers based on silicon subwavelength grating", *Opt. Commun.* 407 (2018) 46–50.
[57] Z. Ren, Y. Sun, Z. Lin, K. Zhang, S. Wang, M. Li, H. Lu, "Active waveband selective switches based on guided-mode resonance for telecommunications", *IET Optoelectron.* 13 (2018) 99–103.
[58] Z. Ren, Y. Sun, S. Zhang, K. Zhang, J. Hu, Z. Lin, "Active optical switches based on polarization-tuned guided-mode resonance filters for optical communication", *Opt. Commun.* 426 (2018) 383–387.
[59] B. Sadani, B. Boisnard, X. Lafosse, T. Camps, J.B. Doucet, E. Daran, C. Paranthoen, C. Levallois, L. Dupont, S. Bouchoule, V. Bardinal, "Liquid-Crystal Alignment by a Nanoimprinted Grating for Wafer-Scale Fabrication of Tunable Devices", *IEEE Photonics Technol. Lett.* 30 (2018) 1388–1391.
[60] E.J. Turner, S.A. McDaniel, N. Tabiryan, G. Cook, "Rapidly tunable HIP treated Cr: ZnSe narrow-linewidth laser", *Opt. Express.* 27 (2019) 12282–12288.
[61] J. Wu, Y. Du, J. Xia, T. Zhang, W. Lei, B. Wang, "Dynamically Tunable Light Absorbers as Color Filters Based on Electrowetting Technology", *Nanomaterials.* 9 (2019) 70.
[62] A. Taheri, M. Shokooh-Saremi, "Tunable two-dimensional optical filter based on guided-mode resonance", *JOSA A.* 36 (2019) 1109–1116.
[63] Y.-J. Hung, C.-W. Kao, T.-C. Kao, C.-W. Huang, J.-J. Lin, C.-C. Yin, "Optical spectrometer based on continuously-chirped guided mode resonance filter", *Opt. Express.* 26 (2018) 27515–27527.

[64] Y. Han, J. Yang, X. He, Y. Yu, D. Chen, J. Huang, Z. Zhang, J. Zhang, S. Xu, "Multiband notch filter based guided-mode resonance for mid-infrared spectroscopy", *Opt. Commun.* 445 (2019) 64–68.
[65] H. Hsu, Y. Lan, C. Huang, "A Gradient Grating Period Guided-Mode Resonance Spectrometer", *IEEE Photonics J.* 10 (2018) 1–9.
[66] F.-C. Lin, K.-M. See, Y.-X. Huang, Y.-J. Chen, L. Ouyang, J. Popp, J.-S. Huang, "Designable spectrometer-free index sensing using plasmonic Doppler gratings", *Anal. Chem.* 91 (2019) 9382–9387.
[67] A. Gervais, P. Jean, W. Shi, S. LaRochelle, "Design of Slow-Light Subwavelength Grating Waveguides for Enhanced On-Chip Methane Sensing by Absorption Spectroscopy", *IEEE J. Sel. Top. Quantum Electron.* 25 (2019) 1–8.
[68] K.B. Crozier, K. Seo, H. Park, A. Solanki, S. Li, "Controlling the Light Absorption in a Photodetector Via Nanowire Waveguide Resonances for Multispectral and Color Imaging", *IEEE J. Sel. Top. Quantum Electron.* 24 (2018) 1–12.
[69] Q. Liu, W. Wang, "Free-standing GaN grating couplers and rib waveguide for planar photonics at telecommunication wavelength", *Opt. Laser Technol.* 98 (2018) 257–263.
[70] T. Hemati, B. Weng, "Theoretical study of leaky-mode resonant gratings for improving the absorption efficiency of the uncooled mid-infrared photodetectors", *J. Appl. Phys.* 124 (2018) 053105.
[71] M. Vahdani, S. Yaraghi, H. Neshasteh, M. Shahabadi, "Narrow-Band 4.3μm Plasmonic Schottky-Barrier Photodetector for CO_2 Sensing", *IEEE Sens. Lett.* 3 (2019) 1–4.
[72] Y. Kanamori, D. Ema, K. Hane, "Miniature Spectroscopes with Two-Dimensional Guided-Mode Resonant Metal Grating Filters Integrated on a Photodiode Array", *Materials.* 11 (2018) 1924.
[73] J. Inoue, S. Ura, K. Kintaka, "Cavity-Resonator-Integrated Guided-Mode Resonance Filters for Compact WDM Light Source", *in: 2018 20th Int. Conf. Transparent Opt. Netw. ICTON*, 2018: pp. 1–4.
[74] J. Inoue, A. Tsuji, K. Kintaka, K. Nishio, S. Ura, "Wavelength division multiplexer based on cavity-resonator-integrated guided-mode resonance filters for a compact multi-wavelength light source", *Opt. Express.* 26 (2018) 2212–2219.
[75] X.-Y. Guan, J.W. Leem, S.H. Lee, H.-J. Jang, J.-H. Kim, S. Hann, J.S. Yu, "Fabrication and analysis of highly-reflective metal-dielectric mirrors for high-performance semiconductor laser applications", *Curr. Appl. Phys.* 16 (2016) 155–159.
[76] K. Yamada, K. Asai, Yeong Hwan Ko, K. Kintaka, Kyu Jin Lee, J. Inoue, S. Ura, R. Magnusson, "External mirror with steep reflection phase spectrum by guided-mode resonance for short-cavity VECSEL", *in: 2016 Int. Semicond. Laser Conf. ISLC*, 2016: pp. 1–2.
[77] G. Quaranta, G. Basset, O.J.F. Martin, B. Gallinet, "Color-Selective and Versatile Light Steering with up-Scalable Subwavelength Planar Optics", *ACS Photonics.* 4 (2017) 1060–1066.
[78] W. Liu, G. Hu, H. Zhu, Y. Chen, "Waveguide-metal–dielectric bi-layer gratings for reflective filtering and color security", *Optik. 126* (2015) 1245–1248.
[79] Y. Chen, L. Chen, X. Wang, W. Liu, "A novel metal/dielectric combined grating structure incorporating optically thin plasma metals with the properties of controllably polarization and spectral filtering", *Optik. 168* (2018) 598–604.
[80] G. Quaranta, G. Basset, Z. Benes, O.J.F. Martin, B. Gallinet, "Light refocusing with up-scalable resonant waveguide gratings in confocal prolate spheroid arrangements", *J. Nanophotonics.* 12 (2018) 016004.

[81] B. Chen, X. Zhang, X. Wen, Z. Ruan, Y. Zhu, L. Liu, "High efficiency and polarization insensitive two-dimensional grating coupler on silicon", *in: 2018 Asia Commun. Photonics Conf. ACP*, 2018: pp. 1–2.
[82] W. Fang, C. Yue, X. Fan, H. Niu, X. Zhang, H. Xu, N.-K. Chen, C. Bai, "Polarization Insensitivity Filter Using 2D Sub-wavelength High Contrast Gratings", *2018 Asia Commun. Photonics Conf. ACP*. (2018) 1–3.
[83] D. Wang, Q. Wang, Z. Zhan, "Polarization-Independent Filter Based on 2-D Crossed Grating Under Oblique Incidence", *IEEE Photonics J.* 10 (2018) 1–9.
[84] Y. Huang, L. Liu, M. Johnson, A.C. Hillier, M. Lu, "One-step sol–gel imprint lithography for guided-mode resonance structures", *Nanotechnology*. 27 (2016) 095302.
[85] Custom Blazed Gratings | Blazed Grating, Hologr. LLC. https://holographix.com/custom-blazed-gratings/ (Oct.2020).
[86] L. Berthod, "La photolithographie cylindrique sur revêtement sol-gel photogravable", *thesis*, Lyon, 2017.
[87] Two-dimensional (2D) Diffraction Gratings, Plymouth Grating Lab. https://www.plymouthgrating.com/product/two-dimensional-2d-diffraction-gratings/ (Oct.2020).
[88] V. Gâté, "Ecriture de motifs périodiques submicrométriques sur films TiO_2 sol-gel par lithographie interférométrique dynamique sur de grandes surfaces", *thesis*, Université Jean Monnet - Saint-Etienne, 2013.
[89] M. Bichotte, A. Cazier, F. Celle, C. Veillas, T. Kämpfe, Y. Jourlin, "Very short period grating printing combining UV interferential exposure and mechanical strain", *Microelectron. Eng.* 177 (2017) 66–69.
[90] J. Sauvage-Vincent, S. Tonchev, C. Veillas, S. Reynaud, Y. Jourlin, "Optical security device for document protection using plasmon resonant transmission through a thin corrugated metallic film embedded in a plastic foil", *J. Eur. Opt. Soc. - Rapid Publ.* 8 (2013).
[91] C.J. Chang-Hasnain, W. Yang, "High-contrast gratings for integrated optoelectronics", *Adv. Opt. Photonics.* 4 (2012) 379–440.
[92] How to Choose the Right UHF RFID Antenna, RFID Insid. (2014) https://blog.atlasrfidstore.com/choose-right-rfid-antenna (Oct.2020).
[93] "ΕΙΣΑΓΩΓΗ - ΤΟ ΦΑΙΝΟΜΕΝΟ ΤΗΣ ΠΟΛΩΣΗΣ - "PDF Free Download
[94] S.N. Khonina, I. Golub, "Time behavior of focused vector beams", *JOSA A.* 33 (2016) 1948–1954.
[95] C.-Y. Han, Z.-H. Wei, Y. Hsu, K.-H. Chen, C.-H. Yeh, W.-X. Wu, J.-H. Chen, "Generating Radially and Azimuthally Polarized Beams by Using a Pair of Lateral Displacement Beamsplitters", *Appl. Sci.* 6 (2016) 241.
[96] "Controlling vortex light beams", https://spie.org/news/4965-controlling-vortex-light-beams (Oct.2020).
[97] Z. Bomzon, V. Kleiner, E. Hasman, "Formation of radially and azimuthally polarized light using space-variant subwavelength metal stripe gratings", *Appl. Phys. Lett.* 79 (2001) 1587–1589.
[98] A.P. Porfirev, A.V. Ustinov, S.N. Khonina, "Polarization conversion when focusing cylindrically polarized vortex beams", *Sci. Rep.* 6 (2016) 6.
[99] I. Moreno, J.A. Davis, I. Ruiz, D.M. Cottrell, "Decomposition of radially and azimuthally polarized beams using a circular-polarization and vortex-sensing diffraction grating", *Opt. Express.* 18 (2010) 7173–7183.
[100] M.P. Lipson, Integrated Photonics, 2004th ed., Springer.

[101] G.A. Golubenko, A.S. Svakhin, V.A. Sychugov, A.V. Tishchenko, "Total reflection of light from a corrugated surface of a dielectric waveguide", *Sov. J. Quantum Electron.* 15 (1985) 886.
[102] Z.S. Liu, S. Tibuleac, D. Shin, P.P. Young, R. Magnusson, "High-efficiency guided-mode resonance filter", *Opt. Lett.* 23 (1998) 1556–1558.
[103] D. Rosenblatt, A. Sharon, A.A. Friesem, "Resonant grating waveguide structures", *IEEE J. Quantum Electron.* 33 (1997) 2038–2059.
[104] M. Rumpel, B. Dannecker, A. Voss, M. Moeller, C. Moormann, T. Graf, M.A. Ahmed, "Thermal behavior of resonant waveguide-grating mirrors in Yb:YAG thin-disk lasers", *Opt. Lett.* 38 (2013) 4766–4769.
[105] Y. Jourlin, S. Tonchev, A.V. Tishchenko, F. Lacour, O. Parriaux, "Resonant-grating reflection extended to wide-band, large-aperture beams by waveguide-mode coalescence", *Opt. Express.* 20 (2012) 29155–29163.
[106] D. Shin, S. Tibuleac, T.A. Maldonado, R. Magnusson, "Thin-film optical filters with diffractive elements and waveguides", *Opt. Eng.* 37 (1998) 2634–2647.
[107] E. Bonnet, A. Cachard, A.V. Tishchenko, O.M. Parriaux, "Scaling rules for the design of a narrow-band grating filter at the focus of a free-space beam", *in: International Society for Optics and Photonics*, 2004: pp. 217–223.
[108] O. Parriaux, V.A. Sychugov, A.V. Tishchenko, "Coupling gratings as waveguide functional elements", *Pure Appl. Opt. J. Eur. Opt. Soc. Part A.* 5 (1996) 453–469.
[109] V.A. Sychugov, A.V. Tishchenko, B.A. Usievich, O.M. Parriaux, "Optimization and control of grating coupling to or from a silicon-base optical waveguide", *Opt. Eng.* 35 (1996).
[110] N. Lyndin, T. Kämpfe, S. Tonchev, S. Reynaud, O. Parriaux, "Transverse-mode selective resonant grating-mirrors for high power and high brightness emission", *Opt. Express.* 23 (2015) 17275–17289.
[111] P. Lalanne, D. Lemercier-Lalanne, "Depth dependence of the effective properties of subwavelength gratings", *JOSA A.* 14 (1997) 450–459.
[112] P. Lalanne, J.-P. Hugonin, "High-order effective-medium theory of subwavelength gratings in classical mounting: application to volume holograms", *JOSA A.* 15 (1998) 1843–1851.
[113] M.G. Moharam, D.A. Pommet, E.B. Grann, T.K. Gaylord, "Stable implementation of the rigorous coupled-wave analysis for surface-relief gratings: enhanced transmittance matrix approach", *JOSA A.* 12 (1995) 1077–1086.
[114] M.G. Moharam, E.B. Grann, D.A. Pommet, T.K. Gaylord, "Formulation for stable and efficient implementation of the rigorous coupled-wave analysis of binary gratings", *JOSA A.* 12 (1995) 1068–1076.
[115] M. Foresti, L. Menez, A.V. Tishchenko, "Modal method in deep metal-dielectric gratings: the decisive role of hidden modes", *JOSA A.* 23 (2006) 2501–2509.
[116] I.C. Botten, M.S. Craig, R.C. McPhedran, J.L. Adams, J.R. Andrewartha, "The Dielectric Lamellar Diffraction Grating", *Opt. Acta Int. J. Opt.* 28 (1981) 413–428.
[117] N.M. Lyndin, O. Parriaux, A.V. Tishchenko, "Modal analysis and suppression of the Fourier modal method instabilities in highly conductive gratings", *JOSA A.* 24 (2007) 3781–3788.
[118] J. Chandezon, M.T. Dupuis, G. Cornet, D. Maystre, "Multicoated gratings: a differential formalism applicable in the entire optical region", *JOSA.* 72 (1982) 839–846.
[119] T.W. Preist, N.P.K. Cotter, J.R. Sambles, "Periodic multilayer gratings of arbitrary shape", *JOSA A.* 12 (1995) 1740–1748.
[120] T. Vallius, "Comparing the Fourier modal method with the C method: analysis of conducting multilevel gratings in TM polarization", *JOSA A.* 19 (2002) 1555–1562.

CHAPTER 2

Technology of thin layer deposition and microstructuring

2.1 Introduction

In the previous chapter, the main principles of a multilayered grating structure (WRG) were reported and the resonance efficiency (according to wavelength, angles and polarization of incident light) was shown to be closely related to its structural characteristics. In practice, to obtain high quality resonances we need to optimize the microstructuring process. In this chapter, we will introduce all the techno-optical processes that are necessary to fabricate uniform layers and well-controlled gratings on planar or/and cylindrical substrates. To achieve this, adapted resists, suitable deposition and patterning methods should be attentively chosen. In the framework of this PhD thesis, we chose a negative-based solgel resist developed internally in the laboratory Hubert Curien for waveguide deposition and a positive resist for micro pattering. Dip coating and spin coating were used as solgel deposition methods and photolithography, i.e. the printing of a pattern on a material with the aid of light, was applied to create the diffraction gratings. In particular, as fundamental photolithography processes, the laser interferential lithography and the phase mask lithography were performed. After photoresist deposition and light exposure, the sample underwent the development step to reveal the pattern on the photosensitive layer. At this stage of the process, possible misfits of the grating may occur. A plasma technique is proposed to partially adjust the size and shape of the corrugation.

2.2 Introduction to photolithography and overview protocol for WRG fabrication

The photolithography, also called optical lithography comes from the Greek origin words photo, litho, and graphy that etymologically mean light, stone and writing. The technique was first invented by Nicephore Niepse for photography processing and developed extensively to contribute to the creation of Integrated Circuits and microchips for the needs of semiconductors [1–4], micro-nanoelectromechanical (MEMS/NEMS) devices [5–10], micro sensors [11–14], and biomimetic surfaces [15–17] **(Figure 2.1)**.

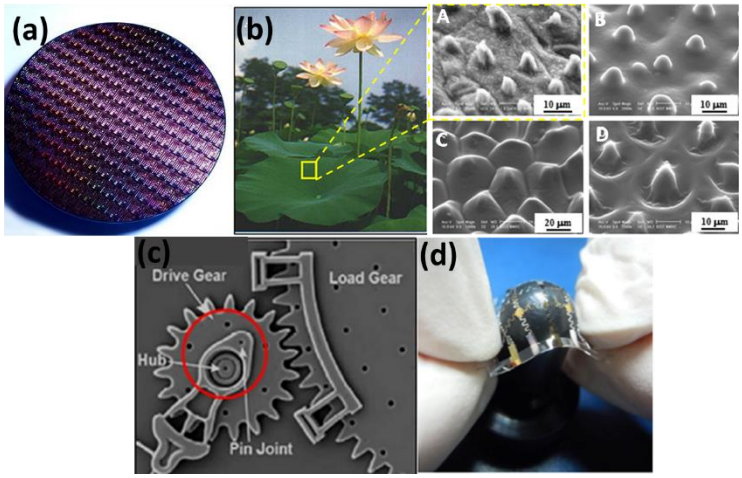

Figure 2.1: Representation of integrated circuits on a semiconductor wafer [18] (a), lotus plant characterized by hydrophobicity and SEM images (A-D) for the corresponding replicated biomimetic surfaces [19] (b), micro gears for tribology on Si/MEMS [19] (c) and pressure sensors developed on textiles [20] (d).

The constant demand to shrink the dimensional features of devices in the semiconductor and IC industry in accordance with Moore's law [21], has placed optical lithography at the center of technologies to provide excellent performances approaching the 10nm scales. For more than 50 years, photolithography remained among the most standard technics with continuous advances in the construction of high-resolution microstructures that bulky mechanical methods could not attain.

The technique is used to pattern complex motifs onto substrates using light. To begin photolithography a layer of a viscous UV reactive substance called photoresist is deposited on the wafer, the substrate. Under illumination, the light pattern image represented on a photomask is projected on the substrate photosensitive resist layer **(Figure 2.2).**

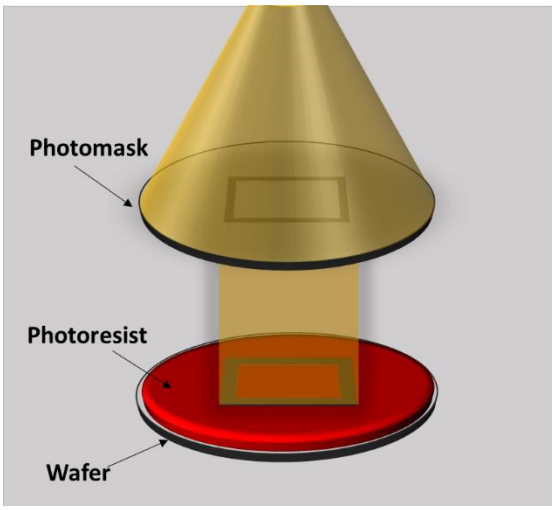

Figure 2.2: Pattern transfer from air to the photoresist-coated substrate.

Upon exposure to light, the photoresist depending on the chemical properties of the resist material may become more or less soluble. Thus, we can classify two types of photoresists: positive and negative resists **(Figure 2.3-a, b)**. The positive resist becomes soluble upon exposure to UV light whereas the exposed regions of negative resist become cross-linked and insoluble. The soluble part is then removed using a developer solution leaving a positive or a negative image of the pattern respectively.

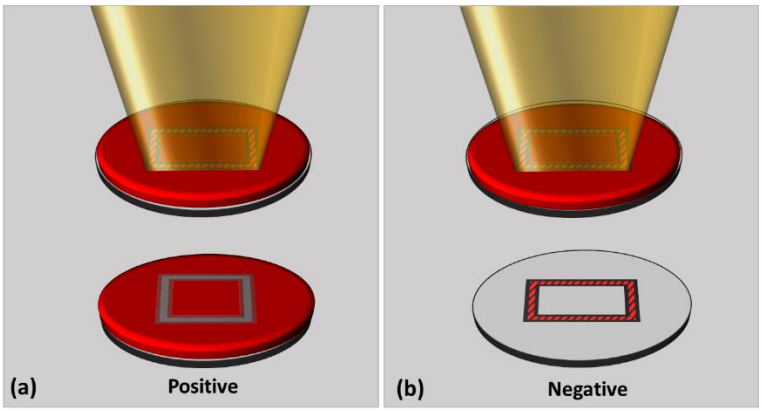

Figure 2.3: Positive and negative photoresist rinsed with a developer solution leaving a positive (a) or negative pattern (b) behind.

During this PhD thesis, the photolithography process is the main technique, which has been used and developed for our sample elaboration. Below, a graphical flow chart **(Figure 2.4)** presents all the general sequential steps followed. The WRG of our study is mainly composed of a waveguide, made with various materials and processes (see Chapter 4 & 5) while the final coating layer is always a positive photoresist intended for patterning.

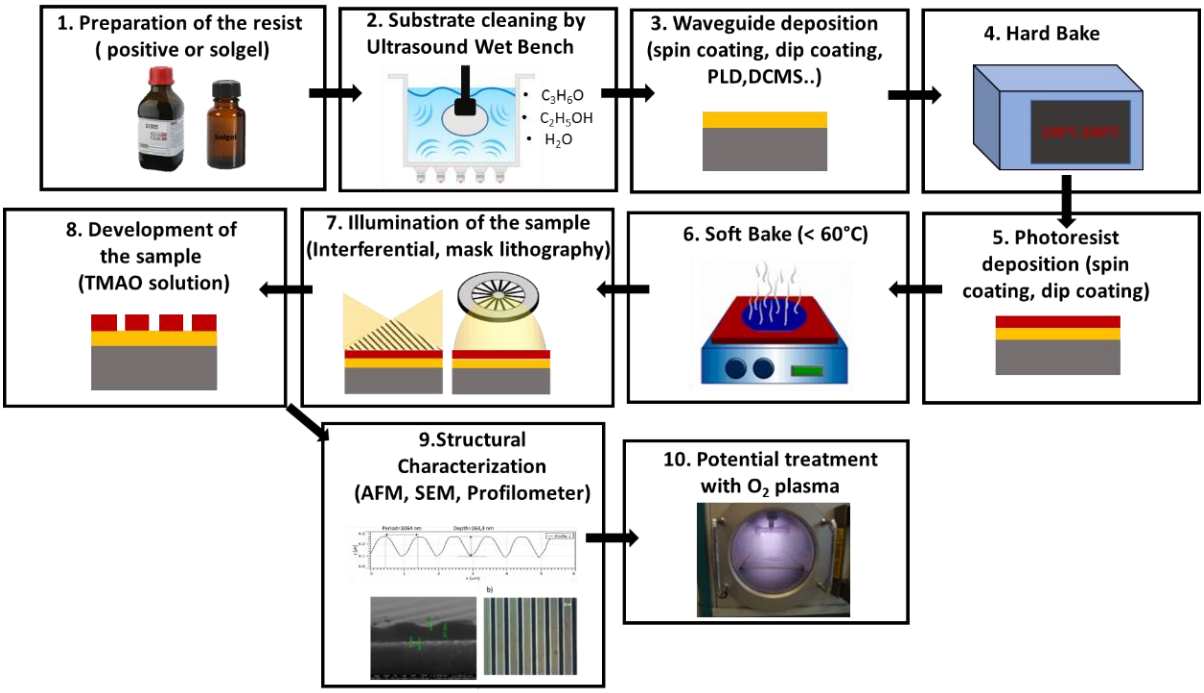

Figure 2.4: Overall protocol step for the construction of WRG samples.

2.3 Characteristics and preparation of the resists

The compatibility of the resist with the deposition and exposure techniques with determined functionality is the subject of intense studies [22–25].

Photoresist along with exposure wavelength affect the critical dimension for any application. The appropriate choice of the resist and the increasingly shorter wavelength may allow smaller feature sizes with higher resolution. Due to the constant demands, the technology of photoresist's fabrication has evolved steadily to keep up with the lithographic innovations and to transfer the pattern with the highest possible fidelity. Fundamentally, some basic requirements need to be fulfilled for the photoresist synthesis [26]:

1. Transparency– The photoresist film needs to be transparent enough to enhance the pattering process and enable the transfer of the aerial image on and through the whole film thickness. Photoresists are usually optimized for a given insolation wavelength, often in the UV that lowers the diffraction limit.

2. Contrast– The ability to distinguish the exposed and unexposed areas of given resist thickness after a suitable radiation rate and development processing.

3. Material stability– During the integration process (etching or implantation steps) the resist must withstand sufficient thermal shocks and exhibit good chemical resistance. The resist film

has to be carefully prepared to offer compound homogeneity and good substrate adhesion after coating and posterior steps to minimize defect issues.

Extending the technology of resist fabrication, some chemical compounds are additionally introduced to amplify the sensitivity (the minimum required energy to produce a well-defined pattern of the photoresist on the substrate, measured in mJ/cm^2) to the particular light source and to the dissolution.

Nowadays, the photoresists provide a standard composition protocol respecting the aforementioned quality factors. Within this PhD thesis, we have employed the commercial positive photosensitive solution (S1805 from Shipley) for grating patterning and the TiO_2/BzAc solgel manufactured in the laboratory Hubert Curien for waveguide deposition.

2.4 Photosensitive Resists

2.4.1 Positive Resist

2.4.1.1 General Characteristics

The positive photoresist or novolac is a long-chain aromatic ring polymer consisting of two methyl groups and an OH group **(Figure 2.5)**. Thanks to the OH group, it dissolves easily in organic solvents such as acetone or base developer solution.

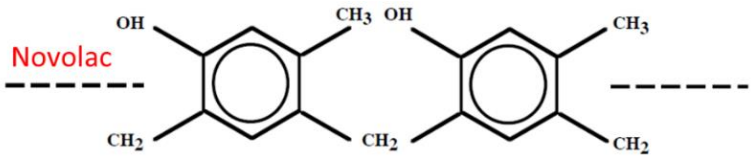

Figure 2.5: Organic polymer of novolac-resist.

The origin of this polymer comes from the mixing of the phenol and formaldehyde in an acid medium **(Figure 2.6)**.

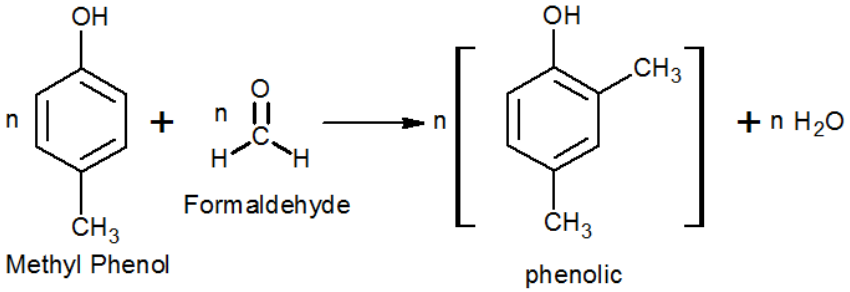

Figure 2.6: Polymerization reaction of the phenolic photoresist.

The phenolic resist, otherwise called, is not intrinsically photosensitive under the light exposure but it is transformed after the introduction of the DNQ (diazo naphthoquinone), a photoactive chemical compound. The quantum efficiency of the photoreaction determines how many photoreactions will take place proportionally to the number of photons absorbed by the resist film. Moreover, the DNQ when bound to the novolac resist acts as an inhibitor reducing the dissolution rate in a base solution (pH > 7). This inhibitor character is radically eliminated immediately upon a photolysis process that renders the DNQ organic molecule soluble in aqueous basic solvents. Specifically, as illustrated in **Figure 2.7**, the DNQ molecule (left) after light exposure to a suitable wavelength, releases a nitrogen. This carbon site chain becomes more stable by extracting one carbon with its covalent bonded oxygen outside the ring. The rearranged chain is called ketene and when absorbing H_2O, it is converted into an indene carboxylic acid (ICA). Likewise, the inhibitor concentration decreases and the rate of development increases rapidly.

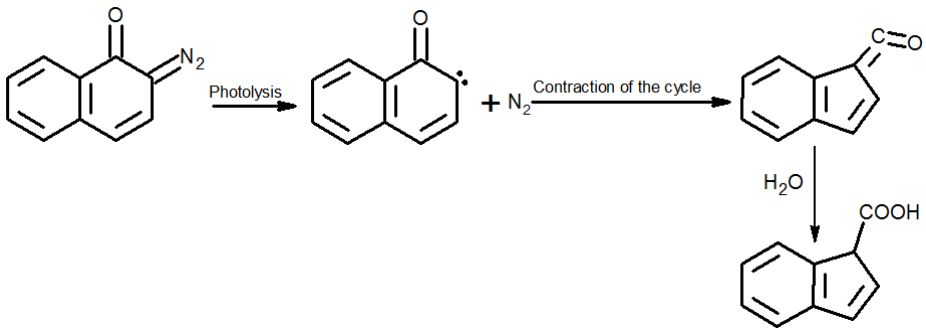

Figure 2.7: Conversion of the photoinitiator molecule (DNQ) into an indene carboxylic acid allowing the dissolubility to solubility transformation in the developer.

The solubility tendency of the DNQ novolac resist **(Figure 2.8)** can be clearly observed by the following graph known also as Meyerhofer plot. Independently the DNQ rate of concentration, the resist remains inactive without the light exposition (red curve) whereas the concentration becomes more critical on the solubility effect during the resist radiation (blue curve).

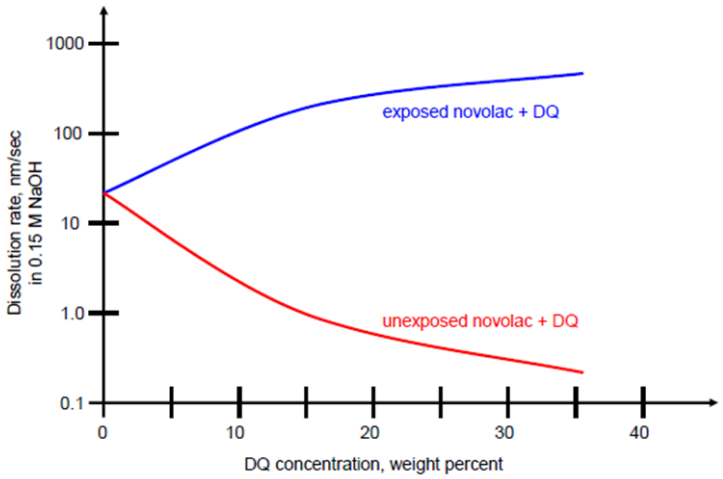

Figure 2.8: Solubility of the novolac-DNQ mixture as a function of the DNQ concentration [27].

The DNQ-novolac resists are most often sensitive in the UV range but can also be selectively sensitive to specific wavelengths. Hence, they are called g-line, h-line or i-line (emission lines of H_2) when they absorb at (437 nm), (405 nm) and (365 nm) respectively. The illustrated graph **(Figure 2.9)** summarizes the absorption overlap for each Novolac, DQ (diazo naphthoquinone) and ICA (indene carboxylic acid) in proximity to the emission Hg lines. It demonstrates that the operational spectral range for the novolac resist is indeed the UV.

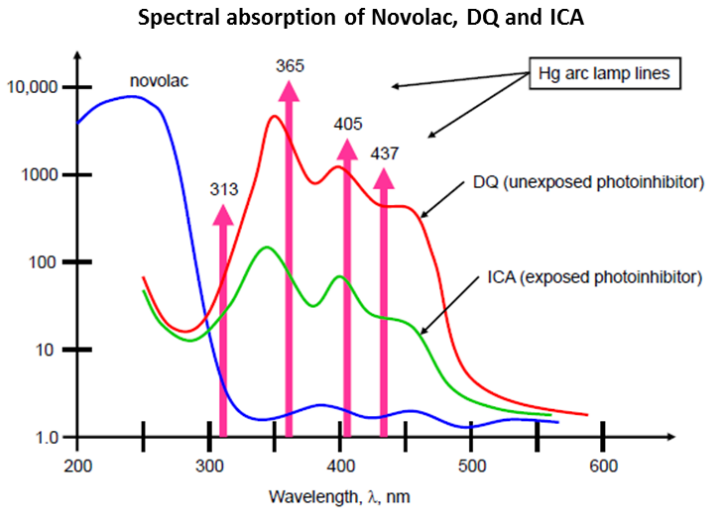

Figure 2.9: Absorption for separate resist ingredient in the UV wide spectra [27].

2.4.1.2 Preparation of the solution

The positive S1805 resist is occasionally diluted with the Ethyl Lactate in order to obtain the desired thickness according to the targeted application. The photoresist must be dosed very precisely since a minor excess or deficiency can alter the viscosity of the liquid.

2.4.1.3 Exposure Dose

For positive resists, the exposure dose is close to the value of the saturation of the development rate. This effect is not unique but depends on the type of photoresist, developer and on the soft bake as well. The prevailing atmospheric characteristics such as humidity and temperature of the clean room can also influence the form of the curve.

For the sensitivity of our proper positive resist, we have tested a range of power density ($\mu W/cm^2$) multiplied by the specific exposure time (seconds). Then, we have defined the exposure dose ($\mu J/cm^2$). For a thick photoresist of initial layer of 600-650 nm, we have developed during 3 sec after the light exposition and we have measured the thickness of our new formed layer resulting in the rate of development. The exposure wavelength was 442 nm, the substrate BK7 and the soft bake at 60°C for 60s. From the curve **(Figure 2.10)**, we can deduce that the increase of light exposure dose helps the photoiniator to a complete conversion and results in a larger development rate down to the substrate. The photoresist has a threshold and can only be developed after a minimum exposure dose. Moreover, increasing the soft bake temperature, we decrease the sensitivity and thus the penetration depth of the light.

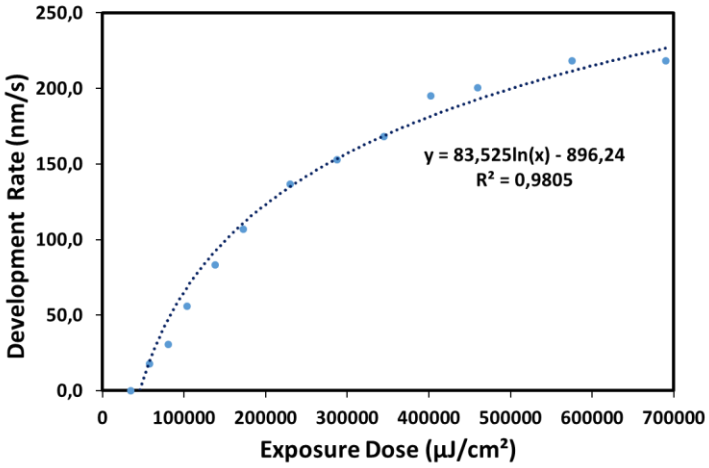

Figure 2.10: Sensitivity curve of the positive photoresist S1805 used at Laboratory Hubert Curien.

In general, it exists a critical exposure dose (which depends on the photoresist type), which permits the construction of an ideal vertical resist profile. Usually, a medium exposure dose with a moderate development time is employed. Overall, the photoresist profile is difficult to predict and it must be found experimentally.

2.4.2 Negative Resist: TiO_2/BzAc Solgel

For negative resists, the higher the exposure dose is, the higher the cross-linking and the lower developing time are. In the case of excessive exposure, dark resist areas tend to remain after development. For an ideal negative resist, the **Figure 2.11** relates the contrast to the curve slope. The logarithmic scale gives the exposure dose and the energy D_0 denotes the part of the resist that begins to be affected by the light, whereas the D_f demonstrates the part of the resist that becomes solid. Beyond an exposure threshold D_0, the resist stops further polymerization and the level of solidification remains stable.

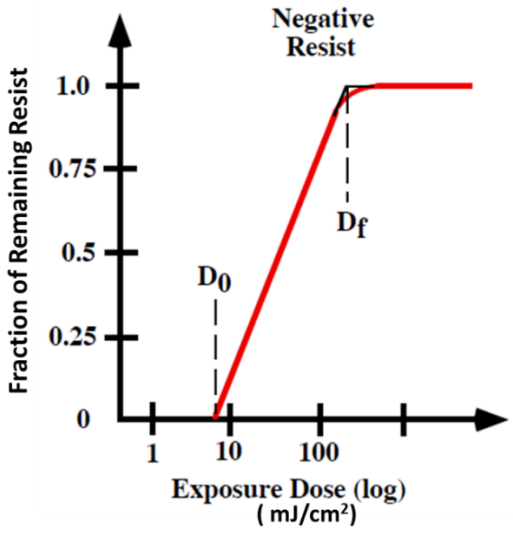

Figure 2.11: Contrast curve for ideal negative resist [28].

In the Laboratory Hubert Curien and for sensing applications, we use a TiO_2 solution as negative resist that is transformed into gel via the solgel method. The synthesis and the protocol has been developed by the LMGP group [29] and further developments have been pursued during the thesis of Valentin Gaté [30]. Regarding our targeted needs and after its operation, the TiO_2 solgel proved to be more stable compared to the current commercial SU-8 resist. Notably, when used for grating structures it has exhibited high contrast and stability, while for thin films intended for wave guiding it has provided good adhesion and compatibility even for large surfaces. In the context of this PhD thesis, the TiO_2 resist will not be employed as a

photosensitive resist but as a thin waveguide layer. Therefore, special sensitivity measurements were not performed since no photo activity will be used. The chemical formulation of the TiO_2 synthetized solgel will be analyzed below and the choice of its waveguide use will be progressively explained based on the protocol benefits.

2.4.2.1 Sol-Gel Method

Among the different methods used for the synthesis of materials, the Sol-Gel process is particularly well suited to manufacture homogeneous materials, in the form of powders and films [31], with high optical performance [32]. The possibility to deposit on large or complex surfaces and its low cost attracts more and more the attention for optical applications [33–36].

The Sol-Gel method is a process for converting a liquid (solution) into gel (gelling) from precursors in solution. This so-called soft chemistry process implements reactions at temperatures close to ambient under atmospheric pressure [37] and is an interesting method due to its ease of implementation.

The overall scheme of the Sol-Gel process can be described in two steps. In the first step, the sol is formed by partial hydrolysis of the precursor metal alkoxide (of general formula M (OR)) with M the metal and R the radical alkyl according to the reaction (**Equation 2.1**).

Hydrolysis

$$\text{-M-OR}+H_2O \rightarrow \text{-M-OH}+\text{ROH} \qquad \textbf{Equation 2.1}$$

Then, a succession of reactions leads to condensation by two different possible ways. Particularly, in the second step, the partially hydrolysed compounds (resulting from the previous hydrolysis reaction) react with the precursor through the alkoxolation reaction, or on themselves through the oxolation reaction **Equation 2.2(ii)**. The formed dimers will then evolve into broad polymeric chains. The resulting gel is constituted by an oxide network surrounded by the solvent, linked by Van der Waals bonds.

Condensation

(i) *Alkoxolation*: $\text{-M-OH}+\text{RO-M-} \rightarrow \text{OR-M-O-M}+\text{ROH}$

(ii) *Oxolation*: $2(\text{M-OH}) \rightarrow \text{OR-M-O-M}+H_2O$ **Equation 2.2**

The contribution of each of these reactions to the formation of the oxide group depends both on internal parameters (nature of the metal atoms and on the alkyl groups, precursor structure) and

on the external parameters (ambient humidity / alkoxide ratio, catalysis, solvent, temperature) [38].

After removal of the liquid by drying the gel, one obtains either a xerogel (drying under atmospheric conditions) or an aerogel (drying under supercritical conditions). An aerogel is a gel, which has a volume porosity between 80-90% while a xerogel is denser with a porosity of about 60-70% [39]. It should be noted that a basic pH slows the hydrolysis reactions and favors the polymerization, whereas an acidic pH induces the opposite effect and promotes the formation of the gel.

2.4.2.2 Experimental Protocol of the TiO_2 based sol gel preparation

The process begins with the preparation of the solution by the sol gel route. The TiO_2 is formed by the TiPT (tetra-isopropoxide-Sigma-Aldrich, 97%), the metallic precursor, diluted in an alcoholic solvent and a BzAc chelating agent (Benzoylacetone- Sigma-Aldrich, 99.9%). In more details, the synthesis of TiO_2 is due to the combination of a mother solution which consists of TiPT, H_2O, HCl (Hydrochloric acid) and BuOH (butanol-Fisher, 99%) with a molar composition 1 / 0.82 / 0.13 / 23.9, with the daughter solution of BzAc, TiPT and MOH (methanol-Sigma-Aldrich) and a molar composition 1 / 0.75 / 20.4 respectively **(Figure 2.12)**. The mother solution is particularly stable in time (for about 6 months) and is aged during two days before being used. Once the solutions Sol_1 and Sol_2 are mixed, the new obtained solution has a TiPT concentration of 0.5 M for a molar ratio BzAc / TiPT of 0.5. This solution is 2 months self-life maintained, whereas when exceeding the two months' time interval, the photosensitivity stays unchanged at the expense of a poorer reproducibility.

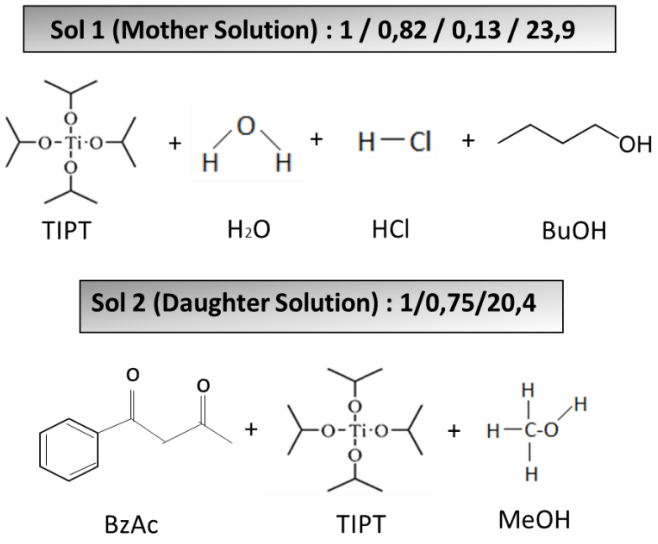

Figure 2.12: Molar composition of mother and daughter solution.

The above protocol focuses on the presence of BzAc that is essential to avoid the polymerization of TiO_2. Under standard conditions and without the chelating agent presence, the TiPT after hydrolysis, carried out with an aqueous-acid bond, reacts entirely during the condensation step leading to a TiO_2 polymer. The introduction of BzAc into the TiO_2 sol blocks the condensation, decreases the reactivity of the TiPT and renders the TiO_2 soluble in different solutions. After deposition, the TiO_2 film becomes sensitive to UV light. After illumination, the TiO_2 behaves like a negative resist (the insolated parts remain insoluble) thereby we get patterns without the need to etch or lift off.

2.4.2.3 General characteristics of TiO_2 element and properties of TiO_2/BzAc based sol-gel film

The TiO_2 solution resulting from the sol gel route is suitable for the deposition of thin films. Hence, after deposition the TiO_2 yields to a xerogel film when the latter is treated thermally in a range of 100°C to approximate 600°C with an appropriate time depending on the chosen temperature. At the end of the annealing, the xerogel layer possesses high stability, good adhesion to the substrate, and a refractive index that can be modified depending on the applied heat treatment.

The graph below **(Figure 2.13)** indicates the correlation between the refractive index at a visible wavelength of 633 nm, the annealing temperature and the thickness of the layer. As observed, the refractive index increases with temperature since the layer becomes more dense, thus with reduced thickness. The highest refractive index is obtained at the crystalline phase after annealing at 500°C where the TiO_2 is said to be at its anatase phase.

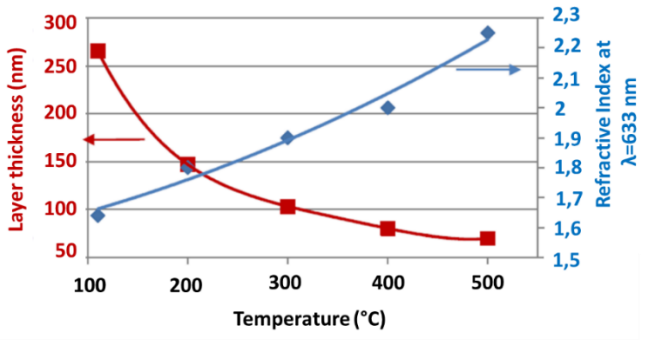

Figure 2.13: Interaction of layer thickness with refractive index and annealing temperature for a TiO_2 xerogel layer [30].

The TiO_2 layer can present different crystalline phases, the most common ones being the anatase, brookite and rutile. The anatase phase presents an elongated tetrahedral structure with irregular oxygen octahedra, the brookite has an orthorhombic crystalline structure and finally the rutile is equally characterized by a tetragonal structure like this of anatase **(Figure 2.14)**.

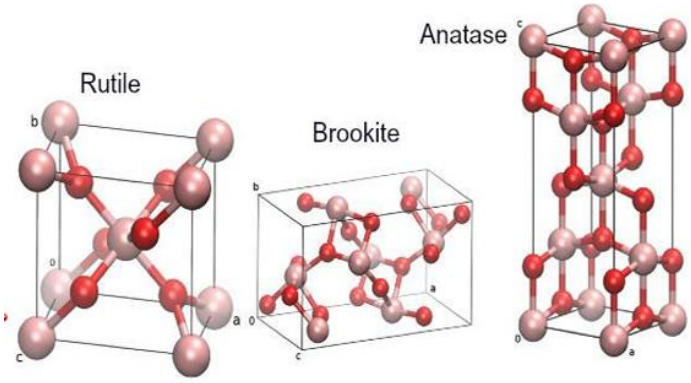

Figure 2.14: Unit cell of the three crystalline phases of TiO_2 with Ti illustrated as colorless spheres while O_2 as little solid spheres [40].

The transition from one state to another takes place by increasing the temperature or the pressure. The specific diagram of pressure-temperature gives some general information about the set points of crystalline phases **(Figure 2.15)**. For example, the anatase phase can be obtained at temperatures below 600°C using low pressures whereas rutile can be created from 600°C under the same conditions. On the other hand, at high pressures, TiO_2 II (called Srilankite) is formed. The brookite phase is a metastable phase and may be found mixed with anatase [41]. However, it is rarely encountered as pure phase, which actually makes it difficult to predict [42].

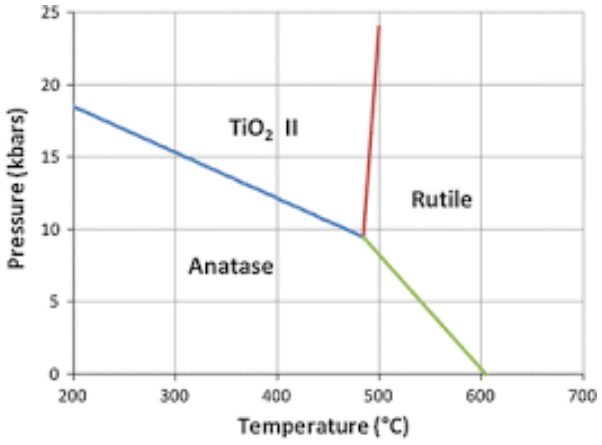

Figure 2.15: Pressure-temperature diagram of TiO_2 [43].

According to the graph of **Figure 2.15**, our synthetized xerogel layer permits the existence of two states as a function of the chosen annealing temperature. The first state is defined as amorphous, characterized by a complete disordered inner structure at a baking temperature close to 100°C while the second is the anatase phase in a possible mixture with the brookite phase.

To verify the exact state of our xerogel, Raman spectral measurements have been performed. The obtained experimental spectra are compared to the theoretical ones [40, 43] and demonstrate a pure anatase phase with distinct peaks at 144, 399, 515 and 639 cm^{-1} **(Figure 2.16)**. The xerogel layer was further characterized by ellipsometric measurements for both amorphous and anatase state. As observed, the absorption coefficient is below detection limit from 350 nm up to NIR whereas the refractive index increases from 1.75 to 2.2 from amorphous to anatase phase **(Figure 2.17)**. It is also important to notice that the extinction coefficient k is close to zero in the visible and NIR wavelength range, which leads to a low loss layer that is suitable for a waveguide.

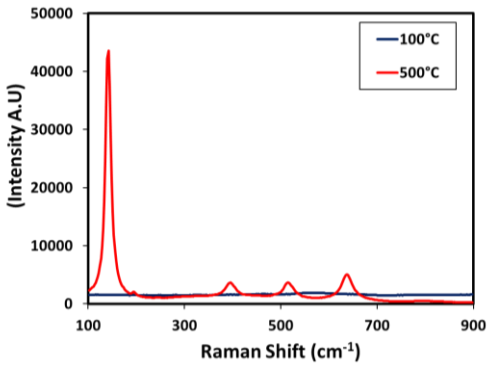

Figure 2.16: Raman spectra (ARAMIS Lab RAM spectrometer) of TiO_2 on silica substrates with heating temperatures at 100 ° C and 500 ° C for 1h. Excitation wavelength at $\lambda = 633$ nm.

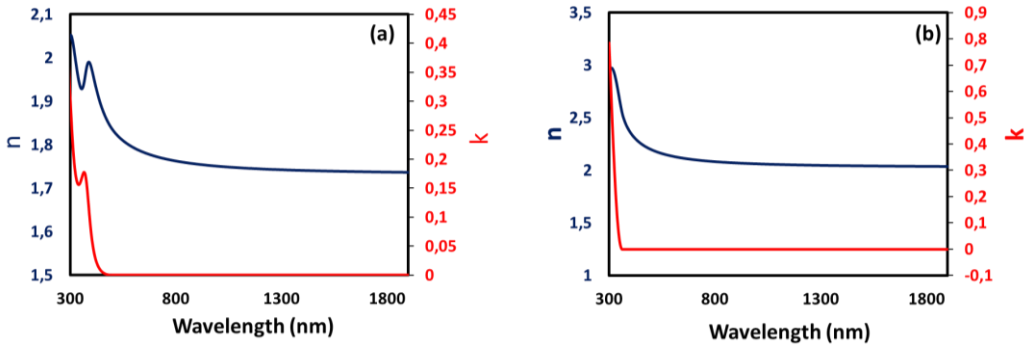

Figure 2.17: Determination of refractive index n and absorption coefficient k of TiO_2 Amorphous (a) and anatase (b) by ellipsometry (HORIBA Jobin Yvon UVISEL).

Additionally, the transmittance of the **(Figure 2.18)** demonstrates the optical properties of the two annealed layers deposited on a SiO_2 substrate. In amorphous state one can distinguish a high transmission in the visible band with a characteristic absorption at 365 nm attributed mainly to the presence of TiO_2/BzAc complex. In the anatase phase and in the visible range there is a slight variation of the intensity in transmission (from T = 0.9 to T = 0.8) due to the refractive index increase of the layer from 1.67 to 2.25 during annealing, which promotes reflection losses. The absorption peak at 365 nm vanishes, indicating the complete degradation of the BzAc.

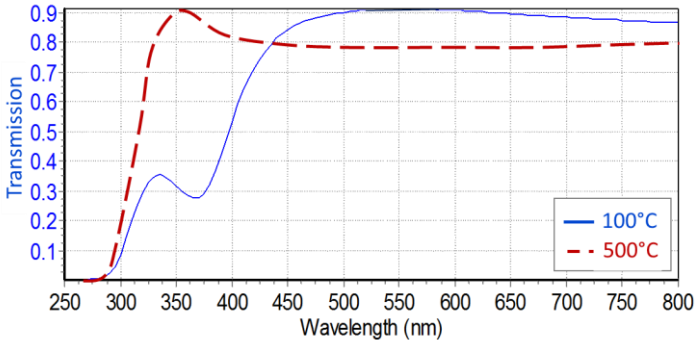

Figure 2.18: Transmission of TiO_2 xerogel layer treated thermally at 110°C during 90 min (blue plain line) and 500°C during 3 h (red dashed line).

2.5 Deposition methods and sample preparation

2.5.1 Choice and preparation of the substrate

The nature and surface condition of the substrate dominates the microstructure and the quality of the deposition. Before deposition, the substrate must be attentively cleaned to limit possible contamination of the deposited layer. For this reason, a successive immersion under ultrasound in acetone, ethanol and ultrapure water is performed. The physico-chemical properties between the substrate and the solution prescribe the adhesion of the liquid solution on the substrate and thus the fabrication of a homogeneous film. Subsequent uniform depositions can be favored on homogeneous surfaces. In addition, the optical index of the substrate may be important; for example, optical guided measurements impose the index of the substrate to be lower than that of the thin layer deposited.

The nature of the substrate can be critical during the exposure process, for instance if metallized substrates are reflective. The incident light interferes with the reflected light and thus it is difficult to cross-link the resist layer down to the substrate.

Transparent substrates such as quartz, glass, polymers can conduct light directly at the back side of the substrate. The addition of glycerol between the substrate holder and glass substrate can reduce the parasite reflections at the substrate backside. Since the glycerol has almost equal refractive index with the glass, the reflections are vanished compared to the case of glass-air gap. Hence, these parasite reflections do not affect the final resist profile.

In general, to prevent the reflections we need to find the optimal exposure dose and preferably use anti-reflective coatings such as BARC (Bottom Anti reflective coating). The use of negative resists would be also helpful since it is not essential for the light exposure to reach down to the substrate. In the present work, the substrate is silica (or glass) to minimize back reflection so that no BARC is needed.

2.5.2 Dip Coating

This method involves soaking the substrate in a liquid coating solution and then withdrawing it vertically with a controlled speed **(Figure 2.19)**. This technique offers high optical quality and is suitable to coat planar and non-planar substrates to form waveguide layers [45–47], optical protective layers [48–50], sensors [51–53] etc.

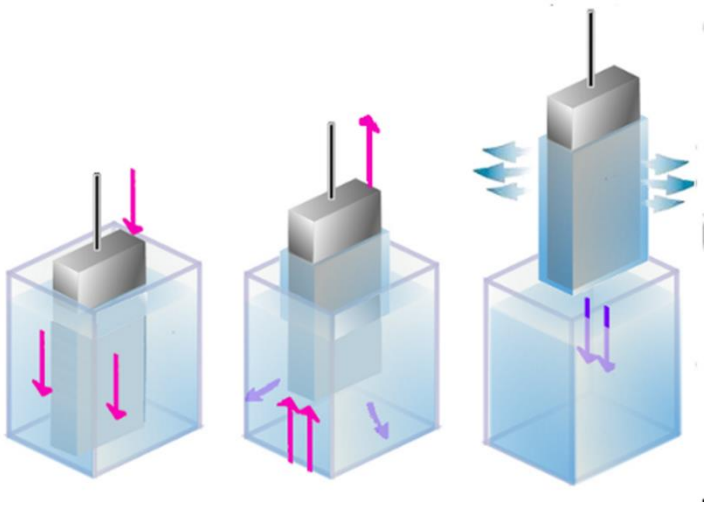

Figure 2.19: Dip Coating including immersing, layer formation and solvent evaporation [54].

Its compatibility with the sol gel process enables the fabrication of films of different composition and thickness on various types of substrates. Nevertheless, concerning the Titanium based solgel coatings, the substrates onto which the solution will be deposited is of critical importance [55].

Apart the proper choice of the substrate, the high quality of thin films depends on multiple parameters. Primarily, it is required a precise control of the drawing speed and a clean environment. The viscosity of the solution, the pH of the solution and the wettability of the substrate also affect the thickness of the films. Recently, a group from the CBI laboratory at ESPCI Paris and from the College de France has investigated the importance of an axial symmetry between the cylindrical rod and the cylindrical reservoir on the thickness of coatings. In their study, they have additionally shown that the movement of the rod with respect to the fluid flow, the dimensions and geometry of the container with respect to the substrate size can affect the deposited layer thickness [56].

Therefore, to ensure a fine quality of films it should be paid attention at every step of the process.

The dip coater device is composed of a motor used to introduce and remove the substrate into the solution at a constant speed and a reservoir containing the solution to be deposited. To obtain thin films the withdrawal speed must be calibrated to a moderate speed while for thicker films higher speeds are needed. A study of our own dip coater evidences this trend by a graph, where the thickness of the deposited TiO_2/BzAc solgel layer is plotted versus the withdrawal speed (**Figure 2.20**). The same calibration was performed for the novolac positive resist.

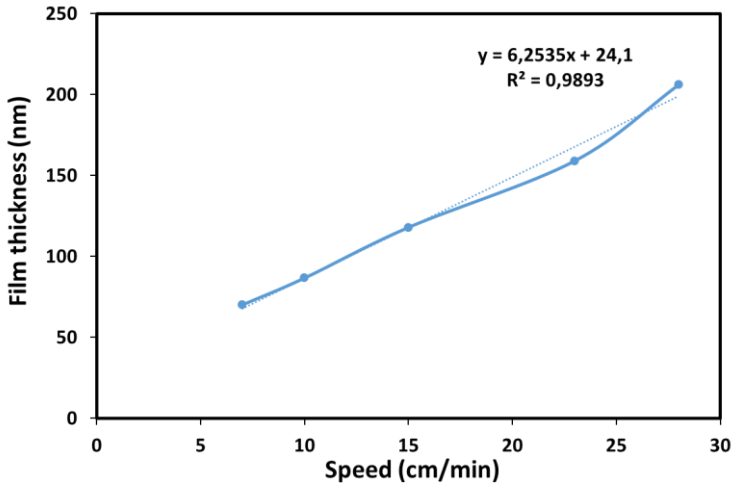

Figure 2.20: Thickness evolution (full line) and trend line (dashed line) of TiO_2/BzAc solgel film as a function of pulling speed.

Moreover, it is worth noting that the whole set-up (engine, container) should be stable and free of vibrations so that the surface of the solution remains stationary during the deposition. The slightest disturbance can cause horizontal streaks on the film.

The liquid is deposited in 5 main steps **(Figure 2.21)**.

1. Immersion: the substrate is immersed into a container filled with the solution to be deposited at a constant rate.

2. Start-up: the substrate remains immersed for a determinate time to guarantee complete wetting of the substrate in the solvent and thereafter starts to be pulled up.

3. Deposition and Drainage: while pulling the substrate up, the film is deposited on the substrate. The excess of solution is drained from the surface.

4. Evaporation: the final coating is formed after the evaporation of the solvent from the deposited liquid film.

5. Drainage: after the complete removal of the substrate, the drainage of the coating continues.

The mechanism of thin film formation begins during the extraction of the substrate out of the solvent. The substrate on its rise drifts a part of the solution in the form of a fluid film, which splits into two at the proximity of the meniscus. The part which is in the immediate vicinity of the substrate accompanies the upward movement of the substrate, while the other returns to the reservoir. The point S defines the stagnation point where entraining and draining forces are in balance. The upper part of the stagnation line determines the thickness of the deposited film **(Figure 2.22)**.

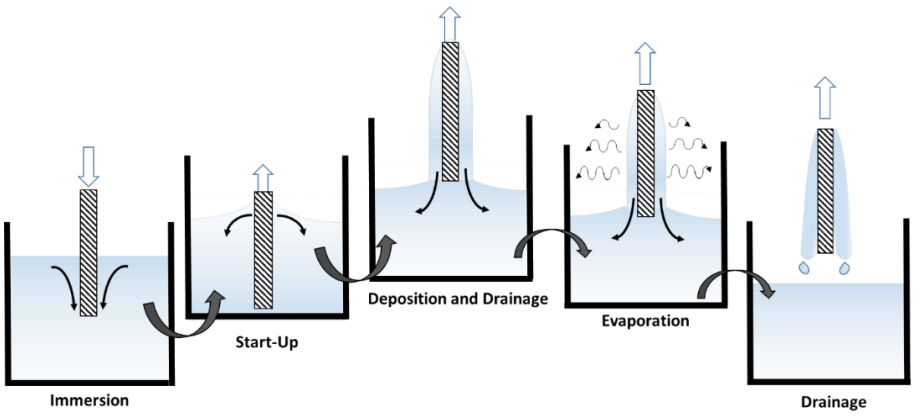

Figure 2.21: Principle steps of the dip coating process.

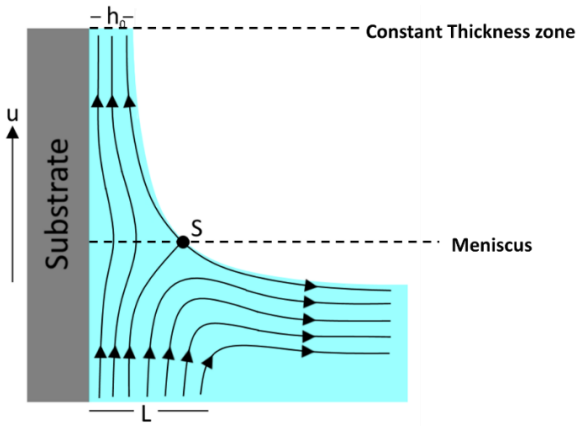

Figure 2.22: Physical mechanism of the film formation by dip coating [57].

2.5.3 Spin Coating

This method consists in depositing a few drops of solution on a planar substrate that rotates with constant angular velocity. During the rotation, the drops will spread uniformly thanks to the centrifugal driving force. The surface tension and viscous force retain the thin residual film on the flat substrate. When applying to Newtonian fluids it gives excellent results. It is also suitable for film formation on substrates whose dimensions are of the order of 2-3 cm and further. This technique is easily implemented and is mainly used in the semiconductor industry [58–60], photovoltaics [61–63], optical mirrors [64, 65] etc.

The spin coater device includes a bath that contains a spin vacuum chuck that maintains the plate, on which is deposited the substrate **(Figure 2.23)**. After the solution injection on the substrate with the aid of a syringe, the plate follows an accelerated rotation with the predefined velocity set on the control panel. The substrate is hold by vacuum. A protective lid is placed during the deposition process for full solvent resistance and for contamination avoidance. This protective lid is also used to maintain photoresist vapors (from solvents) constant in the chamber during the spin coating. This effect is necessary to obtain homogenous deposition, mainly for large substrates. The process takes place in a clean environment.

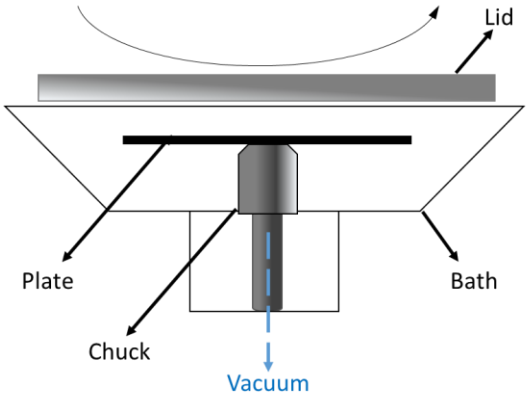

Figure 2.23: Schematic of spin coater processor.

This deposit method can be separated into four stages **(Figure 2.24)**.

1. The fluid solution deposition: The solution is deposited on the substrate, which is on the rotational wafer.

2. Spin-up: At the beginning of the rotation, the acceleration makes the liquid flow to move towards the outer boundaries of the substrate.

3. Spin off: Constant speed rotation allows the ejection of the liquid excess in the form of droplets, which causes the reduction of the film thickness.

4. Evaporation: The evaporation from most of the volatile solvents results in coating thinning.

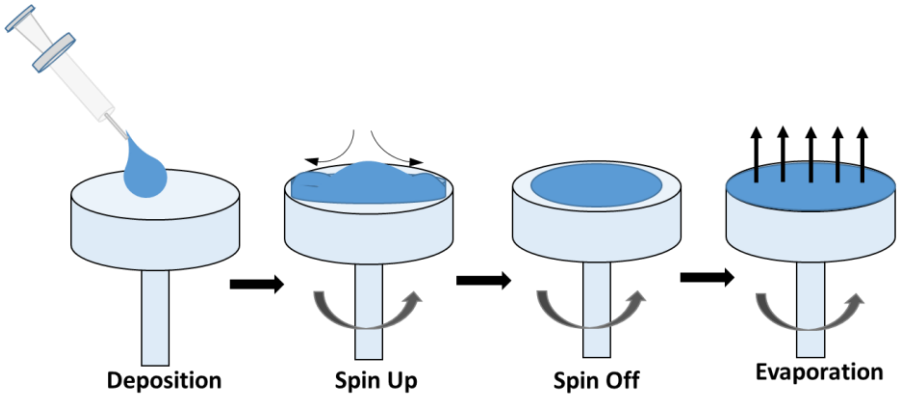

Figure 2.24: Stages for thin film deposition by spin coating.

However, for the spin coating, the film thickness can be controlled when using a solution with known viscosity and fixed rotational speed. Even if it is still a multi-parametric factor, a model proposed by Meyerhofer [66], can help to calculate the layer thickness *h* by the following relation **(Equation 2.3)**:

$$h = c\left(\frac{3\eta e}{2\rho\omega^2}\right)^{1/3}$$ **Equation 2.3**

where c is a constant, η the viscosity of the solvent, e the evaporation speed, ρ the density of the solution and ω the rotational speed.

For our TiO_2/BzAc solgel, an empirical graph (**Figure 2.25**) is plotted to relate the coating thickness with the rotation speed. The same calibration was performed in the same way for the novolac positive resist.

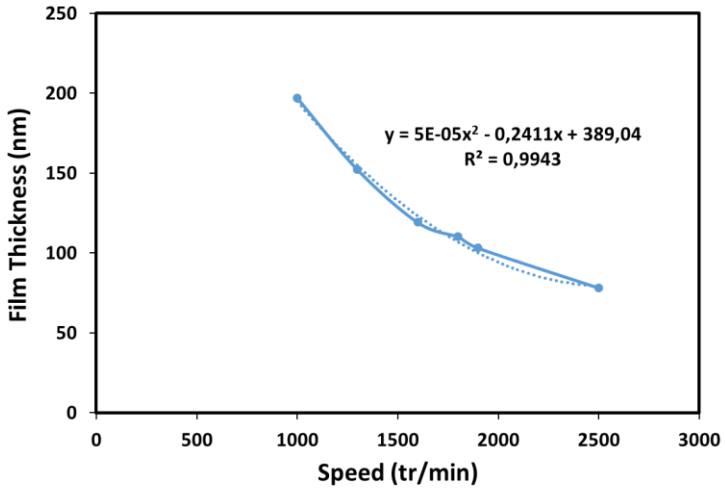

Figure 2.25: Thickness evolution (full line) and trend line (dashed line) of TiO_2/BzAc solgel film as a function of the rotational speed.

2.5.4 Thermal treatment of the layers

For spin and dip coating, the thin layers of our use are naturally dried at room temperature and then heated to evaporate all the solvents. This step of drying and heat treatment aims to transform the amorphous thin layers after drying operation into crystalline layer applying an appropriate heat treatment for variable dwell times. Specifically, for the sol gel deposited film and after drying phase, some organic groups of alkyl type (-OR-) are still present on its surface. Therefore, the film needs to be subjected to soft or hard bake to eliminate the residual organic species and to get densified for crystallization [67]. For a soft bake treatment, the substrate is placed on a heating plate and with heat diffusion, a stabilization is achieved. For a hard bake, thermal induction ovens are employed.

2.6 Exposure Techniques

2.6.1 Laser Interferential lithography (LIL) or Holography set-up

Unlike self-assembly [68–70] or construction-based [71,72] approaches, laser interferential lithography (LIL) is a simplified and cost-effective method appropriate for large areas [73–75]. Being part of photolithography, this technique is based on recording a fringe pattern (interferogram) on a photosensitive layer (created by the interference of two or more coherent monochromatic light waves of wavelength λ [76–78]).

Dealing with the simplest case, when the wave fronts of two beams overlap, dark and bright zones (interference fringes) appear. The photosensitive layer that covers the substrate records this pattern and reveals it after the development. The period Λ of this registered grating is the same as the interferences pattern between the two beams and is related to the angle 2θ (angle between the two incident beams) through:

$$\Lambda = \frac{\lambda}{2n \sin\theta} \qquad \textbf{Equation 2.4}$$

where n is the refractive index of the propagation medium of the wavelength and θ the half angle between the two beams. Likewise, different patterns with different periods are feasible by varying the angles (for a constant wavelength). The dependence on the angle θ of the period and the beam cross section size determines the interfering area. The coherence length of the laser is also another factor that limits the exposed size of the sample due to the path length difference. Gas lasers like (Ar-ion or He-Cd) have the ability to treat samples up to ~30 cm of diameter.

The typical configuration of interference holography splits the light into two beams with equal optical arm length through a semi-reflective mirror or a cube splitter **(Figure 2.26)**. The laser source is suitably selected to be compatible with the sensibility band of the resist and the optical arms are well calibrated to deliver the same amount of power on the substrate. Before the two beams arrive at the photosensitive surface, they undergo a spatial filtering with objective lens, pinholes and beam expanders.

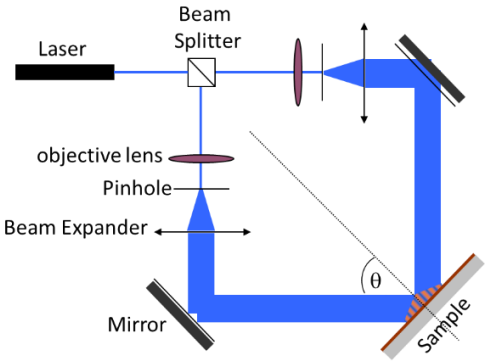

Figure 2.26: Interferential Lithography principle.

The bench at the H. Curien laboratory is slightly different and uses two point sources issued from optical fibers (polarization maintaining fibers) and the interferences are created by spherical waves **(Figure 2.27)**.

The set-up of the interferential lithography is considered simple but it is extra sensitive to vibrations that can alter the contrast of the pattern during the exposure. Therefore, the complete optical system is mounted on an air table and one of the fiber output is connected to piezoelectric motors in order to maintain the stability of the fringes. To avoid contamination by particles suspended in the air the holographic bench is protected by a glassy enclosure [79] or it is located in a clean room.

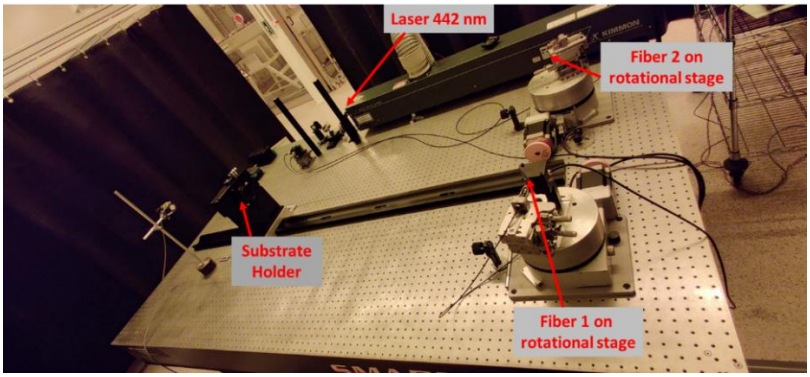

Figure 2.27: Lithographic optical bench in Laboratory Hubert Curien.

All the aforementioned risks are likely to occur when dealing with the technique of holography, fact that renders this method less reproducible. For this reason, gratings obtained by this mean are often used as master samples destined to be duplicated (for example by nano-imprint lithography). Nevertheless, this illumination method is advantageous since a one-step exposition can write a large number of lines in one shot and thus is cost effective. The ease of

implementation permits to write over large areas by widening the incident beams. Moreover, more than 1D patterns are accessible using successive exposures after substrate rotation or multi beam interferential exposition [80,81].

2.6.2 Mask lithography

The phase masks should not be confused with the commercial photomasks consisting of patterns of chromium since in that case no interference occurs. In this case, we are talking about amplitude masks that transfer their pattern directly on the sample surface. Most of the amplitude masks consist of a chromium window on the mask and the projected pattern through UV illumination is the same as that of the mask, due to the chromium absorption/reflection of UV light.

Contrary to amplitude mask lithography, phase mask lithography is part of interferential technique and creates an interferogram underneath the phase mask on the photoresist surface [82], due to interferences between transmitted orders during collimated UV light exposure. Instead of separating the beam by a beam splitter, we use a diffraction grating that separates the coherent beam into diffracted orders. This diffraction grating is called phase mask and is designed to split the beam into -1 and +1 orders or 0^{th} order producing periodic dark and bright zones on the sample. Similar to holography, the pattern will be revealed after development.

Unlike the interferential lithography, the period here cannot be easily modified because it is linked to the characteristics of the mask in use [83,84]. Solely the type of incidence can partially affect the period. Under normal incidence, the period is formed by the combination of ±1 transmitted orders that construct the fringes and fringe period is equal to the half of the mask period (Λ/2). In Littrow incidence where the -1^{st} transmitted order interfere with the 0^{th} transmitted order, the resulted period is exactly equal to the mask period (Λ) **(Figure 2.28)**.

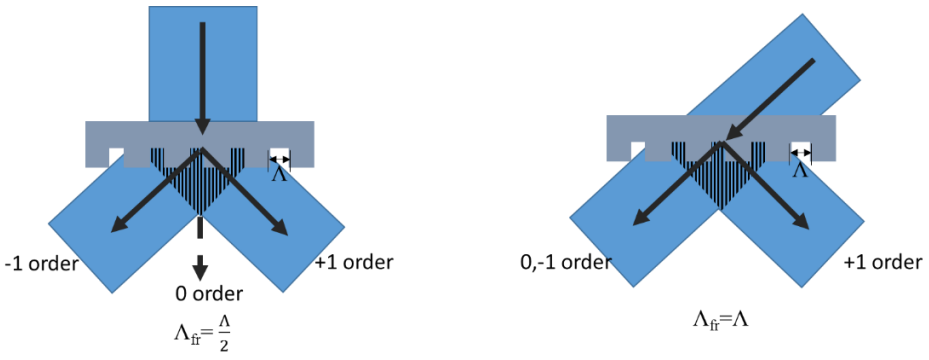

(a) **(b)**

Figure 2.28: Relation between fringes and phase mask period in (a) normal incidence and (b) Littrow incidence.

Another crucial factor for this technique is the distance between the sample and the phase mask. In phase masks, the optical power should be distributed equally to obtain a high intensity profile. Therefore, the quality of the phase mask grating must be optimal and the incident beam should be adapted and well aligned to the mask. In order to illuminate the whole surface, the intradistance between sample and mask must be controlled.

2.7 Development and post-treatment steps

2.7.1 Development

After the exposure of the photosensitive layer, a development step follows to dissolve the exposed parts of the positive photoresist or the unexposed of the negative photoresist layer. The corresponding developers adapted to the nature of resist can configure the contrast and the structural profile of the grating in combination to the specific exposure dose. Besides the optimization of these parameters, further control on the elaboration process is important. To achieve reproducible results the development temperature, the sol agitation, the room conditions (temperature and humidity) need to be set appropriately.

2.7.1.1 Selection Criteria for developer

Not every photoresist can be developed with every developer. For example, the concentration of the developer depends on the targeted application and determines if the developer will be metal ion containing or metal free. A metal ion containing developer is usually diluted with deionized water and is advisable for thick resist films (> 5 µm). The metal ion free developers however, are already diluted and ready for use. Moreover, negative and positive resists use different developers with distinct chemical substance.

Here and for structuration purposes, the positive S1805 resist is used. As discussed in the previous section, the positive resist forms an indene carboxylic acid during exposition that renders it hydrophilic in aqueous alkaline solution. The suitable developer to this photoresist is a basic solution, the TMAOH (trimethylamine N-oxide) which is metal free.

2.7.1.2 Temperature Dependency

Besides the suitable choice of the development associated with the photoresist, a temperature dependence of the processing is relevant too. The thermal activation energy has an impact on the development rate and involves chemical reactions such as dissolution, complex formation and material transport. The dependence follows an Arrhenius behavior **(Equation 2.**5**)**:

$$k = Ae^{-\frac{E_a}{RT}}$$ **Equation 2.5**

Where k denotes the kinetic constant of the reaction, A the pre-exponential factor implying the particles collisions in the reaction, E_a the activation energy, T the absolute temperature in Kelvin and R the ideal gas constant.

For a positive resist, low temperatures slow the kinetic constant, which is preferable in order to limit the dissolution reactions to the unexposed zones. To define though the exact relation between developer-temperature personal investigations are required.

In addition, the environmental conditions are also critical. For a good contrast on the grating, the humidity conditions in the room must be set around 50% and the temperature between 21°C and 23°C. Fluctuating room temperatures can cause evaporation or cooling and consequently over or under development of the exposed layer.

2.7.1.3 Exposure Dose and Development Rate

The equilibrium between the exposure dose and development rate is generally adjusted to the type of the resist, for the thickness of the layer but equally for the desired depth of the grating.

The effect of development has been already examined empirically for the positive photoresist S1805 **(Figure 2.10)** by the measurement of the sensitivity curve. Further experiments were realized for the configuration of the grating profile. What was deduced is that for small periods, it is preferred to use long exposure times and short time development rates. This is because over development time induces lateral erosions of the non-illuminated zones and thus destruction of the thin line structure. In contrast, larger periods are less sensitive to the time duration of the development. Based on this tolerance, we can even limit the exposure time that determines the contrast and increase development time to shape the grating profile.

2.7.1.4 Sol Agitation

In our experiments, the developer bath is placed on a Peltier module to regulate the temperature. A special rotating propeller blade immersed in the developer sol is used for a constant recirculation of the system. The proper agitation in the developer contributes to remove the residual products from the film while allowing fresh developer to diffuse to the grating. Poor agitation limits the development and results in non-uniform patterns. During the development process, the sample is covered in the solution to permit the recycling action of the developer to its whole surface. After the development, the sample is rinsed with water and dried with compressed air to reveal the pattern.

2.7.2 Oxygen Plasma

Finally, to adjust the geometry of the grating to the desired one, oxygen plasma can be used to modify the profile. Plasma treatment is a process of ablating near surfaces of materials without modifying the bulk properties. It is characterized by a high reproducibility better than this of mechanical or chemical process. Depending on the process gases, various plasmas can be employed to reduce the height of the grating [85], to modify the duty cycle [86] of a pattern but also to enhance the adhesion and the wetting of a polymer layer on the substrate [87].

The production method of plasma can be based on magnetic induction or electric field. In our study, we have used a plasma reactor equipped with a RF oscillating electric field source. In particular, the electric field is generated by the RF source and through the use of capacitive plates, the electrons penetrate in the gas region. The acceleration of electrons due to the electric field induces the collision of RF electrons with neutral atoms. After the brutal collisions, the neutral atoms strip out their electrons and lead to ionization with increased kinetic energy. The free electrons provoke further collisions originating progressively the plasma that consists of electrons, ions and neutral atoms emitting a characteristic glow. The surface etching arises mainly from ion bombardment.

As employed gas, we have used oxygen principally because of the sensitivity of photoresists to O_2 plasmas. After the structuration and development of a positive resist grating, O_2 ion bombardment interacts to reshape the profile. Slightly shorter exposure or development time can lead to the formation of a grating not directly open at the surface of the substrate. As seen extensively in the first chapter, the form and profile of the grating can influence the resonance response. A grating with resist residues after development can lower the resonance amplitude and damage the quality factor of the peak due to the optical losses based on the grating roughness. Therefore, the etching technique is used to adjust the grating profile.

Delicate operations are necessary to ensure an isotropic etching from the top to the bottom. To promote the isotropic action we apply a primary vacuum with high pressure in the reactor. In contrast, the working pressure of O_2 needs to be low to avoid the degradation of surface.

The **Figure 2.29** illustrates the image of 1D grating before and after the plasma treatment. The imposed parameters have transformed the height of the grating whilst keeping a sinusoidal profile. More etching time would have led to a deeper grating. However, an excess of time can sometimes modify the overall shape. For this reason, many tests should be made to determine the optimal parameters.

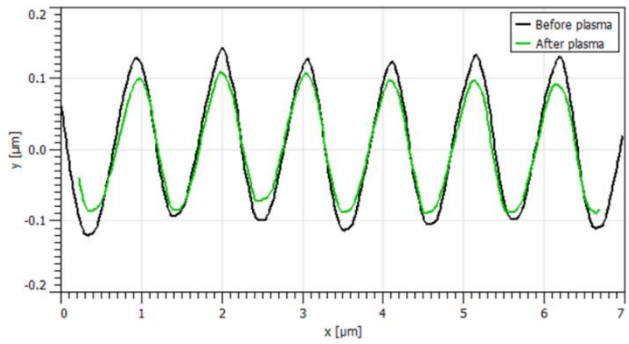

Figure 2.29: AFM image of 1D grating (a) before plasma and (b) after plasma treated for 3 min with 50W and 0.3 mbar of O_2 pressure.

2.8 Conclusion

This chapter encloses a description of photoresists adapted to our photolithographic techniques. Positive and negative photoresists are chemically analyzed and appeared soluble (positive) or insoluble (negative) upon light exposure. According to the type of resist, each has a sensitivity to concrete range of wavelengths and high or poor compatibility with different kind of substrates. Hence, the contrast and material stability distinguished the resists appropriate for targeted applications.

The achievement of high contrast is reflected to the pattern-based resist films. After exposition and development processes, the revealed pattern denotes the quality of processing. Certainly, the exposure dose and development rate are primordial steps, which are evaluated in detail.

For the needs of this PhD thesis, we have specifically focused on the photo activity of the S1805 positive resist for grating structuring and on the negative photoresist or sol-gel based layer for the wave-guide layer of the Waveguide Resonant Grating (WRG). The TiO_2/BzAc negative resist is elaborated via the sol gel method based on the protocol developed by the laboratory Hubert Curien and LMGP group. The inherent properties for each resist are displayed.

The film construction involves three main steps; film deposition, UV illumination and development. The deposition of the films is performed by two methods; spin coating or dip coating and the respective processes are studied. The exposure of the photosensitive layer is tested by either interferential or phase mask lithography. The mechanism for each lithography technique has exhibited the printing steps of a pattern. Finally, the development step has unfolded all the intermediate parameters that affect strongly the final result. The last optional step is to adjust the profile pattern with the oxygen plasma in case of inadequate height or duty cycle of the grating.

Bibliography

[1] M. Yang, Z. Huang, H. You, "A plug-in electrophoresis microchip with PCB electrodes for contactless conductivity detection", *R. Soc. Open Sci.* 5 (n.d.) 171687.

[2] H. Cong, X. Xu, B. Yu, H. Liu, H. Yuan, "Fabrication of anti-protein-fouling poly(ethylene glycol) microfluidic chip electrophoresis by sandwich photolithography", *Biomicrofluidics.* 10 (2016) 044106. "

[3] K.D. Gillis, X.A. Liu, A. Marcantoni, V. Carabelli, "Electrochemical measurement of quantal exocytosis using microchips", *Pflüg. Arch. - Eur. J. Physiol.* 470 (2018) 97–112.

[4] J.W. Lathrop, "The Diamond Ordnance Fuze Laboratory's Photolithographic Approach to Microcircuits", *IEEE Ann. Hist. Comput.* 35 (2013) 48–55.

[5] S. Martínez-Crespiera, E. Ionescu, M. Schlosser, K. Flittner, G. Mistura, R. Riedel, H.F. Schlaak, "Fabrication of silicon oxycarbide-based microcomponents via photolithographic and soft lithography approaches", *Sens. Actuators Phys.* 169 (2011)

[6] H.-P. Phan, T.-K. Nguyen, T. Dinh, A. Iacopi, L. Hold, M.J.A. Shiddiky, D.V. Dao, N.-T. Nguyen, "Robust Free-Standing Nano-Thin SiC Membranes Enable Direct Photolithography for MEMS Sensing Applications", *Adv. Eng. Mater.* 20 (2018)

[7] A. Sherehiy, J.M. Rathfon, H. Abe, S.S. Chowdhury, R.W. Cohn, "Shape Transformation Photolithography: Self-Assembled Arrays of Suspended MEMS Structures from Patterned Polymer Membranes", *ACS Omega. 3* (2018) 18489–18498.

[8] T. Tamura, T. Suzuki, "Seamless fabrication technique for micro to millimeter structures by combining 3D printing and photolithography", *Jpn. J. Appl. Phys.* 58 (2019) SDDL10.

[9] D. Dezest, T. Leïchlé, P. Teerapanich, F. Mathieu, B.T.S. Bui, K. Haupt, L. Nicu, "Multiplexed functionalization of nanoelectromechanical systems with photopatterned molecularly imprinted polymers", *J. Micromechanics Microengineering.* 29 (2019) 025013.

[10] C. Wang, M. Madou, "From MEMS to NEMS with carbon," *Biosens. Bioelectron.* 20 (2005) 2181–2187.

[11] C.-W. Hsu, F.-C. Su, P.-Y. Peng, H.-T. Young, S. Liao, G.-J. Wang, "Highly sensitive non-enzymatic electrochemical glucose biosensor using a photolithography fabricated micro/nano hybrid structured electrode", *Sens. Actuators B Chem.* 230 (2016) 559–565.

[12] M.-J. Yin, Q. Zhao, J. Wu, K. Seefeldt, J. Yuan, "Precise Micropatterning of a Porous Poly(ionic liquid) via Maskless Photolithography for High-Performance Nonenzymatic H_2O_2 Sensing", *ACS Nano.* 12 (2018) 12551–12557.

[13] Y. Pan, C. Miller, K. Trepka, Y. Tao, "Wafer-scale photolithography of ultra-sensitive nanocantilever force sensors", *Appl. Phys. Lett.* 113 (2018) 083103.

[14] I. Jasim, J. Liu, Y. Yang, C. Qu, C. Zhu, M. Roman, J. Huang, E. Kinzel, M. Almasri, "Low-cost fabrication of functional plasmonic fiber-optic-based sensors using microsphere photolithography", *in: Fiber Opt. Sens. Appl. XVI, International Society for Optics and Photonics*, 2019: p. 110000D.

[15] Y. Wang, H. Hu, J. Shao, Y. Ding, "Fabrication of Well-Defined Mushroom-Shaped Structures for Biomimetic Dry Adhesive by Conventional Photolithography and Molding", *ACS Appl. Mater. Interfaces.* 6 (2014) 2213–2218.

[16] S.H. Lee, J.H. Lee, C.W. Park, C.Y. Lee, K. Kim, D. Tahk, M.K. Kwak, "Continuous fabrication of bio-inspired water collecting surface via roll-type photolithography", *Int. J. Precis. Eng. Manuf.-Green Technol.* 1 (2014) 119–124.

[17] E. Davis, Y. Liu, L. Jiang, Y. Lu, S. Ndao, "Wetting characteristics of 3-dimensional nanostructured fractal surfaces", *Appl. Surf. Sci.* 392 (2017) 929–935.

[18] Integrated Circuit Design and the Photolithography Process, COMSOL Multiphysics. https://www.comsol.com/blogs/integrated-circuit-design-photolithography-process/ (Oct.2020).
[19] A. Singh, K.-Y. Suh, "Biomimetic patterned surfaces for controllable friction in micro- and nanoscale devices", *Micro Nano Syst. Lett.* 1 (2013) 6.
[20] S. Lab, "Big Size Textile Pressure Sensor Developed by Chinese Academy of Sciences (Light Weight…", Medium. (2018).
[21] G.E. Moore, "Cramming more components onto integrated circuits, Reprinted from Electronics, volume 38, number 8, April 19, 1965, pp.114 ff.", *IEEE Solid-State Circuits Soc. Newsl.* 11 (2006) 33–35.
[22] H.M. Ali, M.M. Abou-Mesalam, M.M. El-Shorbagy, "Structure and optical properties of chemically synthesized titanium oxide deposited by evaporation technique", *J. Phys. Chem. Solids.* 71 (2010) 51–55.
[23] J.-H. Huang, M.-S. Wong, "Structures and properties of titania thin films annealed under different atmosphere", *Thin Solid Films.* 520 (2011) 1379–1384.
[24] Y. Hirai, K. Sugano, T. Tsuchiya, O. Tabata, "A three-dimensional microstructuring technique exploiting the positive photoresist property", *J. Micromechanics Microengineering.* 20 (2010) 065005.
[25] Z. Zhu, Z.-F. Zhou, Q.-A. Huang, W.-H. Li, "Modeling, simulation and experimental verification of inclined UV lithography for SU-8 negative thick photoresists", *J. Micromechanics Microengineering.* 18 (2008) 125017.
[26] B. Mortini, "Photosensitive resists for optical lithography", *Comptes Rendus Phys.* 7 (2006) 924–930.
[27] PhotoresistPos.pdf, https://labs.ece.uw.edu/cam/tutorials/PhotoresistPos.pdf
[28] "Chapter 5 Lithography Introduction and application", https://slideplayer.com/slide/4502986/ (Oct.2020).
[29] S. Briche, Z. Tebby, D. Riassetto, M. Messaoud, E. Gamet, E. Pernot, H. Roussel, O. Dellea, Y. Jourlin, M. Langlet, "New insights in photo-patterned sol–gel-derived TiO_2 films", *J. Mater. Sci.* 46 (2011) 1474–1486.
[30] V. Gâté, "Ecriture de motifs périodiques submicrométriques sur films TiO_2 sol-gel par lithographie interférométrique dynamique sur de grandes surfaces", (2013).
[31] C.-Q. Ye, "Sol-Gel Processes of Functional Powders and Films", *Chem. React. Inorg. Chem.* (2017).
[32] J. Livage, M. Henry, C. Sanchez, "Sol-gel chemistry of transition metal oxides", *Prog. Solid State Chem.* 18 (1988) 259–341.
[33] O. Shavdina, L. Berthod, T. Kämpfe, S. Reynaud, C. Veillas, I. Verrier, M. Langlet, F. Vocanson, P. Fugier, Y. Jourlin, O. Dellea, "Large Area Fabrication of Periodic TiO_2 Nanopillars Using Microsphere Photolithography on a Photopatternable Sol–Gel Film", *Langmuir.* 31 (2015) 7877–7884.
[34] V. Gâté, Y. Jourlin, F. Vocanson, O. Dellea, G. Vercasson, S. Reynaud, D. Riassetto, M. Langlet, "Sub-micrometric patterns written using a DIL method coupled to a TiO_2 photo-resist", *Opt. Mater.* 35 (2013) 1706–1713.
[35] J. Wang, J. Ge, H. Hou, M. Wang, G. Liu, G. Qiao, Y. Wang, "Design and sol–gel preparation of SiO_2/TiO_2 and $SiO_2/SnO_2/SiO_2–SnO_2$ multilayer antireflective coatings", *Appl. Surf. Sci.* 422 (2017) 970–974.
[36] M.I. Khan, K.A. Bhatti, R. Qindeel, H.S. Althobaiti, N. Alonizan, "Structural, electrical and optical properties of multilayer TiO_2 thin films deposited by sol–gel spin coating", *Results Phys.* 7 (2017) 1437–1439.
[37] C. Sanchez, L. Rozes, F. Ribot, C. Laberty-Robert, D. Grosso, C. Sassoye, C. Boissiere, L. Nicole, "“Chimie douce”: A land of opportunities for the designed construction of

functional inorganic and hybrid organic-inorganic nanomaterials", *Comptes Rendus Chim.* 13 (2010) 3–39.
[38] "Chimie du procédé sol-gel", Tech. Ing. https://www.techniques-ingenieur.fr/base-documentaire/materiaux-th11/traitements-de-surface-des-metaux-en-milieu-aqueux-42359210/films-inorganiques-et-hybrides-protecteurs-obtenus-par-voie-sol-gel-m1722/chimie-du-procede-sol-gel-m1722niv10001.html (Oct.2020)
[39] L. Berthod, "La photolithographie cylindrique sur revêtement sol-gel photogravable", *thesis*, Lyon, 2017.
[40] "Rutile anatase TiO_2 uses titanium dioxide properties", http://www.fangyuan-tio2.com/rutile-anatase-tio2-uses-titanium-dioxide-properties.html (Oct.2020)
[41] F. Dachille, P.Y. Simons, R. Roy, "Pressure-temperature studies of anatase, brookite, rutile and TiO_2-II", *Am. Mineral.* 53 (1968) 1929–1939.
[42] A. Di Paola, M. Bellardita, L. Palmisano, "Brookite, the Least Known TiO_2 Photocatalyst", *Catalysts.* 3 (2013) 36–73.
[43] D.A.H. Hanaor, C.C. Sorrell, "Review of the anatase to rutile phase transformation", *J. Mater. Sci.* 46 (2011) 855–874.
[44] M. Hl, Y. Jy, D. Y, Z. Yb, L. B, M. Gh, "Raman study of phase transformation of TiO_2 rutile single crystal irradiated by infrared feratosecond laser," *Appl. Surf. Sci.* 253 (2007) 7497–7500.
[45] R. Nazempour, Q. Zhang, R. Fu, X. Sheng, "Biocompatible and Implantable Optical Fibers and Waveguides for Biomedicine", *Materials.* 11 (2018) 1283.
[46] L. Berthod, O. Shavdina, F. Vocanson, M. Langlet, O. Dellea, C. Veillas, S. Reynaud, I. Verrier, Y. Jourlin, "Cylinder microstructure on non-planar and functional surface based on photo-patternable TiO_2 sol-gel and colloidal photolithography", in: 2016. https://hal.archives-ouvertes.fr/hal-01381756 (Oct.2020)
[47] S.J. Weinstein, K.J. Ruschak, "Dip coating on a planar non-vertical substrate in the limit of negligible surface tension", *Chem. Eng. Sci.* 56 (2001) 4957–4969.
[48] J. Yang, C. Blawert, S.V. Lamaka, D. Snihirova, X. Lu, S. Di, M.L. Zheludkevich, "Corrosion protection properties of inhibitor containing hybrid PEO-epoxy coating on magnesium", *Corros. Sci.* 140 (2018) 99–110.
[49] N. Felde, L. Coriand, A. Duparré, A. Tünnermann, "Wear-Resistant Nanostructured Sol-Gel Coatings for Functional Applications", *J. Coat. Sci. Technol.* 3 (2016) 100-108–108.
[50] I. Santana, A. Pepe, W. Schreiner, S. Pellice, S. Ceré, "Hybrid sol-gel coatings containing clay nanoparticles for corrosion protection of mild steel", *Electrochimica Acta.* 203 (2016) 396–403.
[51] Y. Wei, S. Chen, Y. Lin, X. Yuan, L. Liu, "Silver nanowires coated on cotton for flexible pressure sensors", *J. Mater. Chem. C.* 4 (2016) 935–943.
[52] C. Ge, C. Xie, S. Cai, "Preparation and gas-sensing properties of Ce-doped ZnO thin-film sensors by dip-coating", Mater. *Sci. Eng. B.* 137 (2007) 53–58.
[53] B. Wang, J. Ding, T. Zhu, W. Huang, Z. Cui, J. Chen, L. Huang, L. Chi, "Fast patterning of oriented organic microstripes for field-effect ammonia gas sensors", *Nanoscale.* 8 (2016) 3954–3961.
[54] New Technology Information of moisture-proof coating | TOA OPTICAL TECHNOLOGIES,LTD.,https://www.toa-rika.co.jp/en/news/news130712.html (Oct.2020)
[55] L.M. Nikolić, L. Radonjić, V.V. Srdić, "Effect of substrate type on nanostructured titania sol–gel coatings for sensors applications", *Ceram. Int.* 31 (2005) 261–266.

[56] W.J. Smit, C. Kusina, J.-F. Joanny, A. Colin, "Stress Field inside the Bath Determines Dip Coating with Yield-Stress Fluids in Cylindrical Geometry", *Phys. Rev. Lett.* 123 (2019) 148002.
[57] Dip Coating Theory | Dip Coating Thin Films, Complete Guide, Ossila. https://www.ossila.com/pages/dip-coating-theory-film-thickness (Oct.2020)
[58] F. Zhang, C. Di, N. Berdunov, Y. Hu, Y. Hu, X. Gao, Q. Meng, H. Sirringhaus, D. Zhu, "Ultrathin Film Organic Transistors: Precise Control of Semiconductor Thickness via Spin-Coating", *Adv. Mater.* 25 (2013) 1401–1407.
[59] D.B. Mitzi, L.L. Kosbar, C.E. Murray, M. Copel, A. Afzali, "High-mobility ultrathin semiconducting films prepared by spin coating", *Nature.* 428 (2004) 299–303.
[60] J.J. van Franeker, D. Westhoff, M. Turbiez, M.M. Wienk, V. Schmidt, R.A.J. Janssen, "Controlling the Dominant Length Scale of Liquid–Liquid Phase Separation in Spin-coated Organic Semiconductor Films", *Adv. Funct. Mater.* 25 (2015) 855–863.
[61] E. Kymakis, E. Stratakis, M.M. Stylianakis, E. Koudoumas, C. Fotakis, "Spin coated graphene films as the transparent electrode in organic photovoltaic devices", *Thin Solid Films.* 520 (2011) 1238–1241.
[62] E. Kymakis, M.M. Stylianakis, G.D. Spyropoulos, E. Stratakis, E. Koudoumas, C. Fotakis, "Spin coated carbon nanotubes as the hole transport layer in organic photovoltaics", *Sol. Energy Mater. Sol. Cells.* 96 (2012) 298–301.
[63] M. Abdelsamie, K. Zhao, M.R. Niazi, K.W. Chou, A. Amassian, "In situ UV-visible absorption during spin-coating of organic semiconductors: a new probe for organic electronics and photovoltaics", *J. Mater. Chem. C.* 2 (2014) 3373–3381.
[64] L.A. DeSilva, R. Gadipalli, A. Donato, T.M.W.J. Bandara, "Reflectivity of 88% for four-period hybrid Bragg mirror from spin coating process", *Optik.* 157 (2018) 360–364.
[65] T. Komikado, A. Inoue, K. Masuda, T. Ando, S. Umegaki, "Multi-layered mirrors fabricated by spin-coating organic polymers", *Thin Solid Films.* 515 (2007) 3887–3892.
[66] D. Meyerhofer, "Characteristics of resist films produced by spinning", *J. Appl. Phys.* 49 (1978) 3993–3997.
[67] L.C. Klein, "Sol-Gel Optical Materials", *Annu. Rev. Mater. Sci.* 23 (1993) 437–452.
[68] C. Park, J. Yoon, E.L. Thomas, "Enabling nanotechnology with self assembled block copolymer patterns", *Polymer.* 44 (2003) 6725–6760.
[69] A.D. Dinsmore, A.G. Yodh, D.J. Pine, "Phase diagrams of nearly-hard-sphere binary colloids", *Phys. Rev. E.* 52 (1995) 4045–4057.
[70] Y. Xia, B. Gates, Y. Yin, Y. Lu, "Monodispersed Colloidal Spheres: Old Materials with New Applications", *Adv. Mater.* 12 (2000) 693–713.
[71] H.-B. Sun, T. Tanaka, K. Takada, S. Kawata, "Two-photon photopolymerization and diagnosis of three-dimensional microstructures containing fluorescent dyes", *Appl. Phys. Lett.* 79 (2001) 1411–1413.
[72] G.M. Gratson, M. Xu, J.A. Lewis, "Direct writing of three-dimensional webs", *Nature.* 428 (2004) 386–386.
[73] S. Kuiper, H. van Wolferen, C. van Rijn, W. Nijdam, G. Krijnen, M. Elwenspoek, "Fabrication of microsieves with sub-micron pore size by laser interference lithography", *J. Micromechanics Microengineering.* 11 (2000) 33–37.
[74] C. Lu, X.K. Hu, S.S. Dimov, R.H. Lipson, "Controlling large-scale film morphology by phase manipulation in interference lithography", *Appl. Opt.* 46 (2007) 7202–7206.
[75] H.H. Solak, C. David, J. Gobrecht, L. Wang, F. Cerrina, "Multiple-beam interference lithography with electron beam written gratings", *J. Vac. Sci. Technol. B Microelectron. Nanometer Struct. Process. Meas. Phenom.* 20 (2002) 2844–2848.
[76] M. Born, E. Wolf, "Principles of Optics: Electromagnetic Theory of Propagation, Interference and Diffraction of Light", *Elsevier*, 2013.

[77] S.H. Zaidi, S.R.J. Brueck, "Multiple-exposure interferometric lithography", *J. Vac. Sci. Technol. B Microelectron. Nanometer Struct. Process. Meas. Phenom.* 11 (1993) 658–666.
[78] C.J.M. van Rijn, "Laser interference as a lithographic nanopatterning tool", *J. MicroNanolithography MEMS MOEMS.* 5 (2006) 011012.
[79] M. Bichotte, A. Cazier, F. Celle, C. Veillas, T. Kämpfe, Y. Jourlin, "Very short period grating printing combining UV interferential exposure and mechanical strain", *Microelectron. Eng.* 177 (2017) 66–69.
[80] X. Chen, Y. Shimizu, C. Chen, Y.-L. Chen, W. Gao, "Generalized method for probing ideal initial polarization states in multibeam Lloyd's mirror interference lithography of 2D scale gratings", J. *Vac. Sci. Technol. B Nanotechnol. Microelectron. Mater. Process. Meas. Phenom.* 36 (2018) 021601.
[81] J. de Boor, N. Geyer, U. Gösele, V. Schmidt, "Three-beam interference lithography: upgrading a Lloyd's interferometer for single-exposure hexagonal patterning", *Opt. Lett.* 34 (2009) 1783–1785.
[82] C. Lu, X.K. Hu, I.V. Mitchell, R.H. Lipson, "Diffraction element assisted lithography: Pattern control for photonic crystal fabrication", *Appl. Phys. Lett.* 86 (2005) 193110.
[83] Y. Bourgin, "Fabrication par masque de phase de réseaux de diffraction d'aire et de période ultimes", (2010).
[84] Y. Bourgin, Y. Jourlin, O. Parriaux, A. Talneau, S. Tonchev, C. Veillas, P. Karvinen, N. Passilly, A.R.M. Zain, R.M.D.L. Rue, J.V. Erps, D. Troadec, "100 nm period grating by high-index phase-mask immersion lithography", *Opt. Express.* 18 (2010) 10557–10566.
[85] K.O. Abrokwah, P.R. Chidambaram, D.S. Boning, "Pattern Based Prediction for Plasma Etch", *IEEE Trans. Semicond. Manuf.* 20 (2007) 77–86.
[86] D.L. Voronov, S. Diez, P. Lum, S.A. Hidalgo, T. Warwick, N. Artemiev, H.A. Padmore, "Fabrication of x-ray gratings by direct write maskless lithography", *in: Adv. X-RayEUV Opt. Compon. VIII, International Society for Optics and Photonics*, 2013: p. 88480Q.
[87] E.M. Liston, L. Martinu, M.R. Wertheimer, "Plasma surface modification of polymers for improved adhesion: a critical review", *J. Adhes. Sci. Technol.* 7 (1993) 1091–1127.

CHAPTER 3

Waveguide Resonant Gratings (WRG) at the inner wall of a tube

3.1 Introduction

Based on the described principles of a WRG and on the techno-optical expertise, this chapter introduces the micro patterning of complex curved geometries. Miniaturized cylindrical supports (such as tubes) are used to model and demonstrate similar resonance phenomena as in planar WRG configurations. The studied structure reproduces the design of a WRG by using the inner cavity of an 8 mm diameter cylinder of fused silica as substrate, a compact TiO_2 layer as waveguide and a photosensitive layer as grating after being patterned by a specially designed radial phase mask. This configuration has been designed to project exclusively the diffractive orders ±1 transversally to the central tube axis, the radial phase mask transfers its 2D planar radial interferogram into parallel fringes to print a stitchingless cylindrical grating. To verify mode coupling and resonance excitation, a 90° apex conical mirror is conceived to transpose plane to cylindrical waves. The mirror is inserted into the cylindrical cavity to reflect the incident light and to take advantage of the holistic illumination in order to obtain both resonances in TE and TM polarizations in the near infrared range measured by optical spectroscopic means.

In this study, the fabrication process of the structure will be extensively analyzed from modelling and design to fabrication and characterization. The operational principle for both, the radial phase mask and the conical mirror, which are technological breakthroughs and the two basic tools for micro patterning and characterization process, will be detailed. This chapter also includes a broad study and evaluation of polarization that plays a critical role in the characterization process. Finally, the experimental results will be presented and discussed.

3.2 A review on cylindrical gratings

Ongoing miniaturization has enabled multi-functional ultra-thin optical devices that manipulate the polarization, direction and frequency of light. According to this tendency, micro optics integrated new modular machines and micro shaping technologies [1] to pattern submicron diffraction gratings in ever shrinking optical components. Until recently, the overwhelming majority of applications was covered by planar Diffractive Optical Elements (DOEs) with one- or two-dimensional waveguide structures.

Diffractive devices with circular symmetry launch a new challenge due to the additional applications that take advantage of radial and azimuthal polarization [2]. However, conventional etching techniques such as optical or mechanical ruling are by far inappropriate for their construction.

Components such as radial phase masks may enable the circular patterning as they were conceived to optically transform a 2D planar radial interferogram of ± 1 orders into periodic parallel fringes by means of projection [3].

Tonchev *et al.* has already used the phase mask technology, with a He-Cd Laser emitting at a wavelength of 442 nm to fabricate a cylindrical grating but without a resonance excitation [4,5]. The holistic planar to cylindrical printing has resulted in an interferogram in the cavity of the tube by a single step exposure whereas a strictly N integer number of corrugations is preserved without any stitching errors. It was then proposed to design a high-resolution rotation sensor. The design encompassed two cylindrical gratings, one transmissive of angular period Λ_φ, and one reflective with an outer grating of period $\Lambda_\varphi/2$. The power of the returned interfered beams would have been modulated at the rate of the rotation of one of the gratings relative to the other [6].

Hirshy *et al.* has also printed a cylindrical grating with the help of the radial phase mask and attempted to create a metal replica of the grating by galvanic growth at the inner wall of the separated nickel shim [7].

Micro scale cavities with similar designs were also stated by Riu et *al.* who placed a Silicon based circular grating resonator in vicinity to an access waveguide capable to detect different OAM (Orbital Angular Momentum) states [8]. The device offered an additional mode of operation with a dual port at the input and output of a waveguide respectively for multiplexing applications. Moreover, the group recommended as alternative modelling to place on the

circular cavity a metal oxide GeSe amorphous grating with GeSe crystal grooves. The proper adjustment of the duty cycle could then induce modifications to the effective mode index of the crystal GeSe tuning quasi linearly the resonant wavelength for arbitrary OAM states.

Cai *et al.* has equally demonstrated a silicon optical vortex emitter consisting of a flat waveguide attached to a ring grating that scatters Whispering Gallery Modes (WGM) in free space with variable OAM states [9].

However, for these grating structures an external waveguide is necessary to couple in and out the resonances, complicating likewise the manufacturing and rendering the on-chip integration difficult.

In contrast to previous articles, the current study presents the construction of a single optical component that encloses a cylindrical WRG structure in its inner cavity exhibiting resonant responses.

Ohtera *et al*. analyzed theoretically comparable resonance characteristics of a cylindrical waveguide grating excited by a cylindrical wave under a very small curvature radius by expressing the field in terms of Bessel functions; the issues of design and fabricability were not addressed [10].

Our reported resonant demonstration concerns millimetric cavities and is proposed for gas or liquid sensing applications. The cavity is appropriate for gas and liquid confinement with continuous measurements. The original resonant event is a technological achievement and will possibly pave the way for cylindrical resonators of a micro gear type [11] if the shrinking of the component size can be achieved.

3.3 Cylindrical grating patterning with the phase mask technology

As shown in the second chapter (**Section 2.5.2**), the phase mask is a diffractive element intended to diffract a coherent beam of light in specific orders in order to print a pattern on a photosensitive layer. Nevertheless, a huge number of phase masks is more adapted to planar and not to cylindrical geometries. To fabricate a pattern inside or outside miniaturized cylindrical substrates, a phase mask compatible to them is required.

3.3.1 Description of the phase mask

A radial phase mask is capable of converting the planar pattern into a set of N straight lines in a 3D cylindrical coordinate system when illuminated by an axial beam under normal incidence.

Thus, the N grating lines generated by the radial phase mask in the cavity of the tube (or a cylinder) of radius R lead correspondingly to an angular period of $\Lambda_{\varphi} = 2\pi/N$ or to a period expressed in length units of $\Lambda = 2\pi R/N$.

The Hubert Curien Laboratory modeled such a radial phase mask by using MC Grating programming [12] and the "University of Eastern Finland" (Joensuu University) [13] fabricated it by electron beam lithography and reactive ion etching on a SiO_2 substrate.

The radial phase mask was designed to have a ring-like radial grating that converges at a central point with a radius equal to r, going from R_i (interior) to R_e (exterior): ($R_i < r < R_e$). The radius R_i is 1 mm and the radius R_e is 1.5 mm. The phase mask then has an angular period $\Lambda_{\varphi\text{-pm}}$ expressed in radians and a length period $\Lambda_{r\text{-pm}}$ in length units, equal to $\Lambda_{r\text{-pm}} = \Lambda_{\varphi\text{-pm}}\, r$ that depends on the position r between R_i and R_e (**Figure 3.1**).

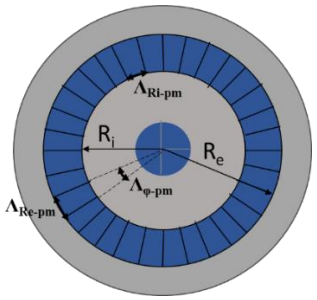

Figure 3.1: Scheme of the phase mask.

Either in the case of cylinder or tube, the resulting patterned interferogram must provide high contrast after the contribution of the diffracted orders.

To fulfill this condition, a thorough modelling guaranteed the elimination of all high orders and the exclusive retention of ±1 diffracted orders with equal maximum power (ideally 50% in each one). However, as the 0 order is difficult to extinguish, it is intentionally modelled not to contribute to the pattern by passing through the central axis of the hollow cavity without any interaction nor overlap with the ±1 orders that interfere with each other to print the interferogram on the wall [5]. The detailed analysis of the proceeding is enclosed in [3].

Following the above considerations, the final simulation required 80% of transmitted power for both orders issued by the optimal modelled structural features: rectangular SiO_2 grating depth of 400 nm, line-space ratio of 35%-65% and angular period $\Lambda_{\varphi\text{-pm}} = 480$ µrad. As expected, when the length period $\Lambda_{r\text{-pm}}$ of the radial phase mask increases as a function of r, the SiO_2 width of the cell increases equally along the radius to keep the line-space ratio constant.

A schematic of the mask with detailed dimensional characteristics is illustrated in (**Figure 3.2**). The radial grating is included in the annular area of the R_i and R_e radii. The outer ring-shaped area and the central cross are used for alignment purpose.

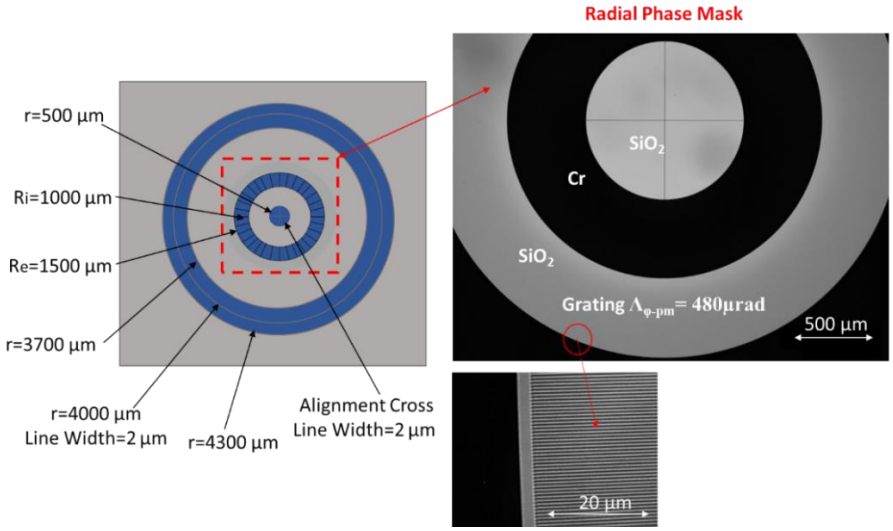

Figure 3.2: Total schematic of the radial phase mask (left) and zoom of the individual element by optical microscopy (top right) at the external border (bottom right.) The grey color denotes the Cr deposited layer while the blue the SiO_2 etched substrate [14].

The phase mask was modeled and fabricated to function with both geometries, cylinders and tubes only by reversing the incident illumination front of the mask.

For the purpose of this thesis, the phase mask is set to operate exclusively for tube supports, where the mask relief is exposed to air, directed to the hollow cavity of the tube, while the incident beam enters by the substrate side.

3.3.2 Principle of the tube exposure with the phase mask

When collimated coherent incident light passes through the phase mask grating, only the ±1 orders are diffracted and interfere with each other to print the interferogram pattern on the walls of a tube.

The grating lines in the tube are formed by the continuous contribution of two complementary points issued from the phase mask grating. The design is such, that the orders from R_e propagate further into the tube in contrast to those from R_i. However, even if they derive from different scales of increasing arcs with R_i or R_e, the interfering orders form the same angle α having travelled a shorter or greater distance respectively to lead to parallel lines throughout the inner wall of the tube (**Figure 3.3**).

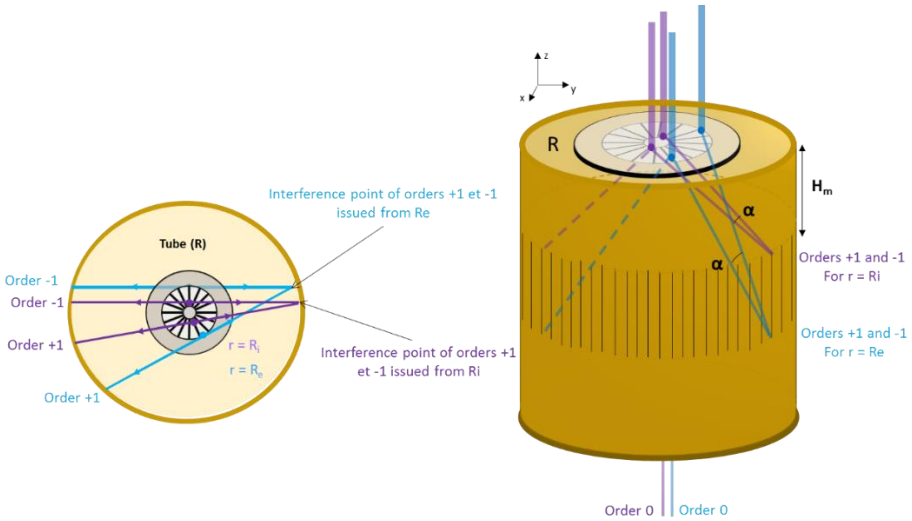

Figure 3.3: Top (left) and side (right) view of the phase mask centered on the tube and illustration of the propagated diffracted orders [14].

The resulting interferogram consists then of a set of lines parallel to each other and to the axis of the tube that must be perfectly aligned with the normal axis that passes through the center of the phase mask.

As in the mask lithography for planar geometries where the period of fringes is half the period of the mask (**Section 2.5.2 and Figure 2.28 a**), the angular period Λ_{φ} of the printed pattern in the tube is half of the angular period $\Lambda_{\varphi\text{-pm}}$ of the phase mask.

$$\Lambda_{\varphi} = \Lambda_{\varphi\text{-pm}}/2 \qquad \textbf{Equation 3.1}$$

The **Equation 3.1** results in Λ_{φ} = 240 µrad.

The corresponding spatial period Λ written in the tube is then

$$\Lambda = (\Lambda_{\varphi\text{-pm}} * R)/2 \qquad \textbf{Equation 3.2}$$

where R is the radius of the tube. Therefore, for a tube of R = 4 mm the period of the fringes in the tube is Λ = 960 nm. Since the terms of the above relation are constants without any dependence on r (radius of the phase mask), it follows that the number N of the patterned lines in the wall of a 4 mm tube is exactly twice the integer number of lines of the radial grating phase-mask.

$$N = 2N_{\text{phase-mask}} \qquad \textbf{Equation 3.3}$$

Therefore, if the phase mask contains 13.090 lines, the overall patterned lines of the tube are equal to 26.180.

3.4 Study of the cylindrical WRG

3.4.1 Design principle of the cylindrical WRG

The problem of a cylindrical WRG can be considerably simplified if it is approached as a planar structure of an infinite corrugated slab waveguide. The Guided Mode Resonance effects can be then transposed to a 3D space cylindrical geometry if it is illuminated with a cylindrical incident wave (Holistic Illumination) **(Figure 3.4)**.

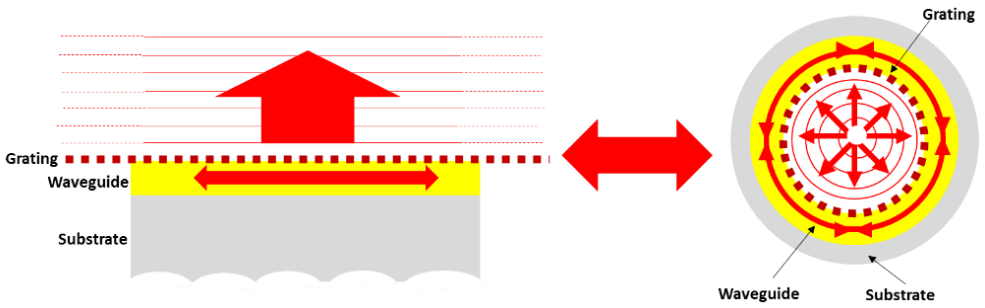

Figure 3.4: Transposition from planar integrated to cylindrical resonant diffractive optics.

Ohtera *et al*. has confirmed the above hypothesis by a theoretical study on the dependence of the resonance quality and the curvature radius. He concluded that for curvature radius larger than 8 grating periods the resonance amplitude and bandwidth reaches the quality factor of planar gratings [15]. Below this limit, the resonance peak degrades due to the added bending losses. This condition is largely satisfied in our cylindrical structure whose radius (R = 4 mm) is 4000 larger than the grating period (Λ = 960 nm). Therefore, the resonance reflection excited by a cylindrical wave is equivalent to the planar WRG excited by a planar wave.

In a cylindrical geometry, the waveguide mode coupling and the expected resonant reflection occur identically over 2π if the waveguide layer and resist thickness are azimuthally uniform. As the incidence is locally normal, the mode coupling condition is $n_{eff}(\lambda)k_0 = K_g$. $k_0=2\pi/\lambda$ is the wave vector modulus in vacuum, n_{eff} (λ) the effective index of the coupled mode of the layer/photoresist assembly at wavelength λ, and $K_g = 2\pi/\Lambda$ is the grating constant with Λ the grating period.

Assuming the coupling condition to be satisfied, the phase ΔΦ of the coupled mode accumulated over a round-trip $L = 2\pi R = N\Lambda$ is $\Delta\Phi = n_{eff}(\lambda)k_0L = K_gL = 2\pi N$ with N being an integer number.

Then the grating-coupled wall-waveguide can be seen as a multi turn ring resonator if a specific spatial coherence quantification condition is satisfied: the number of the coupling grating lines must be an integer number N. Furthermore the scattering and absorption losses of the coupled mode should be small enough and the propagation length L_p of the coupled mode, given as the inverse of the radiation coefficient of the grating waveguide [16] should be larger or much larger than L.

3.4.2 Modelling of the cylindrical WRG

The determination of the grating waveguide opto-geometrical parameters was first performed in a planar geometry. As explained before this is reasonable since the ratio between the tube inner radius R (R ≅ 4 mm) and the wavelength λ (λ in the 1300-1600 nm range) is of the order of 10^3.

The coupled waveguide structure is here composed of a non-corrugated uniform TiO_2 Sol-Gel layer of thickness w and refractive index n_{wg} = 1.7, and a binary photoresist corrugation of 0.5 duty cycle, depth d and refractive index n_g = 1.67. There is air in the fused silica tube of refractive index n_s = 1.45.

To prevent diffraction orders in the silica tube and spurious resonant reflections in the considered wavelength range, the grating-waveguide equivalent thickness w_{eq} will be set between the cutoff thickness w_{c0} of the fundamental TE_0 and TM_0 mode at the long wavelength λ_L = 1600 nm of the wavelength range, and the cutoff thickness w_{c1} of the first higher order TE_1, TM_1 mode at the small wavelength λ_S = 1300 nm of the said range. The equivalent grating-waveguide thickness w_{eq} is defined as the thickness of a gratingless uniform equivalent waveguide having the permittivity n_{wg}^2 of the actual waveguide. Based on effective medium theory we determine for TE polarization:

$$w_{eq} = w + d\sqrt{\frac{1+n_g^2}{2n_{wg}^2}} \qquad \textbf{Equation 3.4}$$

and for TM polarization:

$$w_{eq} = w + \frac{d\times n_g}{n_{wg}}\sqrt{\frac{2}{1+n_g^2}} \qquad \textbf{Equation 3.5}$$

Setting the effective index n_{eff} of the TE_0, TM_0 and TE_1, TM_1 modes to n_s in the TE-TM dispersion equations respectively (**Equation 1.5**) defines the TE_0-TM_0 and TE_1-TM_1 mode cutoff thicknesses w_{c0} and w_{c1} **(Equation 1.6 and Equation 1.7)**, and gives the range of w_{eq} for single mode operation:

$$\frac{\lambda_L}{2\pi\sqrt{n_{wg}^2-n_s^2}}\arctan\left(\xi_{wg,s}\sqrt{\frac{n_s^2-1}{n_{wg}^2-n_s^2}}\right) < w_{eq} < \frac{\lambda_s}{2\pi\sqrt{n_{wg}^2-n_s^2}}\arctan\left(\xi_{wg,s}\sqrt{\frac{n_s^2-1}{n_{wg}^2-n_s^2}}+\pi\right)$$

Equation 3.6

with $\xi_{wg,s} = \frac{n_{wg}^2}{n_s^2}$ for TM and 1 for TE.

The above condition (**Equation 3.6**) leads to 250 nm < $w_{eq\ (TE)}$ < 935 nm for TE and 292 nm < $w_{eq\ (TM)}$ < 970 nm for TM with the present choice of materials and wavelength range.

With respect to the above inequalities, this rigorous design is simulated with the commercial software (”MC Gratings”). The simulation is modelled as a rectangular photoresist structure assuming to have a corrugation of 0.5 duty cycle. The modelled structure results in 0-order resonance in reflection in normal incidence (θ = 0°) issued from a polychromatic source for both polarizations TE and TM. The thicknesses layers correspond to real measured dimensions dictated by the TiO_2 Sol-Gel and photoresist preparation technology by dip coating on planar SiO_2 substrate (**See Section 3.5.2**). The grating period is fixed at 960 nm in relevance to the angular period of the phase mask and the tube inner diameter to reach the aimed resonance in the near IR spectral range (1300 nm < λ_R < 1600 nm). Considering all the structural parameters a resonance of 100% reflectance for both TE and TM polarizations is predicted at the wavelengths λ_{RTE} = 1438.3 nm and λ_{RTM} = 1407.6 nm. In addition, the theoretical FWHM of the TE and TM reflection peaks is 16 nm and 0.7 nm respectively **(Figure 3.5)**.

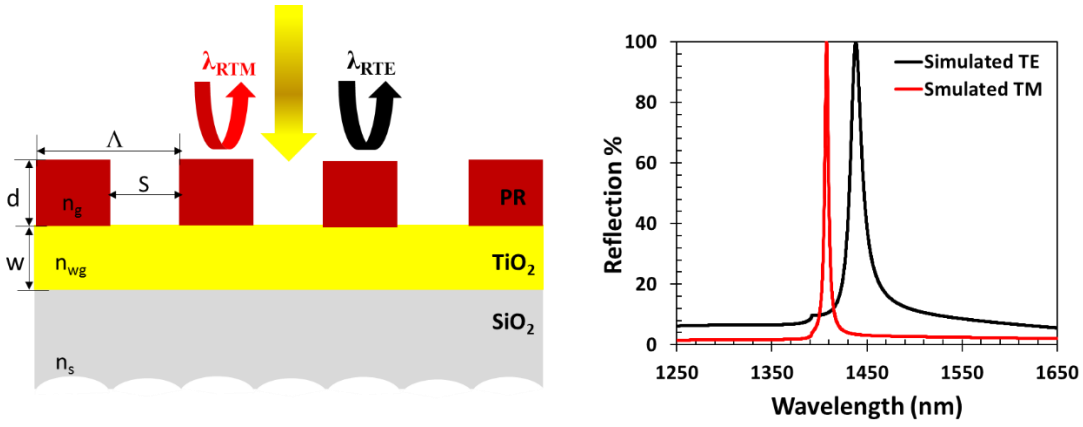

(a) **(b)**

Figure 3.5: Planar waveguide grating modeling of TM and TE polarization resonant reflections (red and black lines, resp.) under normal incidence. w = 340 nm, d = 376 nm, Λ = 960 nm, s = 480 nm. n_s = 1.45, n_{wg} = 1.7, n_g = 1.67. (a) Scheme of the diffractive structure, (b) calculated spectra.

As it will be described in **Section 3.5**, the structural features imposed by the Sol-Gel and photoresist coating at the inner wall of the tube, prescribe a sum of w and d in the range of 700 nm, i.e., w_{eq} about 650 nm for TE and 350 nm for TM according to **(Equation 3.4** and **Equation 3.5)** which is well in the single mode operation range for both polarizations. However, experimentally, the thickness of TiO_2 and the depth of the resist grating may vary inside the tube and may not be sufficient to ensure guidance in the structure. Indeed, a rough calculation of the effective indices of the modes for TE: $\lambda_{RTE}/\Lambda = 1.49$ and for TM: $\lambda_{RTM}/\Lambda = 1.46$, shows that with the values taken in the simulation the TM effective index is close to the refractive index of the SiO_2 substrate ($n_s = 1.45$) and the TM propagation near the cut-off limit. The experimental study of the resonances after fabricating the structure shall confirm or not the existence of one or two modes.

3.5 Fabrication of the resonant structure inside the tube

3.5.1 Substrate pre-treatment

For layer deposition, prior cleaning preparation of the substrate is essential to prevent contamination and organic impurities. The surface experiences a wet bench ultrasound of high frequency (30 kHz) processing in the clean room using acetone, ethanol and deionized water for 10, 10 and 5 min respectively. A complementary oxygen plasma treatment during 1 min in a 0.09 mbar of pressure modifies the physical and chemical properties of silica substrate activating the O-H bonds, thus conferring super-hydrophilic properties and better TiO_2 adhesion. As long as the Sol-Gel is not deposited, the substrates are stored in deionized water in order to maintain their O-H bond and their hydrophilicity.

3.5.2 TiO_2 sol gel waveguide and resist deposition

After the preparation of the TiO_2 solution (**Section 2.4.2.2**), the TiO_2 deposition is carried out by dip coating (**Section 2.5.2**) in a clean room with a descent rate of 7 cm/min until the tube is immersed in the sol over a height of 10 mm. The substrate remained partially submerged for 1 min before being removed from the sol at a constant extraction rate of 7 cm/min. This withdrawal speed was determined on planar fused silica substrates before being applied to the cylindrical substrates with the hypothesis that both depositions can be considered equivalent for layer thicknesses. The obtained layer is first naturally dried at room temperature. After a heat treatment at 110°C during 3 hours, a xerogel layer in amorphous phase was obtained with thickness of 340 nm measured with the profilometer. In the case of the tubes, we suppose that

the Sol-Gel is deposited on the outer wall equally as on the inner wall and in the same way as planar substrates (**Figure 3.6**).

A second layer of 50% positive photoresist (S1805) diluted with 50% ethyl lactate is coated on the TiO_2 layer and soft-baked at 60°C during 1 min. The resulting resist thickness is around d = 380 nm.

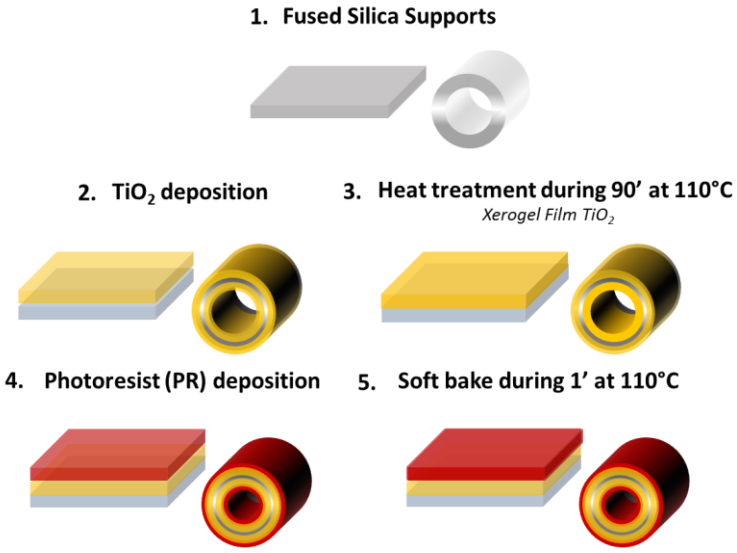

Figure 3.6: Dip-coating layer deposition on the analogous cylindrical-planar substrates.

3.5.3 Cylindrical Photolithography

The phase mask transfer technology is a single-step exposure that produces a high contrast interferogram. This is due to the zero-order transmission parallel to the axis of the tube, which does not interfere with the $\pm 1^{st}$ orders on the cylindrical wall, whereas the 2^{nd} diffraction orders are evanescent.

The phase-mask exposure set-up is illustrated in **Figure 3.7** and consists of a small number of optical components.

The collimated beam of a linearly polarized CW (Continuous Wave) laser at 355 nm wavelength impinges normally onto the phase-mask plane. A beam-expander enlarges the Gaussian beam to ensure a substantial overlap of the phase-mask, and a reasonable dose constancy over its area. The tube is placed against the phase mask so that the incident beam axis and the tube axis are superposed, and the phase-mask center is located on the tube axis.

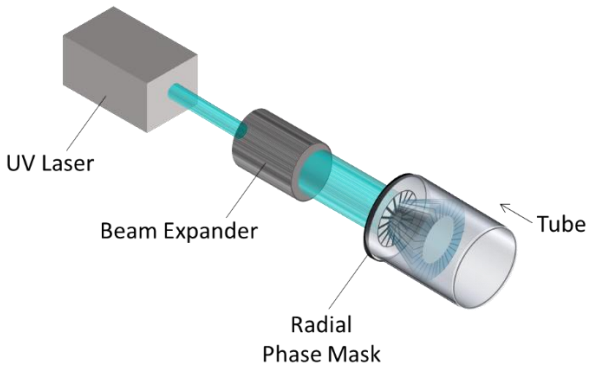

Figure 3.7: Cylindrical wall grating exposure set-up.

The alignment of the phase mask and tube is very critical, as this will ensure a constant grating period at the inner wall of the tube. The tube and phase-mask substrate were placed on micro-displacement stages with the needed degrees of freedom (2 angles, 3 translations).

The alignment was performed under white light illumination and controlled by a camera. Specifically, a white source and a filter were placed before the phase mask and the tube. The filter is a high-pass filter that cuts off the entire wavelength band below 600 nm. The relative position between the phase mask and the tube was monitored by a camera, which was connected to a computer screen. During alignment, we have benefited from the external alignment ring, engraved on the phase mask, as a guide for proper adjustment **(Figure 3.8, Figure 3.9)**.

Once the best alignment was achieved, the white source was turned-off and the filter was withdrawn. The UV laser source was then activated to start the exposure of the tube. For high contrast, the exposure was short and lasted 5 sec under 50 mW. Finally, an automated shutter connected to a timer stopped the light at the exit of the laser cavity when the exposure was completed. The interferogram in the tube appeared after the immersion in trimethylamine N-oxide (TMAO) for 8 sec.

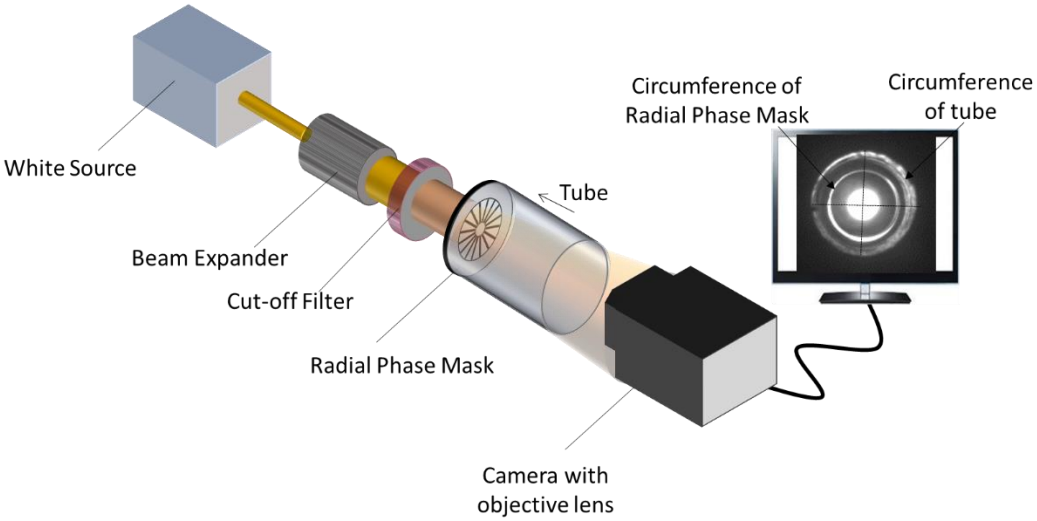

Figure 3.8: Schematic of alignment processing of the phase mask-tube assembly.

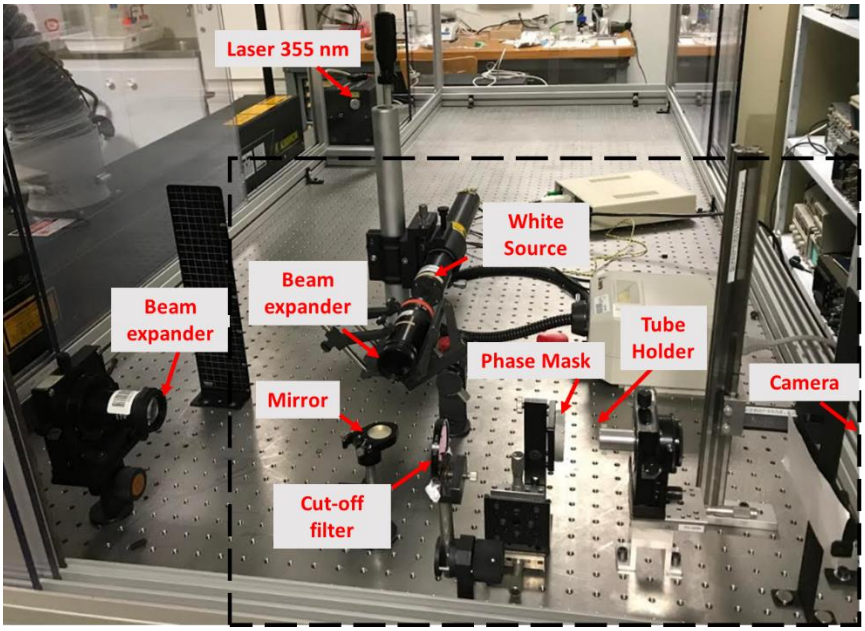

Figure 3.9: Photograph of the total optical bench including the components for the tube-phase mask alignment (rectangle with dashed lines).

3.6 Structural characterization of the tube, the waveguide layer and the grating

The constructed tube includes an annular diffracting grating in a miniaturized SiO_2 substrate of R = 4 mm and length of L = 15 mm **(Figure 3.10)**.

The H_m minimum distance - corresponding to minimum radius R_i of the phase mask - between the grating ring and the front face of the tube is the travelled distance attained by the m=±1 diffracted orders. This distance was estimated to be 3.6 mm adapted to the tube [14] while the fabricated one was measured at 3 mm. The difference of 0.6 mm can be justified, if we consider that the contact between the phase mask and the tube during the alignment process was not zero to avoid damage. Therefore, this leads to an interferogram closer to the front face of the tube than the calculated one. The height of the grating ring was fabricated and measured at 3 mm, which is exactly the value of the previous calculations [14].

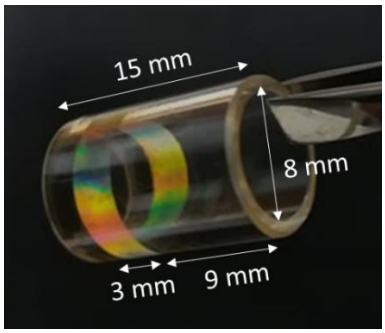

Figure 3.10: Photograph of the final ring-shaped waveguide grating printed on the inner wall of the SiO_2 tube.

An alternative choice of materials could also be proposed; the photosensitive layer at the inner wall of the tube could either be a negative photosensitive sol gel like TiO_2, used as an element of a functional device after pyrolysis. At the present stage of development however, it was preferred to demonstrate the resonant reflection effect using a simple experimental model where the exposed and developed positive photoresist grating layer couples the light into the TiO_2 layer. The reasons are the much lower complexity in patterning a positive photoresist than a sol gel layer since the dose required for the exposure of a photoresist layer is smaller than the one of sol gel (sol gel exposure at 10 min with a full 100 mW power).

3.6.1 Structural characteristics of the irradiated tube

In contrast to the case of a grating at the outer wall of a cylinder [3], the structural characterization of a grating at the inner wall of a tube can only be made destructively by growing a metal replica inside the tube. It is however possible to gain some global evaluation of the grating contrast, and especially of its uniformity, by illuminating it under white light as the picture of **Figure 3.10** illustrates.

Further structural analysis was made destructively by breaking one tube and observing the top surface and the cross section of the concave broken piece **(Figure 3.11)**.

Figure 3.11: Tested sample for structural analysis.

3.6.2 FIB (Focused Ion Beam)

Dual beam FIB/SEM microscopes have emerged quite recently as research tools in common laboratories and platforms. They provide a real benefit to characterize surfaces in three dimensions and more simply to allow the imaging of the cross section of surface structures, such as diffraction gratings, multilayers and waveguides.

To create a cross-section and proceed to the precise dimensional characterization of the waveguide grating on the broken tube we have used a dual beam Thermofisher Helios 600i FIB/SEM microscope. FIB/SEM microscope uses high energy Gallium Ions either to bring energy, to mill the material surface, or to deposit layers thanks to precursors. SEM column and detectors allow detecting a feature or locating a defect of interest.

To do so, a prior processing is necessary mainly when dielectric specimens are tested. This is because FIB/SEM is mostly compatible to semiconductors and conductors. Therefore, carbon layer (C) ex-situ is essential to metallize and convert the dielectric layer into a conductor. The

deposition parameters of the carbon layer were 4x6 sec at 4.2 Volt. Then, the specimen was placed in the FIB/SEM vacuum chamber, at 10^{-6} mbar.

To protect the surface to be characterized the specimen was covered by 200-300 nm of Pt. This electron beam induced deposition (EBID) was performed by means of a Pt precursor, which was injected near the surface thanks to an injector, while the electron beam was scanning the surface to be covered. The electron beam parameters have been set to 2 kV and 0.34 nA. Finally, an ionic deposition using gallium beam has been carried out using carbon precursor. The last step consisted of scanning the gallium ion beam on the surface to be milled. The Ga+ beam sputtered the atoms of the surface and allowed the observation of a cross section of more than 15µm x 2 µm **(Figure 3.12)** underneath the grating's surface.

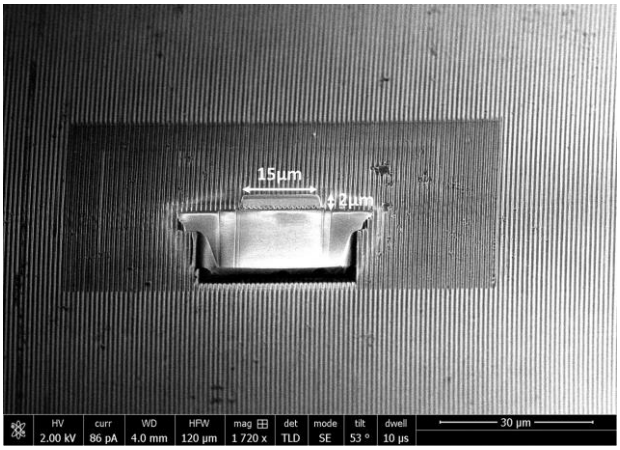

Figure 3.12: Section of the grating area with 15 µm x 2 µm.

The following image **(Figure 3.13)** is the SEM image of the tube, where we can distinguish different zones corresponding to different grey levels around the grating line.

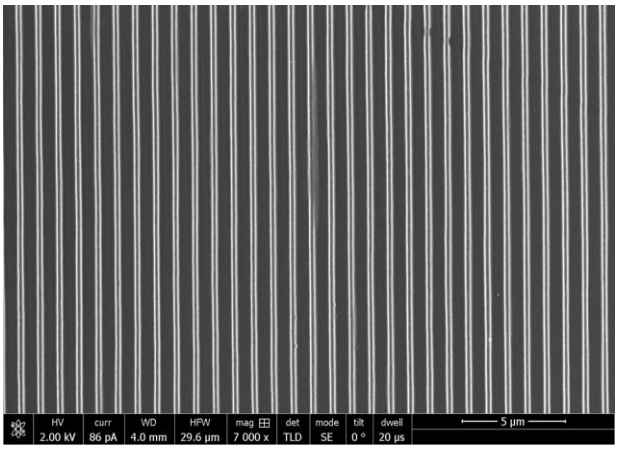

Figure 3.13: SEM image of the top view of the tube grating.

Figure 3.14 exhibits a) the top view and b) the cross section of the waveguide grating. These images reveal the real profile and helps us to measure the final structural features. The cross section shows that the waveguide and the grating thickness are smaller than the initial simulated ones (265.1 nm instead of 340 nm) and (360.9 nm instead of 376 nm) respectively. Moreover, as seen by SEM image, a large deviation is noted for the duty cycle that is far from 0.5 and for the period, that exceeds the predicted one by about 25 nm.

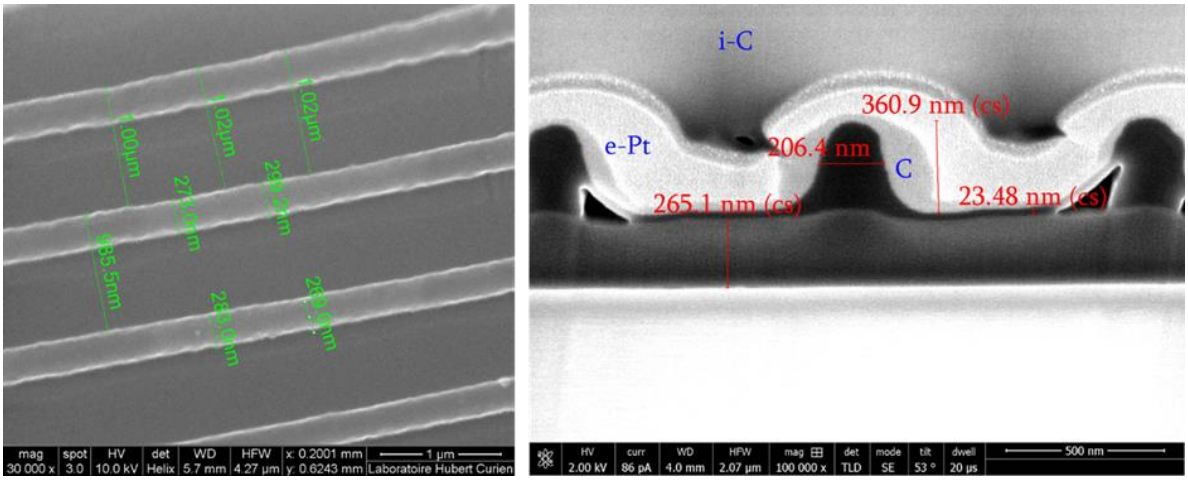

(a) **(b)**

Figure 3.14: SEM top view (a) and FIB cross section images (b) of the waveguide grating assisted by carbon ex-situ (i-C) for metallization, e^--Pt for protection and a final ionic deposition with C precursor for surface sputtering and cross-section.

3.6.3 Period measurement

According to SEM analysis, the measured period was estimated differently from the known period Λ that was strictly obtained by the angular period $\Lambda_{\varphi\text{-pm}}$ of the phase-mask and the radius R of the tube. Such a misjudgment is probably due to an error on R specifications that are approximately known and certainly not in the features of the phase mask, which were extensively studied.

The fused silica tube has so far been considered as perfectly circular with an inner radius according to the specifications of 4 mm. As the actual period is proportional to the inner radius, a precise determination of the tube geometry was undertaken by Kunz Precision AG by means of a stability and accuracy enhanced EROWA – CMM Qi/CNC measuring machine. The false color results of **Figure 3.15** on one of the tubes at our disposal show that the average diameter is 7.8825 mm, the circularity quite good (the diameter varies by ± 3 nm), and the average

diameter varies by ± 10 nm along the axis. Considering the 240 µrad angular period of the printed grating on this specific tube, the expected period at its inner wall is ~ 946 nm (instead of 960 nm in theory). Comparing the 985.5 nm SEM period of **Figure 3.14** with the period determined by the precise diameter measurement reveals that the center of the phase-mask was not properly located on the tube axis prior to resist exposure. The measured period of 985.5 nm results from $R = \Lambda/\Lambda_\varphi = 4.106$ mm distance between the tube inner wall and the phase-mask center. If the tube were perfectly centered with the phase mask, the traveled distance of the ±1 orders would be equal to 3.95 mm for both directions. In the opposite case, the orders propagate unequally; one direction travels farther and reaches 4.106 mm, whereas the diametrical one covers a shorter distance equal to 3.776 mm. This implies that at the diametrically opposed location on the tube wall the period is 906 nm.

Therefore, a 0.165 mm offset from the mask center to the tube causes different angular sections of the cylindrical waveguide grating and slightly different angular and period coupling conditions, which inevitably widen the resulting reflection peak spectrum as, observed experimentally (see results **Section 3.7.4**).

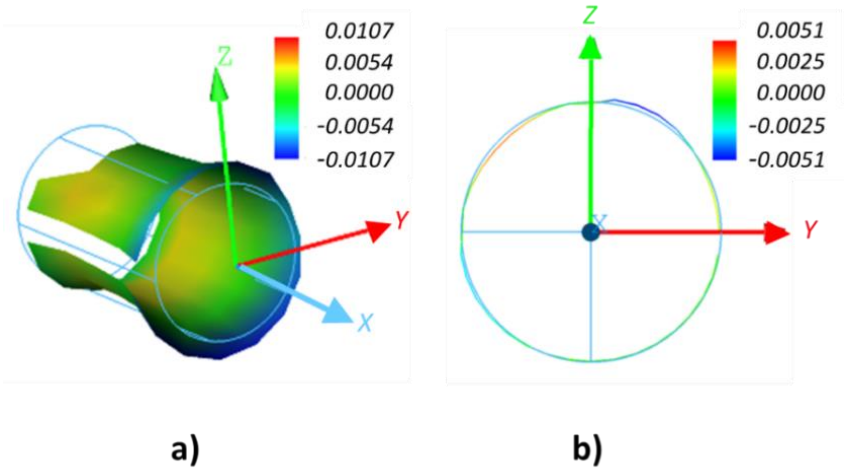

Figure 3.15: False color representation of the high precision characterization of the geometry of a tube. Diameter variation of ± 10 nm along the tube axis (a), inner diameter variations within ± 3 nm with average diameter 7.883 mm (b).

3.7 Optical Resonant excitation

3.7.1 Resonance excitation

After the structural analysis, the device is tested for resonance excitation. Therefore, the tube must be properly illuminated and the incident beam correctly spatially shaped. To proceed, we need to ensure a holistic illumination on the cylindrical grating in the hollow of the tube.

The holistic illumination refers to the isotropic illumination received by a set of points on a surface simultaneously. As seen, to excite a planar waveguide grating and lead to a very narrow resonance, it is required an infinitely long grating addressed by a plane wave of infinite extent. If we had a finite grating or a truncated beam, the resonance would be weaker due to the non-sufficient destructive interference in the transmissive medium.

Similarly, a cylindrical wave can excite the same resonant responses as a plane wave, if it is coupled by a stitchingless grating to a waveguide mode at the wall of a centimeter size tube or cylinder. Hence, emerges the holistic incident wave excitation that leads to multi turn synchronous responses in the ring resonator.

To achieve such an excitation, we relied on the idea that a perfect cylindrical grating is obtained by rolling an infinite linear grating while illuminating it with a cylindrical incident wave.

The needed cylindrical wave is obtained by reflecting a collimated axial beam on a centered metallized cone of 90° apex introduced into the tube hollow **(Figure 3.16)**.

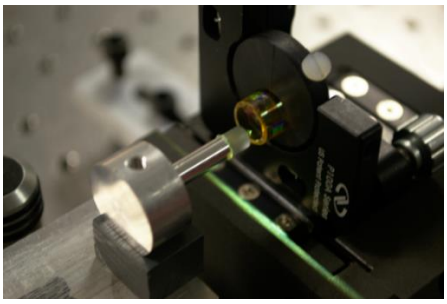

Figure 3.16: Conical mirror inserted in the hollow cavity of the tube, supported by the tube substrate.

A first estimate of the quality of the light reflected from the cone was observed on a wrapped white paper. As illustrated in the **Figure 3.17**, the reflected light does not present any distortion, fact that testifies that the conical mirror has a strictly 90° apex angle and the light source is perfectly aligned to it. In the opposite case, the conical mirror would induce beam aberrations including reduced beam resolution and low uniformity.

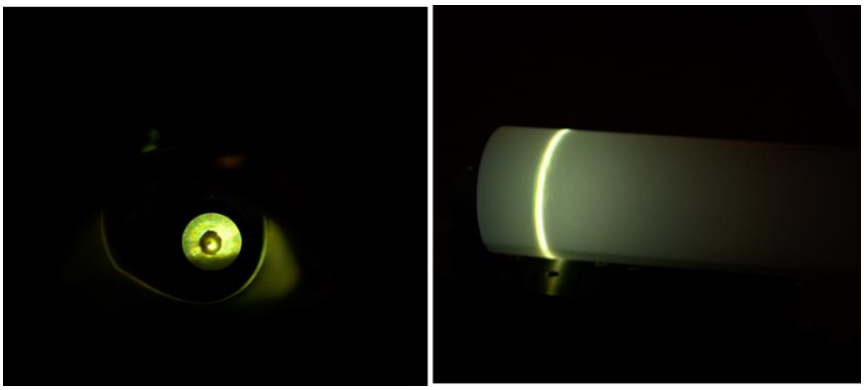

(a) **(b)**

Figure 3.17: Front (a) and side profile (b) of the cylindrical wave issued from the reflective cone observed on a wrapped white paper.

The expected resonant reflection resulting from a waveguide mode excitation is also a cylindrical wave that is reflected back by the cone in form of a collimated beam to be analyzed spectrally.

3.7.2 Effect of the incident beam polarization

By inserting the metallic cone in the hollow cavity of the tube, a normal reflection of the axial beam is generated all over 2π onto the waveguide grating. **Figure 3.18** illustrates the coupling mechanism after the reflection of the incoming incident beam. The resulting IR resonances of the two excited modes TE and TM are directed back to the conical mirror.

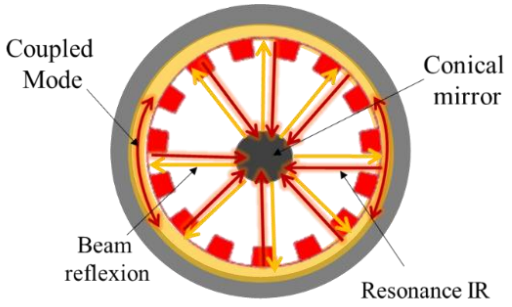

Figure 3.18: Top view of the display and coupling mechanism in the waveguide (yellow color) grating (red color) at the walls of the tube.

The type of polarization of the incident axial beam is an important factor that will intrinsically define the nature of the excited modes.

A linear vertical polarization permits the excitation of the TE modes from the top and bottom areas of the tube and of the TM modes from the lateral areas **(Figure 3.19-a)**. As in the case of the radial grating mask, a hybrid polarization TE-TM appears at the intermediate areas of the circumference. Considering that the wave vector $\vec{k}_i$ of the incident light, changes its direction radially after impinging on the cone, we can deduce the other two TE and TM components at each grating area. After coupling and decoupling, the excited modes propagate towards the cone and the resonance is reflected by the cone until it is detected.

For the linear horizontal polarization, the opposite coupling occurs; at the top-bottom areas, we have a TM mode excitation and at the side areas a TE. The rest areas of the periphery lead always to hybrid polarization **(Figure 3.19-b)**.

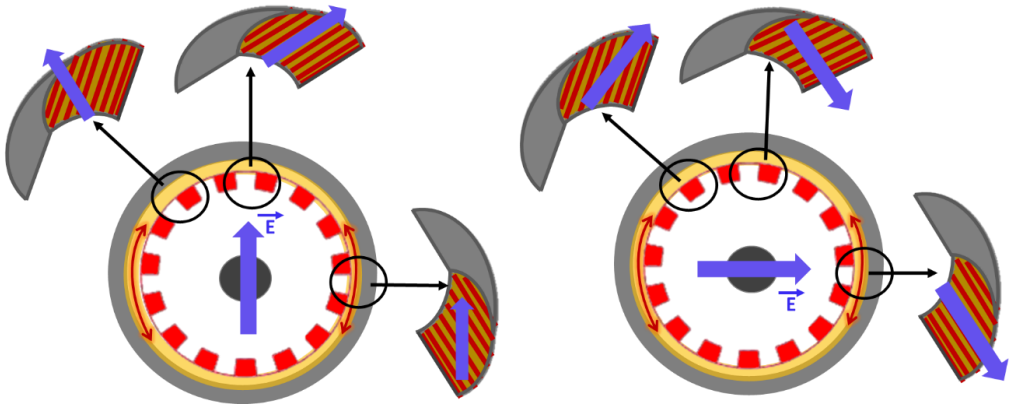

Figure 3.19: Interaction of the polarized vertical (a) and horizontal (b) electric field relative to the grating lines at the top, side and intermediate zone of the tube.

In a radial polarization, the electric field direction is along the radius of the tube, thus parallel to the grating lines at any point **(Figure 3.20-a)**. In azimuthal polarization, the electric field direction is always perpendicular to the grating lines, thus only the TM mode in the waveguide is excited **(Figure 3.20-b)**. However, radial or azimuthal polarizers are specified only at certain wavelengths and do not have the ability to work over a broad spectrum.

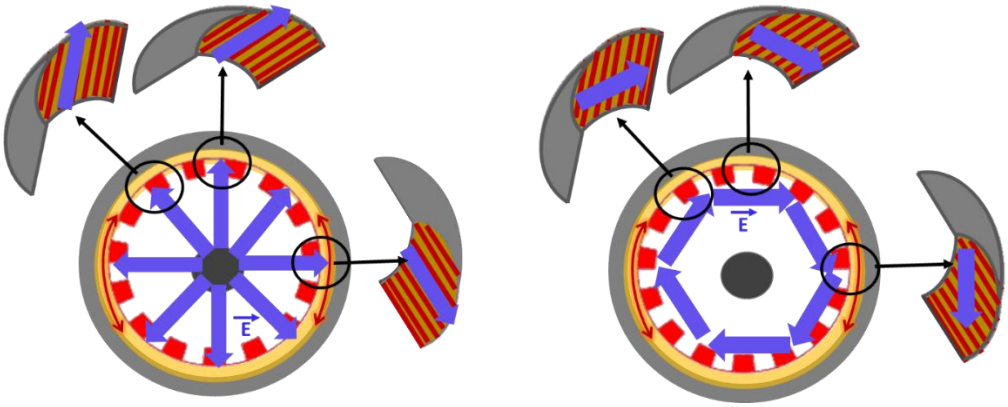

Figure 3.20: Modes excitation: TE by a radial (a) and TM by an azimuthal (b) polarized electric field.

Finally, in circular polarization, every single point of the circumference excites equally TE and TM modes since it is a combination of two orthogonal linear polarizations that are $\pi/2$ phase shifted **(Figure 3.21)**.

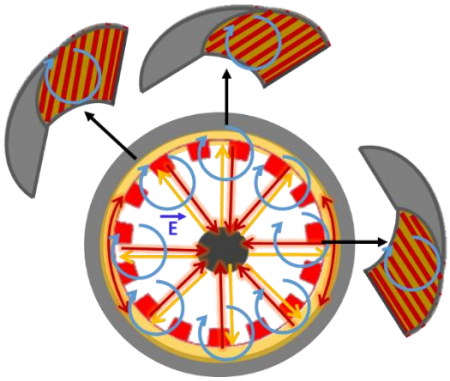

Figure 3.21: Mode excitation by a circular electric field.

In any case, the out coming resonance will have nearly the same polarization as the initial incident beam.

3.7.3 Optical set-up

After the polarization analysis, the most suitable polarization for cylindrical WRG was chosen to be the circular polarization as it operates for a wide range of spectra and can be easily implemented with a linear polarizer and a QW plate. In addition, taking into account possible structural defects in the tube, it is imperative to ensure equal and simultaneous excitation for both TE and TM modes.

Figure 3.22 and **Figure 3.23** illustrate the operating principle and the photo of the designed assembly. The spectroscopic bench uses a WLSC (White Light Super Continuum) collimated source (200 nm < λ < 2400 nm). The light source is a single mode source (LP_{01}) over the entire range of emission wavelengths and is quasi-linearly polarized.

A linear IR polarizer LP (650 nm - 2 µm) is placed after the source in order to impose the polarization and its axis is fixed at 45° from the axes of a quarter-wave (QW) plate. The beam is divided by a beam-splitter BS set at 45° relative to the beam propagation and impinges onto the conical mirror centered on the tube axis where it undergoes a plane to cylindrical wave transform with its k-vector orthogonal to the incident beam axis. The alignment of the cone in the tube center is realized thanks to XYZ and θ_x and θ_y stages with 0.05-degree accuracy.

The expected resonantly reflected spectral component is directed by the beam splitter to an optical fiber connected to a NIR (900 nm - 2100 nm) spectrometer (Ocean Optics NIR Quest 512-2.2) of 24 nm resolution and is analyzed by the Spectra Suite software dedicated to the spectrometer.

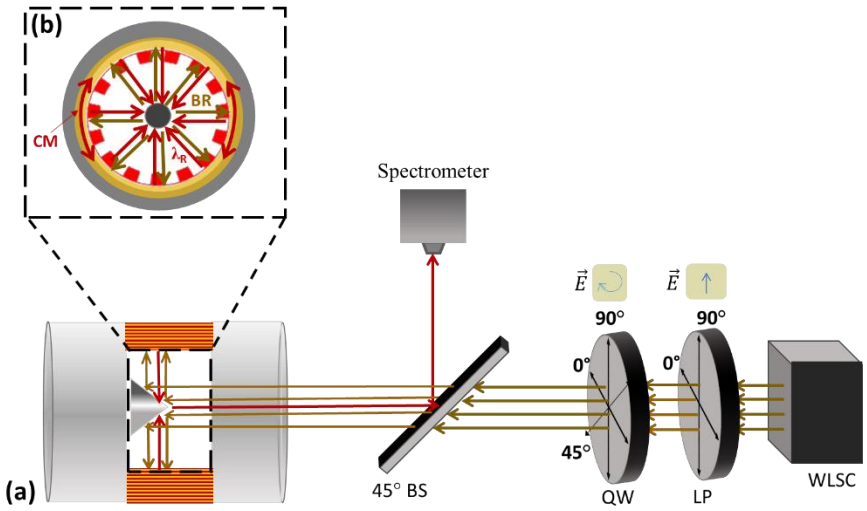

Figure 3.22: Spectroscopic set-up for resonance measurement (a), top view of the tube (b) with coupled mode (CM) in the waveguide, beam reflection (BR) by the conical mirror and λ_R the resonance wavelength reflected by the cone.

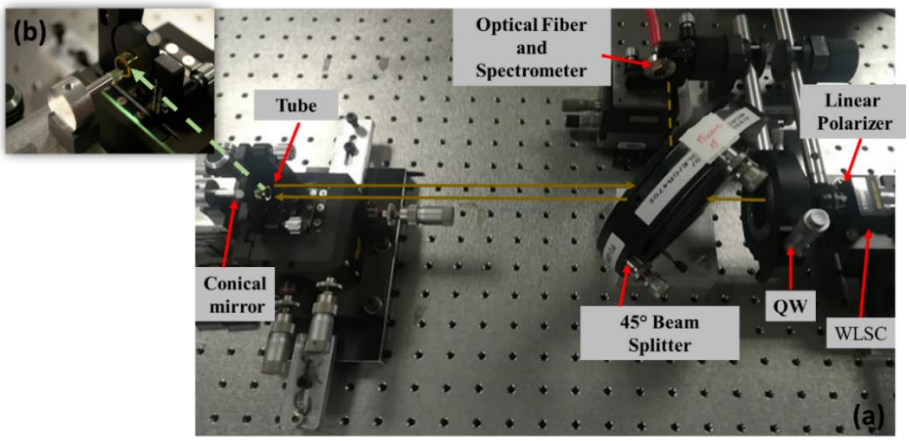

Figure 3.23: Photography of the (a) experimental set-up for resonance measurement, (b) Inset image of the conical mirror and tube substrate.

The tube is placed on the tube holder and by auto-collimation the reflected spectrum of the tube grating is centered on the optical axis by moving the micro positioning steps **(Figure 3.24)**.

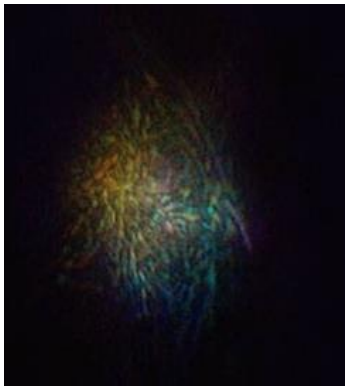

Figure 3.24: Reflected beam by the tube.

The detector was first set in proximity of the BS, at the position 1 to acquire the excitation (reference) spectrum **(Figure 3.25-a)**. The software associated to the spectrometer has saved the reference spectrum and the dark spectrum (noise background).

Finally, the detector was placed at the position 2 without modification of the initial angular, lateral, transversal or height position of the detector and has saved the reflected resonance spectrum **(Figure 3.25-b)** from the tube on the left of the beam splitter (see **Figure 3.23**).

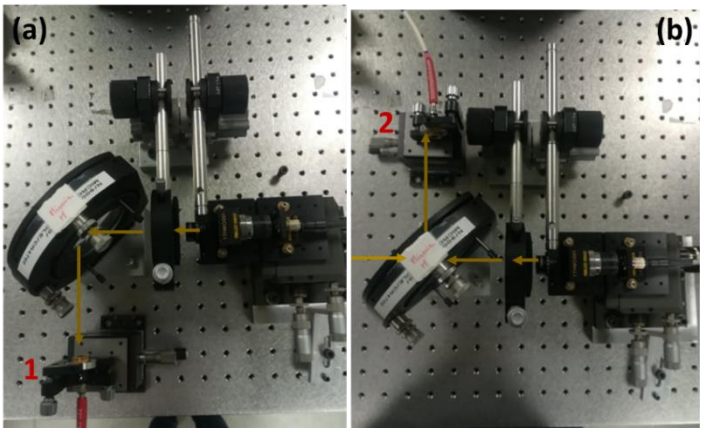

Figure 3.25: Experimental set-up used to acquire the reference spectrum (a) and resonant reflected spectrum (b) detected by the spectrometer.

This specially designed set-up is an innovative system that proceeds to resonance measurements in reflection, which are difficult to implement in case of the cylindrical geometry.

Even with an optimized BS, necessary for reflection measurements, reflection losses and chromatic aberrations for a large wavelength range may be involved. During the resonance measurement, the reflected beam after the auto-collimation ends bigger than the diameter of the collimator that injects light into the optical fiber connected to the detector. This fact implies that a large part of the reflected beam is outside the detector leading to poor signal detection. To increase the signal, we need to increase the spectrometer integration time. Moreover, we have to take into account that the measured reference is not absolute since it is not measured near the tube. Finally, additional losses can be induced by a tube not perfect due to diffusion. All the aforementioned points can certainly affect the resonance detection quality and render the measurement extremely delicate. As one can see, the resonance cannot be measured with an absolute value but only with arbitrary units.

3.7.4 Results and discussion

After FIB and SEM analysis, the real structural parameters are anew launched in the simulation programming to calculate a more accurate optical response. In contrast to the previous simulations in **Figure 3.5-b**, the specific characteristics proved that there is no TM mode propagation **(Figure 3.26)**. The TE peak shifts by 10 nm due to the period difference as discussed in the Section **3.6.3**.

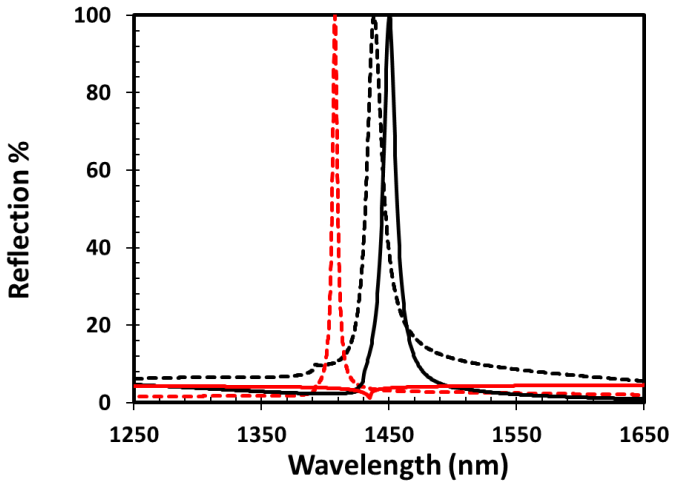

Figure 3.26: Initial (dashed lines) simulated resonant responses of TE (black) and TM (red) modes superposed with the simulated responses based on the real structural profile after FIB and SEM analysis (solid lines).

The non-appearance of the TM mode is mainly attributed to the duty cycle equal to 0.3 instead of 0.5 in combination with the reduced width of the waveguide that leads to a weaker effective index of the TM mode, near the cut-off limit, than the previous calculated. The reduced thickness of the grating does not affect significantly the TE resonant response.

Measurements were performed with two types of polarization: circular using the set-up of the **Figure 3.22** and **Figure 3.23** and linear only by removing the quarter wave-plate.

The reference signal is first measured after the beam splitter with an incident circular polarization. The normalized experimental reflection spectrum is plotted in **Figure 3.27** in arbitrary units together with the simulated TE and TM polarization spectra.

Having so far explained the absence of TM mode, we compare the simulated TE mode resonance with the experimental peak. The superposition graph in **Figure 3.27** reports a good agreement between the two peaks (λ_{exp} = 1449.18 nm and λ_{RTE} = 1451 nm). The effective index n_{eff} corresponding to the resonance of the experimental peak is equal to $\frac{\lambda}{\Lambda} = \frac{1449.18\ nm}{985.5\ nm}$ = 1.47 > 1.45, and respects the propagation criteria for a monomode waveguide.

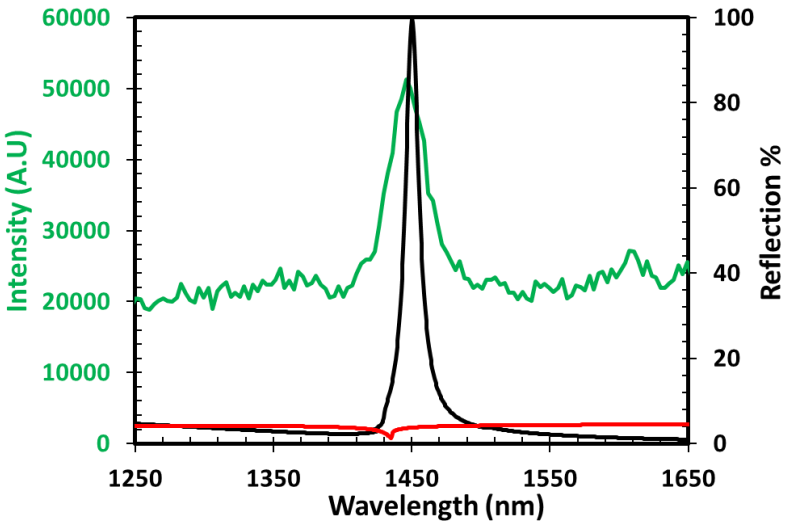

Figure 3.27: Superposition of simulated TE and TM spectra (black and red lines respectively) with the experimental TE (green color) in arbitrary units obtained under circular polarization excitation.

Measurements with incident linear polarization were also performed. **Figure 3.28** demonstrates the superposition of the two experimental resonances using vertical and circular polarization. As one observes, the vertical and circular polarization are alike. This is attributed to the equal excitation of the TE mode over the 2π grating circumference despite the different polarizations. The ideal would be to excite the structure in radial polarization and thus observe a more prominent effect. Such hypothesis must be checked with further measurements.

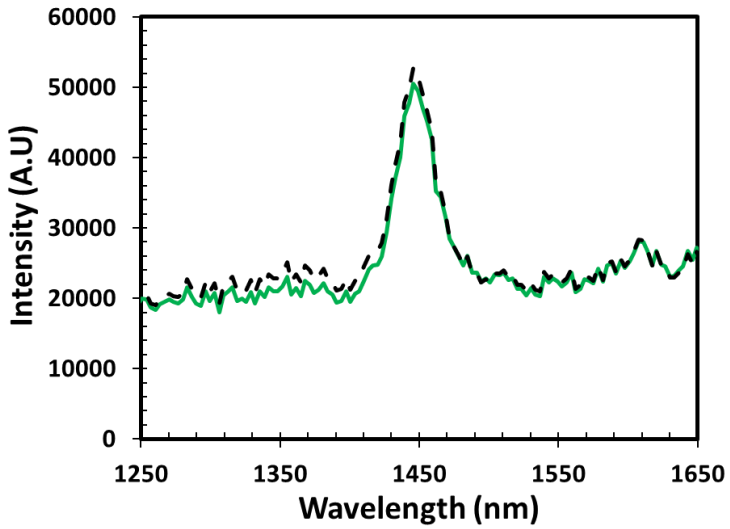

Figure 3.28: Vertical (green color) and circular polarization (dashed black lines) effect on the TE resonant reflected peak.

The FWHM of the experimental peak is about 40 nm, i.e. about 3 times larger than the calculated TE width. The quality factor of the experimental peak is equal to

$$Q = \frac{\lambda}{FWHM} = 36.25$$

This quality factor cannot be easily compared at present with those of other curved cavities reported in the literature that are not similar to the one studied here. However, the above-calculated characteristics give an insight of the peak quality that is inherently dependent on the other structural features. Apart from the misalignment of the tube during the illumination process, another prevalent reason that induces peak broadening is the non-uniformity of the layers in the inner walls of the tube. J. Puetz *et al.* has also demonstrated similar inhomogeneities in the thickness and roughness of the layers in the inner walls of the tube and attributed them to the bad distributed flow conditions and the saturation of solvent vapor during the drying of the wet film [17]. Therefore, a more controlled structural process can further improve the optical responses.

3.8 Conclusion

This chapter presented the simulation, fabrication and experimental demonstration of a Waveguide Resonant Grating in the interior walls of a SiO_2 tube. To our knowledge such a demonstration has never been done. A cylindrical waveguide grating with a radius much larger than the wavelength couples the mode in a multi-turn waveguide ring and stands the exact analogous geometry to an infinite rolled up planar WRG. The resonance excitation occurs through a positive photoresist grating and a calculated monomode solgel TiO_2 cylindrical waveguide structure operates under normal incidence for both TE and TM polarization. The fabrication of such configuration is a major spatial coherence problem that implies the realization of a stitchingless interferogram in the cylindrical cavity with an integer number of periods over 2π. A special phase mask satisfies the latter condition by diffracting an incident UV collimated beam to ±1 diffractive orders equally propagating in the tube that is centered and well aligned to the phase mask. To manifest the resonant effect in the microstructure, a centered reflective conical mirror able to transpose plane to cylindrical waves and conversely is used. The cylindrical illumination is thus submitted to the holistic phenomenon and excitation of TE mode is assured by a circularly or linear polarized light. The optical responses were measured by spectroscopic means and showed only the TE resonant excitation in contrast to the expected theoretical simulations that predicted simultaneous excitation of TM mode. The

deep structural characterization of SEM and FIB revealed the reasons for the single TE mode excitation and further simulation compared the experimental results with the theoretical peak based on the actual characteristics. The superposition exhibited a good proximity of theoretical and experimental TE resonance. All of the structural diagnosis and defects identification will contribute in the future to construct a more robust WRG in the tube intended to be compatible with gas or liquid flow applications.

Bibliography

[1] Y. Qin, A. Brockett, Y. Ma, A. Razali, J. Zhao, C. Harrison, W. Pan, X. Dai, D. Loziak, "Micro-manufacturing: research, technology outcomes and development issues", I*nt. J. Adv. Manuf. Technol.* 47 (2010) 821–837.

[2] O. Parriaux, A.V. Tishchenko, F. Pigeon, "Associating a lossless polarizing function in multilayer laser mirrors by means of a resonant grating", *in: Photon Manag. II, International Society for Optics and Photonics*, 2006: p. 61870B.

[3] L. Berthod, M. Bichotte, I. Verrier, C. Veillas, T. Kämpfe, F. Vocanson, M. Langlet, J. Laukkanen, O. Parriaux, Y. Jourlin, "Efficient reversible phase mask for TiO_2 submicron gratings directly printed on cylindrical surfaces", *Opt. Express.* 25 (2017) 9003–9009.

[4] S. Tonchev, Y. Jourlin, S. Reynaud, O. Parriaux, "Cylindrical Grating Projection by Single-Shot Normal Exposure of a Radial Phase Mask", *IEEE Photonics J.* 4 (2012) 1170–1177.

[5] S. Tonchev, Y. Jourlin, C. Veillas, S. Reynaud, N. Lyndin, O. Parriaux, J. Laukkanen, M. Kuittinen, "Subwavelength cylindrical grating by holistic phase-mask coordinate transform", *Opt. Express.* 20 (2012) 7946–7953.

[6] O. Parriaux, Y. Jourlin, N. Lyndin, "Cylindrical grating rotation sensor", *US8345259B2*, 2013.

[7] H. Hirshy, S.G. Scholz, Y. Jourlin, S. Tonchev, S. Reynaud, A. Boukenter, O. Parriaux, "2N Period submicron grating at the inner wall of a metal cylinder", *Microsyst. Technol.* 20 (2014) 1833–1837.

[8] G. Rui, B. Gu, Y. Cui, Q. Zhan, "Detection of orbital angular momentum using a photonic integrated circuit", *Sci. Rep.* 6 (2016) 1–7.

[9] X. Cai, J. Wang, M.J. Strain, B. Johnson-Morris, J. Zhu, M. Sorel, J.L. O'Brien, M.G. Thompson, S. Yu, "Integrated Compact Optical Vortex Beam Emitters", *Science.* 338 (2012) 363–366.

[10] Y. Ohtera, S. Iijima, H. Yamada, "Cylindrical Resonator Utilizing a Curved Resonant Grating as a Cavity Wall", *Micromachines.* 3 (2012) 101–113.

[11] K.P. Huy, A. Morand, P. Benech, "Modelization of the whispering gallery mode in microgear resonators using the Floquet-Bloch formalism", *IEEE J. Quantum Electron.* 41 (2005) 357–365.

[12] "Modal and C Methods Grating Software", https://mcgrating.com/ (Oct.2020)

[13] Y. Jourlin, S. Tonchev, O. Parriaux, J. Sauvage-Vincent, T. Harzendorf, U. Zeitner, "Waveguide Grating Radial Polarizer for the Photolithography of Circularly Symmetrical Optical Elements", *IEEE Photonics J.* 4 (2012) 1728–1736.

[14] L. Berthod, "La photolithographie cylindrique sur revêtement sol-gel photogravable, *thesis*, Lyon, 2017.

[15] Y. Ohtera, S. Iijima, H. Yamada, "Guided-mode resonance in curved grating structures", *Opt. Lett.* 36 (2011) 1689–1691.

[16] I.A. Avrutsky, V.A. Sychugov, "Reflection of a Beam of Finite Size from a Corrugated Waveguide", *J. Mod. Opt.* 36 (1989) 1527–1539.

[17] J. Puetz, F.N. Chalvet, M.A. Aegerter, "Wet chemical deposition of transparent conducting coatings in glass tubes", *Thin Solid Films.* 442 (2003) 53–59.

CHAPTER 4

Synthesis of Vanadium Oxides

4.1 Introduction

Vanadium dioxide (VO_2) has a huge technological potential due to its reversible first-order insulator-to-metal (IMT) phase transition at a critical temperature of ~68 °C accompanied by significant changes of its electromagnetic properties mainly in the infrared (IR) domains. It is usually synthesized in the form of thin films for integration in multilayer structures. In this context, high material quality and rigorous control of the thermochromic properties are required. Several parameters (phase transition temperature, hysteresis width and transmittance amplitude) have to be optimized and a good understanding of the physics behind the phase transition is needed. It has been shown that growth conditions and post treatment strongly affect the internal phase transition mechanism as well as the VO_2 thin film characteristics (epitaxy, morphology and stoichiometry).

This chapter investigates the combination of Pulsed Laser Deposition (PLD) and Rapid Thermal Annealing (RTA) to synthesize VO_x (with x as close to 2 as possible) thin films exhibiting a phase transition on different kinds of substrates, with the aim to minimize the material's thermal exposure. The influence of the annealing parameters is investigated in order to propose ways to control the transition temperature and hysteresis parameters. Amorphous fused silica and quartz substrates are studied, as well as silicon and SiO_2/anatase-TiO_2 heterostructures. The idea of using anatase (A) titanium dioxide stems from its good optical index match with cold VO_2, which would make it a promising material to devise more complex thermo-switching optical grating-based systems. As VO_2 still exhibits a relatively high absorption at room temperature in the infrared range, we also investigate the possibility to reduce the film thickness, aiming for a 25 nm layer. The VO_x is made by PLD of pure metallic vanadium in various oxygen pressures using a 248 nm KrF laser producing nanosecond pulses. Several annealing procedures are performed using Rapid Thermal Processing, at temperature ranging from 300 °C to 500 °C, with various oxidizing atmospheres and duration. The thermochromic transition parameters are

analyzed by optical transmission spectroscopy. Raman, AFM, and SEM measurements are also performed to investigate the characteristics of the thin films.

Moreover, magnetron sputtering deposition, another common technique to produce thin films, is examined. Magnetron sputtering is reported to be advantageous over PLD for certain parameters, thanks to a better epitaxial film growth that can potentially result in better phase tuning [1]. Using magnetron sputtering and post annealing, we have also achieved thin VO_2 film growth on SiO_2 substrate. The transition behavior and temperature, hysteresis loop and roughness are compared to the PLD made thin films for performance estimation.

4.2 VO_2 characteristics and applications

4.2.1 General Characteristics of Vanadium Dioxide (VO_2)

Vanadium (V) with atomic number 23 is a transition metal, whose combination with oxygen yields several types of oxides. While V_2O_5 is the most encountered state, VO_2 has become one of the most well-known due to its thermochromic properties.

Since the early work of Morin, vanadium dioxide has appeared to be a high interest compound because of its first order phase transition at a critical temperature of 68 °C (~340 K) [2]. Below this temperature threshold, VO_2 has a monoclinic crystal structure and behaves as a dielectric material (space group $P2_1/c$) in the IR range, with lattice constants a = 5.75 Å, b = 4.54 Å, c = 5.38 Å and $\alpha = \gamma = 90°$, $\beta = 122.6°$ **(Figure 4.1-a)** [3]. Above the critical temperature, it becomes metallic and appears as tetragonal-rutile crystal structure (space group $P4_2/mnm$) with lattice constants of a = b = 4.56 Å and c = 2.86 Å, and $\alpha = \beta = \gamma = 90°$ **(Figure 4.1-b)** [4].

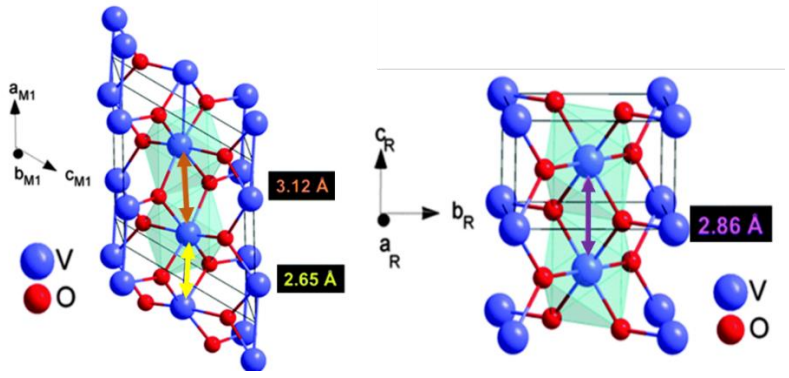

(a) (b)

Figure 4.1: Crystal structure of VO_2 at T<68 °C in the monoclinic phase (a) and T>68 °C in the rutile-tetragonal phase (b) [5]

The reversible IMT (Insulator to Metal) or more correctly the SMT (Semiconductor to Metal) transition manifests through optical modifications in transmittance/reflectivity, mainly noticeable in the IR region (transparent dielectric/opaque metal) and resistivity commutation (dielectric to conductive) **(Figure 4.2).** For a specific wavelength and gradual increase or decrease of temperature, the VO_2's reflectivity and resistance changes show a hysteresis as can be seen on **Figure 4.2**. The characteristic parameters (width, amplitude and transition temperature divergence) related to the hysteresis curve will be further discussed and analyzed **(Sections 4.3 and 4.5)**.

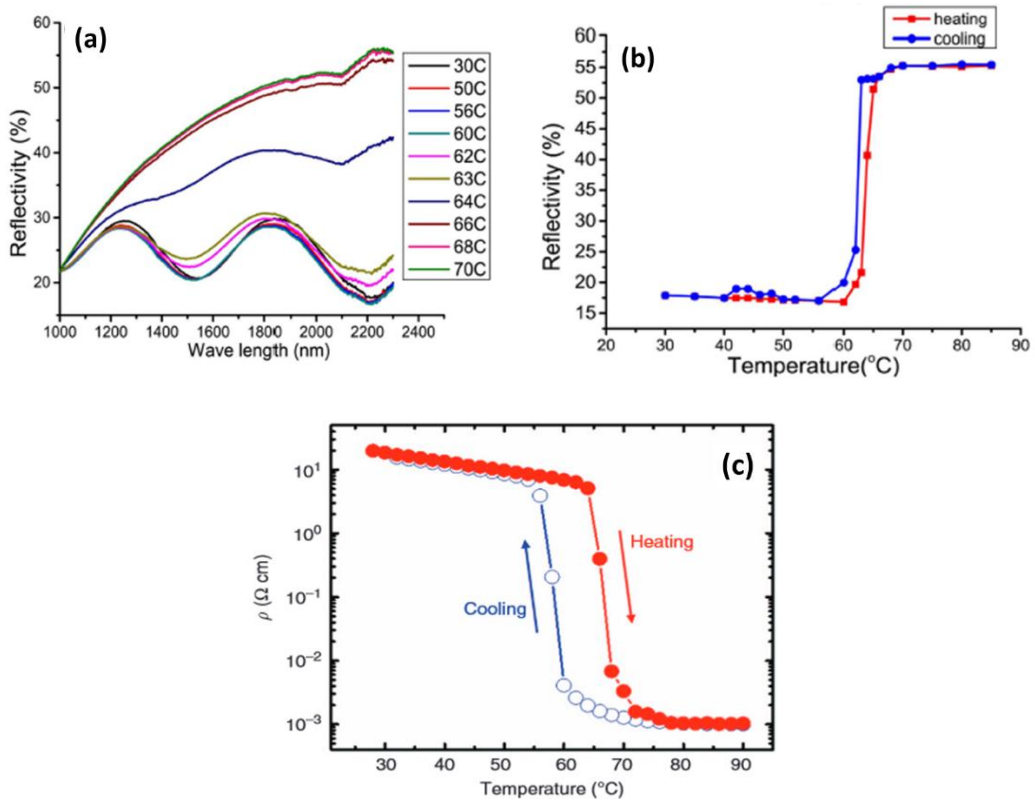

Figure 4.2: SMT based reflectivity spectra as a function of temperature in NIR region [6] (a), reflection hysteresis curve at 2300 nm [6] (b) and resistance hysteresis curve upon heating and cooling [7] (c).

The transition is ultrafast (~100 fs) [8] and can be either triggered optically by photoelectron injection [9], hole doping [10,11], or electrically by DC electric field [12], although it is usually triggered through thermal heating [2].

4.2.2 Applications of VO_2

The reversible character of the VO_2 compound at an easily accessible temperature, classifies it as a smart material with a wide range of applications. The potential to tailor the switching temperature whether decreasing the setpoint by elemental doping with W^{6+}, Mo^{6+}, Nb^{5+} or increasing it by Cr^{3+}, Ga^{3+}, and Al^{3+} to room temperature makes it even more technologically attracting [13].

In glazing industry, thin films of VO_2 could be used as transparent coatings and integrated in Smart Windows for proper control of solar infrared radiation. Their installation in buildings is a promising idea for energy saving and cost reduction of heating **(Figure 4.3)** [14].

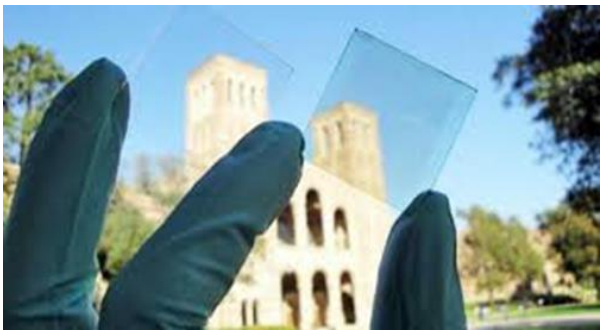

Figure 4.3: Thermochromicity induced by infrared absorption on a VO_2 based Smart Window [14].

Taking advantage of the optical switching effect, optical devices are fabricated as light pulse detectors. A multi-layered sample with a VO_2 embedded film undergoes ultrafast insulator-to-metal phase transition when excited by femtosecond near-infrared laser pulses **(Figure 4.44.4)** [15].

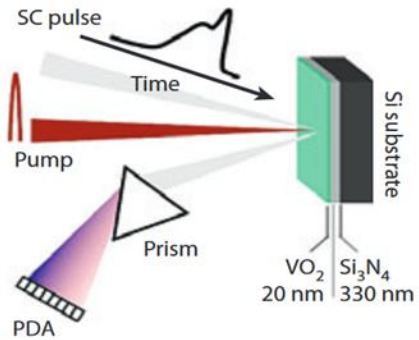

Figure 4.4: Optical sensor triggered by a femtosecond light-pulsed laser [15].

Using an external voltage as stimulation, Kim *et al.* reported the fabrication of two Ni electrodes in contact to a thin VO_2 film that can induce thermal fluctuations in the film when an external voltage bias is applied. They have showed that a voltage jump from 1 V to 22 V induces an abrupt changes in the conductivity of the metallic wires reversing the temperature of the VO_2 film from 68 °C to room temperature **(Figure 4.5)** [16].

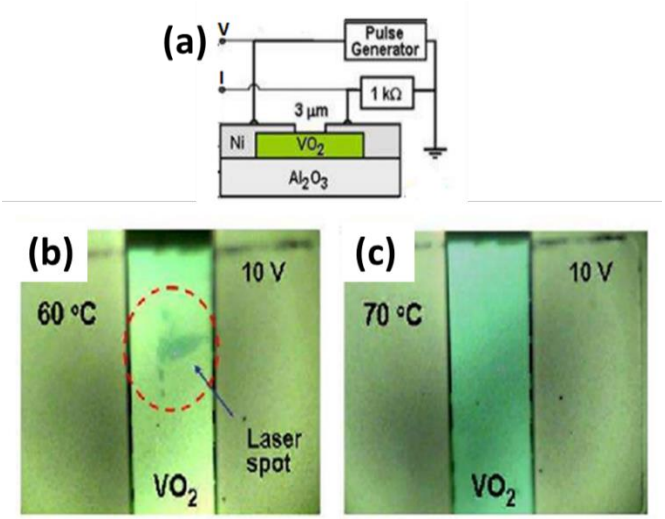

Figure 4.5: Microscopic photos (b), (c) of the two terminal based VO_2 layout (a). Using a local laser spot as an indicator of transition the dielectric phase is signaled by the emergence of a spot at 60 °C and 10V (a) while the metallic phase by spot disappearance at 70 °C and 8V (b) [16].

A voltage tuned gas chemical sensor is also described in [17]. This sensor consists of VO_2 nanowire (NW) suspended between 2 Au electrodes immersed in liquid Ga-In-Sneutectics droplets for temperature stability. The whole system is mounted on a SiO_2/Si wafer. When placed in an Ar gas atmosphere, a self-driving thermal mechanism is triggered. As the pressure increases, the voltage increases and thereby induces simultaneously a joule-heating transfer from the DC wires to the VO_2 NW. Heat dissipation from the NW and Au metals to the gaseous atmosphere relaunches the process until the temperature for MIT transition is reached corresponding to a voltage value characteristic of the gas **(Figure 4.6)**.

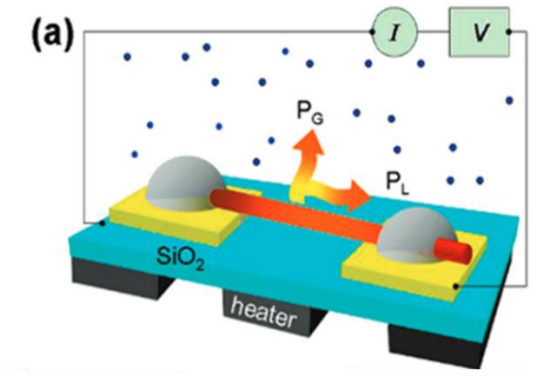

Figure 4.6: Operation principle of VO_2 Nanowire gas sensor. PG and PL denotes the heat fluxes towards the Ar gas and Au electrodes respectively [17].

Traditional Ohmic resistors are overlapped nowadays by the evolved memristors that are resistors with memory capacity able to record the history of the total voltage passing from a system. The VO_2 is an excellent candidate for memristors since it exhibits hysteresis loops i.e. non-binary linear states that can store for instance large amounts of data in multiple states. Driscoll *et al.* observed a memory behavior on a VO_2-based device, characteristic of this kind of memristors, after setting the temperature near to its phase transitional temperature (~68 °C) and performing successive voltage pulses; the top of the lag loop started at the point where the previous one ended **(Figure 4.7)**. In addition, by tuning the pulse duration, the resistivity amplitude could also be tuned [18].

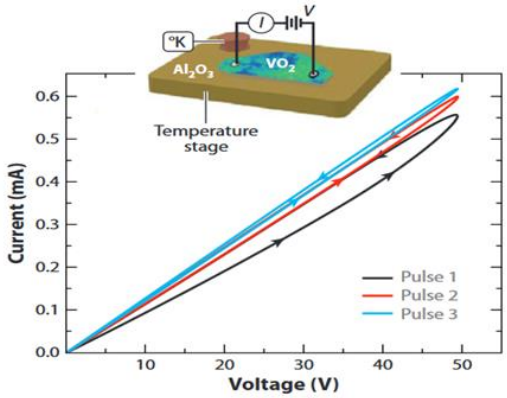

Figure 4.7: I-V hysteric function of the VO_2-based memristor device [18].

The integration of bimodal functional VO_2 films has been constructively exploited in the metamaterial technology. Driscoll *et al.* have demonstrated a hybrid metamaterial device made by a gold Split Ring Resonator (SRR) in combination with a thin VO_2 film **(Figure 4.8)**,

intended to tune properly the far-field optical resonance frequency [19]. The thermally activated VO_2 film approaches the MIT state along with its permittivity modification and the resonance peak decreases. When the temperature exceeds 68 °C, the conductivity rise of the VO_2 is such that it provokes short circuit to the SRR, completely switching the resonance.

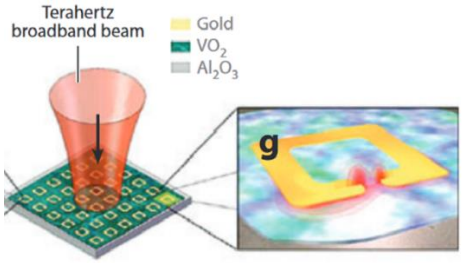

Figure 4.8: Experimental set-up and close up of the Split Ring Resonator lying on a sapphire substrate coated with VO_2 thin film [19].

As VO_2 presents a high temperature coefficient of resistance at ambient temperature, it can be a perfect candidate for microbolometers and thermal cameras generating resistance value shifts after IR radiation absorption **(Figure 4.9)** [20].

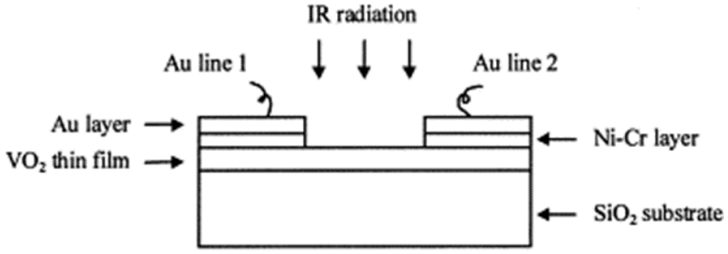

Figure 4.9: Schematic of uncooled microbolometer using VO_2 thin film [20].

Gomez *et al.* has also proposed a thermal VO_2 -based radiative diode [21] after measuring the emissivity hysteresis loops of VO_2 thin films on r-sapphire and Si (100) substrates. 43% of emissivity variations are reached for both samples **(Figure 4.10)**.

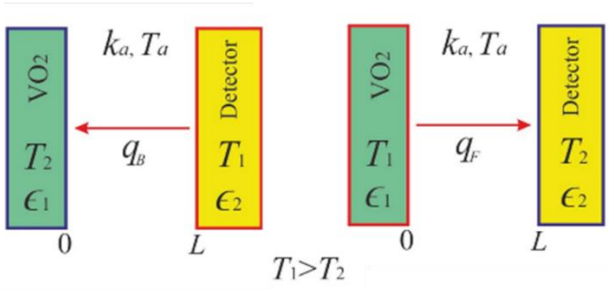

Figure 4.10: Backward (qB) and forward (qF) heat fluxes in a thermal diode consisting of a Thermal Wave Resonant Cavity (TWRC) [21].

Phase shifters also took advantage of the VO_2 compound after observing remarkable short switching time (of the order of 0.1 µs up to 100 ps) over a wide frequency band. Sadiq *et al.* has conceived serial RF switches with embedded VO_2 film to evaluate the switching performance when excited by optical or electrical signals **(Figure 4.11)** [23] .

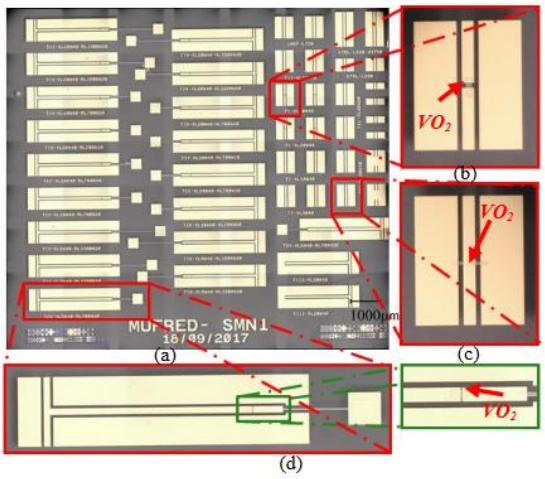

Figure 4.11: RF switches in series made with VO_2 based elements [23].

Recent advances and progress on VO_2 applications are included in [24–26].

4.2.3 Intrinsic properties of Vanadium Dioxide (VO_2)

The driving mechanism behind the low to high temperature transition involves some complex interactions between orbitals (spin), electrons (charge) and crystal structure. A microscopic review in the intrinsic properties of VO_2 reveals interconnected atomic structure rearrangements induced by electronic band displacements.

Figure 4.1-b illustrates the rutile tetragonal phase presented as a symmetric spatial configuration with uniform spacing between the V atoms at 2.86 Å and vertical oriented c_R-axis [27]. The monoclinic phase instead **(Figure 4.1-a)**, breaks this symmetricity by tilting the crystal structure at an angle of <14°. The space group is $P2_1/c$ with a unit cell twice that of rutile of $P4_2/mnm$. According to this, the c_R -vertical axis is occupied by the a_M axis and results in $a_{M1} = 2\ c_R$. The interatomic V spacing varies by pairs due to the dimerization of the V twisted atoms and is equal to 2.65 Å and 3.12 Å rather than the usual 2.86 Å.

One of the most prevalent theory attributes the crystal form modification to the electronic energy dissipated or consumed by the electronic bands to open or overlap the gaps [28]. When

the tetragonal phase with the octahedral crystal field dominates, the V3*d* orbitals split into two states; the lower t_{2g} state and the e_g state that is higher in energy but unoccupied. The t_{2g} multiplet state degenerates further into an α_{1g} (d_{II}) state and an e^{π}_{g} (π^*) (d_{π}) doublet: the e_g^{π}, and e_g^{σ}. The distance between the α_{1g} (d_{II}) state and e^{π}_{g} (π^*) doublet is small so they are considered as overlapping. In monoclinic phase, the V atoms flip the c axis and tilt forming a V–V dimer configuration. The dimerization results in splitting of α_{1g} (d_{II}) state in lower bonding energy state and in antibonding energy state under and above the Fermi energy. The V_d-O_p antibonding e_g^{π} states bounce slightly at higher energies and yield the tilting. A band gap between α_{1g} (d_{II}) orbital and e_g^{π} appears, equal to 1.1 eV also called Peierls band gap in honor of Peierls, the founder of this theory **(Figure 4.12)**. Finally, the opening of the gap and tilting deteriorate the elasticity of the lattice resulting in lattice distortion. The total electronic energy is reduced since it is depleted for the band opening.

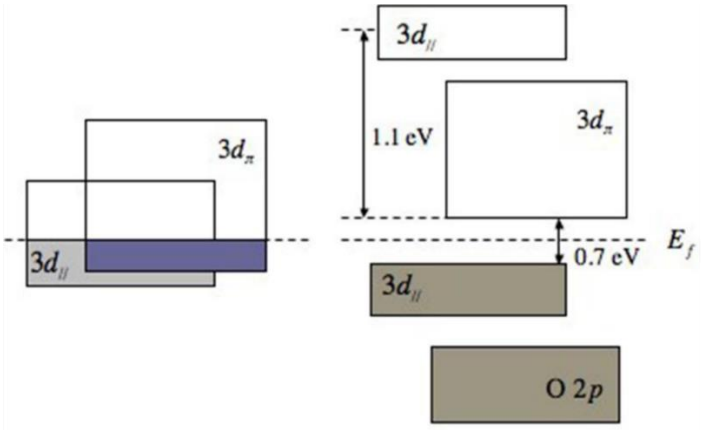

Figure 4.12: Band structures of high temperature rutile-tetragonal phase (left) and low temperature monoclinic phase (right) [28].

This electron–lattice correlation theory is in good agreement with that of Goodenough [29], which also associates orbital and molecular interactions. The validity of the theory is confirmed by Wentzcovitch as well, who has calculated theoretically the proposed model [30]. In any case, neither Goodenough or Peierls theories explain the 0.7 eV electronic band gap.

Mott-Hubbard's theory, the second most popular theory, attempts to explain the wider 0.7 eV electronic band opposed to the narrowest traditional one by an extra energy, the Hubbard (U) energy calculated and confirmed by two techniques (LDA=Local Density Approximations and U) [27]. Moreover, opposed to Peierls theory, the mechanism of Mott-Hubbard stands capable to explain the intermediate metastable phases (M_2, M_3, Triclinic) intervening during the Insulator to Metal (IMT) transition.

Other approaches connect anharmonic phonon vibrations [31] and strong Coulomb forces [32] between V and O atoms to assign the SMT behavior.

However, the fundamentals of the exact switching nature are not yet fully clarified. The intrinsic properties of VO_2 are still under active investigation intertwining more adapted calculations and sophisticated observation techniques.

4.2.4 VO_2 phase diagram

Vanadium as a multivalent metal can form various oxides when mixed with oxygen. Apart from V_3O_5, V_2O_3 and V_2O_5, which also exhibit thermally activated phase transitions at different temperatures seen on **Figure 4.13**, other combinations are possible when subjected to the general stoichiometric formula:

$$V_nO_{2n-1}=V_2O_3 + (n-2)\ VO_2,\ (3\leq n\leq 9)$$

The equation gives all the Magneli phases and is valid for other metals with multiple valence states too.

Summarizing the stoichiometric phases in a phase diagram **(Figure 4.13)**, Vanadium oxides are reported to possess about 52 stable and metastable phases. Besides V_7O_{13} all compounds undergo a SMT at different temperatures.

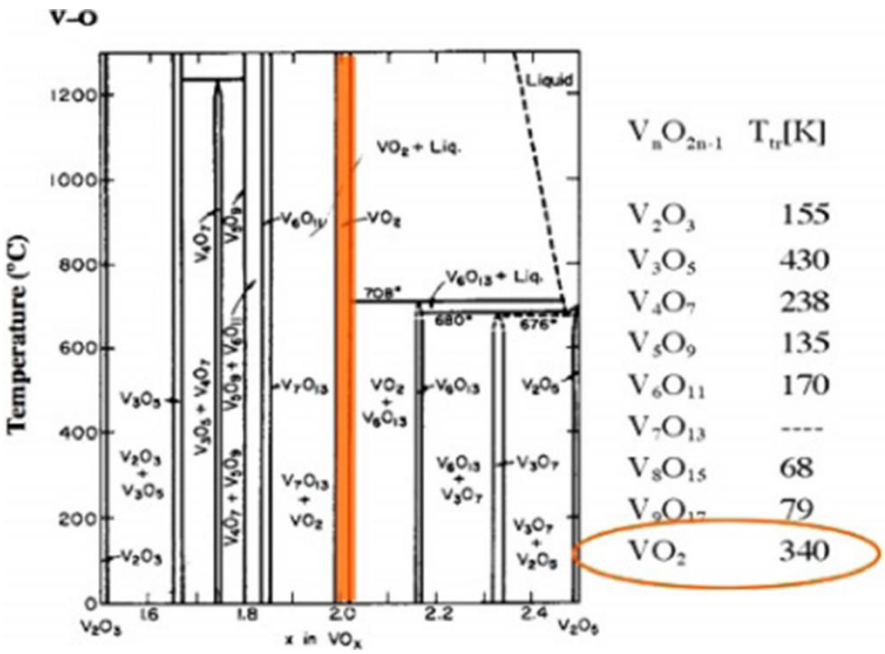

Figure 4.13: Phase diagram of VO_2 and transition temperature of the most encountered compounds [33].

4.2.5 General review in VO_2 thin film formation

As one can see from the diagram in Figure 4.13, all the phases of the vanadium oxides are close, thus obtaining a pure phase seems difficult. A small excess of oxygen can easily lead to metastable transitional phases.

Due to its delicate stoichiometry, the synthesis of pure VO_2 thin films and control of semiconductor-to-metal (SMT) characteristics is a complex and multi-parametric problem that many scientific groups have tried to approach. As reported, in addition to the precise set of deposition and post-treatment parameters that will be discussed in **Sections 4.3** and **4.4**, a good substrate selection is also required. These parameters will determine the film thickness, the grain size and interfacial strain that will affect the SMT behavior [34–37].

Focusing on the suitability of substrates, a large number of groups dealing mainly with smart window applications are interested in the performance enhancement of VO_2 on silicon oxide and quartz substrates.

In 2017, Zhang *et al.* have grown VO_2 films with different thicknesses on quartz substrate by radio frequency RF plasma assisted oxide molecular beam epitaxy [38]. They have stated a remarkable reversible SMT switch with an abrupt change in both electrical resistivity and optical IR transmittance.

Similar studies have been conducted and showed that the characteristics of the phase transition are closely related to the nature of the deposited material, especially in terms of grain size and defects. Small particle size usually leads to a larger hysteresis width thanks to the small density of nucleating defects [39]. Goodenough *et al.* reported that oxygen vacancies in thin films might reduce the transition temperature due to extra free electrons [29]. Tailoring such characteristics, Liu *et al.* found a strong correlation between the particle size and the annealing time and temperature. By increasing the annealing temperature from 450 °C to 650 °C, the film undergoes from an amorphous state to a very large grain size profile, with the best crystallinity with fine, compact particles, being obtained with annealing at 550 °C for 30 min [40].

Surface morphology (roughness, defects), epitaxial lattice match, grain size and nature of grain boundaries can strongly influence the SMT transition [41]. In particular, T_0 (phase transition temperature), ΔT (SMT sharpness) and ΔA (SMT amplitude) can be modified from those of monocrystalline bulk vanadium dioxide when controlling the microcrystalline nature of the films [42–45].

Further research was performed on multiple deposition processes (Radio frequency magnetron sputtering, electron beam evaporation and Pulsed Laser Deposition-PLD) in a variety of substrates (Si, glass and Sapphire) and examined their phase transition [46]. The main conclusion was that films deposited by RF magnetron sputtering conserve the same structure on glass, silicon and sapphire and remain stable for 90 min of annealing. However, for PLD deposition and e-beam evaporation there is a strong correlation between deposition conditions and substrate type that influences the switching contrast.

In the following sections, two popular Physical Vapor Deposition (PVD) methods, the PLD **(Section 4.3)** and Magnetron Sputtering technique **(Section 4.4)**, will be examined and compared for a more appropriate VO_2 film synthesis.

4.3 Pulsed Laser Deposition (PLD)

4.3.1 Principle of PLD

The PLD method is a film growth method in which a high-power laser beam evaporates a material of a well-defined composition. The technique first appeared in the late 1970s when Smith and A.F. Turner [47] used a ruby laser to fabricate dielectric and semiconductor optical thin films. Since then, the versatility of PLD deposition has been further enhanced by the idea of placing the energy source outside the chamber. By tuning the laser energy, the energy of the particles of the material can be adjusted to form thin films with controlled properties [48].

According to this principle, the coordinated laser pulses with the desired parameters exit the external laser source, propagate through the optical window of a chamber and hit the target inside it. The film growth process may take place in vacuum or in the presence of an inert or reactive gas. The latter usually employs gases like H_2, N_2, O_2 or CH_4 that react with metallic compounds and produce hydrides, nitrides, oxides or carbides [49–52]. A short time after striking the target material surface, the ejected particles under the form of a plasma plume (a mixture of atoms and ions) impinge and condensate on the substrate, which lies in front of the target **(Figure 4.14)**.

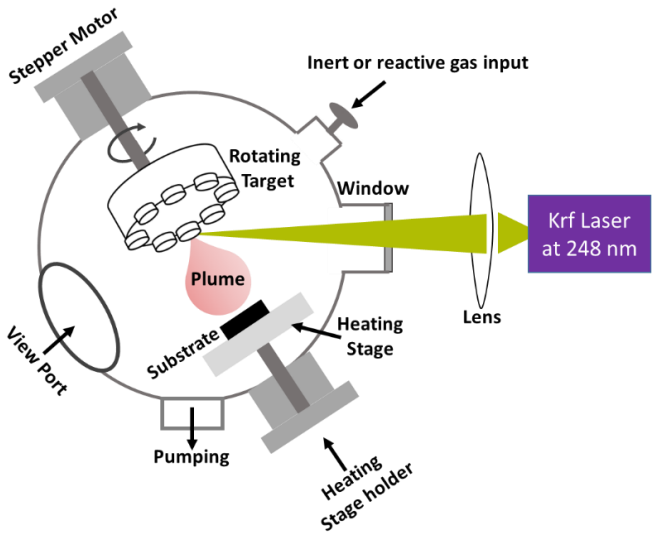

Figure 4.14: A schematic of the PLD setup.

Plasma production requires a minimum power density, which depends on the laser parameters (laser wavelength, pulse duration), the type and morphology of the material. Depending on the gas in the chamber, different colors emerge in the plasma plume. The recombination of ionized atoms and free electrons or excitation and de-excitation of electrons from a higher to a lower energy state induce the emission of the photons with characteristic spectra that make the plasma glow **(Figure 4.15)**.

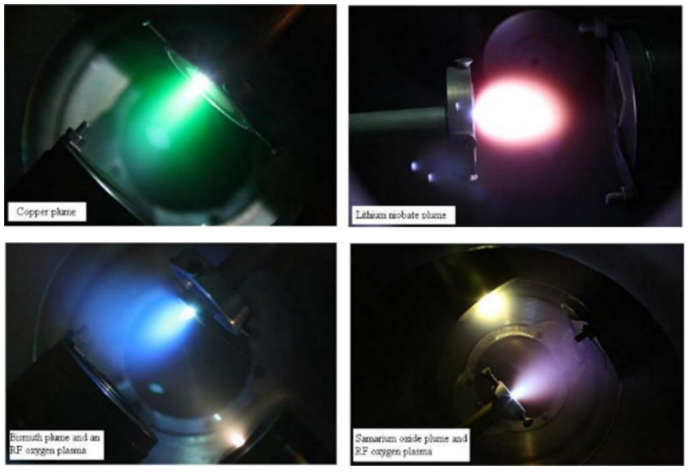

Figure 4.15: Plasma plumes by gas assisted PLD in the chamber [53].

The intrinsic physical mechanism behind the PLD process starts with the absorption of the electromagnetic energy of photons that is consumed by electrons excitation and energy transfer to the lattice of the material [54]. To begin the ablation process, the optical absorption

coefficient of the target material should be high enough at the specific laser wavelength to allow vaporization of the surface region. The resultant plasma will be then able to propagate towards the substrate and condense to form thin films. Analyzing further this seemingly simple process, the PLD process goes through different intermediate phases with subsequent energy conversions to thermal, chemical or mechanical that can produce evaporation, ablation, plasma generation and sometimes exfoliation [55].

Using either a femtosecond or nanosecond laser, the PLD technique can generally be characterized as a non-thermal deposition process. The ablated species can reach a high kinetic energy (up to the KeV) which allows the deposition at relatively low substrate temperatures.

4.3.2 Review on PLD-VO_2 synthesis

Numerous scientific groups have attempted to apply the PLD method to deposit Vanadium Oxide thin films.

Borek *et al.* were the first to use a KrF pulsed excimer laser at 248 nm and a vanadium metallic target in ambient O_2 to deposit on a heated (~500 °C) R-Cut Sapphire Substrates [56]. They showed that the partial oxygen pressure conditions in the chamber could alter the stoichiometry of V_xO_y that undergoes almost 13 metastable phases ranging from V_4O to V_2O_5. To obtain VO_2 films an Ar and O_2 (10:1) atmosphere of 100-200 mTorr was kept in the chamber during deposition by PLD and the films were thermally annealed for 1 hour under high pressures and temperatures (~500 °C).

Bhardwaj *et al.* also investigated the importance of the oxygen pressure during one-step deposition of vanadium oxide by vanadium metal ablation and found that a too low pressure leads to the fabrication of V_2O_3, while $P(O_2)$>25 mTorr results in V_2O_5 [57].

Bukhari *et al.* highlighted in turn the importance of variable flow rates while keeping a background pressure constant at P_{O2}~50 mTorr. He observed that flow rates from 5 to 30 sccm lead to V_xO_y that exhibit steady transition with narrow hysteresis width and low transition temperature. Lower values than 5 sccm lead to V_xO_y with no transition, whereas flows higher than 30 sccm promote V_xO_y with large transition, wide hysteresis loop and transition temperature that shift to longer IR wavelengths [58].

Lee *et al.* demonstrated that a well-controlled oxidizing atmosphere is able to reduce the resistivity ratio between the insulating and conductive phases by one order of magnitude in vanadium oxide thin films [59].

Testing the effect of heating, Kim and Kwok attempted the growth of VO_2 films on sapphire substrates at elevated temperatures during the deposition but without further annealing [60]. On the contrary, another group experimenting with the absence of annealing, has demonstrated a phase transition of VO_2 films prepared only by setting the density of the incident laser beam on the target at ≈1.3 J/cm^2 but without heating the substrate holder [61].

Pauli *et al.* performing synchrotron-based X-ray diffraction during the VO_2 film synthesis by N_2O reactive gas ablation showed that the crystallization of films is highly dependent on the substrates. This relation is clearly defined after annealing in an O_2 environment where the real morphology of the films is revealed [62].

Soon after, Suh *et al.* observed the effect of nucleation when VO_2 films are grown by PLD technique. Studying the hysteresis curve, they have connected the width and shape with the competition between grain size and crystallinity [63].

The substrate compatibility in agreement with PLD deposition has also concerned numerous groups. The silicon substrate [64], the quartz substrate [65] and other wafers [66,67] were evaluated to be fine or poor hosts for VO_2 regarding the optimal epitaxial arrangement.

Overall, achieving the fabrication of high quality VO_2 films (phase stability, good optical and electrical properties..) using ablation techniques still remains an engineering challenge and a topic of research [33, 63–65].

4.3.3 Advantages and Drawbacks of PLD technique

When dealing with thin film formation, the PLD method offers many advantages. Firstly, the location of the energy source outside the vacuum chamber offers flexibility on laser manipulation; setting the laser parameters appropriately, an easy control of film growth is feasible. Moreover, the low temperature deposition provided by PLD favors especially chemical active materials with high temperature sensitivity. The PLD technique was also proved apt to transfer complex oxides while maintaining the stoichiometry and integrity of the target material properties. Any compound material can be ablated rapidly and cost effectively as well as composite thin film formation can be attained by multiple target ablation. Finally, the surface mobility is enhanced compared to the bulk one due to the adapted kinetic energies of the ablated species that does not cause bulk displacements.

On the other hand, the PLD - like every method - presents some fundamental drawbacks. Using highly energetic species can create crystallographic defects in the deposited film. In addition, a

wide range of compounds (clusters, particulates and molten globules) can be ablated simultaneously leading to complex deposition [71]. Finally, possible unequal distribution of flux and angular energy can cause high inhomogeneity of the plasma plume.

To overcome or at least attenuate some of the above drawbacks, the easy manipulation of the laser parameters in the vacuum chamber is judicious.

As some authors report [72–74] fluence, pulse-duration, wavelength, repetition rate as well as distance between target-substrate and substrate temperature can determine the quality of the deposited film. Amorphous, single crystals or polycrystalline films can be obtained by tuning the substrate temperature and pressure in the chamber [75].

4.3.4 PLD experimental process

In this section, we demonstrate a protocol to fabricate VO_x films on different substrates with PLD and Rapid Thermal Annealing (RTA). The challenge in this investigation is to decrease as much as possible the annealing temperature. The characterization techniques at our disposal allowed to partially identify the nature of the VO_x films. Raman and IR spectroscopic observations revealed the synthesis of VO_2-like films with characteristic spectra peaks and films with a MIT transition at ~68 °C.

4.3.4.1 Substrates pre-treatment

Prior to deposition, the Si, SiO_2 and Quartz substrates undergo a three-step cleaning process of successive immersion into three ultrasonic baths of acetone, ethanol and pure water for 10, 10 and 5 min respectively. At the end of the process, the substrates are dried with nitrogen.

Next, TiO_2 solgel (the synthesis protocol is described in detail in 2nd chapter) is spin-coated on some of 2 inches SiO_2 substrates at 3000 rpm for 1min and post annealed at 500 °C during 3 hours in order to reach a thickness of $d_1 \sim 70$ nm in anatase (A) phase.

4.3.4.2 Material synthesis by PLD technique

To ablate and grow VO_x thin films on a variety of substrates, the PLD method is employed. The PLD chamber was evacuated to a background pressure of 1.8×10^{-5} Pa. Pure Vanadium metal target was ablated with a 248 nm KrF excimer laser with 20 ns pulse width and 117 mJ pulse energy at a laser fluence of 5 J/cm^2. The repetition rate was set to 10 Hz. The target-substrate distance was fixed at 5 cm and the substrate was maintained at room temperature (no heating during the process). The oxygen pressure was varied from 0.1 to 30 Pa inside the deposition chamber. The laser beam was at 45° incidence on the target, which was rotated during the

deposition process for uniform ablation on the target surface. The average deposition rate was measured using profilometry for the various deposition pressures. Up to a 3 Pa oxygen pressure, the deposition rate is steady at around 3 nm/minute, slightly decreasing for higher pressures. The deposition time was then adjusted to obtain 25 nm thin films with a deposition rate at around 3 nm/min.

A post Rapid Thermal Annealing (RTA) with a special thermal susceptor is then applied to crystallize the vanadium oxide.

4.3.4.3 RTA (Rapid Thermal Annealing) process

Rapid Thermal Annealing is a fast wafer heating and cooling process in a chamber hermetically closed and temperature-controlled. Thanks to its high heating and cooling speeds, the RTA is cost effective and particularly preferable against typical furnaces. It plays a critical role in thin films since it affects drastically structural and electrical properties [76–78].

The RTA oven in Laboratory Hubert Curien can use a variety of gases ((N_2), oxide (O_2), oxynitride (N_2O)) and low vacuum to interact with the wafers. A series of halogen lamps induce IR radiation and heat the substrate that is placed in a SiC susceptor. A special optic pyrometer calibrated by a thermocouple is used to measure the temperature at the near proximity of the susceptor. The optic pyrometer receives the emitted thermal radiation by the black body (susceptor) at a distance and converts it into an electrical signal. The overall heating temperatures of the system can range from 150 °C to 1100 °C. To complete the process, a natural cooling is used to quench the temperature in the chamber and chill the substrate. The total dwell time takes several minutes or less.

All the above parameters (pressure, selection and debit of gas, heating and cooling temperature, dwell time...) can be set in a recipe and controlled by the dedicated computer program (Annealsys).

Rapid Thermal Annealing (RTA) was performed on the as-grown films. The annealing temperatures were measured on the backside of the SiC susceptor. The annealing chamber was evacuated to a 5 Pa pressure before oxygen insertion. The VO_x films were annealed in various oxygen partial pressures from 20 to 500 Pa with a 50-sccm flow, as well as in 5 Pa low-vacuum. The heating rate was fixed at 5 °C/s and the cooling rate was kept to 5 °C/s or natural rate. The maximum temperature was varied between 300 °C and 500 °C, with a 5 minutes plateau for temperatures below 350 °C and 2 minutes for temperatures higher than 400 °C.

4.3.5 Parametric study of the thermal switch

4.3.5.1 Optical Characterization setup

To measure the optical performance of the VO_2 layers, an optical transmission spectroscopy setup was used. The sample was placed on a metal plate, which in turn was connected to a temperature controller by a thermocouple. Through Joule heating, the sample could reach the setpoint temperature indicated to the controller. A halogen source illuminated the sample and the NIR detector recorded the transmitted optical spectra at both room and high temperature **(Figure 4.16)**. Many samples with different deposition parameters were tested in this way.

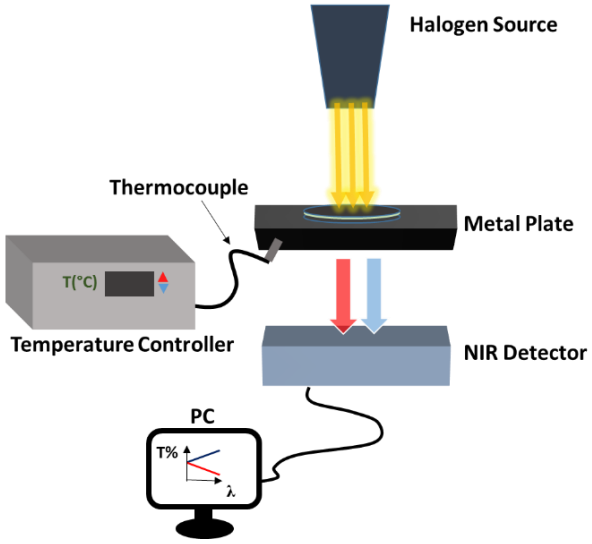

Figure 4.16: Schematic of the setup for characterization in transmittance.

4.3.5.2 Deposition pressure and annealing pressure parameters

The effects of the pressure during PLD and pressure during RTA are illustrated in **Figure 4.17**. The films have been deposited and grown on fused silica at either 0.3 or 3 Pa oxygen partial pressure, and annealed at 450 °C for 2 min at 100 or 500 Pa oxygen partial pressure. The film's transmittance is studied by infrared spectroscopy at two temperatures well beyond and above the standard transition temperature (25 °C and 100 °C in order to ensure a full phase transition of the material).

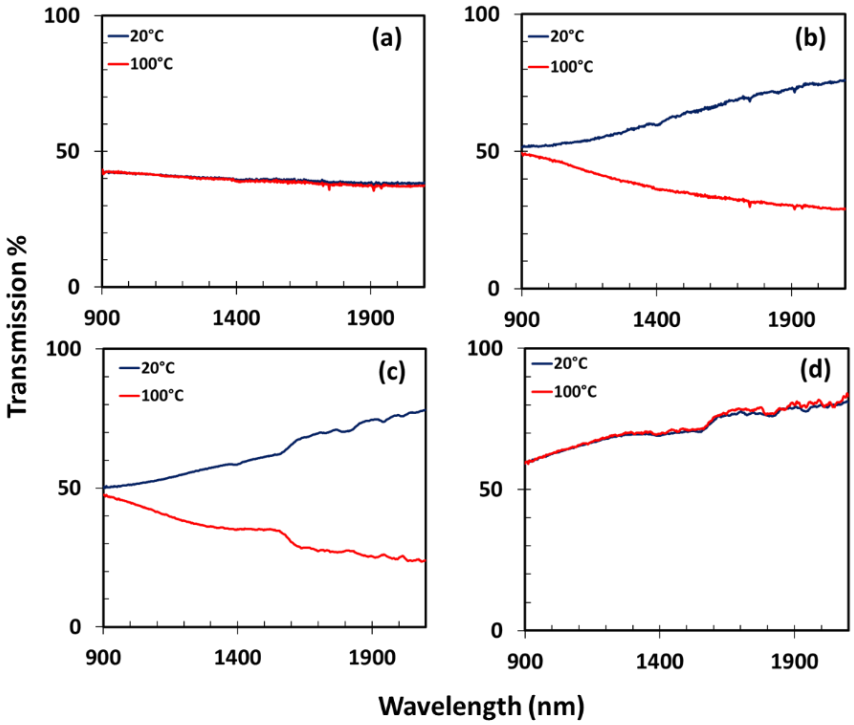

Figure 4.17: Infrared transmittance spectra of vanadium oxide thin films on fused silica substrates recorded at two temperatures for different deposition (P_1) and annealing (P_2) oxygen pressures. (a) P_1 = 0.3 Pa and P_2 = 100 Pa, (b) P_1 = 0.3 Pa and P_2 = 500 Pa, (c) P_1 = 3 Pa and P_2 = 100 Pa and (d) P_1 = 3 Pa and P_2 = 500 Pa.

The film deposited at 3 Pa and annealed at 500 Pa remains transparent, which could indicate that the film was turned into vanadium pentoxide [79], or at least that no rutile or monoclinic phase was obtained during crystallization. On the opposite, the film deposited at 0.3 Pa and annealed at 100 Pa seems to remain conductive. This could mean that the oxygen content was not sufficient to obtain the right stoichiometry, producing a V_2O_3 like film [80].

Good deposition and annealing conditions therefore require oxygen to be available in the ambient atmosphere for the thin films to crystallize in the rutile VO_2 phase. Considering all the observed behaviors, a good compromise between the two processes is mandatory since the oxidizing pressure acts like an “all or nothing” parameter for the synthesis.

The oxygen pressure is therefore kept for PLD at 3 Pa and for RTA annealing at 100 Pa. These conditions satisfy the exigence of a very reliable process for producing phase change material.

4.3.5.3 Annealing Temperature and substrate Influence on Transmittance

The influence of the annealing temperature on the transmission spectra of vanadium oxide deposited on silicium, quartz, fused silica and titanium dioxide thin films was demonstrated. As observed in **Figure 4.18,** when modifying the annealing temperature and the substrate we can induce different transition parameters changes.

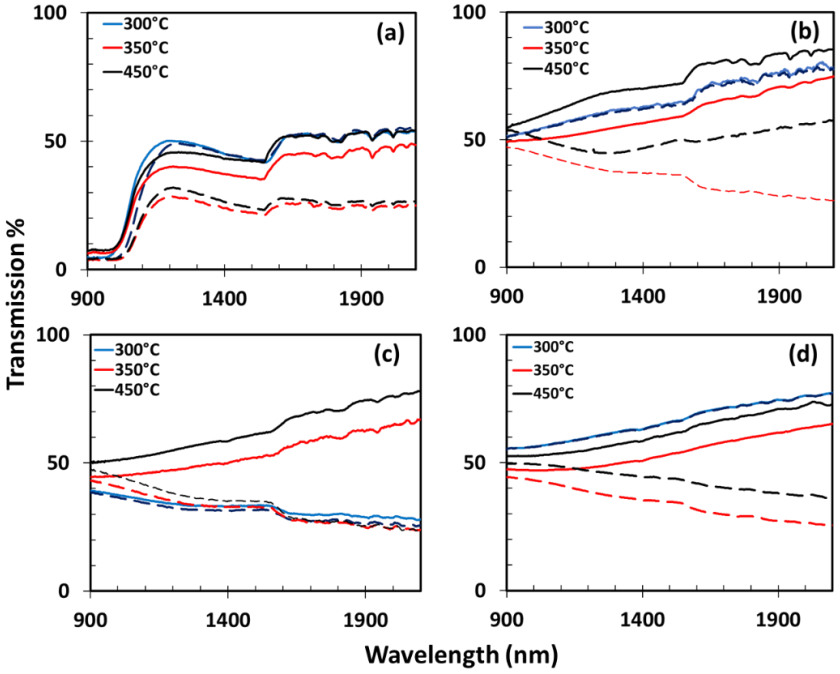

Figure 4.18: Optical transmittance spectra in the spectral range 900 nm-2000 nm recorded at two different temperature: ambient temperature (plain line) and 100 °C (dashed line) of VOx annealed at different temperatures on various substrates: Si (a), Quartz (b), SiO_2 (c), SiO_2-TiO_2 (d).

For all the tested substrates, the minimum annealing temperature leading to a phase change material was recorded at 350 °C.

Whatever the substrate, thin films annealed at the lowest temperature of 300 °C do not exhibit any phase transition. The films deposited on titanium dioxide, silicon and quartz appear “locked” in the insulating phase, with both high and low temperature spectra appearing similar to those of transitioning films measured at room temperature. Conversely, the film deposited on fused silica (SiO_2) has a transmission similar to those of phase change samples recorded at high temperature. This could be linked to the amorphous character of the substrate leading to a different epitaxial growth during deposition when compared to the other monocrystalline substrates.

In any case, once RTA temperatures above 350 °C are used, phase transitions are observed on the four substrates.

When comparing the transmittance spectra recorded at room temperature for the samples annealed at 350° C or 450° C, best transmission response appears when using the highest annealing temperature. Results with annealing at 500° C are not presented here, since they are quite similar to those recorded at 450 ° C. These results demonstrate the ability of annealing at 350° C and to produce vanadium oxide films with phase transition, although this low temperature does not eliminate all defects in the crystal lattice of the deposited vanadium oxide, making these thin films less transparent in ambient temperature than monocrystalline VO_2. Conversely, considering the inherent roughness created by PLD on a sample as thin as 25 nm and the inherent absorption of monoclinic VO_2, the transmission achieved after RTA at 450 °C is quite satisfying, reaching 75-80% at the wavelength of 2 µm.

Generally, all samples whether annealed at 350° C or 450° C exhibit good transition properties in the mid-IR range. The maximum absorption of the sample measured at 100° C appears limited by the 25 nm thickness of the films. A very good contrast between the insulating and conductive phase can be achieved in the mid IR region, on both crystalline and amorphous substrates with a very short annealing time, and a quite low annealing temperature. The low RTA temperature heating process shows the ability of VO_2 to operate easily when processing standard amorphous glasses with low melting point.

4.3.5.4 Annealing Temperature and Substrate Influence on Hysteresis

Apart from the easily observable ΔT in **Figure 4.18**, it is also useful to examine the other transition parameters: the T_0 phase transition temperature and ΔA (SMT amplitude). The hysteresis loops provide such information. The results are presented at a wavelength of 1500 nm, and were recorded while slowly heating (up to 100° C) or cooling (down to ambient temperature) the substrate holder, performing few minutes steps for each measurement. **Figure 4.19** presents clearly the transmission shift ΔT, hysteresis width ΔA and T_0 phase transition temperature. The ΔA is calculated by the FWHM of the T_0 central value.

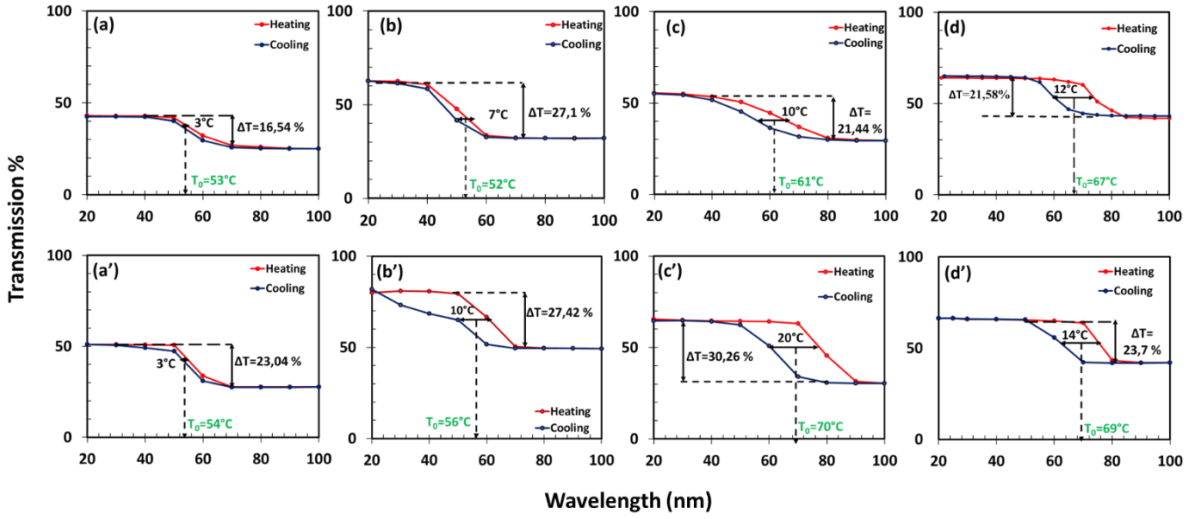

Figure 4.19: Transmission measured at a wavelength of 1500 nm as function of the temperature for vanadium oxide films deposited on various substrates (from left to right: Si, Quartz, SiO_2, SiO_2-TiO_2) and rapidly annealed at 350 ° C (a), (b), (c), (d) and 450 ° C (a′), (b′), (c′), (d′). Measurements were performed while heating and cooling the substrate, showing hysteresis parameters of the films.

As already shown in **Figure 4.18,** all films that are rapidly annealed at 350 °C exhibit a smaller shift in optical transmittance than films annealed at a higher temperature. Worth noting that decreasing the annealing temperature we obtain smaller transition temperature, although the effect is highly dependent on the substrate. While the transition temperature for both silicon and titanium dioxide substrates is only slightly decreased, in the case of quartz and fused silica, the transition temperature is reduced by 4 °C and 10 °C respectively. This means that the choice of RTA parameters can be helpful to finely tune the transition temperature of VO_2 synthesized on those substrate materials.

It has been shown in the literature that the reduction of the critical temperature T_0 could be attributed to the oxygen vacancies at the boundaries of the particles that induce weak hybridization between V 3d and O 2p orbitals [78, 79]. Therefore, the smaller the particles size the more space for oxygen to diffuse. This may explain some of our observations, as the lower annealing temperature yields smaller grained-VO_2 films.

Phase transition temperatures as low as ~ 52 °C are reached for both monocrystalline substrates (silicon and quartz), corresponding to 15 °C below the bulk VO_2 transition temperature. In the case of amorphous fused silica, the phase transition temperature reaches 61°C, which is promising in the search of ways to decrease the switching temperature for smart windows applications.

The low value of annealing temperatures also helps to produce lower hysteresis width of transition for all substrates used, except silicon where it remains unchanged. The change is particularly visible on fused silica, where the hysteresis width drops from 20 °C to 10 °C. An unconventional result is observed with quartz substrate, for which an annealing temperature at 450 °C leads to a peculiar hysteresis curve, with a second transition temperature as a shoulder in the transmission curve during cooling down. This generally reveals inhomogeneities in the nanostructure of the film's grains. This phenomenon is not observed when annealing is performed at 350 °C, yielding a much sharper hysteresis.

The ability to narrow the hysteresis is a key point to address several targeted applications, such as antennas with tunable reception-emission instantaneous functionalities [83], reconfigurable RF and microwave electronics (variable capacitors-varactors, variable inductors, variable resistors-varistors) [84], and recently for two level quantum electric and magnetic dipole emitters [85].

These results demonstrate that very thin 25 nm VO_2 films can be synthesized using PLD and RTA on various substrates with a maximum temperature as low as 350 °C, which may allow to reach numerous kinds of glasses with melting point close to or lower than the usual 550 °C synthesis temperature, especially considering the very small heat exposure durations employed here. Additionally, moving around the various synthesis parameters, in particular annealing temperature, several parameters of the phase transition can be impacted and controlled.

4.3.6 Characterization of the VO_2 layer

4.3.6.1 Microstructural Raman characterization

The Raman spectroscopy is a common characterization technique intended to identify the molecular vibrational modes through the crystal phase of a sample without any degradation. When incident light from a laser source (UV, visible or IR) is scattered by a sample at the same wavelength as the laser source (Rayleigh diffusion), no useful information about its structure is gained. Nevertheless, there is a small amount of light scattered over different wavelengths due to the interaction of the incident photons with the materials phonons (molecular vibrations). This diffusion is inelastic, known also as Raman Scattering, and is associated to the chemical structure of the analyzed sample. The gain (Anti Stokes Raman) or loss of energy (Stokes Raman) of the inelastic emitted photons compared to the incident ones is translated on the Raman spectra by a displacement in frequency (ν_0 - $\nu_{inelastic}$). Finally, the observed Raman

spectra exhibits a number of peaks at different wavelengths corresponding to the material specific bond vibrations.

In our study, Raman characterization analysis is also realized for a better insight of the films quality as deposited and after 350 °C annealing. A Raman (Labram Aramis) spectrometer is used to record the spectra excited by a Helium Neon λ= 632.8 nm laser illumination as the laser beam was focused on the surface of the sample by a (x100) microscope objective **(Figure 4.20)**. No spectra could be recorded on the sample grown on a silicon substrate, as the very strong response of the substrate at those wavenumbers did not allow the observation of any other peaks.

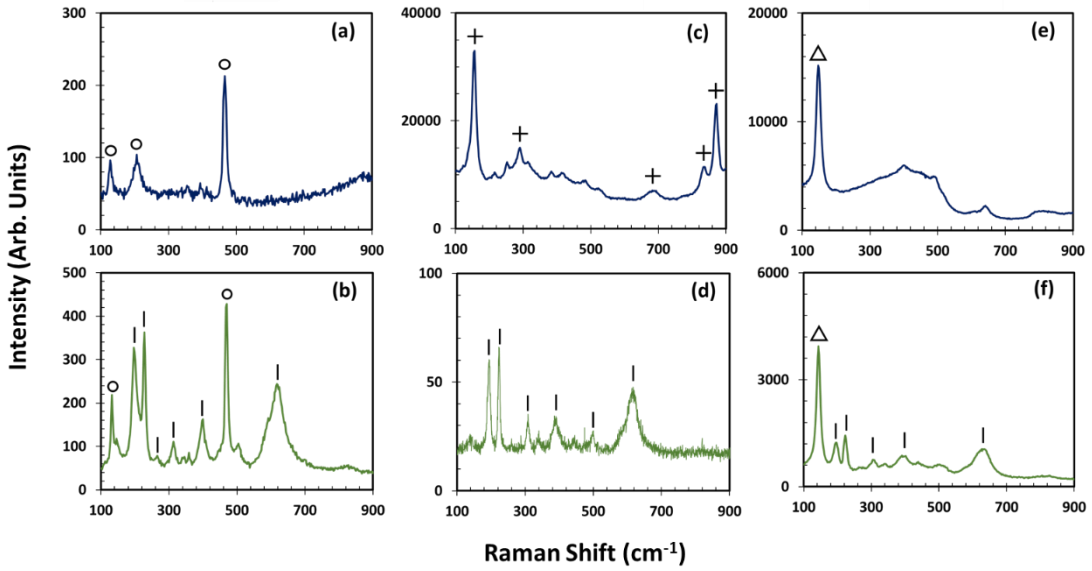

Figure 4.20: Raman spectra of vanadium oxide thin films deposited on various substrates from left to right -Quartz, SiO_2, SiO_2-TiO_2 - recorded at ambient temperature prior to (a, b, c) and after annealing (a′, b′, c′) at 350 °C. The circles, crosses and triangles indicate the peaks of the corresponding substrates while vertical lines exhibit the VO_2 peaks.

All spectra recorded for films grown on quartz, fused silica and titanium dioxide with rapid thermal annealing at 350 °C exhibit essentially the same features, typical of monoclinic VO_2 spectrum. Indeed, Zhang *et al.* report very similar peak positions to those seen here when growing vanadium dioxide on quartz with different temperatures [86], while Li *et al.* have comparable spectra on growing VO_2 coatings on TiO_2 (A) [87]. These are good indications that the vast majority of vanadium oxide in the film is in the monoclinic VO_2 phase, both asserting that the proper stoichiometry and crystallography are achieved, as peaks attributed to V_2O_3 or V_2O_5, or other VO_2 phase cannot be observed. The relatively low transmission obtained when

annealing at 350 °C may then be correlated to grain size and boundaries issues in the thin film rather than the existence of multiple phases.

It is worth noting that the excitation laser was kept at low power to record spectra without triggering a phase shift of the V_xO_y to the rutile phase. However, by intentionally raising the laser power, we could reliably observe the spectra to be converted into a continuous signal for the phase transition material, which should correspond to the metal rutile phase response.

The spectra recorded on the as-deposited thin films show a huge difference depending on the kind of substrates used. Both on quartz and titanium dioxide, no peaks outside of those associated to the substrate can be seen, suggesting that the vanadium oxide does not exhibit any Raman response, which could correspond to an amorphous state of the film. Films deposited on fused silica show a Raman response, which has been attributed in the literature to V_2O_3 [88] or V_7O_{16} [92, 93], the latter being very close to VO_2 in terms of stoichiometry. This crystalline phase appearing only on the amorphous substrate, confirms the effect of the substrate (crystallinity) on the thin film epitaxy and may explain the low transmission of thin films specifically deposited in fused silica and annealed at 300 °C as observed in **Figure 4.18.**

4.3.6.2 AFM (Atomic Force Microscopy) characterization

A noninvasive tapping mode is employed to detect the topography of a thin film deposited on silicon and annealed at 350 °C (**Figure 4.21)**. A general perception of the VO_2 film roughness is taken by the Gwyddion program that indicated the RMS roughness in the order of few nanometers (~ 7 nm), with the presence of particles on the films surface with diameters in the range of few tens of nanometers, as can be expected from the PLD technique.

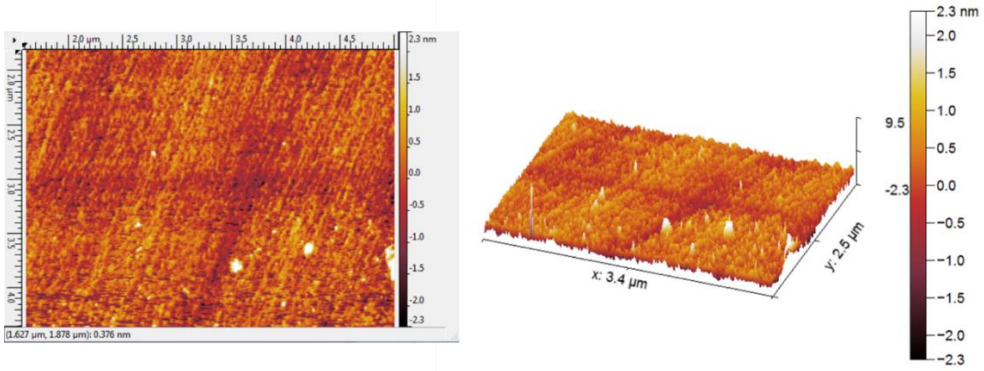

Figure 4.21: AFM images of a vanadium oxide thin film deposited on silicon and annealed at 350 °C.

4.3.6.3 SEM (Scanning Electron Microscopy)

The VO_2 thin films are scanned in environmental conditions with the presence of Helix detector. SEM cross-sectional measurements confirmed the profilometry measurements of a 25 nm thick film **(Figure 4.22-a)**. The film appeared to have a good and homogeneous coverage of the substrate, exhibiting small roughness in the few nanometers range. However, no useful surface diagnosis is gained by the SEM. Even if the mode is selected intentionally to attenuate the discharging of the surface, opposite effect is observed causing damages to the surface **(Figure 4.22-b)**.

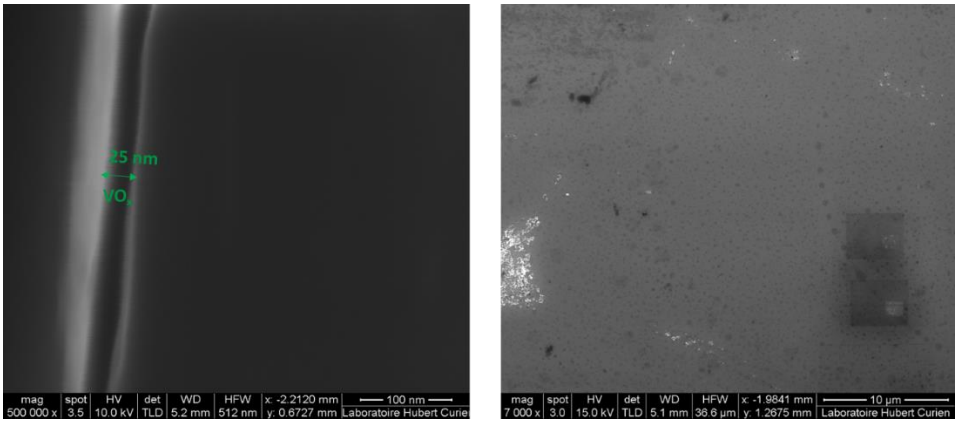

(a) (b)

Figure 4.22: Cross-section (a) and surface scanning (b) image of SEM.

4.4 Magnetron Sputtering

4.4.1 Principle of Magnetron Sputtering

Like PLD, Magnetron sputtering is also a Physical Vapor Deposition (PVD) of thin films but is based on sputtering. The magnetron effect, is discovered by Penning in the late 1930s [91] and developed by Penfold and Thornton in the1970s [92].

In a typical sputtering deposition process, the energetic ions of the generated plasma are accelerated towards the target, striking it and ejecting atoms from the surface. These atoms then move towards the substrate where they are deposited and gradually grow a film.

Magnetron sputtering involves a gaseous plasma, which is confined near the ablation target by a strong magnetic field issued by the target's rear magnets. This results in a high-density plasma with increased deposition rates and minimal damage to the substrate or growing films.

The general sputtering process begins with the evacuation of the chamber and the introduction of the usual working inert gas, the Ar. In the reactive sputtering, common process gases such as O_2 or Nitrogen may be involved, depending on the type of material to be deposited, that are mixed with the initial Ar gas. A negative electrical potential of the order of 1 to 3 kV is applied to the magnetron (target), which is the cathode, and the walls of the reactor are connected to the electrical ground potential, the anode. This cathode electrical potential will cause free electrons to accelerate away from the magnetron, but some of them are likely to be trapped by the magnetic field near the cathode's region. In the simple case of inserting Ar gas into the chamber, these trapped electrons may collide with the gas atom and detach an electron by creating a positively charged process ion gas. Ar^+ ions generated in the discharge accelerate towards the cathode, thus obtaining an energy released during their impact on the surface of the target. This transfer of momentum is capable of knocking off some of the magnetron target materials. These extracted materials form a vapor that will be implanted and condensed on the substrate, located in front of the target **(Figure 4.23)** [93]. The process is repeated in constant rate until the desired thickness is reached. The power is then removed from the cathode.

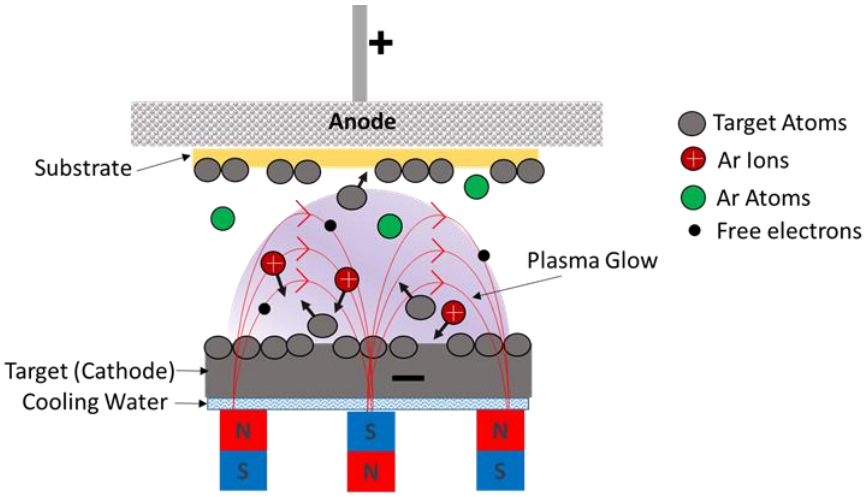

Figure 4.23: Schematic Diagram of Magnetron Sputtering [91].

Depending on the ion's energy, the angle of the impact and the binding energy of the target atoms, the ions will cause different predominant reactions [94] and different sputtering yield.

For ion energy less than 100 eV, direct collision with the target is very unlikely to trigger target atom's ejection. This event could only occur if the target's material has an atomic mass less than that of Ar.

The most common process of sputtering is the collision cascade generated by Ar^+ ions with energies of 100 eV < E <1000 eV. The incident Ar^+ ion transfers momentum to the target atom, which in turn by collision in cascade with neighboring atoms can lead to the removal of a surface target atom. In this energy zone, there is also the possibility of the reflection of the incident ion neutralized by charge transfer or even the excitation of the target atom resulting in the emission of secondary electrons. The latter accelerate away from the target, ionizing neutral gas atoms in order to maintain the plasma **(Figure 4.24-a)**.

For ion energies >2 keV, the ion can be implanted into the target structure with the following cascade collisions and ejection of the target atom **(Figure 4.24-b)**. This violent knock-on sputtering caused by ion implantation may lead to substrate damage.

The light from the plasma is created when the ions recombine with the free electrons into a low energy state due to the excess of voltage. The light is the plasma glow that is observed during processing seen by different colors according to the process gas.

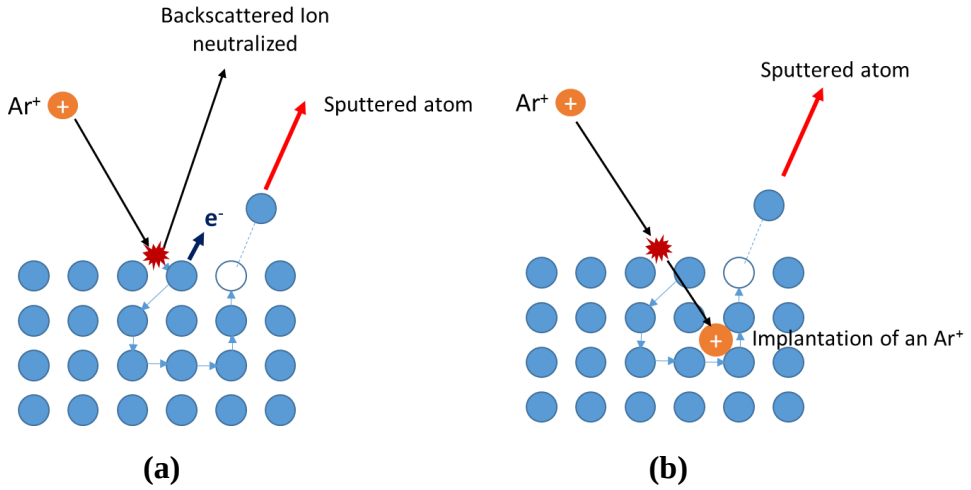

Figure 4.24: Low energy knock-on Ar^+ sputtering (a) and high-energy knock-on sputtering with ion implantation (b) and ejection of target atom by cascade collisions.

Several Magnetron sputtering setups exist differing upon the power delivery system (DC (Direct Current Sputtering Power), RF (Radio Frequency)) and the nature of the deposition process ((Pulsed DC Magnetron Sputtering, HIPIMS (High Power Impulse Magnetron Sputtering)).

DC sputtering is mainly used for the deposition of conductive materials or Transparent Conductive Oxides (TCO's) but not for insulating materials. Indeed some materials possess

high DC impedance and require large amounts of voltage to ignite the plasma that DC fails to give.

RF (Radio Frequency) power, delivered usually at 13.65 MHz, is instead able to change the impedance of these materials. It is AC powered and can be used for both conductive and non-conductive materials. However, RF is slower and more expensive than DC, usually restricted to non-conductive materials [95].

Pulsed DC Magnetron Sputtering is an updated type adaptable to the sputtering deposition of insulating materials without arcing effect. DC magnetron sputtering, usually led to the accumulation of charge and to subsequent formation of arc on the insulating surfaces. During the arcing, the material could evaporate and degrade the deposition quality on the substrates. Pulsed DC magnetron sputtering eliminates this phenomenon by applying pulsing medium frequencies ranging from 10–350 kHz that suppress the formation of arcs [96].

HIPIMS is an enhanced Magnetron Sputtering deposition that increases further the plasma density near the target surface. This is achieved by intense, short pulses that deliver a high-power peak that generates an extremely dense plasma. To prevent the problem of heat excess, a very low duty cycle is used. In a HIPIMs plasma, the sputtered material can be highly ionized and the process is often referred as ionized physical vapor deposition (IPVD). This method offers optimized coverage and conformity of films with lower substrate temperature and reduced film friction [97].

4.4.2 Review on Magnetron sputtering -VO_2 synthesis

In search of better performance, numerous groups have tried to improve the properties of VO_2 films formed by magnetron sputtering.

Testing the substrate compatibility, Yan-Kun Dou *et al*. prepared VO_2 films by DC magnetron sputtering on *a*-plane and *m*-plane sapphire substrates. The films on *a*-plane exhibited equiaxed grains that favored the optical modulation in IR band, while films on *m*-plane sapphire substrates are shown to have stripped grains that benefit the electrical conductivity [98]. Using the same deposition method, Taha *et al.* reported thin VO_2 films with significant optical and electrical transitions indicating a transmittance gap of >60% at 2000 nm and a resistivity switching up to four orders of magnitude respectively, regardless of the nature of the substrate. The effect was reversible and highly repeatable [99].

A pulsed DC magnetron deposition and a post annealing at 500 °C for 20 min under N_2 reactive gas resulted in a higher optical transmittance switching of up to 70% at 2500 nm. The critical transition temperature was lowered to 53 °C [100]. Ho *et al.* used a cost effective V_2O_5 target for RF magnetron sputtering to prepare high quality VO_2 thin films on non-epitaxial Si and Quartz substrates with in-situ annealing at 545 °C with mixed Ar/O_2 gases. The results demonstrated a performant VO_2 thermochromic layer in terms of optical transmittance and resistivity contrast, but also revealed an ease of deposition on large area surfaces [101]. Employing Direct Current magnetron sputtering, Xu *et al.* noticed that annealing in argon rather than vacuum, can lead to a reduction in the grain size of the vanadium particles and thus create more oxygen vacancies ,which are associated with a decrease in the transition temperature [102].

Lin *et al.* synthetized a polycrystalline high quality ultrathin VO_2 on quartz substrate, with a high transmission factor of 54.8 % via high power impulse magnetron sputtering (HiPIMS) [103].

Zhang *et al.* studied the SMT behavior by applying a voltage on Si substrates during VO_2 deposition by DC magnetron sputtering. They observed a decrease in the transition temperature and an increase in the optical efficiency due to the enlarged grain size and the residual stress induced by biasing [104]. VO_2 growth on AZO conductive glass and DC reactive magnetron sputtering exhibited a reduction of the transition temperature to 48 °C with a small hysteresis width of about 2.9 °C when annealed at 300 °C. The influence of annealing is particularly illustrated in SEM images for three films prepared at 250 °C, 300 °C and 350 °C displaying progressive surface smoothening when raising the temperature [105].

Luo *et al.* highlighted the importance of sputtering power on optical and electrical properties of VO_2 thin films. They identified that an applied power on the cathode higher than 350W can bring similar phase change behavior to that of bulk VO_2 [106]. Cheng *et al.* introduced a dual-target magnetron sputtering to fabricate VO_2-SiO_2 composite film on quartz substrate by modifying the Ar/O_2 flow ratio. 50% optical transmittance is obtained at a wavelength of 2 µm [107]. By superposing DC and RF magnetron sputtering, Choi *et al.* deposited high quality VO_2 films by lowering the substrate temperature at 300 °C. Tuning the temperature at low values, they managed to reduce the transition temperature at 59 °C and to narrow the hysteresis loop down to a 3 °C width. The results were exactly comparable with substrate heating at 450 °C and DC magnetron sputtering [108].

4.4.3 Advantages and Drawbacks of Magnetron Sputtering technique

Magnetron sputtering has a low deposition temperature and permits the deposition of a variety of materials with high melting points. It offers strong adhesion of atoms and smoothness mostly for large coating areas. The target can be placed anywhere in the chamber in function of the substrate and coating. Finally, when dealing with alloys or compounds their composition is observed to preserve the same stoichiometric content than the initial of the target material source [109].

On the other hand, according to the principle of the technique, the incident energy of ions on the target can be partially transformed to heat, which must be removed. The installation of cooling systems is not fully efficient if the deposition rates are high. Other restricting parameter concerns the non-homogeneous distribution of ions across the target caused by the collision of electrons conducted by the magnetic field. This may have an impact on the uniformity of the resulting coatings, which is sometimes not high enough even for cathodes of several meters long. This non-uniformity can be limited by using rotating substrates holders, except at the end of long targets where the magnetic field lines are strongly curved. Finally, some materials present low deposition rate rendering the process slow [110].

4.4.4 Magnetron Sputtering experimental process

The next section presents the fabrication process of the triple $Si_3N_4/VO_2/Si_3N_4$ layer elaborated by magnetron sputtering deposition and post annealing. The layer fabrication is exclusively held in HEF Group Company at IREIS site who used Pulsed DC magnetron sputtering as deposition method and a homemade vacuum furnace to anneal thin films. The thicknesses of the fabricated layers were modelled properly to form the Waveguide Resonant Grating (WRG) of our intended application. The bilayer Si_3N_4/VO_2 is compared with the PLD made TiO_2 (A) $/VO_2$ bilayer for the needs of our following study **(See Chapter 5)**.

4.4.4.1 Magnetron Sputtering Deposition

The operational mode set pulse width and frequency at 5μs and 76 KHz respectively. The alimentation at our disposal supplied the cathodes with power. The 1-inch SiO_2 substrates were placed on a pentagonal substrate holder and rotated at 4 rotations/min during the deposition process. Their distance from the target was maintained at 10 cm **(Figure 4.25)**.

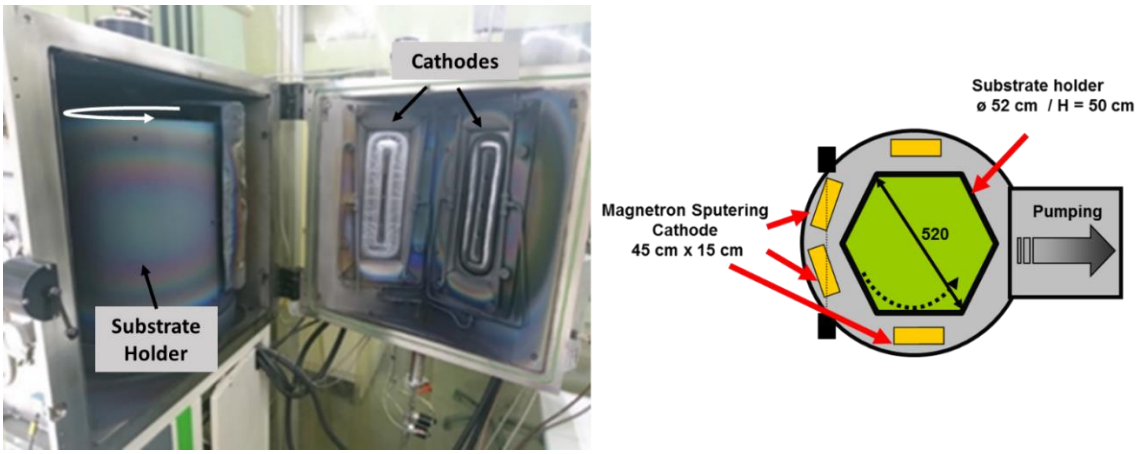

(a) (b)

Figure 4.25: Image (a) and schematic (top view) (b) of the magnetron reactor.

Behind the target, a cooling (20 °C) water system consisting of a membrane conserved the temperature stable along the deposition process and prevented the degradation of the target. The magnetic field issued by the rear magnets (1000 Gauss) of the target kept the pressure at a low level for high speed sputtering. During the deposition, the substrates were heated with a temperature equal to this of a chamber. The substrate temperature (T_s) was controlled by a radiative heater from the front side and was measured before the plasma initialization by a thermocouple. At a fixed temperature in the chamber, we can estimate the T_s measurement to be about $T_{chamber}$ ±5 ° C for all of our depositions. However, the plasma may provide an additional heating by way of ion bombardment, fast neutrals impact and radiation from both the plasma and the target.

The first deposition included a Si_3N_4 composite film on a fused silica substrate. The chamber used a low pressure with a simultaneous heating at 200 °C for evacuating contaminants. When the pressure reached $5x10^{-6}$ mbar ($5x10^{-4}$ Pa) the deposition began. For the Si_3N_4 layer a 5 KW pulsed mode power was employed. The sputtering took place when the ionization of the neutral Argon (working gas) with a debit of 75 sccm was mixed in the chamber with the reactive Azote gas of 100 sccm of debit. The deposition velocity was measured at 4.8 nm/min, thus the 502 nm thickness of our interest lasted ~1h and 44 min.

For the formation of the following VO_2 layer, a vanadium target at 99.9 % purity was employed. As already stated, the creation of VO_2 is very delicate and an excess or deficit of Oxygen may change the stoichiometry. The debit of the introduced oxygen was controlled this time by the light emitted by the plasma and detected by a photo sensor. The Argon flow was set at 400

sccm, the nitrogen was switched off and the light percentage of the oxygen was measured at 10%. The oxygen flow was then regulated to get the right oxidation level. The alimentation provided 5KW of pulsed mode power in the chamber and the deposition rate was 2 nm/min. The duration of our deposit lasted 40 min and yielded a thickness of 80 nm.

Finally, after the post annealing and the crystallization of the bilayer of Si_3N_4 and VO_2 we have separately proceeded at the final layer deposition of Si_3N_4. The conditions of the deposition remained the same as the initial Si_3N_4 layer with ~1h and 31 min process for 435 nm.

4.4.4.2 Post annealing

The annealing of the deposited films is treated by a repurposed vacuum chamber **(Figure 4.26)**. The chamber is evacuated and a neutral Ar gas is inserted as annealing atmosphere.

Figure 4.26: Oven for post-annealing of the deposited films after magnetron sputtering.

For our substrate configuration, the annealing was completed in two consecutive steps. First, the double layer of Si_3N_4 and VO_2 was annealed under reactive oxygen gas with a controlled pressure at a temperature of 550 °C for the crystallization of the VO_2.

The final deposition of Si_3N_4 was treated thermally individually with the same environmental parameters in the chamber and a temperature at 550°C during 60 min.

Indeed, it was observed that a global annealing of the triple layer did not lead to any transition. This is likely expected since a lack of direct annealing of the VO_2 surface does not crystallize the film and no SMT behavior manifests. As the temperature increases, the VO_2 undergoes an amorphous to crystalline phase evidenced by large compact grain sizes.

According to the literature, films prepared by magnetron sputtering on K9 glass substrate are found to have a high quality of crystallization with increasing grain sizes from 49.4 to 77 nm for annealing times ranging from 15 to 90 min [111]. Bigger grain sizes on VO_2 films induce higher efficiency on optical transmittance [112].

4.4.5 Characterization of bilayer Si_3N_4/VO_2

4.4.5.1 Transmission measurements

Before capping the VO_2 film with the subsequent Si_3N_4 layer, the infrared transmission spectroscopy setup **(Figure 4.16)** was used to check the grade and quality of optical commutation. **Figure 4.27** illustrates the hysteresis graph at λ = 1500 nm recorded every 10 °C upon heating the sample up to 100 °C and cooling it down to the ambient temperature. The graph summarizes the transmission shift ΔT, hysteresis width ΔA and T_0 phase transition temperature.

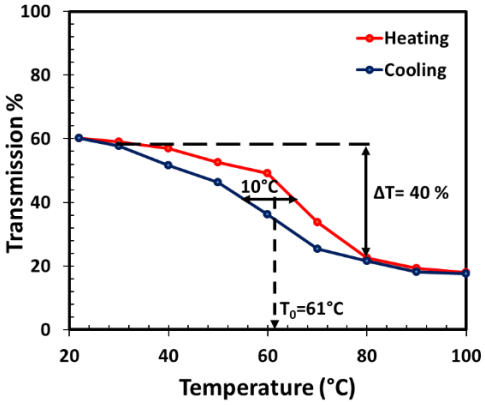

Figure 4.27: Hysteresis curve of the Si_3N_4/VO_2 bilayer at λ=1500 nm.

The magnetron sputtered bilayer reveals 40% transmission shift between hot and cold states and a 10 °C narrow hysteresis width. This may imply a better VO_2 deposition with a finer epitaxial match to the underlying layer compared to the correspondent hysteresis loop of the bilayer TiO_2 (A)/VO_2 when deposited on SiO_2 substrate by PLD **(Figure 4.19-d)**. Principally, smaller hysteresis loops are induced by larger grain sizes. The tested transmittance of the magnetron sputtered bilayer reaches at 60% (similar to that of the VO_2 film fabricated by PLD method) but the transition occurs in lower temperature in the Si_3N_4/VO_2 layer than in the VO_2 PLD film **(Figure 4.19-d)**.

4.4.5.2 AFM characterization

The AFM images treated by Gwyddion can give a hint on the deposition quality through roughness examination and provide information on grain sizes. As illustrated in **Figure 4.28**, the magnetron sputtered VO_2 presents slight greater roughness compared to this of PLD, probably due to the existence of individual defects at the edges. The rest image though, reveals a uniform deposition with bigger-sized grains in front of those of the PLD.

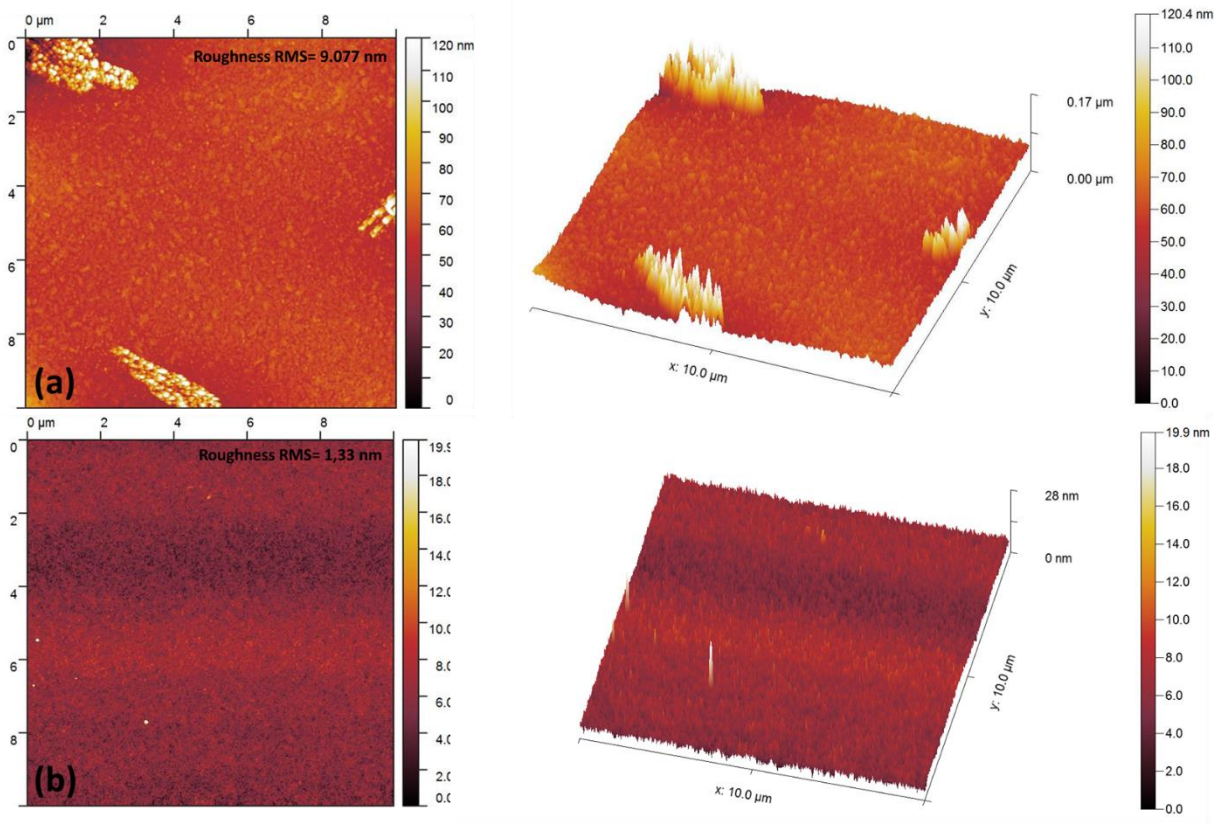

Figure 4.28: AFM surface images for Si_3N_4/VO_2 (a) and TiO_2 (A)/VO_2 (b).

Larger grain sizes probably allow for better heat dissipation that can enhance the optical commutation as evidenced by the measurements. However, apart from the small grain sizes, the deposition and crystallization of VO_2 appears homogeneous in the PLD method as well.

For more detailed analysis of the grain characteristics we would need to apply additional measurements such as Transmission Electron Microscopy (TEM) or Electron Backscatter Diffraction (EBSD) that provide information about grain sizes and crystal orientations respectively.

4.5 Conclusion

In this chapter, vanadium dioxide thin films were synthesized by performing Pulsed-Laser Deposition followed by Rapid Thermal Annealing in oxygen on four different kind of substrates. Raman, AFM, and SEM ensured the stoichiometry, roughness, thickness, homogeneity and covering of the thin film. The method proved to be robust and efficient for producing good quality vanadium dioxide films that exhibit a semiconductor to metal phase transition close to that of bulk VO_2.

While most synthesis method require a long thermal treatment of the thin films at 550 °C, herein is shown that very good transition behavior can be obtained at annealing temperature as low as 350 °C, with the highest infrared transmission shifts being obtained for 450 °C. The method allowed to obtain transition temperature as low as 52 °C on both silicium and transparent quartz, 16 °C lower than the bulk 68 °C usual transition temperatures. Hysteresis as small as 3 °C is obtained for silicium. The PLD method enabled good control of the transition parameters when varying both substrates and annealing temperatures.

In addition, the fabrication protocol of the magnetron sputtered VO_2 is analyzed and compared to that of PLD by performing studies on the optical efficiency of the stacks. The first results for the Si_3N_4/VO_2 bilayer exhibited a 20% improved optical commutation over the TiO_2 (A)/ VO_2 bilayer under high and low temperatures, with lower transition temperature and smaller hysteresis width. This suggests a uniform material deposition and/or good epitaxy match with the underlying layer.

Therefore, comparing the two methods, we conclude that a more homogeneous deposition is achieved by the magnetron sputtering process that leads to better optical responses. The PLD however, is able to produce VO_2 films coated on substrates with low melting points (even lower than 350 °C). The ability to produce VO_2 coated glass with lower melting points than fused silica is a promising idea.

The process compatibility with a variety of substrates makes it advantageous over magnetron sputtering. The PLD in combination with the RTA post-annealing are fast processes with ease of implementation.

The comparative study notifies the advantages and drawbacks for each technique and opens numerous perspectives for various applications. The ability to provide VO_2 on anatase TiO_2 thin film or Si_3N_4 will be exploited to produce thermally controlled switching optical devices (see next chapter), relying on the good refractive index agreement between both materials. The quality of the deposited layers will constructively or destructively affect the optical efficiencies.

Bibliography

[1] "Epitaxial Growth of Complex Metal Oxides", *Elsevier*, 2015. https://doi.org/10.1016/C2013-0-16499-9 (Oct.2020).

[2] F.J. Morin, "Oxides Which Show a Metal-to-Insulator Transition at the Neel Temperature", *Phys. Rev. Lett.* 3 (1959) 34–36.

[3] J.M. Longo, P. Kierkegaard, C.J. Ballhausen, U. Ragnarsson, S.E. Rasmussen, E. Sunde, N.A. Sørensen, "A Refinement of the Structure of VO_2.", *Acta Chem. Scand.* 24 (1970) 420–426.

[4] D.B. McWhan, M. Marezio, J.P. Remeika, P.D. Dernier, "X-ray diffraction study of metallic VO_2, *Phys. Rev. B.* 10 (1974) 490–495.

[5] Y. Wu, L. Fan, W. Huang, S. Chen, S. Chen, F. Chen, C. Zou, Z. Wu, "Depressed transition temperature of WxV1−xO2: mechanistic insights from the X-ray absorption fine structure (XAFS) spectroscopy", *Phys. Chem. Chem. Phys.* 16 (2014) 17705–17714.

[6] S. Kumar, F. Maury, N. Bahlawane, "Electrical Switching in Semiconductor-Metal Self-Assembled VO_2 Disordered Metamaterial Coatings", *Sci. Rep.* 6 (2016) 37699.

[7] H.-T. Zhang, L. Zhang, D. Mukherjee, Y.-X. Zheng, R.C. Haislmaier, N. Alem, R. Engel-Herbert, "Wafer-scale growth of VO_2 thin films using a combinatorial approach", *Nat. Commun.* 6 (2015) 1–8.

[8] M.M. Qazilbash, M. Brehm, G.O. Andreev, A. Frenzel, P.-C. Ho, B.-G. Chae, B.-J. Kim, S.J. Yun, H.-T. Kim, A.V. Balatsky, O.G. Shpyrko, M.B. Maple, F. Keilmann, D.N. Basov, "Infrared spectroscopy and nano-imaging of the insulator-to-metal transition in vanadium dioxide", *Phys. Rev. B.* 79 (2009) 075107.

[9] K. Appavoo, D.Y. Lei, Y. Sonnefraud, B. Wang, S.T. Pantelides, S.A. Maier, R.F. Haglund, "Role of Defects in the Phase Transition of VO_2 Nanoparticles Probed by Plasmon Resonance Spectroscopy", *Nano Lett.* 12 (2012) 780–786.

[10] W.R. Roach, I. Balberg, "Optical induction and detection of fast phase transition in VO_2", *Solid State Commun.* 9 (1971) 551–555.

[11] C. Kübler, H. Ehrke, R. Huber, R. Lopez, A. Halabica, R.F. Haglund, A. Leitenstorfer, Coherent Structural Dynamics and Electronic Correlations during an Ultrafast Insulator-to-Metal Phase Transition in VO_2, *Phys. Rev. Lett.* 99 (2007) 116401.

[12] B.-J. Kim, Y.W. Lee, B.-G. Chae, S.J. Yun, S.-Y. Oh, H.-T. Kim, Y.-S. Lim, "Temperature dependence of the first-order metal-insulator transition in VO_2 and programmable critical temperature sensor", *Appl. Phys. Lett.* 90 (2007) 023515.

[13] Z. Shao, X. Cao, H. Luo, P. Jin, "Recent progress in the phase-transition mechanism and modulation of vanadium dioxide materials", *NPG Asia Mater.* 10 (2018) 581. https://doi.org/10.1038/s41427-018-0061-2.

[14] Y. Cui, Y. Ke, C. Liu, Z. Chen, N. Wang, L. Zhang, Y. Zhou, S. Wang, Y. Gao, Y. Long, "Thermochromic VO_2 for Energy-Efficient Smart Windows", *Joule.* 2 (2018) 1707–1746.

[15] F. Cilento, C. Giannetti, G. Ferrini, S. Dal Conte, T. Sala, G. Coslovich, M. Rini, A. Cavalleri, F. Parmigiani, "Ultrafast insulator-to-metal phase transition as a switch to measure the spectrogram of a supercontinuum light pulse", *Appl. Phys. Lett.* 96 (2010) 021102.

[16] B.-J. Kim, Y.W. Lee, B.-G. Chae, S.J. Yun, S.-Y. Oh, Y.-S. Lim, H.-T. Kim, "Temperature dependence of Mott transition in VO_2 and programmable critical temperature sensor", *Appl. Phys. Lett.* 90 (2007) 023515.

[17] E. Strelcov, Y. Lilach, A. Kolmakov, "Gas sensor based on metal-insulator transition in VO_2 nanowire thermistor", *Nano Lett.* 9 (2009) 2322–2326.

[18] T. Driscoll, H.-T. Kim, B.-G. Chae, M. Di Ventra, D.N. Basov, "Phase-transition driven memristive system", *Appl. Phys. Lett.* 95 (2009) 043503.
[19] T. Driscoll, S. Palit, M.M. Qazilbash, M. Brehm, F. Keilmann, B.-G. Chae, S.-J. Yun, H.-T. Kim, S.Y. Cho, N.M. Jokerst, D.R. Smith, D.N. Basov, "Dynamic tuning of an infrared hybrid-metamaterial resonance using vanadium dioxide", *Appl. Phys. Lett.* 93 (2008) 024101.
[20] C. Chen, X. Yi, X. Zhao, B. Xiong, "Characterizations of VO_2-based uncooled microbolometer linear array", *Sens. Actuators Phys.* 90 (2001) 212–214.
[21] C.L. Gomez-Heredia, J.A. Ramirez-Rincon, J. Ordonez-Miranda, O. Ares, J.J. Alvarado-Gil, C. Champeaux, F. Dumas-Bouchiat, Y. Ezzahri, K. Joulain, "Thermal hysteresis measurement of the VO_2 emissivity and its application in thermal rectification", *Sci. Rep.* 8 (2018) 1–11.
[22] G. Hamaoui, N. Horny, C.L. Gomez-Heredia, J.A. Ramirez-Rincon, J. Ordonez-Miranda, C. Champeaux, F. Dumas-Bouchiat, J.J. Alvarado-Gil, Y. Ezzahri, K. Joulain, M. Chirtoc, "Thermophysical characterisation of VO_2 thin films hysteresis and its application in thermal rectification", Sci. Rep. 9 (2019) 1–10.
[23] M.N. Sadiq, M.L. Roy, A. Pérennec, P. Laurent, N. Martin, D. Passerieux, A. Crunteanu, R. Boyer, F. Dumas-Bouchiat, M. Martin, L. Divay, Q. Levesque, G. Tanné, "Design and Characterisation of VO_2 Based Switches for Ultra-Fast Reconfigurable Devices", *2019 IEEE MTT- Int. Microw. Workshop Ser. Adv. Mater. Process. RF THz Appl. IMWS-AMP*. (2019).
[24] S. Wang, M. Liu, L. Kong, Y. Long, X. Jiang, A. Yu, "Recent progress in VO_2 smart coatings: Strategies to improve the thermochromic properties", *Prog. Mater. Sci.* 81 (2016) 1–54.
[25] K. Liu, S. Lee, S. Yang, O. Delaire, J. Wu, "Recent progresses on physics and applications of vanadium dioxide", *Mater. Today.* 21 (2018) 875–896.
[26] E. Kianfar, "Recent advances in synthesis, properties, and applications of vanadium oxide nanotube", *Microchem. J.* 145 (2019) 966–978.
[27] N.F. MOTT, "Metal-Insulator Transition", *Rev. Mod. Phys.* 40 (1968) 677–683.
[28] More Surprises in Theoretical Physics, 1991. https://press.princeton.edu/books/paperback/9780691025223/more-surprises-in-theoretical-physics (Oct.2020).
[29] J.B. Goodenough, "The two components of the crystallographic transition in VO_2", *J. Solid State Chem.* 3 (1971) 490–500.
[30] R.M. Wentzcovitch, W.W. Schulz, P.B. Allen, VO_2: Peierls or Mott-Hubbard? A view from band theory, *Phys. Rev. Lett.* 72 (1994) 3389–3392.
[31] J.D. Budai, J. Hong, M.E. Manley, E.D. Specht, C.W. Li, J.Z. Tischler, D.L. Abernathy, A.H. Said, B.M. Leu, L.A. Boatner, R.J. McQueeney, O. Delaire, "Metallization of vanadium dioxide driven by large phonon entropy", *Nature.* 515 (2014) 535–539.
[32] A. Liebsch, H. Ishida, G. Bihlmayer, Coulomb correlations and orbital polarization in the metal-insulator transition of VO_2, *Phys. Rev. B.* 71 (2005) 085109.
[33] J. Nag, R.F.H. Jr, "Synthesis of vanadium dioxide thin films and nanoparticles", *J. Phys. Condens. Matter.* 20 (2008) 264016.
[34] R. McGee, A. Goswami, B. Khorshidi, K. McGuire, K. Schofield, T. Thundat, "Effect of process parameters on phase stability and metal-insulator transition of vanadium dioxide (VO_2) thin films by pulsed laser deposition", *Acta Mater.* 137 (2017) 12–21.
[35] Y. Zhao, J. Hwan Lee, Y. Zhu, M. Nazari, C. Chen, H. Wang, A. Bernussi, M. Holtz, Z. Fan, "Structural, electrical, and terahertz transmission properties of VO_2 thin films grown on c-, r-, and m-plane sapphire substrates", *J. Appl. Phys.* 111 (2012) 053533.

[36] M.J. Miller, J. Wang, "Influence of grain size on transition temperature of thermochromic VO_2", *J. Appl. Phys.* 117 (2015) 034307.
[37] L.L. Fan, S. Chen, G.M. Liao, Y.L. Chen, H. Ren, C.W. Zou, "Comprehensive studies of interfacial strain and oxygen vacancy on metal–insulator transition of VO_2 film", *J. Phys. Condens. Matter.* 28 (2016) 255002.
[38] D. Zhang, H.-J. Sun, M.-H. Wang, L.-H. Miao, H.-Z. Liu, Y.-Z. Zhang, J.-M. Bian, "VO_2 Thermochromic Films on Quartz Glass Substrate Grown by RF-Plasma-Assisted Oxide Molecular Beam Epitaxy", Materials. 10 (2017).
[39] H. Zhang, Z. Wu, Q. He, Y. Jiang, "Preparation and investigation of sputtered vanadium dioxide films with large phase-transition hysteresis loops", *Appl. Surf. Sci.* 277 (2013) 218–222.
[40] Y. Liu, J. Liu, Y. Li, D. Wang, L. Ren, K. Zou, "Effect of annealing temperature on the structure and properties of vanadium oxide films", *Opt. Mater. Express.* 6 (2016) 1552–1560.
[41] J. Narayan, V.M. Bhosle, "Phase transition and critical issues in structure-property correlations of vanadium oxide", *J. Appl. Phys.* 100 (2006) 103524.
[42] Y. Sun, S. Jiang, W. Bi, R. Long, X. Tan, C. Wu, S. Wei, Y. Xie, "New aspects of size-dependent metal-insulator transition in synthetic single-domain monoclinic vanadium dioxide nanocrystals", *Nanoscale.* 3 (2011) 4394–4401.
[43] M. Nakano, K. Shibuya, D. Okuyama, T. Hatano, S. Ono, M. Kawasaki, Y. Iwasa, Y. Tokura, "Collective bulk carrier delocalization driven by electrostatic surface charge accumulation", *Nature.* 487 (2012) 459–462.
[44] L.L. Fan, S. Chen, Z.L. Luo, Q.H. Liu, Y.F. Wu, L. Song, D.X. Ji, P. Wang, W.S. Chu, C. Gao, C.W. Zou, Z.Y. Wu, "Strain Dynamics of Ultrathin VO_2 Film Grown on TiO_2 (001) and the Associated Phase Transition Modulation", *Nano Lett.* 14 (2014) 4036–4043.
[45] M.R. Bayati, R. Molaei, F. Wu, J.D. Budai, Y. Liu, R.J. Narayan, J. Narayan, "Correlation between structure and semiconductor-to-metal transition characteristics of VO_2/TiO_2/sapphire thin film heterostructures", *Acta Mater.* 61 (2013) 7805–7815.
[46] R.E. Marvel, R.R. Harl, V. Craciun, B.R. Rogers, R.F. Haglund, "Influence of deposition process and substrate on the phase transition of vanadium dioxide thin films", *Acta Mater.* 91 (2015) 217–226.
[47] OSA | Vacuum Deposited Thin Films Using a Ruby Laser, https://www.osapublishing.org/ao/abstract.cfm?uri=ao-4-1-147 (Oct.2020)
[48] H.-U. Krebs, M. Weisheit, J. Faupel, E. Süske, T. Scharf, C. Fuhse, M. Störmer, K. Sturm, M. Seibt, H. Kijewski, D. Nelke, E. Panchenko, M. Buback, "Pulsed Laser Deposition (PLD) - A Versatile Thin Film Technique", *in: B. Kramer (Ed.), Adv. Solid State Phys.*, Springer, Berlin, Heidelberg, 2003: pp. 505–518. https://doi.org/10.1007/978-3-540-44838-9_36 (Oct.2020)
[49] H. Oguchi, S. Isobe, H. Kuwano, S. Shiraki, S. Orimo, T. Hitosugi, "Pulsed laser deposition of air-sensitive hydride epitaxial thin films: LiH", *APL Mater.* 3 (2015) 096106.
[50] G. Bai, J. Jin, C. Wu, M. Yan, "Microstructure and electromagnetic performance of the FeCoAlON films tuned by N_2 pressure during reactive pulsed laser deposition", *J. Alloys Compd.* 739 (2018) 866–872.
[51] R. Edla, A. Tonezzer, M. Orlandi, N. Patel, R. Fernandes, N. Bazzanella, K. Date, D.C. Kothari, A. Miotello, "3D hierarchical nanostructures of iron oxides coatings prepared by pulsed laser deposition for photocatalytic water purification", *Appl. Catal. B Environ.* 219 (2017) 401–411.

[52] M. Sansone, A. De Bonis, A. Santagata, J.V. Rau, A. Galasso, R. Teghil, "Pulsed laser ablation and deposition of niobium carbide", *Appl. Surf. Sci.* 374 (2016) 112–116.
[53] (13) (PDF) Thin films development by pulsed laser-assisted deposition, ResearchGate. https://www.researchgate.net/publication/264874595_Thin_films_development_by_pulsed_laser-assisted_deposition (Oct.2020).
[54] P.R. Willmott, J.R. Huber, "Pulsed laser vaporization and deposition", *Rev. Mod. Phys.* 72 (2000) 315–328.
[55] H.M. Christen, G. Eres, "Recent advances in pulsed-laser deposition of complex oxides", *J. Phys. Condens. Matter*. 20 (2008) 264005.
[56] M. Borek, F. Qian, V. Nagabushnam, R.K. Singh, "Pulsed laser deposition of oriented VO_2 thin films on R-cut sapphire substrates", *Appl. Phys. Lett.* 63 (1993) 3288–3290.
[57] D. Bhardwaj, A. Goswami, A.M. Umarji, "Synthesis of phase pure vanadium dioxide (VO_2) thin film by reactive pulsed laser deposition", *J. Appl. Phys.* 124 (2018) 135301.
[58] S.A. Bukhari, S. Kumar, P. Kumar, S.P. Gumfekar, H.-J. Chung, T. Thundat, A. Goswami, "The effect of oxygen flow rate on metal–insulator transition (MIT) characteristics of vanadium dioxide (VO_2) thin films by pulsed laser deposition (PLD)", *Appl. Surf. Sci.* 529 (2020) 146995.
[59] S. Lee, T.L. Meyer, S. Park, T. Egami, H.N. Lee, "Growth control of the oxidation state in vanadium oxide thin films", *Appl. Phys. Lett.* 105 (2014) 223515.
[60] D.H. Kim, H.S. Kwok, "Pulsed laser deposition of VO_2 thin films", *Appl. Phys. Lett.* 65 (1994) 3188–3190.
[61] M. Maaza, K. Bouziane, J. Maritz, D.S. McLachlan, R. Swanepool, J.M. Frigerio, M. Every, "Direct production of thermochromic VO_2 thin film coatings by pulsed laser ablation", *Opt. Mater.* 15 (2000) 41–45.
[62] S.A. Pauli, R. Herger, P.R. Willmott, E.U. Donev, J.Y. Suh, R.F. Haglund, "X-ray diffraction studies of the growth of vanadium dioxide nanoparticles", J. Appl. Phys. 102 (2007) 073527.
[63] J.Y. Suh, R. Lopez, L.C. Feldman, R.F. Haglund, "Semiconductor to metal phase transition in the nucleation and growth of VO_2 nanoparticles and thin films", *J. Appl. Phys.* 96 (2004) 1209–1213.
[64] K. Shibuya, A. Sawa, "Optimization of conditions for growth of vanadium dioxide thin films on silicon by pulsed-laser deposition", *AIP Adv.* 5 (2015) 107118.
[65] M. Soltani, M. Chaker, E. Haddad, R.V. Kruzelecky, D. Nikanpour, "Optical switching of vanadium dioxide thin films deposited by reactive pulsed laser deposition", *J. Vac. Sci. Technol. A.* 22 (2004) 859–864.
[66] D. Fu, K. Liu, T. Tao, K. Lo, C. Cheng, B. Liu, R. Zhang, H.A. Bechtel, J. Wu, "Comprehensive study of the metal-insulator transition in pulsed laser deposited epitaxial VO_2 thin films", *J. Appl. Phys.* 113 (2013) 043707.
[67] J. Sakai, M. Zaghrioui, V. Ta Phuoc, S. Roger, C. Autret-Lambert, K. Okimura, "Pulsed laser-deposited VO_2 thin films on Pt layers", *J. Appl. Phys.* 113 (2013) 123503.
[68] B.G. Chae, D.H. Youn, H.T. Kim, S.Y. Maeng, K.Y. Kang, "Fabrication and Electrical Properties of Pure VO_2 Phase Films", *ArXivcond-Mat0311616.* (2003).
[69] S. Zinzuvadiya, U.S. Joshi, "Optical and electrical studies of possible VO_2 thin film nanostructures grown using laser ablated V_2O_5", *AIP Conf. Proc.* 1837 (2017) 040053.
[70] K. Mulchandani, A. Soni, K.R. Mavani, "Effects of deposition temperature on growth and properties of pulsed laser deposited VO_2 thin films and nanostructures", *AIP Conf. Proc.* 2100 (2019) 020051.
[71] R. Eason, "Pulsed Laser Deposition of Thin Films: Applications-Led Growth of Functional Materials", *John Wiley & Sons*, 2007.

[72] A.T.T. Koh, Y.M. Foong, D.H.C. Chua, "Cooling rate and energy dependence of pulsed laser fabricated graphene on nickel at reduced temperature", *Appl. Phys. Lett.* 97 (2010) 114102.
[73] A.V. Moholkar, S.S. Shinde, A.R. Babar, K.-U. Sim, Y. Kwon, K.Y. Rajpure, P.S. Patil, C.H. Bhosale, J.H. Kim, "Development of CZTS thin films solar cells by pulsed laser deposition: Influence of pulse repetition rate", *Sol. Energy.* 85 (2011) 1354–1363.
[74] R. Myerlas, "Key Parameters of Pulsed Laser Deposition for Solid Electrolyte Thin Film Growth", *Int. J. Adv. Eng. Technol.* 10 (2017) 46–51.
[75] K. Nomura, H. Ohta, A. Takagi, T. Kamiya, M. Hirano, H. Hosono, "Room-temperature fabrication of transparent flexible thin-film transistors using amorphous oxide semiconductors", *Nature.* 432 (2004) 488–492.
[76] N. Deo, M.F. Bain, J.H. Montgomery, H.S. Gamble, "Effect of rapid thermal annealing on the structure and magnetic properties of chemical vapor deposition cobalt layers", *J. Appl. Phys.* 97 (2005) 10N307.
[77] J.H. Yu, J.H. Kim, D.S. Park, T.S. Jeong, C.J. Youn, K.J. Hong, "Effect of rapid thermal annealing on Zn1-xCdxO layers grown by radio-frequency magnetron co-sputtering", *Cryst. Res. Technol.* 45 (2010) 1050–1056.
[78] Y. Zhang, H.-L. Lu, Y. Geng, Q.-Q. Sun, S.-J. Ding, D.W. Zhang, "Impact of rapid thermal annealing on structural and electrical properties of ZnO thin films grown atomic layer deposition on GaAs substrates", Vacuum. 103 (2014) 1–4.
[79] L.-J. Meng, R.A. Silva, H.-N. Cui, V. Teixeira, M.P. dos Santos, Z. Xu, "Optical and structural properties of vanadium pentoxide films prepared by d.c. reactive magnetron sputtering", *Thin Solid Films.* 515 (2006) 195–200.
[80] G. Sun, X. Cao, S. Long, R. Li, P. Jin, "Optical and electrical performance of thermochromic V_2O_3 thin film fabricated by magnetron sputtering", *Appl. Phys. Lett.* 111 (2017) 053901.
[81] D. Ruzmetov, S.D. Senanayake, V. Narayanamurti, S. Ramanathan, "Correlation between metal-insulator transition characteristics and electronic structure changes in vanadium oxide thin films", *Phys. Rev. B.* 77 (2008) 195442.
[82] C.C.Y. Kwan, C. h. Griffiths, H. k. Eastwood, "Transport and Structural Properties of VO_2 Films", *Appl. Phys. Lett.* 20 (1972) 93–95.
[83] Z.J. Thompson, A. Stickel, Y.-G. Jeong, S. Han, B.H. Son, M.J. Paul, B. Lee, A. Mousavian, G. Seo, H.-T. Kim, Y.-S. Lee, D.-S. Kim, "Terahertz-Triggered Phase Transition and Hysteresis Narrowing in a Nanoantenna Patterned Vanadium Dioxide Film", *Nano Lett.* 15 (2015) 5893–5898.
[84] K. Pan, W. Wang, E. Shin, K. Freeman, G. Subramanyam, "Vanadium Oxide Thin-Film Variable Resistor-Based RF Switches", *IEEE Trans. Electron Devices.* 62 (2015) 2959–2965.
[85] D. Szilard, W.J.M. Kort-Kamp, F.S.S. Rosa, F.A. Pinheiro, C. Farina, "Hysteresis in the spontaneous emission induced by VO_2 phase change", *JOSA B.* 36 (2019) C46–C51.
[86] D. Zhang, L. Su, H. Li, X. Qian, J. Xu, "Characteristics and optical spectra of V:YAG crystal grown in reducing atmosphere", *J. Cryst. Growth.* 294 (2006) 437–441.
[87] Y. Li, S. Ji, Y. Gao, H. Luo, M. Kanehira, "Core-shell VO_2@TiO_2 nanorods that combine thermochromic and photocatalytic properties for application as energy-saving smart coatings", *Sci. Rep.* 3 (2013) 1370.
[88] Z. Hou, K. Guo, H. Li, T. Zhai, "Facile synthesis and electrochemical properties of nanoflake VN for supercapacitors", *CrystEngComm.* 18 (2016) 3040–3047.
[89] P. Shvets, O. Dikaya, K. Maksimova, A. Goikhman, "A review of Raman spectroscopy of vanadium oxides", *J. Raman Spectrosc.* 50 (2019) 1226–1244.

[90] J. Huotari, J. Lappalainen, J. Eriksson, R. Bjorklund, E. Heinonen, I. Miinalainen, J. Puustinen, A. Lloyd Spetz, "Synthesis of nanostructured solid-state phases of V_7O_{16} and V_2O_5 compounds for ppb-level detection of ammonia", *J. Alloys Compd.* 675 (2016) 433–440.
[91] J.C. Helmer, "Planar penning magnetron sputtering device", *US4629548A*, 1986.
[92] J.L. Vossen, "Thin Film Processes", *Elsevier*, 2012.
[93] P.J. Kelly, R.D. Arnell, "Magnetron sputtering: a review of recent developments and applications, Vacuum". 56 (2000) 159–172.
[94] A. BILLARD, F. PERRY, "Pulvérisation cathodique magnétron", Ref TIP553WEB - Trait. Métaux. (2005). https://www.techniques-ingenieur.fr/base-documentaire/materiaux-th11/traitements-de-surface-des-metaux-par-voie-seche-et-en-milieu-fondu-42360210/pulverisation-cathodique-magnetron-m1654/ (Oct.2020)
[95] W. Yuming, W. Alfred, "An Introduction To Physics And Technology Of Thin Films", *World Scientific*, 1994.
[96] A. Belkind, A. Freilich, J. Lopez, Z. Zhao, W. Zhu, K. Becker, "Characterization of pulsed dc magnetron sputtering plasmas", *New J. Phys.* 7 (2005) 90–90.
[97] G. West, P. Kelly, P. Barker, A. Mishra, J. Bradley, "Measurements of Deposition Rate and Substrate Heating in a HiPIMS Discharge", *Plasma Process. Polym.* 6 (2009) S543–S547.
[98] Y.-K. Dou, J.-B. Li, M.-S. Cao, D.-Z. Su, F. Rehman, J.-S. Zhang, H.-B. Jin, "Oxidizing annealing effects on VO_2 films with different microstructures", *Appl. Surf. Sci.* 345 (2015) 232–237.
[99] M. Taha, S. Walia, T. Ahmed, D. Headland, W. Withayachumnankul, S. Sriram, M. Bhaskaran, "Insulator–metal transition in substrate-independent VO_2 thin film for phase-change devices", *Sci. Rep.* 7 (2017) 1–10.
[100] D. Kim, M. Kim, J. Yi, S.-H. Nam, J.-H. Boo, Y.S. Park, J. Lee, "Growth and Characterization of VO_2 Thin Film by Pulsed DC Sputtering of Optical Switching Applications", (2017).
[101] H.-C. Ho, Y.-C. Lai, K. Chen, T.D. Dao, C.-H. Hsueh, T. Nagao, "High quality thermochromic VO_2 films prepared by magnetron sputtering using V_2O_5 target with in situ annealing", *Appl. Surf. Sci.* 495 (2019) 143436.
[102] H.Y. Xu, Y.H. Huang, S. Liu, K.W. Xu, F. Ma, P.K. Chu, "Effects of annealing ambient on oxygen vacancies and phase transition temperature of VO_2 thin films", *RSC Adv.* 6 (2016) 79383–79388.
[103] T. Lin, Y. Zhang, D. Zheng, "The ultrathin VO_2(M) film with ultrahigh visible transmittance synthesized on the quartz glass substrate by HiPIMS", *Vacuum.* 156 (2018) 449–455.
[104] C. Zhang, O. Gunes, Y. Li, X. Cui, M. Mohammadtaheri, S.-J. Wen, R. Wong, Q. Yang, S. Kasap, "The Effect of Substrate Biasing during DC Magnetron Sputtering on the Quality of VO_2 Thin Films and Their Insulator–Metal Transition Behavior", *Materials.* 12 (2019) 2160.
[105] H. Zhang, Z. Wu, C. Wang, Y. Sun, "VO_2 film with small hysteresis width and low transition temperature", *Vacuum.* 170 (2019) 108971.
[106] Y.Y. Luo, S.S. Pan, S.C. Xu, L. Zhong, H. Wang, G.H. Li, "Influence of sputtering power on the phase transition performance of VO_2 thin films grown by magnetron sputtering", *J. Alloys Compd.* 664 (2016) 626–631.
[107] Q. Cheng, D. Su, Y. Wang, Y. Huang, "Highly transparent VO_2-SiO_2 films with excellent infrared characteristics by dual-target magnetron sputtering", in: *Pac. Rim Laser Damage 2017 Opt. Mater. High-Power Lasers, International Society for Optics and Photonics*, 2017: p. 103391I.

[108] Y. Choi, Y. Jung, H. Kim, "Low-temperature deposition of thermochromic VO_2 thin films on glass substrates", *Thin Solid Films.* 615 (2016) 437–445.
[109] S. Swann, "Magnetron sputtering", *Phys. Technol.* 19 (1988) 67–75.
[110] R. Nishikawa, S. Satoyama, Y. Ito, H. Jyo, "Magnetron sputtering apparatus", *US4441974A*, 1984.
[111] H. Zhang, Z. Wu, X. Wu, W. Yang, Y. Jiang, "Transversal grain size effect on the phase-transition hysteresis width of vanadium dioxide films comprising spheroidal nanoparticles", *Vacuum.* 104 (2014) 47–50.
[112] R. Lopez, T.E. Haynes, L.A. Boatner, L.C. Feldman, R.F. Haglund, "Size effects in the structural phase transition of VO_2 nanoparticles, Phys. Rev. B. 65 (2002) 224113.

CHAPTER 5

Thermally Activated WRG

5.1 Introduction

In the previous chapter, we have studied the VO_2 properties of thin Semiconductor to Metal (SMT) reversible films while we have successfully synthesized films by PLD and reduced thermal treatment with RTA. The combination of both provided films with good transition shifts, narrow hysteresis and lower transition temperature for some of the tested substrates. Moreover, a similar theoretical and experimental approach of magnetron sputtering is completed. The magnetron sputtered VO_2 film on a Si_3N_4 layer presented good deposition quality with a higher SMT transition than the corresponding TiO_2 (A) / VO_2 - PLD film.

The comparison of these two methods revealed the optical properties of thin VO_2 films, especially when deposited on different underlying layers. Such multilayers can be used as sensor devices taking advantage of this characteristic VO_2 switching effect. In the majority, thin VO_2 films are stated to be exploited in vicinity to metals for plasmonic-based detection.

In this chapter, our built-in double layers with VO_2 films grown by PLD and magnetron sputtering method are suggested to be integrated into the Waveguide Resonant Grating (WRG) configurations after depositing and patterning an ontop positive photosensitive resist. These structures are seen as optical devices for wavelength and polarization selectivity. The main idea concerns a thermally triggered emitter/absorber tunable configuration that enables the on / off optical dielectric waveguide resonant excitation in a reversible manner in the NIR band.

According to this principle, two structural models are proposed for each deposition technique. The designs were individually simulated to optimize optical performance, fabricated and finally characterized by optical spectroscopy. A first demonstration of the effect is presented for both configurations. The devices are suggested as passive Q-switching demonstration in laser cavities to prevent overheating.

5.2 Overview on VO_2 based sensors

Optical switches induced by electrical [1], thermal [2], acoustic [3], and magnetic [4] effects are well known. A new generation of modulators based on smart phase change materials behaving as passive control systems could be advantageous thanks to their simplicity and cost effectiveness. In this context, VO_2 has been one of the most attractive element for efficient switching response because of its ability to change dramatically the optical properties in the NIR band when dielectric to metal transition occurs around 68°C.

In nanophotonics, the VO_2 is widely exploited in novel plasmonic-based structures. When is placed near to metal, VO_2 layer induces surface plasmon excitation at the dielectric - metal interface. Such hybrid structures developed for optical switching are strongly dependent on the design and on the geometrical characteristics that tune appropriately the operating wavelength. The responses can be significantly enhanced when a corrugation is added.

In particularly, Ghanekar *et al.* showed boosted thermal rectification for a radiative diode and a thermal transistor when using 1D rectangular VO_2 grating **(Figure 5.1)** [5].

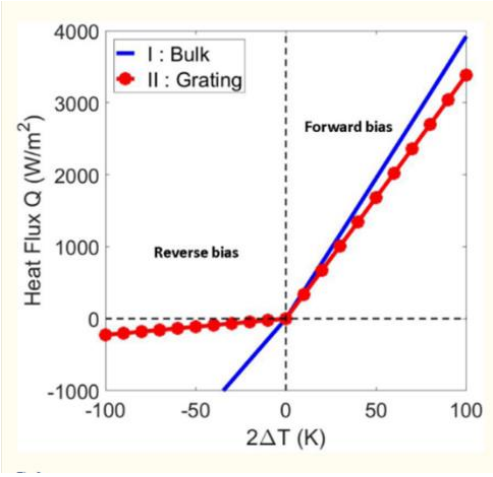

Figure 5.1: Enhancement of thermal rectification in forward bias thanks to the grating patterning for a thermal diode [5].

Similar structure with triangular Au arrays on VO_2 layer and top VO_2 layer was proposed by Liang *et al*. By varying the thickness of the upper VO_2 layer, they achieved controlled modulation of localized surface plasmon resonance peak **(Figure 5.2)** [6].

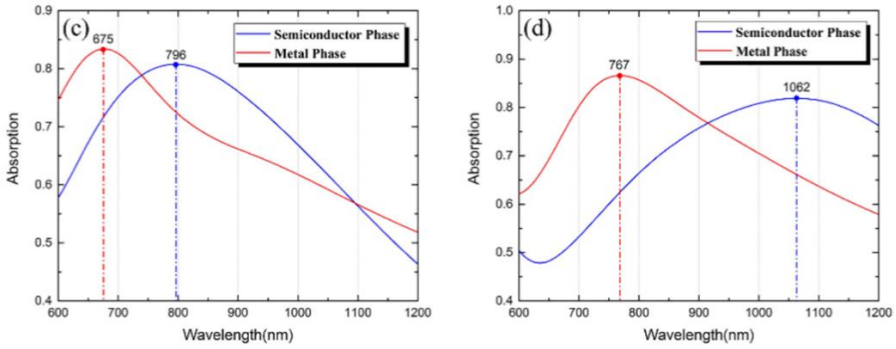

Figure 5.2: Simulated absorption spectra of the triple VO_2/Au/VO_2 layer with adjustable VO_2 top thickness at (a) 50 nm and (b) 80 nm and fixed VO_2 bottom thickness at 50 nm [6].

Since then, several models of structures have been proposed to obtain tunable optical responses. Wang *et al.* proposed and numerically demonstrated a design of a 1D gold grating on a VO_2 film and a bottom Au layer [7]. Through the heating-cooling process and normal incidence, magnetic resonance excitation thus the absorptivity is modified **(Figure 5.3-a, b)**. Later, the same group also numerically demonstrated a tunable metamaterial structure consisting of a one-dimensional VO_2 periodic grating on a stacked MgF_2 and VO_2 film [8]. The structure behaved as a wavelength switch due to the magnetic resonance excitation when examined in absorption **(Figure 5.3-c, d)**.

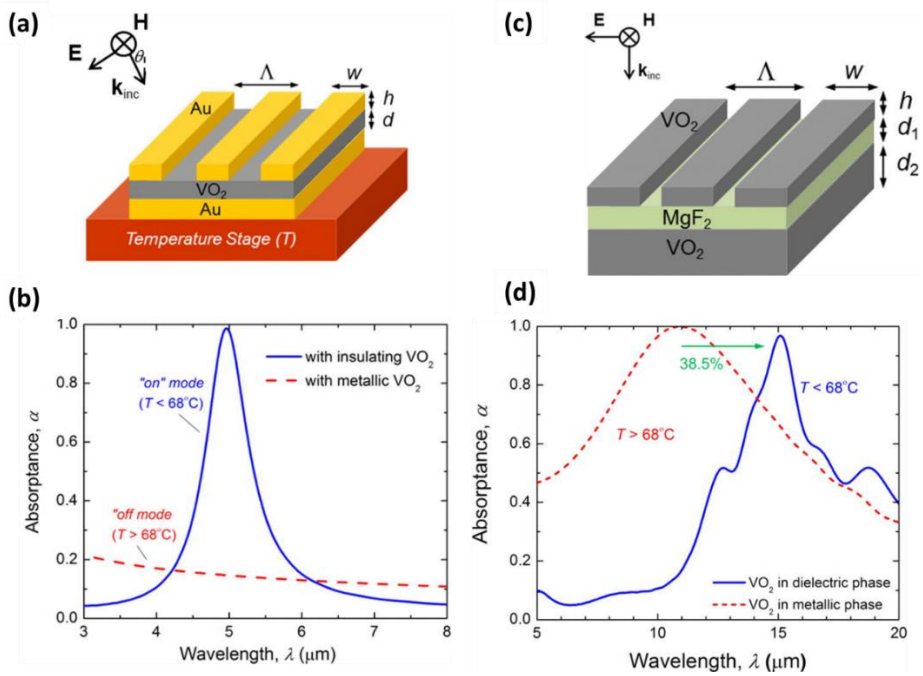

Figure 5.3: Proposed designs (a), (c) and corresponding graphs with tunable magnetic resonances during thermal activation (b), (d) respectively [7], [8].

Based on magnetic resonance, Zhejun *et al.* numerically demonstrated that both 1D and 2D subwavelength VO_2 patterned configurations can be super-efficient absorbers when VO_2 is set at its metallic phase [9].

Intensification of infrared absorption is pointed out by Sun *et al.* with a structured design of VO_2 /Al_2O_3 grating pattern intended as optical reflectors with an intended use in satellites and spaceships [10]. Controlled emissivity was achieved under plasmonic resonance excitation for low and high temperatures.

The Al_20_3 was also employed by Sun-Je Kim *et al.* as a vicinity metal to VO_2 [11]. A diffraction grating of thick dual VO_2 ridges-waveguide on Al_2O_3 layer modified the diffraction directivity according to the plasmonic - dielectric shift upon thermal triggering. With normal incidence, the insulating VO_2 hampered the forward transmission of the incident light in the waveguide, whereas fully guided light propagation for TE polarized mode was achieved in the metallic phase. This ultra-compact structure exhibits high performance as a modulator of the optical transmission **(Figure 5.4)**.

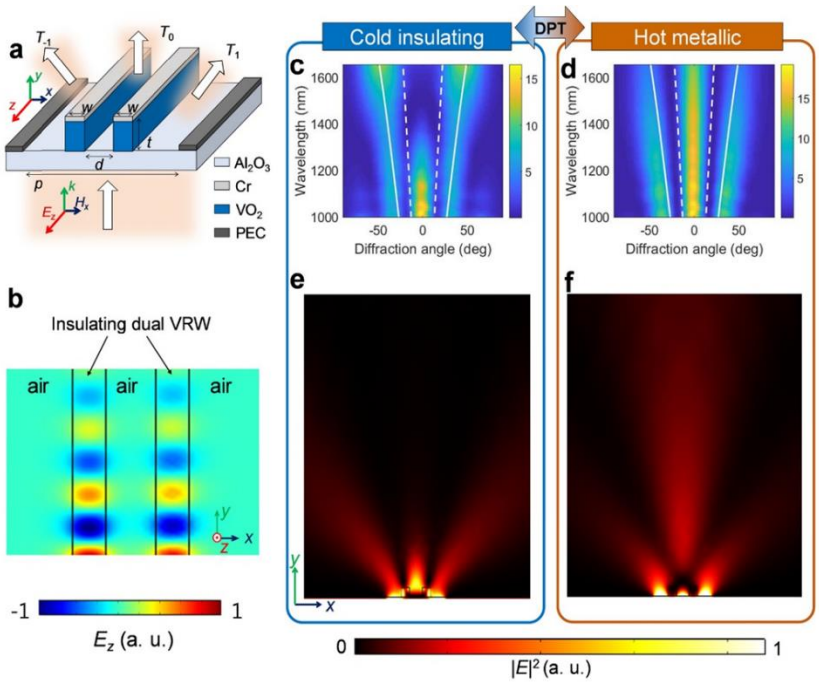

Figure 5.4: Design of the proposed structure consisted of a dual VO_2 ridge waveguide (VRW) (a) and electric field distribution of the TE_0 mode at 1400 nm (b), diffraction angles of the unit cell of the VRW in insulating and metallic phase (c),(d) with the normalized electric field distribution respectively (e),(f) [11].

Recently, Afshari – Bavil *et al.* fabricated and demonstrated an active absorber consisting of a Fabry-Perot cavity sandwiched between a VO_2 layer and a metal **(Figure 5.5)** [12]. Under TM polarization and tuned to the telecommunication band (1.55 μm), the device sensed surface plasmon polaritons with enhanced absorption in the dielectric phase (99%) whereas with lowered rates (30%) in the metallic phase.

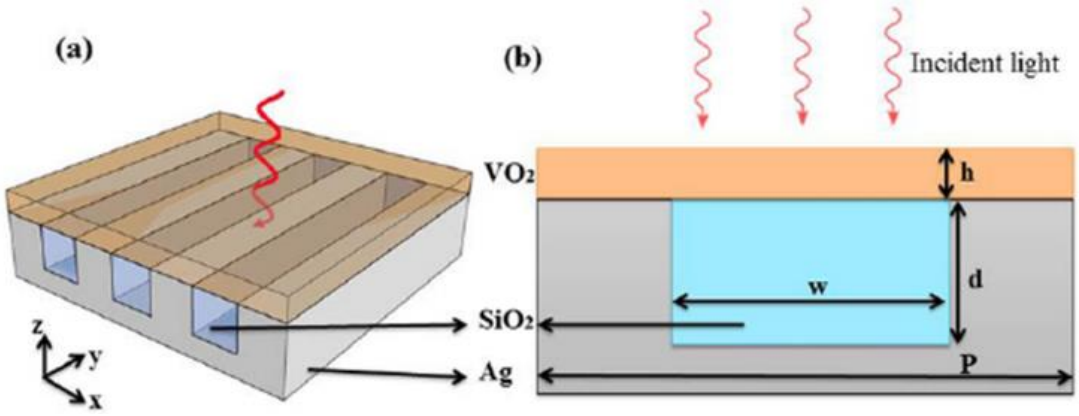

Figure 5.5: Design (a) and unit cell (b) of the absorber formed by cavities in the grooves of an Ag grating and covered by a thin layer of VO_2 [12].

Vadivukkarasi Jeyaselvan *et al*. presented a ring resonator of a 35-μm radius with a VO_2 PLD deposited film on a Si waveguide on a Buried Oxide substrate **(Figure 5.6)** [13]. The operation of the thermally triggered device based on the VO_2 refractive index variation upon the Insulator to Metal Transition. The reduced refractive index of the VO_2 in the metallic state led to the insertion of the mode in the Si waveguide through the grating couplers. In the insulating phase, the refractive index increased and the mode was confined in the VO_2 layer.

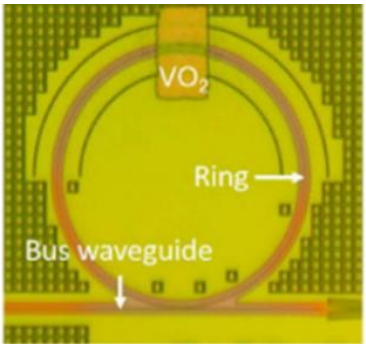

Figure 5.6: Microscopic image of the ring resonator with VO_2 patch, coupled to a plane Si waveguide for mode propagation.

Operating under oblique incidence and measuring the reflectance for both, the dielectric and the metallic phase, a structure composed by Au/VO_2/Au nanowires is recommended for broadband optical tuning **(Figure 5.7)** [14]. Hence, Thomas *et al.* demonstrated large EM field enhancements in the VO_2 waveguide when coupling surface plasmons with incident radiation in less than 20 nm thick VO_2 film through the Au nanowire grating. Decreasing progressively the waveguide thickness, they localized the optimal switching wavelength.

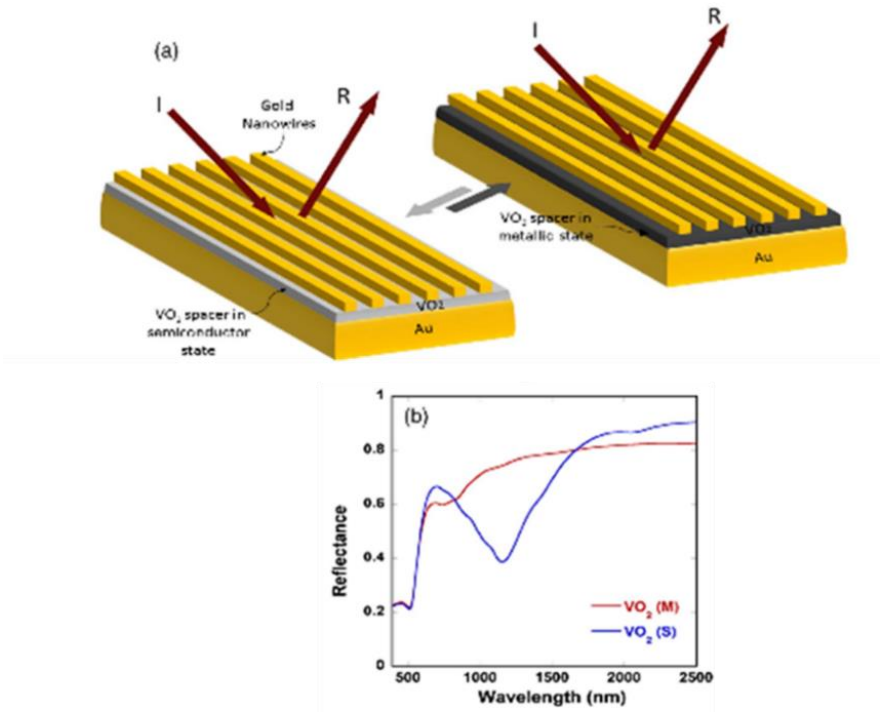

Figure 5.7: Simulated reflectance variation between metallic and semiconductor state for the proposed Au/VO2/Au grating structure.

Yu-Feng Zhang *et al.* proposed a multilayer structure with Si_3N_4/VO_2/Si_3N_4 and a metal grating for improving the absorption efficiency of resistive bolometers [15]. They had specified the crucial purpose of the grating and demonstrated how tailoring its structural dimensions can improve the light absorption rate.

Further extensive studies were proposed [16], [17] on the influence of structural parameters (grating groove depth and grating line width) and wavelength tunability of a VO_2 waveguide-mode plasmonic nanograting for optical switching.

5.3 Designs of VO_2 embedded structures fabricated by magnetron sputtering or PLD method

For this study, two basic designs are proposed in line with the PLD or magnetron sputtering fabrication approaches. The main objective behind the structural devices is to couple light under normal incidence to the waveguide modes and lead to total reflection when VO_2 is in the dielectric state **(Figure 5.8-c)**. On the other hand, the resonance will be canceled at elevated temperatures (above 68°C) when VO_2 is in the metallic state thereby obtaining a thermally activated switch **(Figure 5.8-f)**. The wavelength of interest is set to 1500 nm, where a high commutation between cold and hot state is noticed [18]. The corrugation of the positive photoresist (n = 1.67 and k = 0) is modelled as rectangular due to the ease of implementation. Both configurations are intended to operate under TE polarization and normal incidence, whereas the TM polarization has not been considered.

According to the above principle, the first proposed structure includes a thin VO_2 magnetron sputtered layer embedded in a thick Si_3N_4 layer **(Figure 5.8-a, d)**. This composite layer acts as a waveguide, while the presence of the Si_3N_4 layer near to the VO_2 thin film contributes to the oxidation prevention. This triple layer is deposited on a SiO_2 substrate and covered by a binary corrugation of a positive photoresist. The design uses the TE_1 mode in order to minimize the amplitude of the electric field in the VO_2 layer, thus ensuring minimal absorption and losses. Likewise, an enhancement of the resonance is possible when VO_2 is in dielectric state. To exclude modes of higher orders we calculate the width of the waveguide layer with the dispersion equation and the cut-off of the TE_2 mode **(Equation 3.6)**. Setting $n_{eff} = n_s$ and m = 1 we result in 772.5 nm ≤ w_{eq} < 1401 nm that allows exclusively the propagation of the fundamental and first mode.

The second structure is based on the PLD fabricated VO_2 film grown on an anatase TiO_2 film deposited on a SiO_2 substrate as well **(Figure 5.8-b, e)**. A positive rectangular photoresist is placed ontop of the double VO_2/TiO_2 layer for subwavelength grating filtering. The TiO_2 anatase state is selected to have an almost similar refraction index to that of the VO_2 film in the dielectric phase, in order to compose a compact double layer waveguide that promotes the total reflection. The TiO_2 solution, widely proposed for waveguides layers, offers a good stability and can be indexed matched to VO_2 depending on its baking process. Thus, the TiO_2 refractive index is set to 2.2, close to the 2.19 value of PLD grown VO_2 layer. For this structure, we have selected a single mode (fundamental one) propagation in the waveguide layer. The dispersion

equation leads anew to the cut-off conditions of the modes with $n_{eff} = n_s$ and m = 0 and the allowable thickness results in 92.606 nm < w_{eq} < 499.683 nm.

The VO_2 thickness was chosen to be those used in the previous chapter, i.e. 80 nm for magnetron sputtering technique (first approach) and 27 nm for PLD deposition (second approach). To minimize the VO_2 absorption, we chose different operational mode for the single mode or bimodal waveguide. This comparison will give us a clearer diagnosis on the absorption impact of VO_2 films.

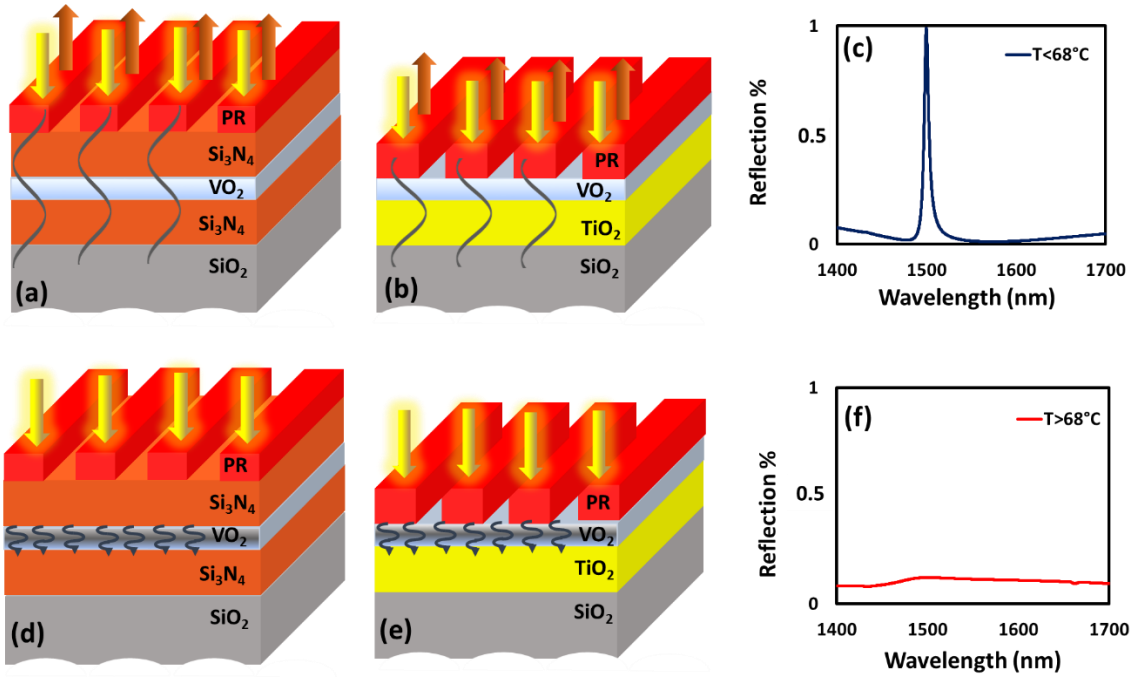

Figure 5.8: Designs of the structures with embedded VO_2 films deposited by magnetron sputtering (a), (d) or PLD (b), (e) method. The configurations are conceived as mode propagators (a), (b) leading to a resonance at λ=1500 nm (c) when VO_2 film is in the dielectric state, whereas as absorbers (d), (e) with simultaneous resonance cancelation (f) when T>68°C. For each configuration, the electric field distribution is represented with a grey line.

For both designs, numerical calculations with "MC Gratings" and Modal Collinear programming were investigated and tailored the structural parameters for maximum reflection efficiency in dielectric state (while keeping the waveguide thickness in the above-mentioned range.

5.3.1 Design of the structure with VO_2 film synthesized by magnetron sputtering (1st approach)

The simulation analysis of the targeted structure **(Figure 5.9)** requires imperatively the knowledge of the refractive indices of the Si_3N_4 layer and VO_2 film fabricated by magnetron sputtering. The temperature-dependent n and k coefficients were measured in the wavelength range from 300 nm to 2000 nm with the HORIBA Jobin Yvon UVISEL ellipsometric device and the aid of a metal plate connected to a thermocouple and a temperature controller capable of changing the temperature over the range of 20°C to 100°C. The experimental ellipsometric parameters were fitted with a Tauc-Lorentz formula using 3 oscillators. The characteristic curves are illustrated in **Figure 5.10.**

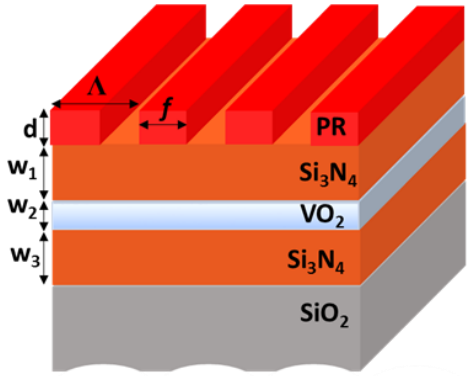

Figure 5.9: Design of the targeted magnetron sputtered configuration.

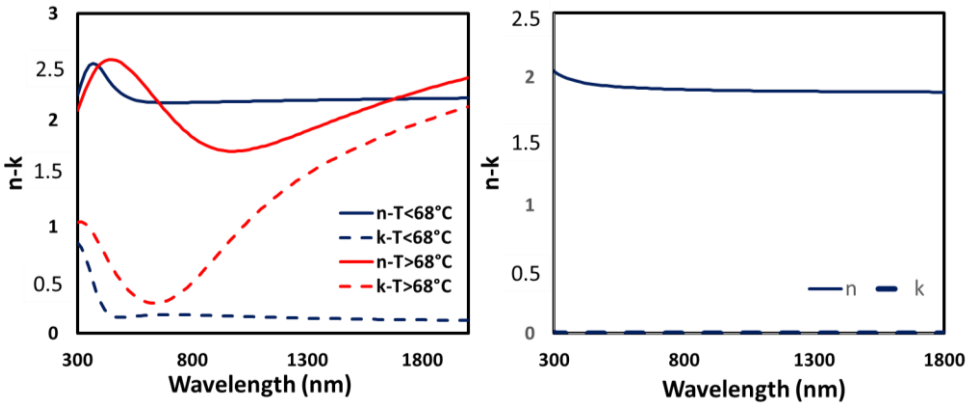

(a) **(b)**

Figure 5.10: Refractive index (n) (plain line) and extinction coefficient (k) (dashed line) of VO_2 (a) and Si_3N_4 thin film (b) deposited by magnetron sputtering.

The Si_3N_4 behaves like a good transparent dielectric material and presents an extinction coefficient below detection limit in all visible and far IR bands. The VO_2 film has a non-zero k coefficient at room temperature, which is further increased when the temperature rises over the 68°C in metallic state notifying a strong absorption above the wavelength of 800 nm. At 1500 nm the n = 2.19 and k = 0.13 in dielectric state.

Other fixed design parameters are the resonance wavelength at λ = 1500 nm and a VO_2 thickness of w_2 = 80 nm. The initial values of Si_3N_4 layer thicknesses are set to $w_1 = w_3$ = 500 nm to fulfill the condition of **Equation 3.6**. Systematically, we have scanned for the other structural values.

Initially, a 2D scan of wavelength (around λ = 1500 nm) versus the period revealed the approximate couple of values that led to resonance (maximum reflected power C_0) for normal incidence in TE polarization **(Figure 5.11)**.

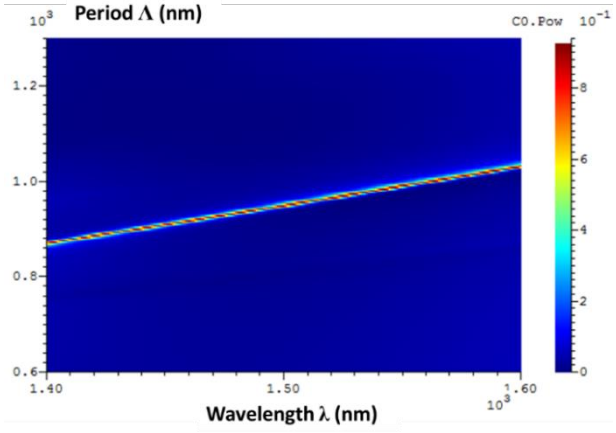

Figure 5.11: Reflected power C_0 2D scan of wavelength (λ) vs period (Λ) for normal incidence in TE polarization when setting approximatively the film widths between the range of 772.5 nm < w_{eq} < 1401 nm, w_2 = 80 nm, $w_1 = w_3$ = 500 nm, f ~ 500 nm and d~ 300 nm.

As observed in **Figure 5.11,** at λ = 1500 nm the corresponding period is equal to Λ = 950 nm. Given that the operational mode is set to be bimodal, two modes should appear on the graph "period vs wavelength". The absence of the first mode with $n_{eff0} > n_{eff1}$ means probably that having a better overlap with the VO_2 layer, it will only become apparent when we set the extinction coefficient of VO_2 at k = 0.

The 1D scan **(Figure 5.12)** gives a clearer insight and points out the effect of absorption for a VO_2 layer thickness of w_2 = 80 nm linked to the extinction coefficient at a wavelength of

1500 nm in TE polarization and normal incidence. As one observes the first mode at Λ ~ 800 nm disappears and the resonant reflection reaches ~ 60% after setting k = 0.13.

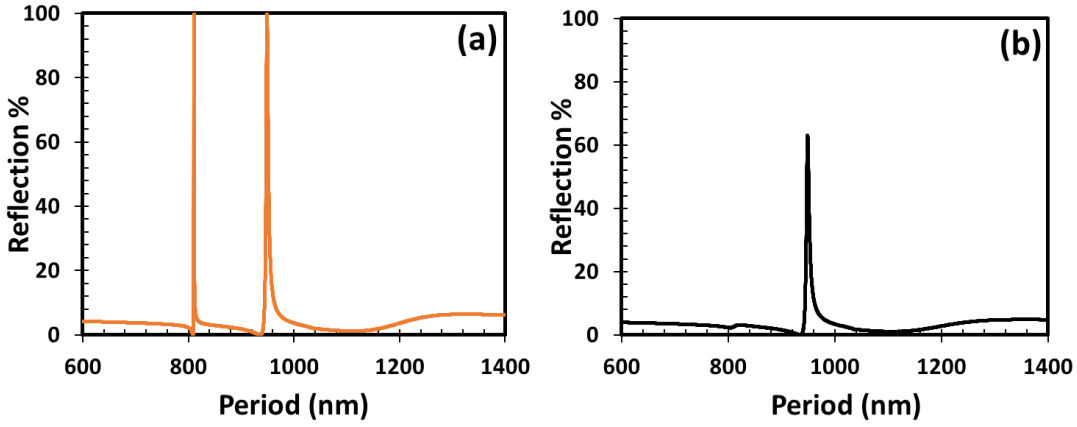

Figure 5.12: 1D scan of period with VO_2 extinction coefficient of dielectric state at k = 0 and k = 0.13. (λ_R = 1500 nm, TE polarization, normal incidence, film widths in the range 772.5 nm < w_{eq} < 1401 nm, w_2 = 80 nm, w_1 = w_3 = 500 nm, *f* ~ 500 nm and d~ 300 nm).

Having defined the period for the second mode that couples into the waveguide, a second 2D scan between period and cell-length *f* can confirm the value of the latter **(Figure 5.13)**.

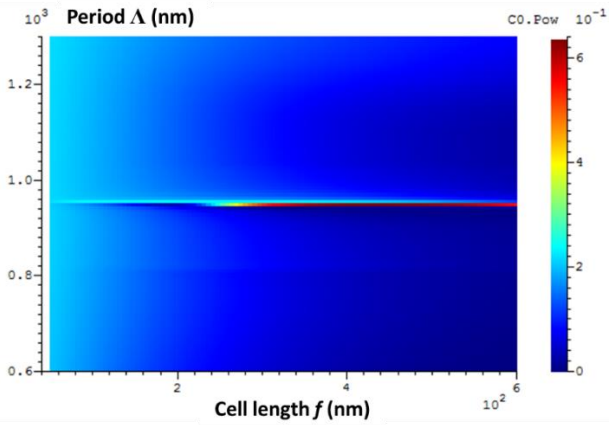

Figure 5.13: 2D C_0 scan of period (Λ) vs cell length (*f*) with d = 300 nm, w_2 = 80 nm and w_1 = w_3 = 500 nm.

For a period of Λ = 950 nm, the reflected power is stable at about 0.63 when the cell length ranges from *f* = 400 nm and onwards. This power stability gives us the option to choose 475 nm for a cell length that corresponds to the exact half value of the period and is compatible with the fabrication criteria.

For a resonance at $\lambda = 1500$ nm, $\Lambda = 950$ nm and duty cycle at 0.5, the thicknesses of the layers are studied more precisely **(Figure 5.14)**.

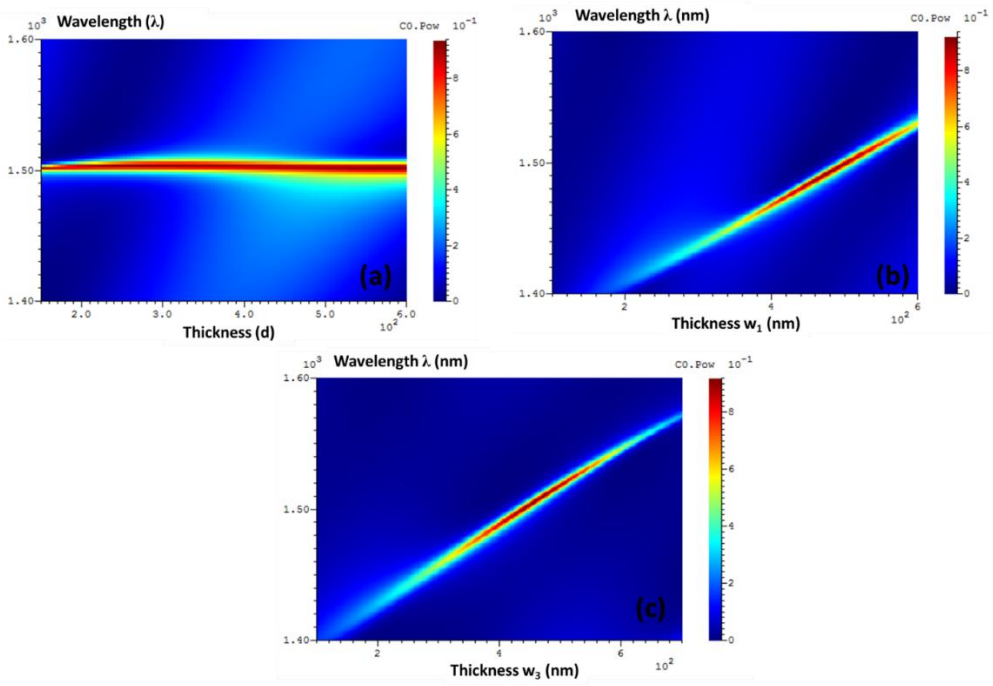

Figure 5.14: 2D scan of: photoresist thickness d with $w_1 = 440$ nm and $w_3 = 500$ nm (a) Si_3N_4 thickness w_1 with d = 200 nm and $w_3 = 500$ nm (b) and Si_3N_4 thickness w_3 with d = 200 nm and $w_1 = 440$ nm (c) vs wavelength (λ) ($w_2 = 80$ nm for all graphs).

Figure 5.14-a illustrates that at $\lambda = 1500$ nm the increase of the reflected power is proportional to the thickness increment of the photoresist coating for fixed thickness of the Si_3N_4 layers ($w_1 = 440$ nm and $w_3 = 500$ nm). For our structure, we select about d = 200 nm for the photoresist thickness. This value does not present significant power losses compared to the more elevated values and can be easily deposited. With this value of d = 200 nm and maintaining $w_3 = 500$ nm, **Figure 5.14-b** shows that for $\lambda = 1500$ nm the highest permitted Si_3N_4 thickness w_1 is about 440 nm whereas **Figure 5.14-c** exhibits a Si_3N_4 thickness w_3 around 500 nm with $w_1 = 440$ nm and d = 200 nm.

Precise determination of these three parameters is given with 1D plots in **Figure 5.15**.

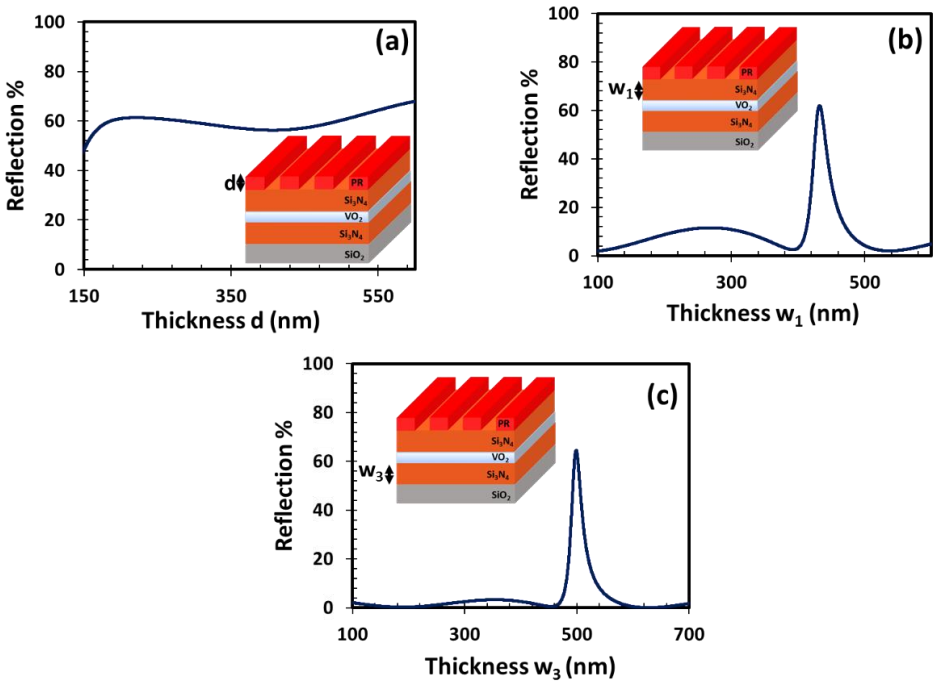

Figure 5.15: 1D scan for layer thickness determination of resist d (w_1 = 440 nm and w_3 = 500 nm) (a), Si_3N_4 thickness w_1 (d = 200 nm and w_3 = 500 nm) (b) and Si_3N_4 thickness w_3 (w_1 = 440 nm and d = 200 nm) (c) for λ = 1500 nm, Λ = 950 nm, duty cycle 0.5 and w_2 = 80 nm.

The optimum thickness of the resist coating is found at d = 225 nm, the Si_3N_4 thicknesses at w_1 = 435 nm and w_3 = 502 nm.

From the above calculations, the final structure with the optimal profile is designed for the highest possible efficiency (60% for reflection) at a resonance of λ = 1500 nm **(Figure 5.16).**

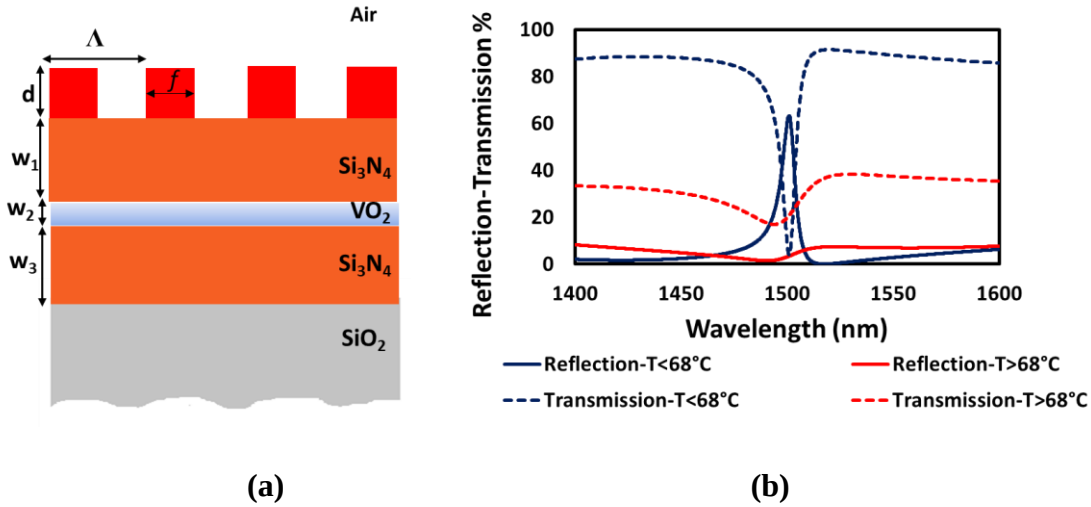

(a) **(b)**

Figure 5.16: Final structure for a resonance at λ = 1500 nm under normal incidence and TE polarization; d = 225 nm, w_1 = 435 nm, w_2 = 80 nm, w_3 = 502 nm, Λ = 950 nm and *f* = 475 nm (a), Simulated reflection and transmission amplitude of the structure when VO_2 layer is in dielectric or/and metallic phase (b).

The electric field distribution (E_y component for TE polarization) at the resonance peak wavelength λ = 1500 nm gives evidence on the switching features of the composite structure. **Figure 5.17** illustrates the inverted cross section of one-unit cell scanning at a large-scale z (propagation direction). When VO_2 is in its dielectric phase **(Figure 5.17-a)**, the structure confines a strong electric field which is 8 orders higher than that of metallic state. For resonance excitation, there is a strong coupling between the normal incident beam and the second propagating mode in the waveguide. On the contrary, the metallic phase leads to total absorption due to the VO_2 refractive index variation **(Figure 5.17-b)**. The electric field distribution of the TE_1 mode is mainly distributed in the Si_3N_4 layer.

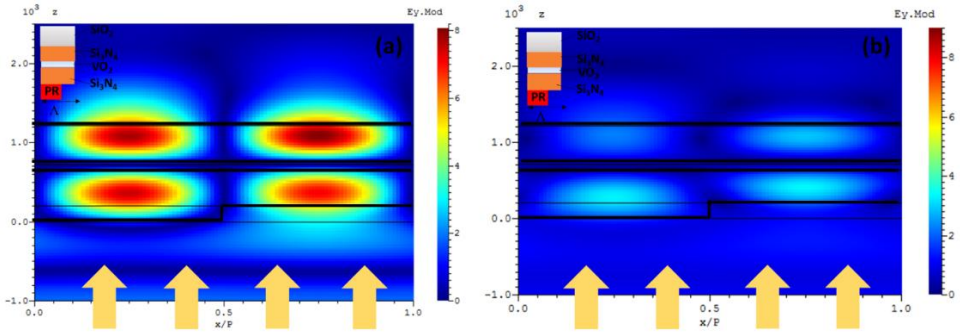

Figure 5.17: Distribution of the electric field of the second mode at the resonance wavelength of λ = 1500 nm. Activation of resonance when VO_2 is in dielectric phase with n = 2.13 and k = 0.13 (a), or total depletion of resonance when VO_2 is in metallic state with n = 2.06 and k = 1.72 (b).

5.3.2 Design of the structure with VO_2 film synthesized by PLD (2nd approach)

The present structure **(Figure 5.18)**, maintains anew the resonance at λ = 1500 nm and the VO_2 thickness at 27 nm as the thinner attainable layer fabricated by PLD technique.

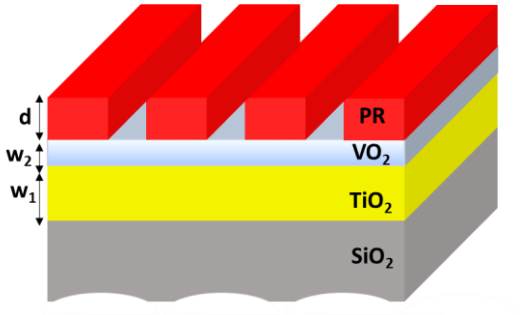

Figure 5.18: Design of the targeted PLD configuration.

To check the parameters of the synthesized vanadium dioxide, ellipsometry measurements were performed with the same operational principle as before that allowed registering the dispersion curves for the two extreme temperatures 20°C and 100°C **(Figure 5.19)**.

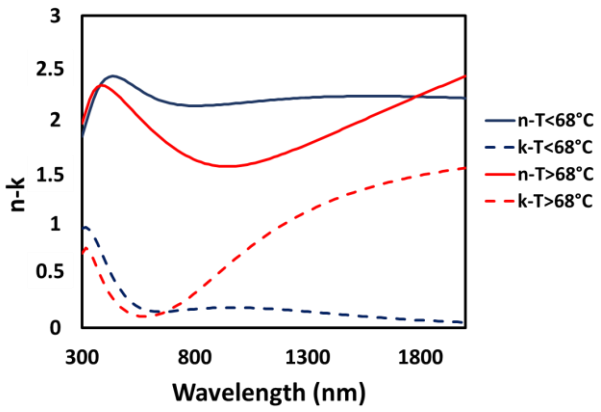

Figure 5.19: Refractive index (n) (plain line) and extinction coefficient (k) (dashed line) of vanadium dioxide PLD thin films deposited on silicium and annealed at 450°C.

At λ = 1500 nm and room temperature the refractive index and absorption coefficient result in n = 2.22695 and k = 0.11922 (dielectric state).

With these n and k values, further simulation analysis with 2D and 1D scanning has determined the optimized structural features as presented below.

As previously, the 2D scan of wavelength versus period, with w_2 = 27 nm, w_1 = 70 nm, d = 210 nm and duty cycle at 0.5, revealed a period equal to 1000 nm for a resonance wavelength at 1500 nm in normal incidence and TE polarization **(Figure 5.20)**. In this case, the grating couples the fundamental mode TE_0 into the monomode waveguide.

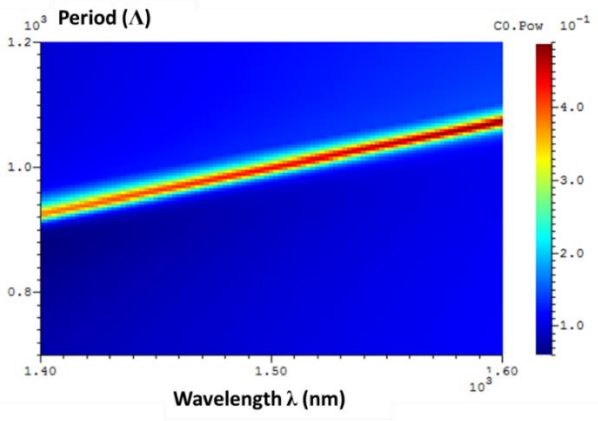

Figure 5.20: 2D scan of wavelength (λ) vs period (Λ) with w_2 = 27 nm, w_1 = 70 nm, d = 210 nm and duty cycle at 0.5.

A 2D scan of period versus cell length, calculated for a period at Λ = 1000 nm, exhibits a maximum power of 44.5% for a cell length between 400 nm and 500 nm **(Figure 5.21)**.

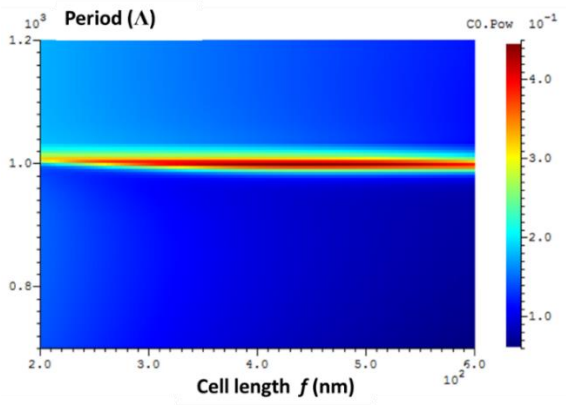

Figure 5.21: 2D scan of period (Λ) vs cell length (*f*) with w_2 = 27 nm, w_1 = 70 nm, d = 210 nm and duty cycle at 0.5.

Finally, the 2D scans of wavelength versus photoresist and TiO_2 thickness, give the last rough approach of the structural profile **(Figure 5.22)**. The values for better device performance correspond to d ~ 210 nm for grating thickness and to w_1 ~ 70 nm for TiO_2 thickness when keeping the VO_2 thickness at w_2 = 27 nm, the grating period at Λ = 1000 nm and the duty cycle at ~ 0.5.

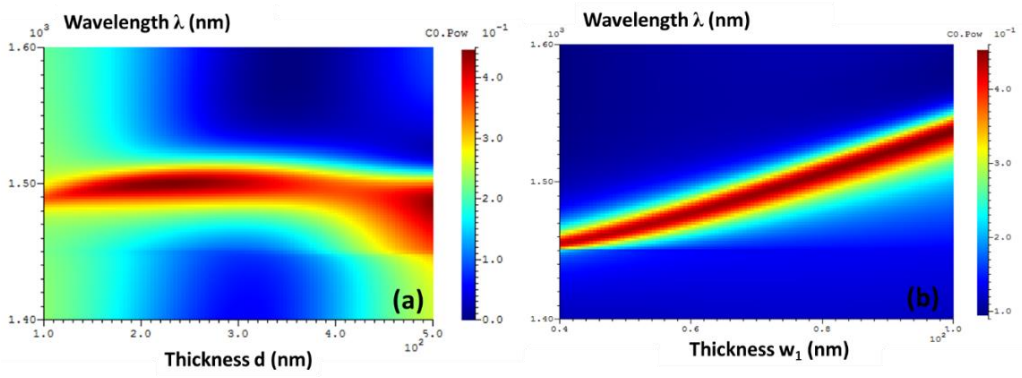

Figure 5.22: 2D scan of wavelength (λ) vs photoresist thickness d with w_1 = 70 nm, w_2 = 27 nm, Λ = 1000 nm and duty cycle at 0.5 (a) versus TiO_2 thickness w_1 with d = 210 nm, w_2 = 27 nm, Λ = 1000 nm and duty cycle at 0.5 (b).

The above values are determined more precisely after the 1D spectra plots **(Figure 5.23)**. The grating depth with maximum power is located at d = 216 nm, for the TiO_2 layer at w_1 = 75 nm and for the cell length at f = 440 nm.

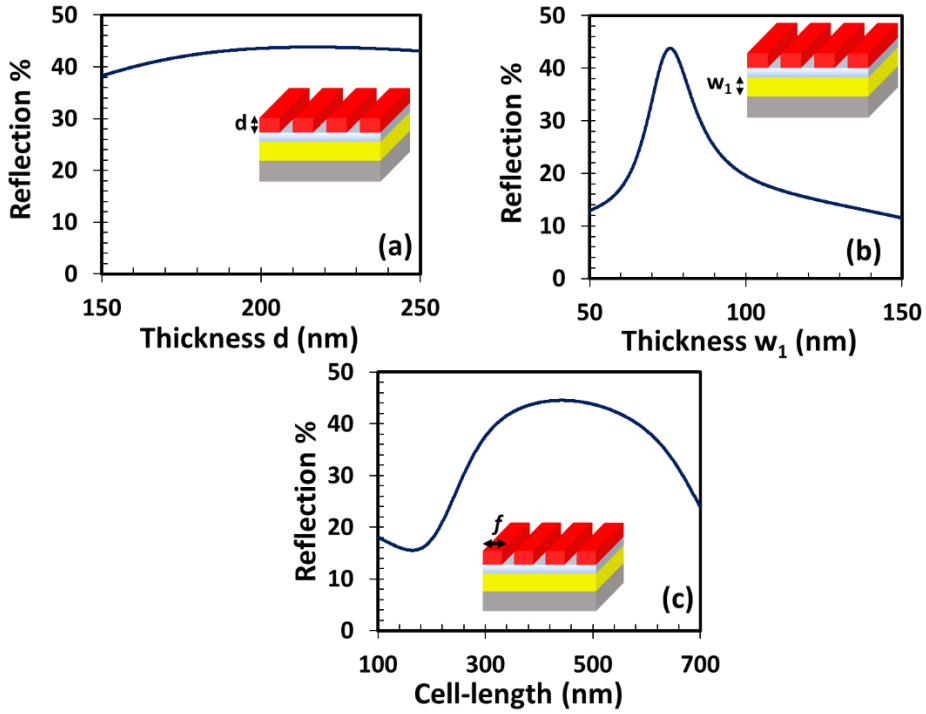

Figure 5.23: 1D scan of photoresist thickness d (w_1 ~ 70 nm, Λ = 1000 nm, f ~ 500 nm) (a), TiO_2 thickness w_1 (d ~ 210 nm, Λ = 1000 nm, f ~ 500 nm) (b) and cell length f (w_1 ~ 70 nm, d ~ 210 nm, Λ = 1000 nm) (c) vs reflection for exact value determination.

The above calculations complete the profile illustrated in the **Figure 5.24** with the following characteristics.

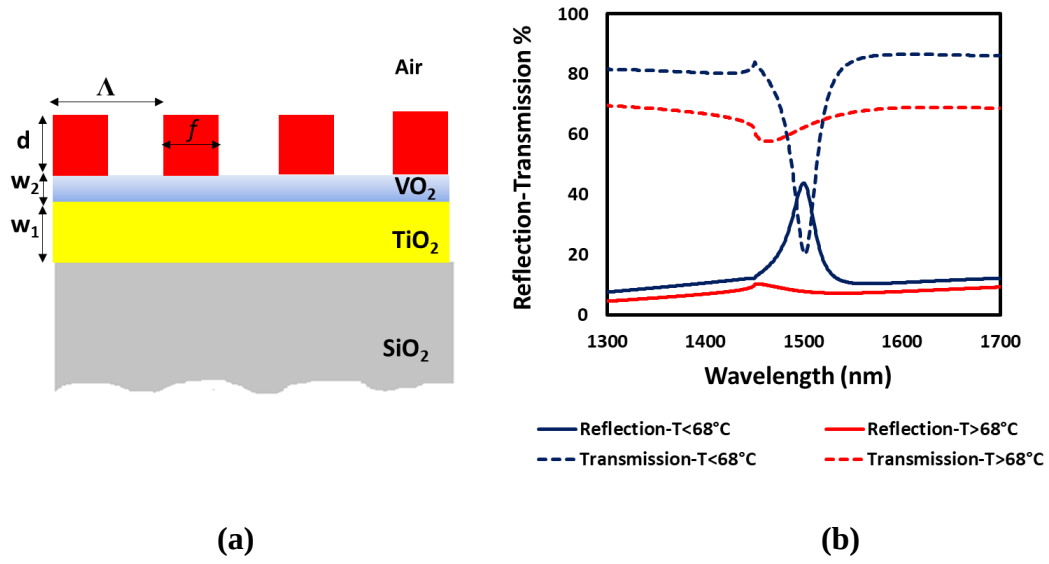

(a) **(b)**

Figure 5.24: Final structure for a resonance at λ = 1500 nm under normal incidence and TE polarization; d = 216 nm, w_2 = 27 nm, w_1 = 75 nm, Λ = 1000 nm and f = 440 nm (a), Simulated reflection and transmission amplitudes of the structure when VO_2 is in dielectric or metallic phase (b).

As observed in the 2D scan of **Figure 5.22** and in the **Figure 5.24-b** an emerging discontinuity is revealed at 1450 nm in both reflection and transmission. This artifact is attributed to Wood's anomalies that are responsible for appearance or disappearance of evanescent orders in the non-propagative layers. To localize better the phenomenon, a "wavelength vs reflection" scan is performed while the positive photoresist or the substrate refractive index is alternatively modified.

Setting for instance, n_g = 1.9 or n_g = 1.6 for the photoresist layer and fixing n_s = 1.45 for the substrate, the same discontinuity remains at λ = 1450 nm **(Figure 5.25)**. On the opposite, when reducing or increasing the refractive index of the substrate with a fixed photoresist at n_g = 1.67, the discontinuity shifts to inferior or superior wavelengths according to: $\lambda = n_s\Lambda$. This can clarify the hypothesis that the emergence or disappearance of evanescent orders takes place likely in the substrate region.

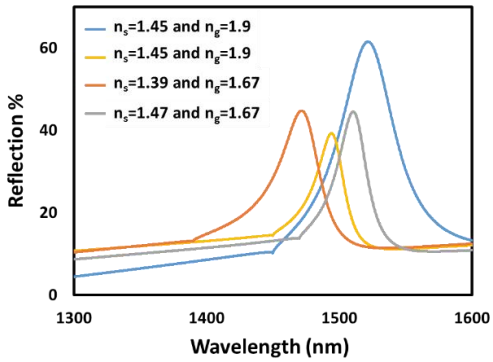

Figure 5.25: 1D Wavelength vs Reflection scan for Wood's anomaly detection in grating or substrate region.

The on and off effect of the proposed VO_2-based device is additionally confirmed by the electric field distribution in TE polarization (E_y component) along the propagation direction z for one grating period along x **(Figure 5.26)**.

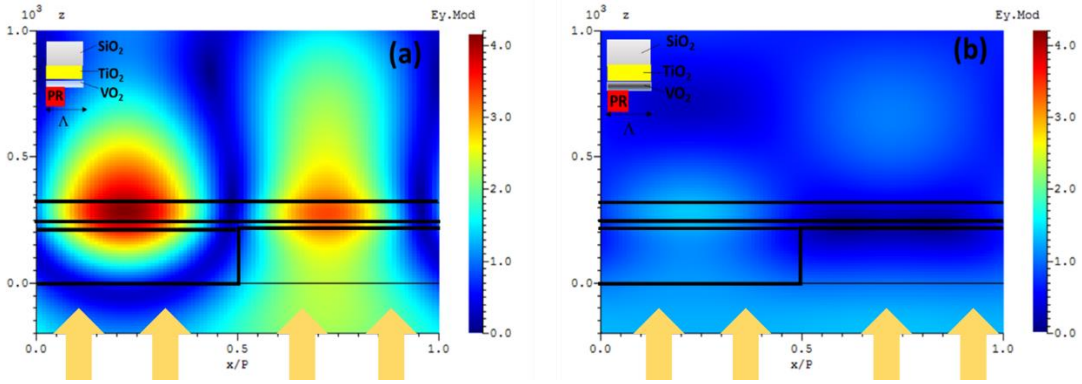

Figure 5.26: Distribution of the electric field of the fundamental mode at the wavelength of λ = 1500 nm. Activation of resonance when VO_2 is in the dielectric phase with n = 2.22 and k = 0.11 (a), or total depletion of resonance when VO_2 is in the metallic state with n = 1.95 and k = 1.29 (b).

The inverted cross section of one-unit cell at a large-scale z **(Figure 5.26)** contains an energy of 4 orders higher for the dielectric state than the corresponding of the metallic phase. In the proposed thin monomode structure, a small amount of electric field crosses the VO_2 film bearing absorption whereas a part scatters in the substrate. Since we consider the fundamental mode, the electric field amplitude is distributed in the bi-layer (TiO_2 and VO_2 layers). This leads to reduced performance with less reflection amplitude compared to the previous VO_2 magnetron sputtered structure. However, the targeted device can still exhibit the required switching effect since the ratio between cold and hot state is rather significant.

In both approaches, the maximum resonance efficiency is between 40% and 60%, which confirms VO_2 layer is a lossy layer even in its dielectric phase.

5.4 Fabrication and structural characterization for PLD and magnetron sputtering based designs

5.4.1 Fabrication

Having confirmed the activation and efficiency of VO_2 film by spectroscopy measurements **(Chapter 4, Section 4.5.1)** we proceed to the additional deposition of Si_3N_4 layer for the first design and further photoresist deposition and patterning for both.

A positive S1805 photoresist diluted with 50% Ethyl Lactate is spin-coated at 3000 rpm and soft-baked for 1 min for strong substrate adhesion. The set-up of **Figure 2.27** enabled a proper adjustment of period at Λ = 950 nm and Λ = 1000 nm by moving forward or backward the substrate holder. Using the interferential lithography method, we have UV light exposed the multilayers under a 442 nm continuous laser radiation for 5 min. A following 15 sec development in a basic solution revealed the interferogram pattern.

5.4.2 Structural characterization

The diagnosis by AFM and SEM analysis identified the profile and structural features of the structure and allowed to determine the actual parameters of the fabricated structures. Prior Littrow measurements have confirmed the accuracy of the 1D linear grating period at 1μm for the PLD VO_2 design (2^{nd} approach) and 950 nm for the magnetron sputtering VO_2 design (1^{st} approach).

AFM grating profiles exhibit sinusoidal-like forms for both structures **(Figure 5.27)**. The grating depth of PLD VO_2 design is measured at 163.3 nm instead of the simulated 216 nm, whereas this of magnetron sputtering VO_2 structure results in about 30 nm less than the anticipated 225 nm. The PLD VO_2 profile specifically, noticed discontinuities at the half of the grating depth attributed probably to unequal distribution of radiation during light exposition.

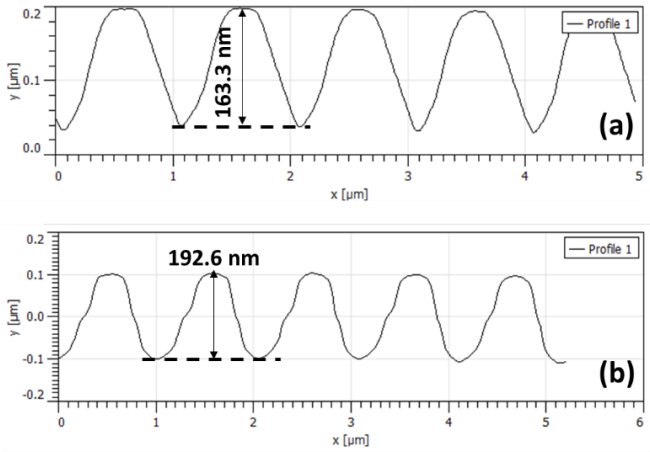

Figure 5.27: AFM images of grating profile of magnetron sputtering VO_2 design (a) and PLD VO_2 design (b).

The other structural parameters are extracted from SEM cross-section images illustrated in the **Figure 5.28**.

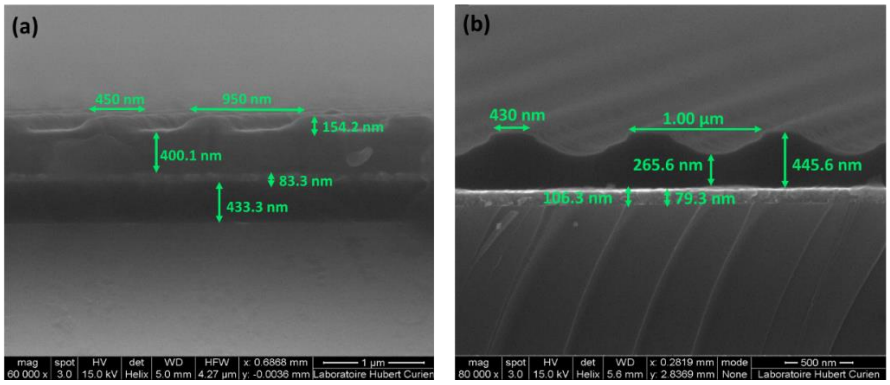

Figure 5.28: Cross section of SEM image of the $SiO_2/Si_3N_4/VO_2/Si_3N_4$/ PR (a) and SiO_2/TiO_2 (A)/VO_2/PR (b) samples.

Combining cross-sectional SEM and AFM images, we obtained a sinusoidal rather than a rectangular grating profile. Furthermore, a large deviation for the grating depths is revealed in both cases.

Even if the standard photoresist deposition method on TiO_2 layers leads to a thickness of approximately 250 nm following the described fabrication protocol, the photoresist layer is highly dependent to the underlying layers. In Magnetron sputtering, the Si_3N_4 layer on which the photoresist is deposited is probably sufficiently porous and causes strong adhesion leading thus to thinner coating. In contrast, in the PLD design, the main reason for the grating depth decrease is the high reflection coefficient of the VO_2 layer that blocks the insolation process,

due to standing waves in the photoresist layer during the exposure. This can reduce the exposure intensity and cause interference between the reflected light with the incoming light. A deposition of an anti-reflection BARC layer is however excluded due to its absorption and the mismatch of its refractive index. In both cases, the optical responses will be modified compared to the ones described in **Section 5.5.3.**

Concerning the fabricated layers, the VO_2 thicknesses (w_2 = 83 nm and 27 nm) are the same as those simulated (w_2 = 80 nm and 25 nm) for both designs.

For the magnetron sputtering VO_2 structure, the Si_3N_4 layers thicknesses show an average mismatch of ~ 50 nm compared to these of the design (w_1 = 400 nm instead of 435 nm and w_3 = 433 nm instead of 502 nm) whereas the TiO_2 layer thickness (w_1 = 79 nm) for the PLD VO_2 structure agrees with the initial design (w_1 = 75 nm).

5.5 Highlighting the thermal switching effect

5.5.1 Analysis of the simulated optical responses

After SEM and AFM diagnosis, the real structural parameters were set in the simulation program and the optical responses were compared to the initial simulated values of the optimized structures shown in **Figure 5.16-b** (for the structure performed with magnetron sputtering) and in **Figure 5.24-b** (for the PLD structure) **(Figure 5.29)**.

The magnetron sputtering VO_2 design is now simulated with the measured values of: Λ = 950 nm, d = 154.2 nm, w_1 = 400.1 nm, w_2 = 83.3 nm and w_3 = 433.3 nm, whereas the PLD VO_2 design with Λ = 1000 nm, d = 180 nm, w_1 = 79.3 nm and w_2 = 27 nm.

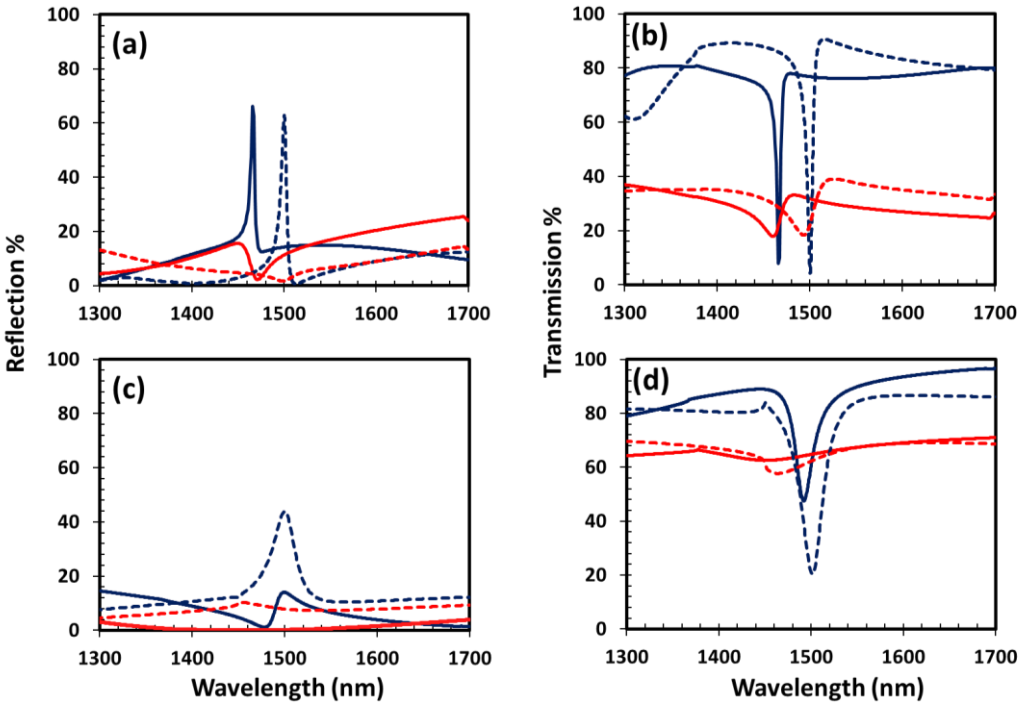

Figure 5.29: Comparison of reflection and transmission of the simulated resonance responses for both approaches during heating (T > 100°C-red lines) and cooling (room temperature-blue lines) of the structures: optimized structures (dashed lines) and structures after SEM and AFM diagnosis (solid lines), $SiO_2/Si_3N_4/VO_2/Si_3N_4$/ PR (a) (b) and SiO_2/TiO_2 (A)/VO_2/PR (c) (d).

As observed in the graphs, the superposed simulated responses exhibit some significant differences in amplitude and shape. As first estimate, these dissimilarities are mainly due to change in the grating patterns. In both cases, the grating depths are smaller than the initial simulated ones and the profiles are rather sinusoidal than rectangular according to the SEM and AFM images. As simulated, non-binary profiles, reduce the optical responses by ~ 15% compared to the optimized initial structures (rectangular profile).

For the magnetron sputtered structure, the resonance peak in reflection and transmission is shifted towards the smaller wavelength of λ = 1470 nm instead of that of λ = 1500 nm. This is attributed to the reduced thickness of layers, which results in the displacement of the peak at a shorter wavelength, the increase of the baseline level and the decrease of ~ 15% of the total amplitude.

For the PLD structure, the SEM simulated responses exhibit also lower resonance efficiencies compared to the ones initially simulated (10% amplitude in reflection instead of 40%). Except from the non-rectangular profile, additional suppression is caused by the unstructured part of the photoresist layer that weakens the mode coupling. However, the resonance peak coincides with the initial simulated peak position at λ=1500 nm.

5.5.2 Measurement Principle

After the fabrication of the PLD or magnetron sputtered layers, the photoresist was deposited and patterned. Then, the completed switching devices were tested with infrared spectrometry in reflection and transmission for resonance efficiency measurements **(Section 5.5.3)**.

Transmission measurements for both structures are performed with the spectroscopy set-up shown in Chapter 4, which is used to evaluate the optical resonance of VO_2 based layers. (**Figure 4.16**).

The adapted set-up for reflectance is configured with a 50/50 fiber coupler of three arms; one connected to Halogen Source, one to the NIR spectrometer and one in front of the sample **(Figure 5.30)**. A NIR linear polarizer (LP) controls the polarization of the incident beam. The assembly for heating control is remained identical as for the transmittance measurements **(Section 4.3.5.1**).

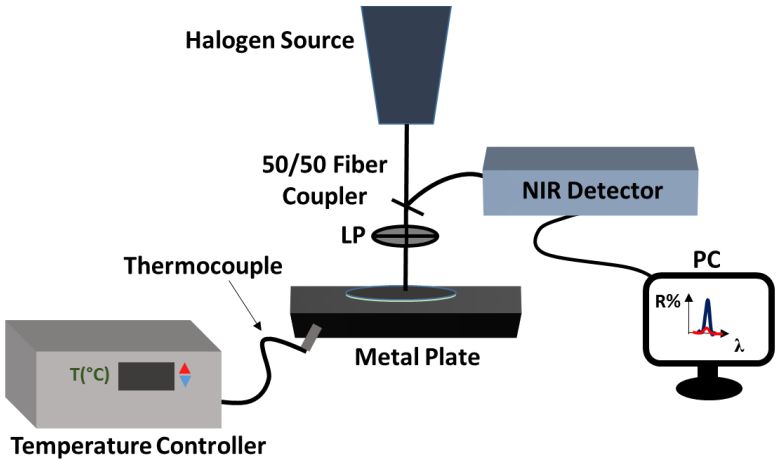

Figure 5.30: Schematic of the set-up for characterization in reflectance (corresponding set-up in Figure 4.16 for transmission measurements).

The measured values are obtained by normalizing the signal passing through - or reflected by - the sample with the direct transmitted signal in air - or with the reflected signal by a reference mirror. The software associated to the NIR spectrometer provides the normalized spectra for T < 68°C or T > 68°C.

5.5.3 Results and discussion

Figure 5.31 presents the experimental spectra of the first demonstrators (for both approaches) for the dielectric and metallic state superposed to the simulated spectra, after SEM and AFM analysis

The graphs testify a minor experimental response, yet thermally controlled resonance effect. The measured curves demonstrate a good proximity to the theoretical values but the obtained experimental amplitudes are significantly reduced. However, the measured curves present the same forms as the simulated peaks.

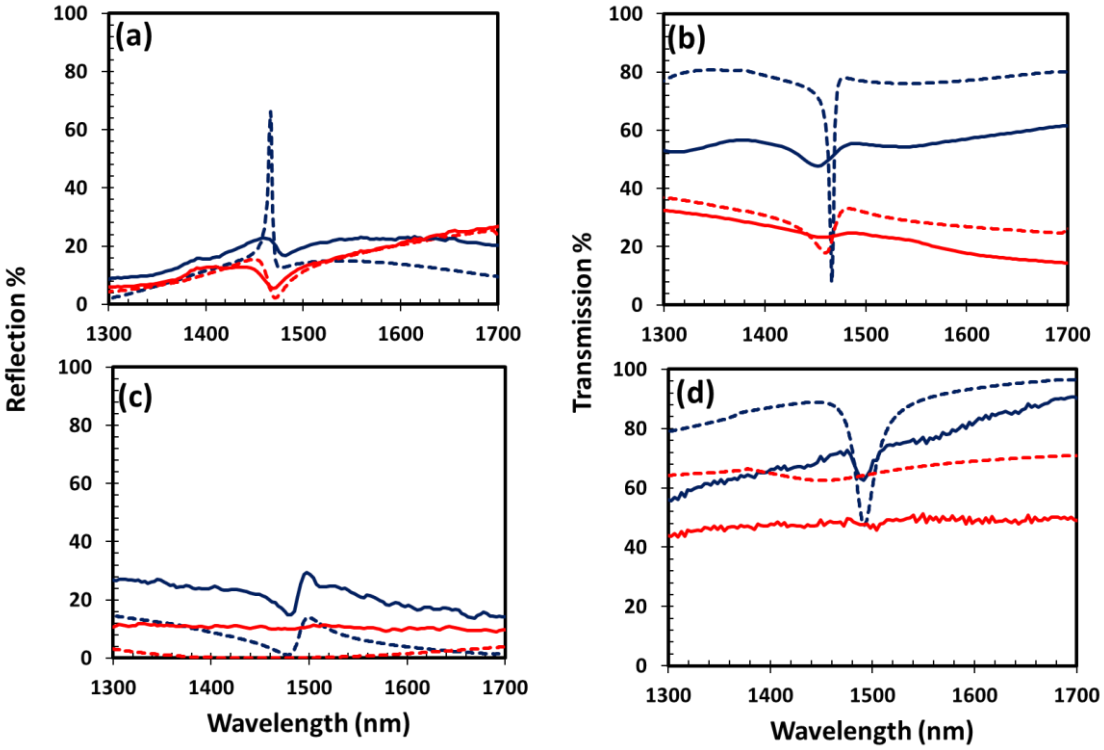

Figure 5.31: Superposition of the simulated spectra (dashed lines) - calculated with the real parameters of the structures - (solid lines) for magnetron sputtering VO_2 design (a), (b) and PLD VO_2 design (c), (d) in reflection and transmission.

For the magnetron sputtered VO_2 design, the experimental resonance peak in the dielectric state appears at 1470 nm with a 22% reflection and ~10% amplitude. In transmission, the peak reaches 50% and its amplitude is 5%.

For the PLD VO_2 design, the peaks are excited at 1495 nm in a very good proximity to the desired 1500 nm position. In the heated state, the experimental transmission peak is fully

canceled as forecasted by the simulation. At 1495.8 nm in the dielectric state, the resonance peak presents 13% amplitude in reflection while 15% amplitude in transmission.

For both devices, it is noted a resonance widening.

There are several assumptions for explaining these poor resonances for both demonstrators.

First, the grating inhomogeneities in terms of duty cycle, grating depth, roughness and photoresist residual in the grating lines reduce the resonance efficiency due to non-constant effective index along the propagation length of the waveguide mode and provoke scattering losses. Main problem of the grating printing is probably the fact that the grating is not opened down to the underlying layers (VO_2 or Si_3N_4) and the residual photoresist layer is still present. This effect reduces considerably the mode coupling with the grating. Major improvements must be performed in order to pattern gratings with laser interference lithography.

Secondly, the roughness between the interfaces of the stacked layers must also be taken also into account because it can lead to scattering and diffusion effects and once again reduce the resonance efficiency.

Finally, the experimental measuring set-up must be significantly improved mainly for the reflection measurements with an accurate measurement of the reference (100% reflection mirror) in order to perform calibrated spectra.

In the overall and comparing both devices, the optical responses of PLD VO_2 structure proved to be more performant than those of magnetron sputtered VO_2 configuration. This fact allows roughly in concluding that a thinner VO_2 layer can lead to better resonance responses due to less absorption losses.

5.6 Conclusion

This chapter demonstrates two different designs for thermally activated optical switches in reflection operating under the dielectric resonance effect. The proposed designs couple modes into the waveguides or absorb incident light thanks to the integrated VO_2 layer acting as a lossy waveguide or a complete absorbing layer (metallic phase). Using the principle of a monomode (TiO_2 (A)/VO_2) or bimodal (Si_3N_4/VO_2/ Si_3N_4) waveguide structure, the designs were optimized by simulation programs to achieve the highest resonance in reflection at 1500 nm. The first results from the simulation analysis revealed greater efficiency for the bimodal approach due to the adjusted field distribution away from the absorbent VO_2 film. The bimodal

configuration is fabricated by magnetron sputtering method whereas the monomode by PLD technique and TiO_2 solgel deposition. For both designs, a positive photoresist layer is structured on the top to form a grating.

The final optical characterization step of the first WRG demonstrators exhibited the worst resonance response for the magnetron sputtered structure while mediocre performance for the PLD VO_2 device. The AFM and SEM analysis exhibited structural deficiencies in both configurations resulting in differences from the initially simulated profiles, which contribute to inadequate optical efficiencies.

In reviewing this study, even the minor resonant responses were able to exhibit the first demonstrator of a VO_2 thermally induced sensor. Future work will try to resolve the structural (mainly grating) issues and reduce the absorption losses. The targeted application is the development of a VO_2 based optical switch for integration in laser cavities and demonstration of Q-switching effect.

Bibliography

[1] Q. Wang, J. Yao, "A high speed 2×2 electro-optic switch using a polarization modulator", *Opt. Express.* 15 (2007) 16500–16505.

[2] X. Fang, L. Yang, "Thermal effect analysis of silicon microring optical switch for on-chip interconnect", J. Semicond. 38 (2017) 104004.

[3] D.A. Smith, R.S. Chakravarthy, Z. Bao, J.E. Baran, J.L. Jackel, A. d'Alessandro, D.J. Fritz, S.H. Huang, X.Y. Zou, S.- Hwang, A.E. Willner, K.D. Li, "Evolution of the acousto-optic wavelength routing switch", J. Light. Technol. 14 (1996) 1005–1019.

[4] S. O'Brien, D. McPeake, S.A. Ramakrishna, J.B. Pendry, "Near-infrared photonic band gaps and nonlinear effects in negative magnetic metamaterials", Phys. Rev. B. 69 (2004) 241101.

[5] A. Ghanekar, Y. Tian, M. Ricci, S. Zhang, O. Gregory, Y. Zheng, "Near-field thermal rectification devices using phase change periodic nanostructure", *Opt. Express.* 26 (2018) A209–A218.

[6] J. Liang, J. Guo, Y. Zhao, Y. Zhang, T. Su, "Localized surface plasmon resonance modulation of totally encapsulated VO_2/Au/VO_2 composite structure", *Nanotechnology.* 29 (2018) 275710.

[7] H. Wang, Y. Yang, L. Wang, "Switchable wavelength-selective and diffuse metamaterial absorber/emitter with a phase transition spacer layer", *Appl. Phys. Lett.* 105 (2014) 071907.

[8] H. Wang, Y. Yang, L. Wang, "Wavelength-tunable infrared metamaterial by tailoring magnetic resonance condition with VO_2 phase transition", *J. Appl. Phys.* 116 (2014) 123503.

[9] Z. Liu, M. Zhao, J. Gao, Y. Li, S. Jiang, "Thermally tunable broadband omnidirectional and polarization-independent super absorber using phase change material VO_2", *Results Phys.* 7 (2017) 4222–4225.

[10] K. Sun, C.A. Riedel, A. Urbani, M. Simeoni, S. Mengali, M. Zalkovskij, B. Bilenberg, C.H. de Groot, O.L. Muskens, "VO_2 Thermochromic Metamaterial-Based Smart Optical Solar Reflector", *ACS Photonics.* 5 (2018) 2280–2286.

[11] S.-J. Kim, S. Choi, C. Choi, Y. Lee, J. Sung, H. Yun, J. Jeong, S.-E. Mun, Y.W. Lee, B. Lee, "Broadband efficient modulation of light transmission with high contrast using reconfigurable VO_2 diffraction grating", *Opt. Express.* 26 (2018) 34641–34654.

[12] M. Afshari-Bavil, M. Dong, C. Li, S. Feng, L. Zhu, "Thermally controllable perfect absorber at telecommunication spectrum based on phase change material and cavity grating", *Laser Phys.* 30 (2019) 026201.

[13] V. Jeyaselvan, A. Pal, A. Pal, P.S.A. Kumar, S.K. Selvaraja, "Thermally-induced optical modulation in a vanadium dioxide-on-silicon waveguide", *OSA Contin.* 3 (2020) 132–142.

[14] A. Thomas, P. Savaliya, K. Kumar, A. Ninawe, A. Dhawan, "Au nanowire-VO_2 spacer-Au film based optical switches", *JOSA B.* 35 (2018) 1687–1697.

[15] Y.-F. Zhang, Y. Wang, Y.-Q. Wu, C.-M. Liu, X.-D. Lu, T. Zhou, "Study on Improving the Absorption Efficiency of Uncooled Infrared Sensor by Using Grating", *DEStech Trans. Comput. Sci. Eng.* 0 (2018).

[16] Y. Sharma, V.A. Tiruveedhula, J.F. Muth, A. Dhawan, "VO_2 based waveguide-mode plasmonic nano-gratings for optical switching", *Opt. Express.* 23 (2015) 5822–5849.

[17] J. Jeong, A. Joushaghani, S. Paradis, D. Alain, J.K.S. Poon, "Electrically controllable extraordinary optical transmission in gold gratings on vanadium dioxide", Opt. Lett. 40 (2015) 4408–4411.

[18] V. Melnik, I. Khatsevych, V. Kladko, A. Kuchuk, V. Nikirin, B. Romanyuk, "Low-temperature method for thermochromic high ordered VO_2 phase formation", *Mater. Lett.* 68 (2012) 215–217.

General Conclusion

The principal axis of this PhD thesis focuses on the study of Waveguide Resonant Gratings (WRG). These structures use subwavelength gratings of high spatial frequency to couple incident light into waveguide modes supported by thin waveguides. The out-coupling of light leads to an anomalous sharp reflection with strong dependence on wavelength, polarization and incident angle. Hence, a fine optical filtering is allowed, which is exploited in sensing applications.

Interested in the properties of optical filtering, this thesis experiments with original WRG designs, either by presenting special and less common geometries or by introducing smart materials as waveguide layers in such configurations. Particularly, it investigates the operation principle, design and fabrication of WRG by organizing its content in five Chapters.

The 1st Chapter provided an overview of the history of Waveguide Resonant Gratings, which includes a thorough research of different groups over the years to understand and develop these structures. In this context, mathematical and geometrical representations (Ewald sphere) are used to represent the interaction of the wave vectors within the resonant configurations. A separate study of angles, polarization and structural profile also revealed the impact on optical responses, especially in amplitude and bandwidth, when adjusting these characteristics. Therefore, for proper feature tailoring and resonance optimization, a rigorous design is necessary. Some popular numerical methods, such as C-method, RCWA or integral methods have been developed to simulate all the aforementioned parameters for maximum control of optical responses. In this thesis, “MC Gratings”, based on the RCWA method, with Modal Collinear programming was dedicated to accurately simulate the targeted WRG structures, which are mainly binary. A brief description of the numerical methods is given. During this PhD thesis, no further developments in modeling took place, as the commercial codes used were accurate enough to propose well-adapted designs.

After the theoretical study, the 2nd Chapter introduced all the techno-optical processes employed to construct well-controlled gratings and uniform layers. For the accomplishment, proper expertise, detailed engineering and suitable optical microstructural tools were involved. The properties of photoresists were described while the importance of the good selection was highlighted in compatibility to the deposition methods (spin and dip coating) and laser interferential lithography. In the frame of this work, a solgel-based resist was chosen for the

waveguide fabrication, whereas the deposition of the positive photo resist was applied exclusively for grating micro patterning.

The 3rd Chapter, presented one of the main projects of this thesis; the cylindrical WRG. These geometries were designed to support WRGs thanks to the radial phase mask technology that enables easy grating patterning only by diffracting the ±1st orders. Such WRG configurations benefit from the same operational principle as the common flat WRGs, since they are based on the idea that an 8 mm cylindrical diameter (much larger than 8 grating periods) is comparable to planar WRGs, as demonstrated by Ohtera *et al.* Then, cylindrical waves can be considered similar to plane waves and excite the same resonant responses. Unlike to the already demonstrated cylindrical WRG (PhD thesis of Loic Berthod), this project exhibits the WRG, consisted of a solgel-based waveguide and a positive photoresist grating, in the interior walls of an 8 mm silica tube. The structure is proposed for gas or liquid sensing applications. The fabrication process was the same, since the phase mask is capable to operate equally well for cylinders and tubes. However, this time the functionality of the structure is perceived by the setting of a special 90° apex conical mirror that transposes plane to cylindrical waves. The mirror was inserted into the hollow of the tube and reflected the incident light holistically in order to excite both TE and TM resonances in the near infrared range as it was originally modelled. Nevertheless, the experimental measurement by spectroscopic means revealed only the TE resonance at λ~1450 nm. The structural analysis with FIB and SEM sheds light to the deficiency, which was attributed to the smaller diameter of the tube than the industrial indicated, to grating defects and to slight misalignments of tube with the radial phase mask. The knowledge of the above parameters permitted to overcome these weaknesses by improving the current technique during the fabrication and characterization process as well.

In contrast to the previous geometric challenge, Chapter 4 now presented a material challenge by first studying the properties and the synthesis protocol of the interesting VO_2 material for further WRG integration. Therefore, it proceeded in the fabrication of VO_2 thin films by using two different techniques; the Pulsed Laser Deposition (PLD) and the magnetron sputtering process with the necessary post-thermal treatment for both. An almost comparative study between the two techniques was carried out and outlined the advantages and the drawbacks of each process.

The VO_2 displays a reversible first-order phase transition around the critical temperature of T~ 68 °C. Below this temperature limit, the material is in its dielectric state accompanied by a monoclinic crystal structure, while above it becomes metallic with a tetragonal-rutile structure.

According to the cooling or heated state, significant optical and electromagnetic changes in the visible and infrared (IR) range follow.

The PLD method tested different substrates such as amorphous fused silica, quartz and silicon substrates as well as SiO_2/anatase-TiO_2 heterostructures. The exact recipe of VO_2 was determined after various oxygen pressures during deposition and annealing process with rapid thermal annealing (RTA), but also after different annealing temperatures. To avoid optical absorptions from the VO_2, the PLD process was used to fabricate the thinnest possible layer at 25 nm. The oxygen pressure that led this film to phase transition was found to be at 3 Pa for PLD and at 100 Pa for RTA annealing. Concerning the annealing temperature, it was observed that 300 °C did not exhibit any phase transition while 450 °C offered the best transmission response. However, the transition temperature maintained at 350 °C during the experimental process, as it provided almost the same optical transition as 450°C at λ=1500 nm after heating and cooling. In an effort to minimize the annealing temperature as much as possible compared to the majority of synthesis methods that require higher temperatures and longer thermal treatments, low annealing temperatures such as 350 °C, favor annealing with many substrates such as standard amorphous glasses with low melting point.

Alternatively, the magnetron sputtering method managed to deposit 80 nm, as the minimum thin layer. The synthesis protocol included also a post annealing at 550°C by a homemade vacuum furnace. The VO_2 was deposited and incorporated inside a Si_3N_4 layer to prevent oxidation. However, before capping with the top Si_3N_4 layer, the Si_3N_4/VO_2 bilayer was tested spectrally and compared with the corresponding PLD stack of TiO_2 (A)/ VO_2, exhibiting a better optical transition by 20%, lower transition temperature and smaller hysteresis width.

The final Chapter applied the study and expertise of Chapter 4, in order to integrate the thin VO_2 layers of PLD or magnetron sputtering into WRG configurations under different designs for Q-switching applications. The present work aims the demonstration of the resonant effect. The proposed structures were designed as follows: SiO_2/ TiO_2 (A)/VO_2 with a monomode TiO_2 (A)/VO_2 waveguide and a $SiO_2/Si_3N_4/VO_2/Si_3N_4$ with a bimodal $Si_3N_4/VO_2/Si_3N_4$ waveguide. Both are covered by a positive photoresist corrugation. The designs are prior simulated and optimized for a waveguide resonant excitation at λ=1500 nm. After fabrication, they were spectrally tested in reflection. They showed minimum resonant responses with the magnetron sputtered design having a slight worse optical response than this of PLD. For both, the poor responses were mainly attributed to the high reflective VO_2 layers, which prevented proper deposition of the grating leading to sinusoidal rather than rectangular profiles. After AFM and

SEM analysis, structural defects are also revealed that impoverished further the responses. To resolve such problems, alternative designs or different methods of depositing the photoresist layer will be proposed.

As a general conclusion, this PhD thesis permitted to start and evaluate perspectives with two different approaches. Even though results in terms of efficiencies are far from the expected ones, perspectives concern both approaches.

As for the WRG in the tube, further developments are taking place, as we have already demonstrated that resonant reflection occurs in a coherent (stitchingless) grating inside a tube. Current developments mainly concern the measurement set-up that alternatively can use a monolithic tube with the cone fabricated directly inside the tube avoiding the complex alignment procedure.

Concerning the thermally activated VO_2 based WRG, we have to consider compromises between losses and efficiency of the 0^{th} resonant reflection to propose ambitious and ingenious structures. Nevertheless, we plan to continue the developments within a new project financed by the Labex Manutech SISE. Scientific objective of the project aims to achieve such resonant component at different switching temperatures (using various dopants), significantly below 67 ° C, while maintaining acceptable amplitudes and hysteresis, in order to broaden the fields of application of optical switches.

In the overall, this PhD thesis has revealed the challenge to fabricate and measure respectively complex waveguide resonant gratings that lead to efficient resonant reflections. After facing the issues of fabrication and measurements (mainly for the WRG in the tube), we can conclude that lithography remains a critical process to achieve homogenous gratings. Our approach to printing gratings on a photosensitive layer should be pursued by direct photo patterning, for instance, Nanoimprint lithography (NIL) especially when considering planar gratings.